

# Nanophotonic split-ring resonators as dichroics for molecular spectroscopy

Alasdair William Clark

A THESIS SUBMITTED TO  
THE DEPARTMENT OF ELECTRONICS AND ELECTRICAL ENGINEERING  
FACULTY OF ENGINEERING  
UNIVERSITY OF GLASGOW  
IN FULFILMENT OF THE REQUIREMENTS FOR  
THE DEGREE OF DOCTOR OF PHILOSOPHY

## Abstract

The unique optical properties of metallic nanostructures have enabled the creation of a new generation of ultra sensitive biosensors based on vibrational spectroscopy. Through strict engineering of structural morphology, a nanometal's free electrons can be tuned to resonate at a particular frequency, resulting in amplification and confinement of the electromagnetic field around certain areas of the structure. Molecules situated within these areas experience a greater degree of polarisation due to the oscillating plasmon field, a phenomena which, when combined with resonance Raman spectroscopy, has been shown to enable single molecule detection.<sup>1, 2</sup>

This thesis describes the fabrication and plasmonic characterisation of Au and Ag circular nano split-ring resonators using a combination of electron beam lithography, finite difference time domain simulation and transmission spectroscopy. Through alteration of ring radius, arc length, wall width, metal thickness and metallic composition it is shown that the asymmetric split-ring structures exhibit a multi-modal, polarisation dependent plasmonic response that can be tuned over several microns. Such a response enables these geometries to be employed as novel multi-wavelength biosensors via surface enhanced Raman spectroscopy and surface enhanced resonance Raman spectroscopy.

This work goes on to demonstrate that by using electron beam lithography to manipulate the nano-scale geometry of Ag split-ring resonators, their optical properties can be tuned such that the structures exhibit two independently addressable, high frequency plasmon resonance modes for SERRS. In a series of sensing experiments it is shown that this tailored, multi-modal, polarisation dependent activity enables the split-rings to act as discriminating sensors, with each resonance tuned for a particular sensing purpose. Ultimately the structures are used as multi-wavelength, multi-analyte DNA SERRS sensors, with each resonance tuned both to the absorption wavelength of a differently coloured Raman reporter molecule and its corresponding laser excitation wavelength. In doing so, the ability of each resonance to independently sense clinically relevant concentrations of single DNA strand types from within a mixed population on the sensor surface is demonstrated.

## Publications

### Journals

A.W. Clark, A. Glidle, D.R.S. Cumming and J.M. Cooper, *Plasmonic split-ring resonators as dichroic nanophotonic DNA biosensors*, Journal of the American Chemical Society, UNDER REVIEW, 2009.

A.W. Clark, A.Glidle, D.R.S. Cumming and J.M. Cooper, *Nanophotonic split-ring resonators as dichroics for molecular spectroscopy*, Applied Physics Letters, 93, 2, 023121, 2008.

A.W. Clark, A.K. Sheridan, A.Glidle, D.R.S. Cumming and J.M. Cooper, *Tuneable visible resonances in crescent shaped nano-split-ring resonators*, Applied Physics Letters, 91, 093109, 2007.

A.K. Sheridan, A.W. Clark, A.Glidle, D.R.S. Cumming and J.M. Cooper, *Multiple plasmon resonances from gold nanostructures*, Applied Physics Letters, 90, 14, 143105, 2007

### Conference Papers

A. Cleary, A.W. Clark, A.Glidle, D.R.S. Cumming and J.M. Cooper, *Fabrication of double split metallic nanorings for Raman sensing*, Microelectronic engineering, 86, 4-6, 1146, 2009.

A.K. Sheridan, A.W. Clark, A.Glidle, D.R.S. Cumming and J.M. Cooper, *Fabrication and tuning of nanoscale metallic ring and split-ring arrays*, Journal of vacuum and science technology B, 25, 6, 2628, 2007.

## Table of contents

List of Figures .....	9
Acknowledgements .....	20
Author's declaration .....	21
Chapter 1 - Introduction and theory .....	22
Abstract .....	22
1.1 Nanoplasmonic biosensors .....	22
1.2 Interaction of light with metal .....	23
1.2.1 Surface Plasmons and Surface Plasmon Resonance (SPR) .....	23
1.2.2 Localised surface plasmons in nanoparticles .....	26
1.3 Tuning localised surface plasmon resonances and characteristics in metallic nanoparticles .....	28
1.3.1 Size dependence of isolated, non-interacting nanoparticles .....	29
1.3.2 Shape dependent field enhancements - Hot-spot generation at sharp tips .....	30
1.3.3 Interparticle interactions .....	30
1.3.4 Multipolar resonances .....	31
1.3.5 Nano-rings and Nano-crescents .....	32
1.3.6 Nano split-ring resonators .....	32
1.4 Raman spectroscopy .....	33
1.4.1 The Raman scattering effect .....	33
1.4.2 Molecular vibrations .....	35
1.4.3 Resonance Raman .....	35
1.4.4 Surface enhanced Raman scattering (SERS) by nanoparticle plasmonics .....	37
1.5 Theoretical summary and preamble of experimental work described herein .....	39
Chapter 2 - Materials and Methods .....	41
Abstract .....	41
2.1 Introduction .....	41
2.2 Materials .....	41
2.3 Methods .....	42
2.3.1 Fabrication of Au and Ag split-ring structures .....	42
2.3.1.1 Cleaning .....	42
2.3.1.2 Resist Spinning .....	43
2.3.1.3 Charge Conduction Layer .....	43
2.3.1.4 Patterning the resist using electron-beam lithography .....	43
2.3.1.5 Development .....	44
2.3.1.6 Au Metallisation and lift-off .....	44
2.3.1.7 Ag Metallisation .....	44
2.3.1.8 Surface modification with 3-aminopropyltriethoxysilane .....	45
2.3.1.9 Ti/Ag evaporation .....	45
2.3.2 Fabrication of a free standing, nanoporous membrane aligned to plasmonic split-ring structures. ....	45
2.3.2.1 Patterning split-rings with alignment markers .....	46

2.3.2.2 Patterning and etching of the nanopores .....	47
2.3.2.3 Fabricating nitride membrane .....	47
2.3.3 Physical and optical characterisation.....	49
2.3.3.1 Absorption spectroscopy .....	49
2.3.3.2 Scanning electron microscopy (SEM).....	50
2.3.3.3 Atomic force microscopy (AFM) .....	50
2.3.4 Finite difference time domain (FDTD) simulations .....	50
2.3.5 Chemical and biological modification of sensor surface.....	50
2.3.5.1 Modifying the Ag sensor surface with 2-mercaptopyridine.....	50
2.3.5.2 Modifying the Ag sensor surface with cysteamine/Cy5 NHS .....	50
2.3.5.3 Modifying the Ag sensor surface with thiolated oligonucleotides.....	51
2.3.5.4 Hybridisation .....	51
2.3.6 Surface characterisation via X-ray photoelectron spectroscopy (XPS) .....	51
2.3.7 Fluorescence microscopy .....	51
2.3.8 Raman spectroscopy and surface enhanced Raman spectroscopy (SERS).....	52
2.3.8.1 Raman spectroscopy at 633 nm and 785 nm.....	52
2.3.8.2 Raman spectroscopy at 532 nm.....	52
2.4 Results and Discussion - Problems and solutions associated with nano split-ring fabrication.....	52
2.4.1 Effect that resist thickness has on high resolution patterns .....	52
2.4.2 Consequences of over and under exposure through incorrect choice of electron beam dose .....	53
2.4.3 Consequences of inconsistent Ti - Ag adhesion .....	53
2.5 Conclusion.....	54
Chapter 3 - Characterisation of Au split-ring resonators .....	55
Abstract .....	55
3.1 Introduction.....	55
3.2 Materials .....	56
3.3 Methods.....	56
3.3.1 Fabrication of 135 nm radius Au rings with varying arc-lengths.....	56
3.3.2 Fabrication of Au split-rings with varying radius.....	56
3.3.3 Fabrication of 75 nm radius Au rings with varying arc-lengths .....	57
3.3.4 Fabrication of split-rings with varying height/thickness of Au .....	57
3.3.5 Fabrication of Au split-rings with varying periodicity.....	57
3.4 Results and discussion .....	57
3.4.1 Tuning and characterisation of 135 nm radius rings.....	57
3.4.2 Plasmonic effect of radius alteration in Au split-rings.....	64
3.4.3 Tuning and characterisation of 75 nm radius rings .....	66
3.4.4 Plasmonic effect of height/thickness alteration in Au split-rings.....	70
3.4.5 Plasmonic effect of periodicity alteration in Au split-rings .....	72
3.5 Conclusion.....	73
Chapter 4 - Ag split-ring resonators as molecular sensors .....	74

Abstract .....	74
4.1 Introduction.....	74
4.2 Materials .....	75
4.3 Methods .....	75
4.3.1 Fabrication of 75 nm radius Ag split-rings .....	75
4.3.2 Fabrication of 80 nm radius Ag split-rings .....	75
4.3.3 SERS of 2-mercaptopyridine using 532 nm and 633 nm lasers .....	76
4.3.4 SERS of 2-mercaptopyridine using 633 nm and 785 nm lasers .....	76
4.3.5 SERS of 2-mercaptopyridine immobilised on split-ring arrays with varying second order resonance peak wavelengths using a 633 nm laser .....	76
4.3.6 Storage of Ag and Au capped Ag rings in PBS.....	76
4.4 Results and discussion .....	76
4.4.1 Plasmonic comparison of 75 nm Au and Ag rings with changing arc-length .....	76
4.4.2 Tuning the dichroic resonances of Ag split-rings to common laser wavelengths .....	79
4.4.3 Reproducibility of resonances using chemically adhered Ag.....	80
4.4.4 Ti as an adhesion layer.....	81
4.4.5 Ag split-rings as molecular sensors.....	83
4.4.5.1 Ag split-rings as dichroics for molecular spectroscopy at 633 and 532 nm .....	83
4.4.5.2 Ag split-rings as dichroics for molecular spectroscopy at 785 and 633 nm .....	90
4.4.5.3 Demonstrating the significance of specifically tuned resonances .....	92
4.4.6 Curbing the degradation of plasmonic response in Ag rings using Au capping .....	94
4.5 Conclusion .....	95
Chapter 5 - Plasmonic Split-Ring Resonators as Dichroic Nanophotonic DNA Biosensors .....	97
Abstract .....	97
5.1 Introduction.....	97
5.2 Materials .....	98
5.3 Methods .....	98
5.3.1 Modification of sensor with thiolated, Cy5 labelled oligonucleotides and Cy5 N-Hydroxysuccinimide ester .....	99
5.3.2 Hybridisation of fully, partially and non-complementary sequences to probe oligonucleotides immobilised on the sensor .....	99
5.3.3 Hybridisation of oligonucleotides with different dye arrangements (Cy5 located at either the 3' or 5' position) to a probe sequence immobilised on the sensor.....	99
5.3.4 Competitive hybridisation of labelled and non-labelled oligonucleotides.....	100
5.3.5 Hybridisation of Cy7 labelled oligonucleotides to probe strands immobilised on the sensor .....	100
5.3.6 Competitive hybridisation of Cy5 and Cy7 labelled oligonucleotides to a probe sequence immobilised on the sensor - 1:1 ratio.....	100
5.3.7 Competitive hybridisation of different ratios of Cy5: Cy7 labelled oligonucleotides to a probe sequence immobilised on the sensor.....	100
5.4 Results and Discussion .....	101
5.4.1 Nano Split-ring resonators as sensors for labelled DNA detection .....	101

5.4.2 Detection via hybridisation.....	104
5.4.3 Impact of label proximity to sensor surface.....	106
5.4.4 Competitive hybridisation assay using labelled and unlabelled sequences.....	107
5.4.5 Dichroic plasmonic split-rings as multiple-analyte optical nanosensors .....	109
5.5 Conclusion.....	113
Chapter 6 - Future Work .....	114
Abstract .....	114
6.1 Introduction.....	114
6.2 Materials .....	114
6.3 Methods.....	114
6.3.1 Fabrication of nanoporous membrane aligned a plasmonic split-ring resonator array ..	114
6.3.2 Fabrication of a 60 nm radius Au split-ring resonator array .....	115
6.3.3 Fabrication of an 80 nm radius Au split-ring resonator array with split sizes of 2-3 nm	115
6.4 Results and discussion .....	115
6.4.1 Nanofluidic delivery system for real-time molecular detection.....	115
6.4.2 Reducing feature size for greater sensitivity.....	117
6.5 Conclusion.....	119
Appendix.....	120
A.1 Supplementary device and process information .....	120
A.1.1 Electron beam lithography using the Vistec VB6 UHR EWF .....	120
A.1.1.1 Electron beam lithography.....	120
A.1.1.2 Vistec VB6 UHR EWF tool.....	121
A.1.1.3 Electron beam resist .....	121
A.1.2 Metal Evaporation .....	122
A.1.2.1 Plassys MEB 400S electron-beam evaporator.....	122
A.1.2.2 Resistive heating evaporator .....	123
A.1.3 Optical characterisation using a Shimadzu UV3101PC absorption spectrometer .....	124
A.1.4 Hitachi S-4700 Scanning electron microscopy (SEM) .....	125
A.1.5 Atomic Force Microscopy (AFM) .....	125
A.1.6 TEMPEST Finite Difference Time Domain (FDTD) software .....	125
A.1.7 X-ray Photoelectron Spectroscopy (XPS) using a Scienta ESCA300 XPS tool.....	128
A.1.8 Zeiss LSM 510 META confocal fluorescence microscope .....	129
A.1.9 Horiba Jobin Yvon Raman spectrometer .....	129
A.1.10 532 nm Raman set-up with Ocean Optics Spectrometer .....	131
A.1.11 Chemical structure of 2-mercaptopyridine .....	132
A.1.12 Chemical structure of 3-aminopropyltriethoxysilane.....	132
A.1.13 Chemical structures and binding mechanisms of Cysteamine and Cy5 N-Hydroxysuccinimide (NHS).....	133
Figure A.18 depicts the molecular structure of Cy5 N-Hydroxysuccinimide; consisting of a cyanine derived Cy5 dye and an NHS ester compound. ....	133
A.1.14 Modifying the Ag sensor surface with DNA .....	134
A.1.15 Chemical structure of Cy5 and Cy7 linked to an oligonucleotide strand .....	135

A.1.16 Reduction of the thiol groups on the DNA.....	136
References .....	138

## List of Figures

- Figure 1.1. A depiction of the surface charge distribution and electric field lines of a surface plasmon on a metal film.<sup>22</sup> The plasmon is confined to the interface between metal and dielectric, its field diminishing exponentially into each medium. ....24
- Figure 1.2. Dispersion relations of a surface plasmon and photons with and without a coupling mechanism.<sup>23</sup> The frequency dependent plasmon dispersion relation (black line) does not meet the photon's, in air, (blue line) for any incident angle (the photon line shown here is for the theoretically shallowest incident angle). However, when a prism coupler is used (the dispersion relation in this medium is depicted by the green line) the two lines meet at a point of resonance. ....24
- Figure 1.3. Coupling configurations for SPR.<sup>23</sup> Displayed are the Kretschmann (a) and Otto (b) coupling arrangements. Attenuated total internal reflection of the light produces an evanescent wave that excites the surface plasmon (depicted here by the surface charge distribution). ....25
- Figure 1.4. Diagram of metallic nanoparticle interaction with external electric field. The electron shell of the particle is displaced in the presence of the E-field, producing an electric dipole. The oscillation of this cloud due to the induced dipole restoring force is what accounts for the nanoparticle's plasmonic resonance. This diagrammatic representation is commonly used as a visual aid to describe nanoparticle plasmonics and was originally published by Kelly et.al.<sup>27</sup> ....26
- Figure 1.5. Diagram of the Raman effect. The energy of the electron cloud is promoted to, and subsequently decays from, an intermediate "virtual" state somewhere between the ground and first electronic state. Since this state does not represent an atomic equilibrium state it is highly unstable and exists only briefly, the molecule's energy decaying rapidly back to a vibrational level of the electronic ground state. Depending on the molecule's initial energy this may result in either a Stokes or and anti-Stokes shifted photon being scattered. The majority of photons are Rayleigh scattered, undergoing no energetic change. ....34
- Figure 1.6. Diagram of resonant Raman scattering process. Comparison of Stoke shifted Raman (left) and resonance Raman (right). Unlike Raman scattering, the vibrational energy level that the molecule attains is real. ....36
- Figure 2.1. Schematic of fabrication procedure: 1- Cleaned Pyrex glass silde; 2&3- bi-layer of PMMA resist spun onto the glass substrate; 4- Evaporation of 30 nm Al onto the resist to act as charge conduction layer; 5- Exposure of pattern by electron beam tool; 6- Removal of Al layer; 7- Development of PMMA in MIBK, revealing patterned areas. The low molecular weight of the first resist layer, relative to the second layer, results in an undercut profile. At this point the patterned glass area may be modified with 3-aminopropyltriethoxysilane if

necessary; 8- Evaporation of Au or Ag. 9- Sample is soaked in warm acetone, lifting-off the unwanted resist and metal. ....42

Figure 2.2. Composite image of typical alignment marker arrangement. This image is a composite and not to scale, the features in a scale image would be too small to see. The global markers were 20  $\mu\text{m}$  large and were spaced 600  $\mu\text{m}$  from the pattern's centre. The cell markers (faintly visible in the figure) were 6  $\mu\text{m}$  large and were spaced 150  $\mu\text{m}$  from the pattern's centre. The cross was 200  $\mu\text{m}$  large and was located 1650  $\mu\text{m}$  from the pattern's centre. Since more than one lithographic alignment step may be needed, several groups of markers were patterned. This also ensured that if the alignment process fails due to defective markers, or the markers become damaged during the electron beam search, the procedure can be carried out again without loss of the sample. The distances quoted above relate to the spacing of the most commonly used markers, the other, reserve markers, were rarely utilised. ....46

Figure 2.3. Schematic of nanopore fabrication procedure. 1-  $\text{Si}_3\text{N}_4$  / Si /  $\text{Si}_3\text{N}_4$  wafer cleaned by sonication in acetone for 5 mins. 2- 30% UVIII resist spun onto the topside at 3000rpm for 60secs. 3- Patterning of pores by electron beam lithography. 4- Post-bake and development of resist. 5- Dry-etch of the exposed  $\text{Si}_3\text{N}_4$  using  $\text{CHF}_3$  gas. 6- Removal of remaining resist layer by acetone soak. ....47

Figure 2.4. Schematic of membrane fabrication. 1-  $\text{Si}_3\text{N}_4$  / Si /  $\text{Si}_3\text{N}_4$  wafer cleaned by sonication in acetone for 5 mins. 2- S1818 resist spun onto the backside of the wafer. 3- Exposure of the resist through the pre-patterned chrome mask. 4- Development of the pattern. 5- Dry-etch of the exposed  $\text{Si}_3\text{N}_4$  using  $\text{CHF}_3$  gas, residual resist is removed with a warm acetone soak. 6- Wet-etching of the exposed Si using KOH at 80°C. ....48

Figure 2.5. Markers used for backside alignment. Picture of circular Au markers fabricated on the wafer's topside. An identical pattern is included on the chrome mask used to pattern the backside, allowing the two patterns to align correctly. ....49

Figure 2.6. SEM comparison of identical patterns fabricated using thin (left) and thick (right) resist. Increased electron scatter caused by the extra resist material results in a less uniform structure with inconsistent feature sizes. As a result, the thinner of the resists was used throughout the research. ....53

Figure 2.7. Influence of dose on structural geometry. SEMs displaying an under-exposed (left) and over-exposed (right) split-ring structure. ....53

Figure 2.8. SEMs of poor (left) and good (right) Ag adhesion to Ti. The panel on the left of this Figure shows complete Ti rings, faintly visible below the Ag layer, with irregular Ag coverage. Inconsistent metal layer adhesion of this nature made a significant impact on device yield. On the right is an example of good adhesion; each ring is fully defined in Ag. 54

- Figure 3.1. High resolution scanning electron micrographs of split ring arrays A-D. (a) shows an SEM of array C, illustrating the uniformity of fabrication; (b) shows high resolution SEMs of split ring crescents found in arrays A-D. The roughness of the edges seen in (b) is an artefact due to charging from the SEM, not the fabrication process. ....58
- Figure 3.2. Resonant response of 135 nm radius split rings. Experimental transmission spectra of 135 nm radius split-rings with varying gaps (arrays A-D) as well as a complete 135 nm radius ring. Section (a) of the figure shows the resonances when the electric field is polarised perpendicular to the split, whereas section (b) shows the resonances when the electric field is polarised parallel to the split. The terminology “parallel” and “perpendicular” polarisation used from this point onwards in the Thesis refers to the geometric orientation specified in this figure.....59
- Figure 3.3. Comparing experimental (a) and (b) with simulated (c) and (d) data for 135nm radius split-rings. The simulated data points were fitted to Lorentzian curves using Sigma-plot software for a better visual representation of their peaks. The simulated data agrees very well with the experimental measurements. This correlation allows the plasmonic resonances of new structural designs to be tested first using FDTD, saving the need for expensive and time-consuming iterative electron beam fabrication. ....60
- Figure 3.4. Localised electric field enhancement at resonance for 135 nm radius rings A-D. FDTD simulations of normalised electric field in the z-plane, at the surface of array A-D’s ring structure, at each resonance frequency. The arc length of Array A is insufficient to support a third resonance. For N=1 & 3 the electric field of the exciting light was polarised along the y-axis, whereas for N=2 the polarisation was along the x-axis.....61
- Figure 3.5. Localised electric field enhancement at resonance for a complete 135 nm radius ring. FDTD simulation of the normalised electric field in the z-plane, at the surface of the ring structure. The electric field component of the exciting wave was polarised in the y-direction. An identical distribution was observed when the electric field was polarised in the x-direction, except rotated through 90 degrees (with nodes appearing in the y-plane rather than the x-plane as seen above). ....63
- Figure 3.6. Dispersion of plasmon resonances with changing arc length for 135nm radius Au split-rings. Resonance frequency vs. Au arc-length for N=1, N=2 and N=3 plasmon modes in arrays A-D. Experimentally and numerically measured peaks show good correlation. ....64
- Figure 3.7. Plasmonic response of Au split-rings E-H with changing ring radius. Transmission spectra of arrays E-H at both polarisations. The even modes, N=2, are generated when the light is polarised parallel to the split (left), whereas odd modes, N=1 and N=3, are generated when light is polarised parallel to the split (right). The mode numbers for the odd modes have been marked for clarity. ....65

- Figure 3.8. Dispersion of plasmon resonances with changing radius, showing resonance frequency vs. radius for N=1, N=2 and N=3 plasmon modes in arrays E-H. Plasmon resonance frequencies scale in an approximately linear fashion as the radius is increased - as was the case with the arc-length studies shown in Figure 3.5. ....66
- Figure 3.9. High resolution scanning electron micrographs of split ring arrays I-K (left-right). ...66
- Figure 3.10. Plasmonic response of 75 nm radius split rings. Experimental (a,b) and simulated (c,d) transmission spectra of 75 nm radius split rings with varying gaps (arrays I-K). Figures a and c show the resonances when the electric field is polarised perpendicular to the split, whereas figures b and d show the resonances when the electric field is polarised parallel to the split. Good correlation is seen between the experimental and numerical data, although, as was the case in Figure 3.3, the experimental peak values are blue-shifted with respect to their numerical counterparts.....67
- Figure 3.11 Plasmon resonance dispersion with changing arc length of the 75nm radius Au split-rings I-K. Experimental and numerically measured values for resonance frequency vs. Au arc-length for N=1, N=2 and N=3 show good correlation. ....68
- Figure 3.12 Electric field enhancement at resonance for 75 nm radius rings. FDTD simulations of the normalised electric field in the z-plane at the surface structures found in arrays I-K at each plasmonic resonance. Array E is not of sufficient arc-length to display an N=3 resonance. For N=1 & 3 the electric field of the exciting light was polarised along the y-axis, whereas for N=2 the polarisation was along the x-axis. ....69
- Figure 3.13. Electric field enhancement inside the split of a 75 nm radius Au split ring. FDTD simulations of the normalised electric field through the centre of the split (in the x-plane) at each resonance mode for the ring structure found in array K. Field enhancements of approximately 8 and 4 can be found in the centre of the split for the 1<sup>st</sup> and 3<sup>rd</sup> order resonances respectively. No enhancement is experienced in the centre of the split for the 2<sup>nd</sup> order resonance. ....70
- Figure 3.14. Plasmonic response of 75 nm radius rings fabricated with increasing thickness of Au. Resonances shift to higher frequencies and increase in intensity as the height of the rings increases from 10 nm - 20 nm. The third resonance mode, N=3, can only be resolved when 20nm of Au has been evaporated. ....71
- Figure 3.15 Dispersion of plasmon resonances with changing Au thickness, showing resonance frequency vs. Au thickness for N=1 and N=2 plasmon modes of 75nm radius rings. A linear frequency shift is observed for the increasing levels of Au. N=3 mode is not shown in the above Figure because only one array (20 nm thick Au) displays this resonance. ....71
- Figure 3.16. Plasmonic response of 75 nm radius rings fabricated with varying particle periodicity. No significant shift in resonance wavelengths is seen (the differences seen are

within the expected standard deviation experienced due to the fabrication process), confirming that the resonances exhibited by these structures are due to geometry, not interparticle effects. ....72

Figure 4.1. Experimental, (a) and (b), and simulated, (c) and (d), transmission spectra of 75 nm radius Ag split-rings with varying arc-lengths. The simulated data points were fitted to Lorentzian curves using Sigma-plot software for a better visual representation of their peaks. This Figure shows the plasmonic activity of rings at both polarisation states, with (a) and (c) displaying even resonance modes (N=2), and (b) and (d) displaying odd resonance modes (N=1 & 3). The trend of plasmonic red-shifting with increased particle length is seen in both experimental and simulated data, agreeing well with the trend seen in Chapter 3 for Au rings. The peak positions of the experimental and numerical curves do not match exactly, the reasons for this have been previously mentioned in Section 3.4.1. ....77

Figure 4.2. Resonance dispersion for all modes of identical Ag and Au rings with varying arc-lengths. The Ag structures behave in the same manner as the Au structures, their resonances red-shifting in a predictable fashion with increasing arc length. However, the resonance frequency of the Ag rings is higher than the Au rings for each comparable mode. ....78

Figure 4.3. Scanning electron micrographs of Ag split rings. High resolution SEMs of arrays L-N (top) and a wide area SEM of array M (bottom). As seen in this figure, chemical adhesion can occasionally lead to structures with rougher features than those previously fabricated using Ti as an adhesion layer. This is most likely due to varying 3-aminopropyltriethoxysilane SAM coverage from sample to sample. Although the samples are slightly less uniform throughout the length of their arc, the variation in feature size does not exceed  $\pm 5$  nm (Section 4.4.3). ....79

Figure 4.4. Plasmonic response (top) and high resolution SEM (bottom) of 80 nm radius, 10 nm gap Ag split-rings. Rings display second and third resonances at 774 and 631 nm respectively, resonances corresponding to common laser wavelengths of 785 and 633 nm. ....80

Figure 4.5. Peak resonance wavelengths and standard deviation of 80 nm Ag split-rings fabricated using separate adhesion methods. The rings fabricated using the Ti adhesion method exhibit higher resonance wavelengths, yet do not show improved sample to sample resonance reproducibility. ....82

Figure 4.6. High resolution XPS spectra of 2-Mercaptopyridine attached to metallic surface via thiol linkage. The ratio of C to N in mercaptopyridine is 5:1, approximately the ratio exhibited in this spectra. Along with the presence of S, this confirms the modification procedure. The use of Au for this experiment is irrelevant, as it is merely to confirm the attachment protocol. ....84

Figure 4.7. SERS spectra of 2-mercaptopyridine attached to an array of Ag split rings and excited with 633 nm laser light. Raman scatter was collected at both polarisation states. The N=2

mode (excited when the external electric field is polarised perpendicular to the split in the ring geometry) provides the largest scattering intensity, over 5x greater than when the “off-resonance” condition (using the  $1000\text{cm}^{-1}$  band as a reference). Spectra were collected over 20 seconds using a 5mW laser and a Horiba Jobin Yvon LabRam INV Raman spectrometer. Spectra calibrated using the  $520\text{cm}^{-1}$  band of Silicon. ....85

Figure 4.8. FDTD simulations showing the electric field enhancement, as well as the predicted Raman enhancement factor at resonant (a) & (b) and non-resonant (c) & (d) polarisation directions for the second order resonance of the 75 nm radius Ag rings. FDTD simulation of the normalised electric field in the z-plane at the surface the ring structure shows a significant decrease in the enhanced field’s surface coverage from (a) to (c). This is reflected in plots of the Raman enhancement factor (Equation 1.17) over the ring’s surface in (b) and (d), where the predicted enhancement is greater and more widespread over the surface of the structure when the incident radiation is polarised to excite the second order plasmon resonance ( $N=2$ ). Therefore, more molecules will experience an enhanced field when the exciting radiation is polarised perpendicular to the split in the ring geometry (in the x-axis), accounting for the increasing the Raman scattering seen in Figure 4.7. ....86

Figure 4.9. SERS and Raman spectra of 2-mercaptopyridine. Spectra collected using a 633 nm laser. This Figure shows SERS from a monolayer of 2-mercaptopyridine attached to a Ag sensor array (black line) as well as Raman spectra of a 10mM 2-mercaptopyridine solution (blue line). ....87

Figure 4.10. SERS spectra of 2-mercaptopyridine attached to an array of Ag split rings and excited with 532 nm laser light. Raman scatter was collected at both polarisation states. The  $N=3$  mode (excited when the external electric field is polarised parallel to the split in the ring geometry) provides the largest scattering intensity, ~ 2x greater than when the “off-resonance” condition (using the  $1000\text{cm}^{-1}$  band as a reference). Spectra were collected over 20 seconds using a 1mW laser and an Ocean Optics QE65000 Raman spectrometer. Spectra calibrated using the  $520\text{cm}^{-1}$  band of Silicon. ....88

Figure 4.11. FDTD simulations showing the electric field enhancement, as well as the predicted Raman enhancement factor at resonant (a) & (b) and non-resonant (c) & (d) at resonant polarisation directions for the third order resonance of the 75 nm radius Ag rings. The  $N=3$  mode, excited when the incident field is polarised parallel to the split (y-axis), shows considerably higher localised field strengths ( $>20$ ) than when the incident field is polarised perpendicular to the split, the “off-resonance” condition ( $\sim 7-8$ ). As was the case for the second order resonance (Figure 4.8), this is reflected in plots of the Raman enhancement factor (Equation 1.17) over the ring’s surface in (b) and (d), where the predicted enhancement is greater and more widespread over the surface of the structure when the incident radiation is polarised in the y-axis, exciting the ring’s third order plasmon resonance ( $N=3$ ). ....89

Figure 4.12. SERS spectra of 2-mercaptopyridine attached to an array of Ag split rings and excited, in turn, with 785nm and 633 nm laser light. Raman scattering for each lasers was collected at both polarisation states. The N=2 and N=3 modes provide scattering intensities of ~9x and ~6x greater than when in their “off-resonance” condition (taken over several measurements using the  $1000\text{cm}^{-1}$  band as a reference). Spectra were collected over 20 seconds using a Horiba Jobin Yvon LabRam INV Raman spectrometer, and calibrated using the  $520\text{ cm}^{-1}$  band of Silicon. ....90

Figure 4.13. FDTD simulations of the enhanced electric fields, (a) & (c), and their associated Raman enhancement factors , (b) & (d), for the second and third order resonances of an 80nm radius Ag ring. Areas of electric field enhancement, and as a result the expected Raman enhancement factor, are proportionally larger than seen in the 75 nm radius ring at resonance. Furthermore, the maximum values of electric field enhancement are larger for the N=3 mode; ~25, resulting in larger Raman enhancement for this mode. This is likely due, in part, to increased coupling between he ring arms due to the smaller, 10 nm, gap. ....91

Figure 4.14. Comparison of Raman scattering from engineered structures, an area of plain Ag and glass. The intensity of the Raman signal from the resonating rings was ~60x greater than the Ag area, even though there were ~4x less molecules underneath the focused laser (due to the fill factor of the rings). No signal was recorded from the glass substrate. ....92

Figure 4.15. Normalised Raman spectra of 2-Mercaptopyridine attached to 4 arrays with different second order peak resonance wavelengths. Section (a) of the figure shows the spectra from all 4 arrays, whereas section (b) focuses on the smaller spectra obtained from arrays O, M and L. All arrays were excited with a 633 nm laser polarised perpendicular to the split. Scattering is significantly greater (~21x) from array N, since this array’s resonance is the only one to encompass the 633 nm laser excitation wavelength. ....93

Figure 4.16. Transmission spectra taken over a series of time intervals for a Ag split-ring array and a Au capped Ag split-ring array kept in PBS for 84 hours. Steady degradation of the resonance can be seen over the 84 hour period for the Ag rings. Oxidation of the Ag surface leads to the damping of the structures plasmon, until, after the full 84 hours have elapsed, the ring displays no plasmonic activity. The Au capped sample also shows some plasmonic degradation over time, but the results are far less pronounced. After 84 hours the array retains a plasmonic response, albeit red-shifted by approximately 93 nm. ....94

Figure 4.17. Plasmonic degradation of the second order resonance mode of plain Ag structures and Au capped Ag structures. (a) is a plot of each array’s FWHM values vs. time, (b) is a plot of the relative strength of the Plasmon peak vs. time (100% being the strength of the plain Ag peak at 0 hours). Although the plain Ag resonance shows a significant drop in strength (decreasing to 15% of the resonance’s original value) and an increase in breadth (the FWHM increases from 92nm - 253nm), the Au capped structures remain strong (dropping to 70% of

its initial value) and sharp (the FWHM increases from 106nm - 159nm) over the same time frame.....	95
Figure 5.1. Attachment and hybridisation arrangement of Cy5 labelled oligonucleotides. (a) represents sequence A; (b) represents sequences B & C; (c) represents sequences B & F (see Section 2.2 and text below for details). SH represents the thiol group present on the oligonucleotides, enabling their attachment to metal.....	102
Figure 5.2. High resolution XPS spectra of oligonucleotides attached to metallic surface via thiol linkage. The ratio of P to N in an oligonucleotide strand is approximately 1:4, a ratio present in this spectra. The presence of S confirms the reduction chemistry was successful and that the oligonucleotide is specifically bound to the surface. The use of Au for this experiment is irrelevant, as it is merely to confirm the reduction and attachment protocol of the oligonucleotide. ....	103
Figure 5.3. Raman spectra of both Cy5 modified DNA and Cy5 dye immobilised on sensor surface. The 633 nm laser line excites the N=2 mode of the ring. The two Raman spectra agree well, exhibiting only slight wavenumber variations, most likely due to the different dye attachment arrangements. ....	104
Figure 5.4. SERRS spectra of differently sequenced oligonucleotides hybridising to probe DNA attached to the sensor surface. The complementary sequence exhibits the greatest hybridisation efficiency, producing the strongest Raman signal. A weak signal is displayed by partially mismatched sequence, while the signal from the fully mismatched sequence is indistinguishable from the system noise.....	105
Figure 5.5. Influence of dye position on Raman and fluorescence signal quality. The sequence modified such that when hybridised the dye is spaced proximal to the surface, exhibits approximately twice the Raman scatter (a)-left, and 22% less fluorescence, (b)-right, than the sequence modified such that the dye is spaced several nm away from the surface. ...	106
Figure 5.6. FDTD simulation displaying the electromagnetic decay at the surface of the resonant split-ring structure. EM enhancement in the z-plane at N=2 (excited by a 633nm laser), taken as a slice through the split in the ring (dotted line).....	107
Figure 5.7. Competitive hybridisation of labelled and unlabelled sequences to the sensor surface. A steady decline in the intensity of the $1360\text{cm}^{-1}$ band was observed at both polarisations (N=2 readings are shown in red, “off-resonance” readings in black). At 5% (200 molecules per ring) the sensor was only effective in its resonant state, the scattering from the “off-resonance” condition is undetectable. Therefore, the sensor acts as a dichroic switch. ...	108
Figure 5.8. Raman spectra of a Cy7 modified oligonucleotide hybridised to the sensor. The second order resonance mode provides 5x greater scattering than the “off-resonance” condition.....	110

- Figure 5.9. Raman scattering from single array modified with sequences of Cy5 and Cy7 labelled oligonucleotide sequences hybridised to thiolated oligonucleotide strand (detailed in the text). Spectra were collected using a 633 nm laser (a) (exciting N=3) and a 785 nm laser (b) (exciting N=2) for the electric field polarised both parallel and perpendicular to the split in the ring geometry. SERRS dominates both graphs, (a) shows scattering from the Cy5 dye labelled sequence, whereas (b) shows scattering from the Cy7 dye labelled sequence. The Raman scattering intensity of each dye is far greater when the ring is in a resonant condition compared to when the electromagnetic field is polarised in the ‘off’ direction (4 times greater at N=3 and 6 times greater at N=2)..... 111
- Figure 5.10. Raman spectra collected from arrays of Ag split-rings modified with varying ratios of the two sequences: Excitation was at 633 nm and 785 nm for both polarisations. The resonance Raman signals dominate at each wavelength, so that for the concentrations stated above, only Cy5 is detected at 633 nm and only Cy7 at 785 nm. The limit of detection for N=3 was 10% Cy5 coverage, and for N=2 was 25 % Cy7 coverage..... 112
- Figure 6.1. High resolution SEMs of engineered nanoporous Si<sub>3</sub>N<sub>4</sub> etched through the centre of Au split-ring structures. Ring radius is ~240 nm, pore radius is ~80 nm. The membrane is ~1 mm<sup>2</sup> and 200 nm thick. .... 116
- Figure 6.2. Backside wafer patterning before the KOH wet-etch step. Windows created in the silicon nitride by the CHF<sub>3</sub> dry-etch process, expose the underlying Si in preparation for selective wet-etching..... 117
- Figure 6.3. SEM of 60 nm radius split-ring. Ring has a radius of 60 nm and a wall width of 40 nm, demonstrating that it is possible to produce feature sizes smaller than those demonstrated in the previous chapters. .... 118
- Figure 6.4. SEM of 80 nm radius split ring with ~2-3 nm gap size. Although nanometre sized gaps are possible, fabricating features of this size leads to higher levels of array irregularities than have previously been seen. .... 118
- Figure A.9. Schematic of Plassys MEB 400S electron-beam evaporator. A valve separates the sample chamber from the metal crucibles, which remain permanently at high vacuum. The details of this schematic were obtained from the Plassys MEB 400S’ operation software. . 123
- Figure A.10. Schematic of modified evaporator. All valves are manually operated. .... 123
- Figure A.11. Experimental layout of the Shimadzu UV3101PC absorption spectrometer. A Thor Labs linear thin film polariser is used to control the electric field orientation of the radiation passing through the sample. The sections marked “sample holder” and “reference arm” consist of home built metal holders with a variety of pinhole sizes drilled through them. The sensor arrays are aligned to the pinhole in the “sample holder” before measurement and held in place using Blu-Tack adhesive (only the 1 mm pinhole is used in measurements as

this corresponds to the size of the square arrays being tested). A clean piece of Pyrex glass was placed over the pinhole on the reference arm. The pinholes were then aligned to the narrow beam emitted from the spectrometer light source through a 5 mm slit. Transmission measurements were taken from 400 nm to 2500 nm. .... 124

Figure A.12. A graphical representation of the three-dimensional simulation domain used to model the split-ring nanostructures (side view, left; top view, right). The ring structure was defined using 2 cylinders, one metal the other air. A rectangular block with the same z-dimension was used to define the split in the ring geometry. Typically the glass and air blocks had a z-dimension of 100nm each. X and y dimensions were chosen according to the periodicity of the array being modelled. The refractive index of Pyrex glass and air used throughout were 1.47 and 1 respectively. .... 127

Figure A.13. Schematic showing the basic set-up and primary components of X-ray photoelectron spectrometer (not to scale).<sup>130</sup> ..... 129

Figure A.14. Optical diagram of LabRam spectrometer: A- moveable mirror allowing 633 or 785 nm laser to be selected; B- neutral density filters; C- focusing lens; D- Pinhole; E- interchangeable notch filter; F-secondary notch filter; G- confocal hole; H- focusing lenses; I- spectrometer entrance slit; J and L- collimating lenses; K- interchangeable diffraction gratings. .... 130

Figure A.15. Set-up for performing SERS at 532 nm. The beam passes through a neutral density filter at A, before being collimated, and subsequently refocused, by lenses B and C. Once inside the microscope, a dichroic, D, transmits the laser line toward the sample and reflects all inelastically scattered light out of the microscope's front/camera port, where it is coupled into a fibre optic cable by lens E. This fibre carries the light to the Ocean Optics portable Raman spectrometer. .... 132

Figure A.16. Structure of 2-mercaptopyridine. The thiol group ensures attachment to the silver sensor. The chemical structure seen in this figure was obtained from Sigma-Aldrich's website. .... 132

Figure A.17. Structure of 3-aminopropyltriethoxysilane. The chemical structure seen in this figure was obtained from the Sigma-Aldrich website. Details of glass slide modification with 3-aminopropyltriethoxysilane can be found in Section 2.3.1.8. .... 133

Figure A.18. Cy5 Mono NHS ester. Cy5 is a cyanine derived dye, the number 5 referring to the number of carbon atoms in the molecule's methine chain<sup>131</sup> (the structure seen in this figure was taken from Amersham Biosciences data sheet supplied with the chemical). .... 133

Figure A.19. Cysteamine interaction with Cy5 mono NHS-ester. The amine group of cysteamine (attached to the sensor surface by virtue of its thiol group) reacts with the NHS-ester, forming a covalent amide bond, with the subsequent release of N-hydroxysuccinimide. The

sensor surface is modified with a monolayer of Cy5 as a result. The structure of cysteamine was taken from the Sigma-Aldrich website. .... 134

Figure A.20. DNA structure and base pairing diagram. The sugar-phosphate backbone can be seen on the left of the diagram, also shown are the molecular structures of the bases and a representation of their exclusively complimentary pairing via hydrogen bonding.<sup>100</sup> ..... 135

Figure A.21. Structure of Cy5 and Cy7 dye attached to oligonucleotide. The basic structure of Cy5 and Cy7 is the same, differing only by the length of their methine chain; n=2=Cy5, n=3=Cy7. Side chains show how the dye can be linked to the oligonucleotide using either the free phosphate group (5') or the free hydroxyl group (3'). The chemical structures in this figure were obtained from Atdbio, University of Southampton, the suppliers of the chemicals. .... 136

Figure A.22. DTT structure and Thiol-disulphide exchange. 1- DTT and DNA in solution, pairs of DNA are bound together due to disulphide bridges forming between thiol groups. 2- First thiol-disulphide exchange takes place, leaving one oligonucleotide with a reduced thiol group while the other strand forms a disulphide bond with the DTT's recently deprotonated thiol group. 3- The second thiol-disulphide exchange occurs through oxidation of DTT's other thiol group, closing the ring and leaving behind two separated DNA strands, each with a complete thiol group.<sup>100</sup> The structure of DTT was taken from the Sigma-Aldrich website. 136

## Acknowledgements

I would firstly like to thank Prof. Jon Cooper for giving me the opportunity to carry out this research within his group. His advice and guidance have been invaluable. Thanks also go to Dr. Andrew Glidle, Dr. Anna Sheridan, Dr. Huabing Yin and Prof. David Cumming for their helpful insight and discussion.

Special thanks go to my fiancé Clair Cormie for her strength, support and encouragement throughout my studies.

**Author's declaration**

The work presented in this thesis was conducted by the author and has not previously been submitted for a degree or diploma at this university or any other institution.

## Chapter 1 - Introduction and theory

### Abstract

Chapter 1 introduces the theory of light interaction with bulk and nanoscale metals, explaining the concept of surface plasmon resonance (SPR) and localised surface plasmon resonance (LSPR). This Chapter also describes how these resonances can be used to facilitate biosensing via thin-film SPR sensors and surface enhanced Raman spectroscopy (SERS).

### 1.1 Nanoplasmonic biosensors

The word “biosensor” can refer to a wide-ranging field of devices that provide quantifiable responses when in the presence of biological molecules and events<sup>3-7</sup>. More specifically, nano-plasmonic biosensors utilise the unique optical properties of nanostructured metals to directly facilitate bio-detection, or to boost the effectiveness of existing sensing mechanisms. Surface plasmon resonances, discussed in more detail in Section 1.2 and 1.3, are collective oscillations of the valence electrons on a metal’s surface, induced by external radiation. In nano structures the general phenomenon affects the structure’s interaction with light (i.e. its absorption and scattering properties), with resonant oscillations leading to an amplification and confinement of the local electromagnetic field around particular facets of the geometry. This behaviour can be used in a variety of ways to facilitate different levels of molecular detection; Single particles can be used in conjunction with dark field microscopy as molecular labels, with multiplexing possible due to their size dependent scattering cross sections<sup>8-10</sup> (these can be used much in the same way as a fluorophore would be, but without the associated problem of photo bleaching); Molecularly mediated plasmonic coupling between nanoparticle dimers and clusters can lead to a detectable shift in the particle’s peak resonance wavelength, resulting in a change in extinction spectra, indicating the presence of a the specific target molecule<sup>11-13</sup> (for example; aggregation of particles in solution due to hybridisation of complimentary DNA sequences immobilised on separate nanoparticles); Modification of a nanoparticle’s surface with a target analyte can alter its extinction and scattering spectra, the greater the surface coverage the more pronounced the shift;<sup>14, 15</sup> The intense, localised electromagnetic near-fields generated by resonating particles can significantly enhance existing spectroscopic biosensing techniques such as Raman scattering, providing multiplexed detection and characterisation of molecules situated within these areas, often without the need for prior labeling.<sup>1, 2, 4, 5, 16, 17</sup>

The interest in nanoplasmonics as a sensing tool has grown rapidly in the last decade as advances in lithographic engineering have allowed the creation of sensors on a scale comparable with the target molecules, providing sensors with dimensions appropriate for probing extremely small quantities of molecules. The ability to specifically engineer the optical and geometric properties of nanometals allows for the creation of highly sensitive, function specific biosensors; sensors which, with the advent of cheaper, faster and more robust fabrication techniques, are increasingly applicable to the fields of biomedical research, diagnostics and therapeutics.<sup>18-20</sup>

## 1.2 Interaction of light with metal

The conduction band electrons in a metal are delocalised and can be considered free with respect to the atomic lattice structure of the bulk material. Collective fluctuations of the free electron gas are referred to as the metal's plasmon. These fluctuations are characteristic of the particular metal in question and have a frequency determined by the equation:<sup>21</sup>

$$\omega_p^2 = \frac{n_e e^2}{m_{\text{eff}} \epsilon_0} \quad (1.1)$$

where  $n_e$  is the electron density,  $e$  is the charge on an electron,  $m_{\text{eff}}$  is their effective mass, and  $\epsilon_0$  is the vacuum dielectric constant. Oscillation of this free electron gas can be driven by application of an external electromagnetic field, a phenomena that defines the metal's optical properties. The dielectric response of a metal in the presence of external electromagnetic radiation is determined by its wavelength dependent complex dielectric constant (in the case of metallic nanoparticles this constant specifies the particle's scattering and absorptive properties):

$$\epsilon_{\text{met}} = \epsilon_1 + i\epsilon_2 \quad (1.2)$$

where  $\epsilon_1$  and  $\epsilon_2$  are the real and imaginary components respectively.  $\epsilon_1$  defining the extent to which the material polarises due to the external field, while  $\epsilon_2$  represents the phase shift of the polarisation relative to external field:<sup>21</sup>

$$\epsilon_1 = 1 - \frac{\omega_p^2}{\omega^2 + \gamma^2} \quad (1.3)$$

$$\epsilon_2 = \frac{\omega_p^2 \gamma}{\omega(\omega^2 + \gamma^2)} \quad (1.4)$$

where  $\omega_p$  is the plasma frequency (see Equation 1.1),  $\omega$  is the frequency of the incident radiation and  $\gamma$  is the damping constant (related to the average time between collisions in a system with free electron motion).<sup>21</sup>

### 1.2.1 Surface Plasmons and Surface Plasmon Resonance (SPR)

Equation 1.1 relates to the metal's bulk plasmon, however the term surface plasmon refers to such oscillations confined to the boundary between a metal and a dielectric. An electromagnetic field, provided by an incident light wave, can interact with the free boundary electrons, inducing polarisation of the electrons at the metal/dielectric boundary. If the incident field satisfies the required criteria, i.e. its frequency and momentum match that of the electron cloud, resonant fluctuation of the surface bound electrons can take place. This interaction between metal's oscillatory electron wave and the incident photons can be termed a surface plasmon polariton (SPP), but is more commonly referred to as surface plasmon resonance (SPR). The polariton propagates along the surface of the metal, its electric field component in the z-axis, perpendicular to the surface, decaying exponentially into both mediums, Figure 1.1.<sup>22</sup>

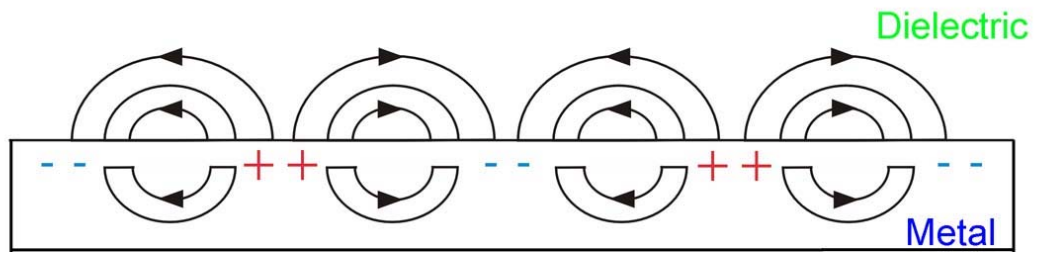


Figure 1.1. A depiction of the surface charge distribution and electric field lines of a surface plasmon on a metal film.<sup>22</sup> The plasmon is confined to the interface between metal and dielectric, its field diminishing exponentially into each medium.

The excitement of surface plasmon polaritons in bulk metals and thin films cannot be achieved without a coupling medium. Figure 1.2 shows a representation of the dispersion relation of a surface plasmon at a metal-dielectric boundary, along with the dispersion relation of light in a homogeneous dielectric (such as air), and illustrates the immediate problem faced when attempting to excite a surface plasmon polariton on a planar surface.

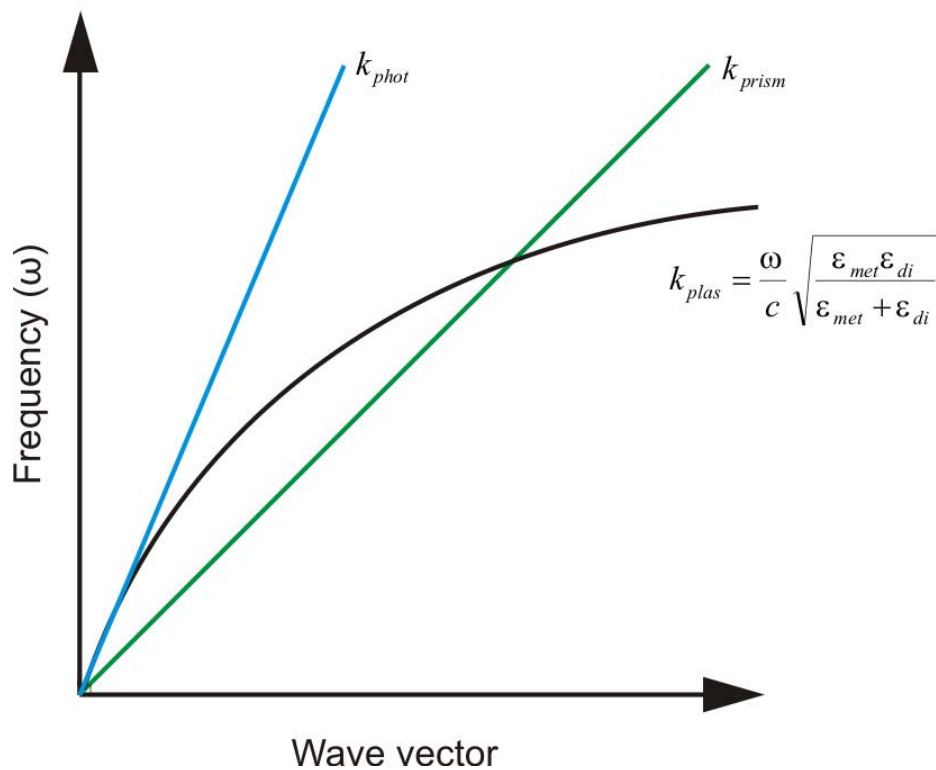


Figure 1.2. Dispersion relations of a surface plasmon and photons with and without a coupling mechanism.<sup>23</sup> The frequency dependent plasmon dispersion relation (black line) does not meet the photon's, in air, (blue line) for any incident angle (the photon line shown here is for the theoretically shallowest incident angle). However, when a prism coupler is used (the dispersion relation in this medium is depicted by the green line) the two lines meet at a point of resonance.

As can be seen from Figure 1.2 the wave vectors for the surface plasmon and the light do not match, an essential parameter for excitation of a polariton. The dispersion relation of the

plasmon approaches that of the light asymptotically, without intersection. The dispersion relation of the plasmon's and photon's wave vectors can be described as:<sup>24</sup>

$$k_{plas} = \frac{\omega}{c} \sqrt{\frac{\epsilon_{met} \epsilon_{di}}{\epsilon_{met} + \epsilon_{di}}} \quad (1.5)$$

$$k_{phot} = \frac{\omega}{c} \sqrt{\epsilon_{di}} \quad (1.6)$$

Where  $\omega$  is incident light frequency,  $c$  is speed of light,  $\epsilon_{met}$  is dielectric constant of the metal,  $\epsilon_{di}$  is dielectric constant of the dielectric at the metal/dielectric interace, and  $\theta$  is angle of incidence.

Figure 1.2 illustrates that these two relations can never meet by simply illuminating the interface. The dispersion relation of the plasmon is always larger than the wavevector of the light, preventing coupling. The incident light's momentum must be altered in order for the two dispersion relations to meet, resulting in plasmon excitation. This can be realised for a thin metallic film by coupling the incident p-polarised light to the film's plasmon through the use of a high refractive index prism (grating coupling methods also exist). Light passing through the prism has its dispersion relation altered (from that seen in Equation 1.6 to that seen in Equation 1.7), increasing its wavevector and allowing it to match that of the plasmon at the interface between the metal and the lower refractive index dielectric. The resonant condition is met when  $k_{plas} = k_{phot} \sin\theta$ . When the light reflects off the prism base, the resultant evanescent field extends a few hundred nanometres to the metal/lower index dielectric interface, exciting the plasmon. Two configurations are common; the Kretschmann configuration<sup>25</sup> in which a thin film of metal is deposited onto the base of the prism, and the Otto configuration<sup>26</sup> in which the prism base is positioned proximal to the metal/dielectric interface.

$$k_{prism} = \frac{\omega}{c} \sqrt{\epsilon_{prism}} \quad (1.7)$$

Where  $\epsilon_{prism}$  is the dielectric constant of the prism.

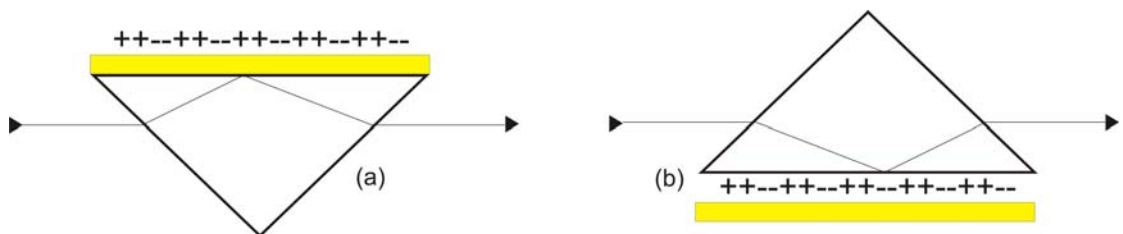


Figure 1.3. Coupling configurations for SPR.<sup>23</sup> Displayed are the Kretschmann (a) and Otto (b) coupling arrangements. Attenuated total internal reflection of the light produces an evanescent wave that excites the surface plasmon (depicted here by the surface charge distribution).

Once the excitation requirements have been met, the system can be used as a photonic biosensor. Introduction of an analyte into the evanescent field will alter the plasmon coupling conditions, requiring a modification of the incident light angle to maintain the resonance. The angle required to achieve resonance can be monitored by recording the reflected light intensity (resonance being achieved when the reflected light is at a minimum). Plotting reflectivity as a function of angle can be used to detect the presence of material in the evanescent field, resulting in a shift in angle of the “dip” in reflectance.

### 1.2.2 Localised surface plasmons in nanoparticles

It was seen in Section 1.2.1 that coupling light to the surface plasmon of a bulk metal is problematic. In contrast, plasmonic excitations in isolated nanoparticles are rather more simple to induce.

The penetration depth of an electromagnetic field into a metal is of the order of tens of nanometers, meaning only electrons within this region can interact with it. However, when an electromagnetic field impinges on a nanoparticle whose size is smaller than this penetration depth, the field can interact with all of the particle’s free electrons. An electric dipole is created on the particle as the electrons are displaced from the metal atom cores. The opposing surface charges create a restoring force, the strength of which is determined by the magnitude of the electron shift, and as such the particle can be considered an electromagnetically driven oscillator, Figure.1.4. If the incident electromagnetic wave matches the natural oscillatory frequency of the nanoparticle (a frequency determined by the bulk metal plasma frequency and the nanoparticle shape), resonant enhancement of the surface plasmon takes place. The resulting surface plasmon may have an amplitude many times greater than that of the exciting field, leading to enhancement of the local electromagnetic field around particular facets of the structure. Confined as they are to the nanoparticle, and unable to travel like the plasmons in bulk metals, the resonances are considered to be localised surface plasmon resonances (LSPR).

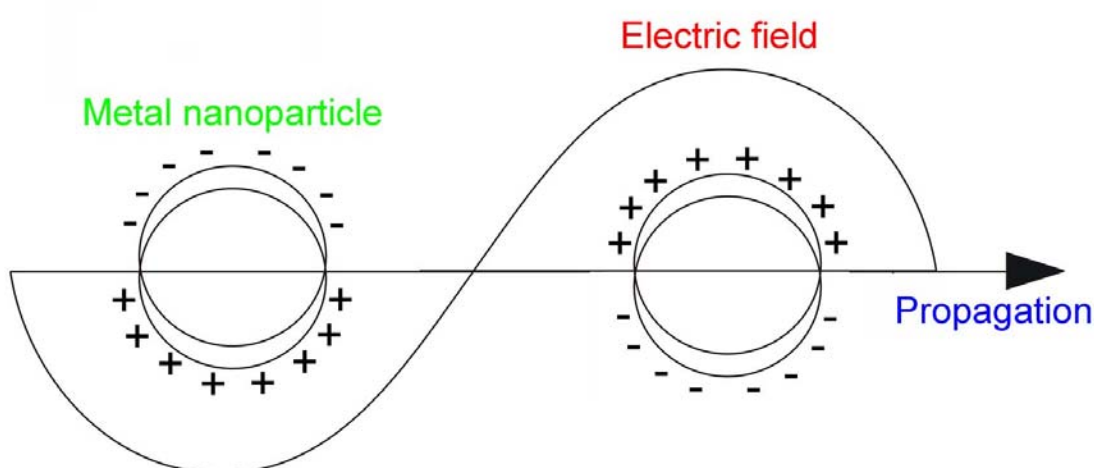


Figure 1.4. Diagram of metallic nanoparticle interaction with external electric field. The electron shell of the particle is displaced in the presence of the E-field, producing an electric dipole. The oscillation of this cloud due to the induced dipole restoring force is what accounts for the nanoparticle’s plasmonic

resonance. This diagrammatic representation is commonly used as a visual aid to describe nanoparticle plasmonics and was originally published by Kelly et.al.<sup>27</sup>

The polarisability of the electron gas in the presence of an applied electromagnetic field can be defined as:<sup>23</sup>

$$\alpha = 4\pi a^3 \frac{\epsilon_{met} - \epsilon_{di}}{\epsilon_{met} + 2\epsilon_{di}} \quad (1.8)$$

where  $a$  is the particle radius,  $\epsilon_{met}$  is the complex dielectric constant of the metal and  $\epsilon_{di}$  is the dielectric constant of the surrounding medium.

The localised electric field strength at the surface of a metal sphere can be expressed by:

$$E = E_0 \cos \theta + g \left( \frac{a^3}{r^3} \right) E_0 \cos \theta \quad (1.9)$$

where  $E_0$  is the incident field strength,  $\theta$  is the angle relative to the direction of the electric field,  $a$  is the sphere's radius,  $r$  is the distance from the surface of the sphere, and

$g = \left( \frac{\epsilon_{met}(v_L) - \epsilon_{di}}{\epsilon_{met}(v_L) + 2\epsilon_{di}} \right)$ , where  $v_L$  is the frequency of incident light. This expression

demonstrates the distance dependence of the field enhancement, showing it to drop as  $\frac{1}{r^3}$  with respect to distance from the metal surface. Although a good model for nano-metallic spheres, more complex shapes require numerical solution.

It is this localised field enhancement, which in some cases can approach 1000,<sup>28</sup> along with the ease in which these LSPRs can be excited that make metallic nanoparticles of particular interest to the sensing community. Note, one need only frequency match the exciting wave and the nanoparticle plasmon, disregarding the angle of excitation or any of the complex arrangements seen in Section 1.1 for matching dispersion relations.

Determining the LSPR of a particular nanoparticle, or a number of identical nanoparticles, can be achieved through observing their interaction with light. The localised surface plasmon resonance of a nanoparticle causes both scattering and absorption of the exciting electromagnetic field to take place. Scattering is a consequence of the particle's fluctuating charge distribution re-radiating the exciting waves, while absorption can be attributed to energy losses from within the LSPR (i.e. localised heating, the generation and subsequent decay of electron-hole pairs, etc).<sup>21, 24, 29</sup> The extinction cross-section ( $\sigma_{ext}$ ) of the particle, a combination of its absorption cross-section ( $\sigma_{abs}$ ) and scattering cross-section ( $\sigma_{sca}$ ), indicates the frequency of its LSPR.

$$\sigma_{ext} = \sigma_{sca} + \sigma_{abs} \quad (1.10)$$

Mie theory, developed by Gustav Mie after observing colour changes in colloidal gold nanoparticles, is a solution of Maxwell's equations that describes electromagnetic interaction

with spherical particles.<sup>21, 29</sup> A simplified version of Mie theory, one commonly referred to throughout the literature<sup>29, 30</sup> and adequate for establishing a basic knowledge of dipolar nanoplasmonics, describes the extinction and scattering of spherical nanoparticles for wavelengths greater than two times the particle radius, R:

$$\sigma_{ext} = 9 \frac{\omega}{c} (\varepsilon_{di})^{3/2} V \frac{\varepsilon_2}{(\varepsilon_1 + 2\varepsilon_{di})^2 + (\varepsilon_2)^2} \quad (1.11)$$

$$\sigma_{scatter} = \frac{3}{2\pi} \left( \frac{\omega}{c} \right)^4 \varepsilon_{di}^2 V^2 \left( \frac{(\varepsilon_1 - \varepsilon_{di})^2 + (\varepsilon_2)^2}{(\varepsilon_1 + 2\varepsilon_{di})^2 + (\varepsilon_2)^2} \right) \quad (1.12)$$

where  $\omega$  is the angular frequency of the exciting wave,  $c$  is the speed of light in a vacuum,  $\varepsilon_{di}$  is the dielectric function of the surrounding medium,  $V$  is the nanoparticle's volume,  $\varepsilon_1$  is the real dielectric function of the metal,  $\varepsilon_2$  is the imaginary dielectric function of the metal. Resonance conditions are met when the denominator,  $(\varepsilon_1 + 2\varepsilon_{di})^2 + (\varepsilon_2)^2$ , is at a minimum, i.e. when  $\varepsilon_1 \sim -2\varepsilon_{di}$ . The absorption can be determined by subtracting the scattering cross section from the extinction cross section.

Although these equations are suitable for the description of dipolar resonances in small nanoparticles, they do not hold true for cases where  $2R > 30\text{nm}$ , or when the particle is not a perfect sphere. In such cases the particle may support a variety of multipolar resonances, and require calculation via numerical simulations.

The strength and spectral width of a particular resonance are determined by the damping mechanisms associated with absorption and scattering of the exciting radiation.<sup>24, 31</sup> Scattering, as mentioned above, is a re-radiation of the incident light. The energy of this re-radiated light is provided by the energy stored within the localised surface plasmon, hence the process can be considered radiative damping. Absorption, on the other hand, can lead to an energetic relaxation of the plasmon, taking the form of localised particle heating (the plasmon energy being converted to and consequently lost to heat radiation) as well as the creation and subsequent decay of electron-hole pairs (a feature of visible and NIR radiation interaction with metal). Both mechanisms play a part in the overall shape of the particle's resonance, however, referring back to Equations 1.11 and 1.12, it is clear that for smaller particles it is absorption which dominates, while larger particles are influenced more strongly by scattering due to each equation's different dependence on particle volume,  $V$ .

### 1.3 Tuning localised surface plasmon resonances and characteristics in metallic nanoparticles

The synthesis, fabrication and characterisation of metallic nanoparticles are extensive fields of interest that cover a variety of scientific disciplines. Although much of the pioneering work done in understanding the physical properties and phenomena related to nanoparticle plasmonics was done through the preparation and observation of colloidal suspensions, this Thesis will concentrate primarily on nanoparticle engineering using a lithographic technique.

Several types of nanolithography are commonly used, each with their own advantages and disadvantages: Nanosphere lithography, an inexpensive procedure which uses monolayers of nanospheres to create evaporation/etch masks in a variety of patterns;<sup>32, 33</sup> colloidal lithography, which employs electrostatically self-assembled polystyrene spheres as templates, onto which metal can be evaporated at various angles to produce the required 2-D or 3-D structure;<sup>34-39</sup> nano-imprint lithography, which uses nanopatterned polymer stamps to imprint a design onto a substrate, allowing rapid creation of multiple devices;<sup>40, 41</sup> and direct-write lithography, including electron-beam lithography (the method employed throughout this work) and focused ion beam milling, which uses a focused beam of particles to scan a pre-designed pattern into a resist material, or into the substrate itself.<sup>42-44</sup>

The plasmonic response of a metal nanoparticle, or indeed an array of nanoparticles, is highly dependent on the particle's size, geometry, local dielectric environment, metallic composition, and interparticle spacing.<sup>27, 30, 43, 45, 46</sup> By carefully controlling these factors using nanolithography, the particle's LSPR can be tuned over a range of wavelengths and therefore tailored to a specific application.

### 1.3.1 Size dependence of isolated, non-interacting nanoparticles

It has long been known that colloidal suspensions of gold nanoparticles can produce brilliant colours, and that increasing the particle diameter will decrease the frequency of the particle's plasmon, altering its colour.<sup>19</sup> In the case of colloidal suspensions, the number of particles involved often means that the plasmonic light scattering can easily be seen with the naked eye. The size dependent scattering colour can be easily understood by considering the plasmon resonance of a nanosphere; as the sphere's diameter is increased, the restoring force provided by the charges on opposite sides of the particle is decreased, lowering the frequency of the oscillation.<sup>23</sup> To date, the plasmons of a wide variety of nanoparticle shapes have been experimentally observed, all of which demonstrate a similar dependence on size.

Simple disk shapes are among the most commonly seen and easily fabricated nanostructures. Craighead and Niklasson<sup>44</sup>, who fabricated arrays using electron-beam lithography, measured the first extinction spectrum obtained from a regular array of identical disk shaped particles. A number of groups have since shown that the LSPR wavelength can be tuned by altering the diameter of such shapes.<sup>47, 48</sup> Gotschy *et al.*<sup>47</sup> used electron beam lithography to show a 60nm LSPR red-shift (from 460nm to 520nm) in gold disks by increasing their diameter from 44nm to 95nm. While, in a similar demonstration, this time using colloidal lithography in place of electron beam lithography, Hanarp *et al.*<sup>48</sup> showed that increasing the diameter of 20nm tall gold disks from 74nm to 137nm, whilst maintaining a constant interparticle spacing of approximately 280nm, produces an extinction peak shift in the region of 150nm.

Using different metal types also has a marked effect on the plasmon wavelength of a nanoparticle. Ag structures show a similar size dependence<sup>32, 46, 49</sup> but have a higher excitation frequency than Au due to a higher bulk plasmon frequency.<sup>50</sup> Studies tend to focus on gold and silver, as they have favourable bulk dielectric properties.<sup>50</sup> However, more recently, studies have been conducted on metallic nano-disks fabricated using Al, Pt and Pd<sup>49, 51, 52</sup>, all of which

demonstrate size dependent properties in line with those seen in Ag and Au (ie. the resonances red-shift with increasing particle size).

### 1.3.2 Shape dependent field enhancements - Hot-spot generation at sharp tips

When engineering a biosensor based on LSPR it is not only important to tune that device's plasmon resonance to a particular wavelength, but also to have control over the specific areas of electromagnetic field enhancement. Knowing the location and magnitude of the field surrounding the nanoparticles is essential for designing experiments where small numbers of molecules will be probed. Slightly more complex structures, in particular structures that contain areas of high curvature (sharp points or edges), such as triangles,<sup>46, 53</sup> are becoming of increasing interest due to their plasmonic antenna properties. Uneven surface plasmon distribution causes charge to accumulate at these sharp points, leading to an increase in surface charge density and a concurrent increase in localised field strength. This effect can be modeled numerically and has been shown to produce localised field strengths hundreds of times that of the exciting field<sup>54, 55</sup>.

### 1.3.3 Interparticle interactions

Although there are potential sensing applications for single field-enhanced nanoparticles<sup>37</sup>, it is more common, and often more experimentally practical, to use groups or arrays of identical particles. These can be colloidal particles deposited onto a substrate<sup>56</sup>, or specifically engineered particles fabricated from the ground up,<sup>43, 57, 58</sup> dispersed semi-randomly,<sup>48</sup> in a tightly controlled array format,<sup>45, 59</sup> or as dimers (pairs of closely spaced particles)<sup>58, 60, 61</sup> on a substrate. It is at this point that interparticle interaction becomes an important consideration as it can affect both the LSPR wavelength of the particles and the strength of the localised field generated around them. Two interactions mechanisms exist; far-field interactions and near-field plasmonic coupling.

Far-field interactions in nanoparticle arrays can be observed when the array periodicity (or grating constant) is in the range of the exciting light's wavelength. Arranging nanoparticles on a substrate in a uniform two-dimensional array leads to them exhibiting the properties of a grating, which, depending on the grating constant, can lead to a broadening of the LSPR band and small shifts in the LSPR wavelength. If the grating constant is much smaller than the LSPR wavelength, (yet significantly large so that no near-field coupling takes place) no scattering occurs as a consequence of the grating, and the nanoparticles behave as if isolated. The lack of significant radiative damping produces a sharp, uniform resonance peak. If the grating constant is much larger than the LSPR wavelength, scattering can occur for all wavelengths near the plasmonic resonance band (as a consequence of grating orders existing over this range). The peak LSPR wavelength is the same as expected for an isolated particle, but the increase in radiative damping results in a longer plasmon decay time, which in turn makes the plasmon resonance band weaker and much broader. However, in the case that the grating constant is close to the LSPR wavelength of the individual particles, far field dipolar interaction can alter the resonant condition of the array. As the grating constant approaches the wavelength of incident light, light begins to couple to the grating's first order, which scatters parallel to the plane of the particles, creating an evanescent field on the substrate surface. If this grating

constant matches the LSPR wavelength of the nanoparticles, in-phase combination of plasmonically scattered light from adjacent particles and the original evanescent field generates a strong electromagnetic field. This field interacts with local plasmon fields of the individual particles, shifting their resonance condition to longer wavelengths.<sup>43</sup>

Near field interactions occur when the interparticle distance is much smaller than the wavelength of the exciting light, in which case the plasmonic dipoles of two closely spaced particles can interact. The surface charges on each particle are dependent on the polarisation of the exciting field, and if the exciting light is polarised parallel to the pair axis<sup>58</sup> the particles are excited together and their charge distributions will be identical. The consequence is that the surface charges in the gap between the particles will be opposite, leading to dipole coupling of each particle's plasmon, which in turn leads to the coupled particle pair exhibiting a lower resonance frequency than that seen in the individual particles.<sup>58</sup> Concurrently, the dipole field between the particles strengthens, increasing the magnitude of the electromagnetic field enhancement seen between the particles.<sup>28, 61, 62</sup> Should the exciting light be polarised perpendicular to the particle pair axis, surface charge distribution will act to increase repulsive forces between the particles, increasing the resonance frequency of the system,<sup>58</sup> and decreasing the interparticle field enhancement.<sup>62, 63</sup> As this is a near-field effect it is strongly distance dependent; several groups have demonstrated a continually red-shifting plasmon as two particles are brought closer together at parallel polarisation.<sup>58, 60, 64</sup> The blue-shift at perpendicular polarisation however is less pronounced. The main driving force behind this coupled particle research stems from the realisation that near-field electromagnetic enhancement between two coupled particles is amongst the largest seen in nanoparticle plasmonics, and can be thousands of times that of the incident field.<sup>61</sup> As such, these systems prove to be excellent platforms for ultra-sensitive molecular detection via SERS<sup>62, 63</sup> (covered in more detail in Section 1.4.4).

#### 1.3.4 Multipolar resonances

This increase in size and complexity of the particles can result in structures that exhibit multiple plasmon resonance modes. Such multipolar resonances have been described in a variety of structures including triangular prisms,<sup>53, 55, 65, 66</sup> nanocubes,<sup>67</sup> and nanorods.<sup>68-70</sup> Not only do structures of increased complexity often display multipolar resonances, but, in the case of non-symmetrical structures, the excitation of these resonances can be dependent on the polarisation of the incident electromagnetic field. In Section 1.3.3 the polarisation dependence of coupled particle arrays was mentioned, and whereas that was an effect due to plasmonic interaction between two or more separate particles, the following cases demonstrate that isolated non-symmetrical particles themselves can too be influenced by the exciting field's orientation. Gotschy *et al.*<sup>71</sup> fabricated elongated Ag nanoparticles and measured their extinction spectra when the electric field was polarised both parallel and perpendicular to the particles long axis. Two distinct resonances were apparent, one for each polarisation direction. The weaker, blue-shifted resonance occurred when the electric field was polarised parallel to the short axis, whereas a stronger red-shifted resonance appeared at long axis polarisation. Nano-rods display similar polarisation dependence. As with Gotschy's<sup>71</sup> elongated particles, two resonances are

observed in very short nano-rods, one for each polarisation direction. However, as the aspect ratio of the rod increases, many higher order resonances can be supported when the electric field is polarised along the rod's long axis, the frequency of which are determined by the length of the rod.<sup>69, 70</sup>

### 1.3.5 Nano-rings and Nano-crescents

Recent advances in electron-beam lithography resolution, as well as nanosphere/colloidal lithography, have shown a move toward ever more complicated structures with increased functionality. Ring, crescent, and split-ring structures<sup>34, 39, 72, 73</sup> have been shown to be among the more tunable of such structures, with small changes in their structural morphology resulting in dramatic LSPR shifts.

Aizpurua *et al.*<sup>39</sup> demonstrated the tunable modes in ring-shaped gold nanoparticles prepared by colloidal lithography. In this case Au was evaporated over Polystyrene nanospheres so that when the spheres are removed by solvent a free standing Au ring remains. Maintaining a fixed outer radius of 60nm, and increasing the wall width, from 9nm to 14nm, the authors showed that the ring's LSPR could be tuned over approximately 400nm in the infrared region of the electromagnetic spectrum. Numerical simulations of the ring's electromagnetic field at resonance showed there to be a large, uniform area of enhancement inside the ring cavity, an area that could be exploited for bio-sensing applications.

The same group recently showed that the sensitivity to bulk refractive index changes of the Au ring's LSPR was far greater (>5x) than that of Au disks with resonances in the same spectral region. The potential of use of these structures as refractive index bio-sensing platforms was demonstrated by monitoring the LSPR peak shift of the rings when monolayers of protein were absorbed.<sup>36</sup>

Crescent shaped structures also possess highly tunable plasmon modes, the frequency of which can be controlled by altering the crescent's diameter, wall width and arc-length.<sup>34, 38, 74</sup> Fabrication of crescent geometries via colloidal lithography, whether they be "flat" structures<sup>34, 38, 74</sup> or crescent-spheres,<sup>35, 37</sup> leads to areas of extremely high curvature at their tips. The fields generated by these sub-10nm tips at LSPR have been shown to be as high as  $10^{2.6}$ , and used effectively for biomolecular detection via SERS.<sup>37</sup>

### 1.3.6 Nano split-ring resonators

Similar in plasmonic response to nano-crescents, square shaped split-ring resonators are often used to create materials that generate a negative index of refraction. In order to achieve a negative value for the refractive index, both the materials electric permittivity,  $\epsilon$ , and magnetic permeability,  $\mu$ , must be negative. Negative  $\epsilon$  occurs naturally in metals for any frequency up to the metal's plasma frequency, so creating negative  $\mu$  presents the engineering challenge. One way to engineer these so-called metamaterials is to fabricate highly ordered, closely packed arrays of nano-split-ring resonators. The individual rings can be thought of as LC resonators, the base-wire representing one wind of an inductance loop, and the gap representing capacitor plates<sup>75</sup>. The first plasmonic resonance, the LC resonance, can be estimated by:

$$\omega_{LC} = \frac{1}{\sqrt{LC}} \quad (1.13)$$

where  $L$  and  $C$  are the inductance and capacitance of the circuit.<sup>75</sup> Coupling to the magnetic resonance of the split-ring requires that the magnetic field of the exciting light is perpendicular to the plane of the base wire. The current in the base wire can generate a magnetic field that opposes the exciting magnetic field, leading to a negative value of magnetic permeability, allowing the material to display negative refractive index.<sup>75, 76</sup> This phenomenon may yield a variety of new optical applications, including perfect lensing.<sup>77</sup> Although the inductance/capacitance analogy has long been popular for describing split-rings,<sup>42, 75, 76, 78-83</sup> more recent studies, both numerical and experimental, have shown the multiple resonances exhibited by these geometries, including the first order mode, are in fact plasmonic resonances of the entire structure,<sup>72, 84</sup> and have more in common with the multiple resonances seen in nanrods<sup>70</sup>. Although it is the first order resonance in which metamaterial engineers are interested, the multiple higher order modes exhibited by nano split-rings make them excellent candidates for nanophotonic biosensing, due to their tunable, polarisation dependent nature.<sup>72, 73</sup>

## 1.4 Raman spectroscopy

### 1.4.1 The Raman scattering effect

The Indian physicist C.V. Raman first observed inelastic scattering from molecules in 1928; an observation for which he was later awarded the Nobel Prize for physics. The phenomenon, which now bears his name, refers to the inelastic scattering of light as a consequence of vibrational modes existing within certain “Raman active” molecules. The technique can be used for both molecular detection and characterisation, since it confers structural information about the molecules under investigation. As such it is a powerful, potentially label-free tool for bio-molecular sensing.

In order for a molecule to be Raman active, molecular bond vibrations must result in a change in molecular polarisability (the ease with which distortion of the electron cloud surrounding the molecule can occur). When an external light field interacts with the molecule it can shift the electron cloud with respect to the molecule’s atomic nuclei. The polarisation of the electrons promotes them to a higher energetic state. This new vibrational energy level is not a real electronic state, and is commonly referred to as a virtual state. Unlike absorption, where energy transfer will only take place if the incident photon’s energy exactly matches the difference between two electronic states, the energy increase seen in the Raman effect is dependent solely on the energy of the incident photon. As such, the process is not quantised, with any number of virtual states achievable. These virtual states are unstable, quickly decaying in the form of a scattered photon.

If the electron distortion results in no movement of the nucleus, the photon undergoes no change and scatters with the same energy and wavelength as it had when first incident on the molecule. This is referred to as Rayleigh scattering. However, should the distortion of the electron cloud result in nuclear motion, energy is transferred between the incident photon and

the molecule and the photon will scatter with a shifted energy. It is this inelastic scattering that is referred to as Raman scattering.

Two types of Raman scattering exist, Stokes and anti-Stokes scattering, depicted in Figure 1.5. If an incident photon polarises the electron cloud and increases its vibrational energy from the lowest vibrational level to a virtual state (somewhere between the ground state and lowest electronic state), before returning to the first vibrational level of the electronic ground state, the scattered photon is said to be Stokes shifted. The molecule must absorb a portion of the incident photon's energy in order to do this, resulting in a scattered photon of lower energy and longer wavelength. Anti-Stokes scattering occurs if the molecule is already in the first vibrational level of the electronic ground state when the exciting photon interacts with its electron cloud. In this case, after being excited to a virtual state, the molecule returns to a lower vibrational level than it started in. Energy is transferred to the scattered photon, blue-shifting its frequency comparative to the incident photon. This case is far less common than Stokes scattering since a lower proportion of molecules are likely to be in their first vibrational level at room temperature (the proportion of molecules in each state can be determined using Boltzmann's equation.)<sup>85</sup>

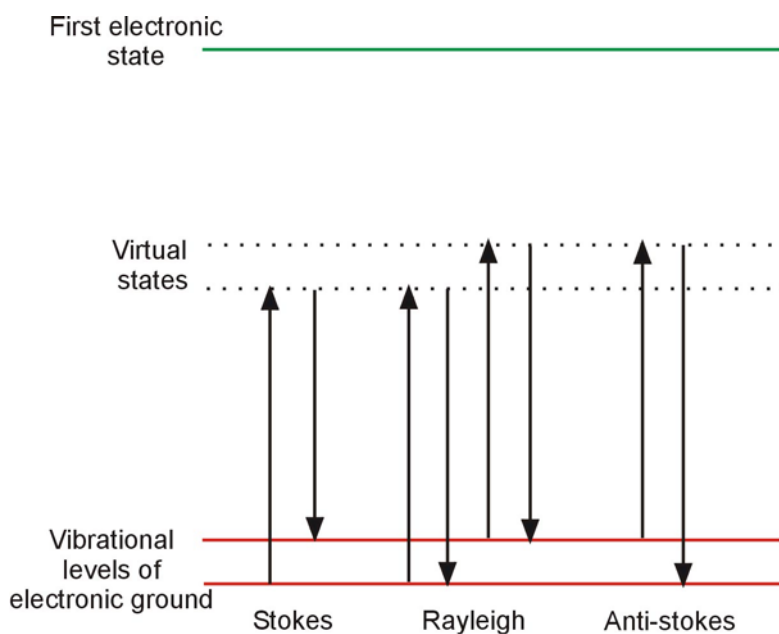


Figure 1.5. Diagram of the Raman effect. The energy of the electron cloud is promoted to, and subsequently decays from, an intermediate “virtual” state somewhere between the ground and first electronic state. Since this state does not represent an atomic equilibrium state it is highly unstable and exists only briefly, the molecule's energy decaying rapidly back to a vibrational level of the electronic ground state. Depending on the molecule's initial energy this may result in either a Stokes or an anti-Stokes shifted photon being scattered. The majority of photons are Rayleigh scattered, undergoing no energetic change.

The intensity of the Raman scatter can be expressed as:

$$I = Kl\alpha^2 \omega^4 \tag{1.14}$$

where  $l$  is the laser power,  $\alpha$  is molecular polarisability,  $\omega$  is the frequency of the laser, and  $K$  consists of constants.<sup>85</sup> Therefore, in terms of the experimental process itself, there are two ways that one can increase the amount of inelastic scatter without resorting to plasmonics, namely increase the power of the laser beam, or increase the frequency of the laser source. With this in mind, it would seem sensible to work at the highest frequencies possible, using UV lasers as light sources. However, problems associated with UV absorption by a wide range of materials including biomaterials such as proteins and DNA, as well as sample damage due to the highly energetic radiation, often make this choice impractical.

#### 1.4.2 Molecular vibrations

As described above, Raman scattered photons have an energy change equivalent to that needed to increase (Stokes) or decrease (Anti-Stokes) the vibrational energy level within the electronic ground state of the molecule. The number of vibrational modes present in a particular molecule is determined by its size, shape and symmetry, while the energy of these vibrations is determined by the mass of the atoms involved and the strength of their chemical bonds.

A molecule will have a number of degrees of freedom that dictate its range of motion, not all of which will be due to vibration. Every molecule will have three degrees of freedom which describe its translational motion in free space, and another three, in the case of non-linear molecules, which describe rotation about its x, y and z axis (linear molecules have only two rotational degrees of freedom since rotation around their bond axis does not result in an atomic position change). Therefore, the number of vibrational degrees of freedom in a particular molecule will be  $3N-6$  for non-linear molecules and  $3N-5$  for linear molecules, where  $N$  is the number of atoms.

In order for a molecule to be Raman active its bond vibrations must increase its level of polarisability. Not all vibrations achieve this and should a vibration instead create a change in electric dipole, the molecule will be susceptible to infra-red absorption (termed IR active). Since a molecule may have a large number of vibrational modes, it is possible that some will be Raman active vibrations, some will be IR active vibrations, and some may satisfy both conditions by producing a polarisability change and a change in the molecular dipole. Typically, symmetric vibrations result in the largest Raman scatter because they induce the greatest polarisability, whereas asymmetric vibrations cause a molecular dipole change and thus the greatest IR absorption. The only case where a vibration may not be both IR and Raman active is when the molecule has a defined centre of symmetry. These centrosymmetric molecules conform to the mutual exclusion rule, which states that a vibration may induce a polarisability change (symmetric) or a change in molecular dipole (asymmetric) but not both.

#### 1.4.3 Resonance Raman

Raman scattering has very low quantum efficiency, making the scattered light difficult to detect. Approximately one in every  $10^7$  photons incident on the molecule will be scattered inelastically. Resonance Raman can enhance this scattering by several orders of magnitude,<sup>85</sup> making the signal far easier to detect and allowing lower concentrations of molecules to be probed. Resonance Raman occurs when the frequency of the external light wave matches that of

an electronic transition within the molecule. The molecule's energy increases from the ground electronic state to an excited electronic state, as is analogous with absorption. However, unlike absorption, the new energetic state quickly decays back to the ground state, in either a Stokes or anti-Stokes fashion as described previously, producing an inelastically scattered photon (Figure 1.6).

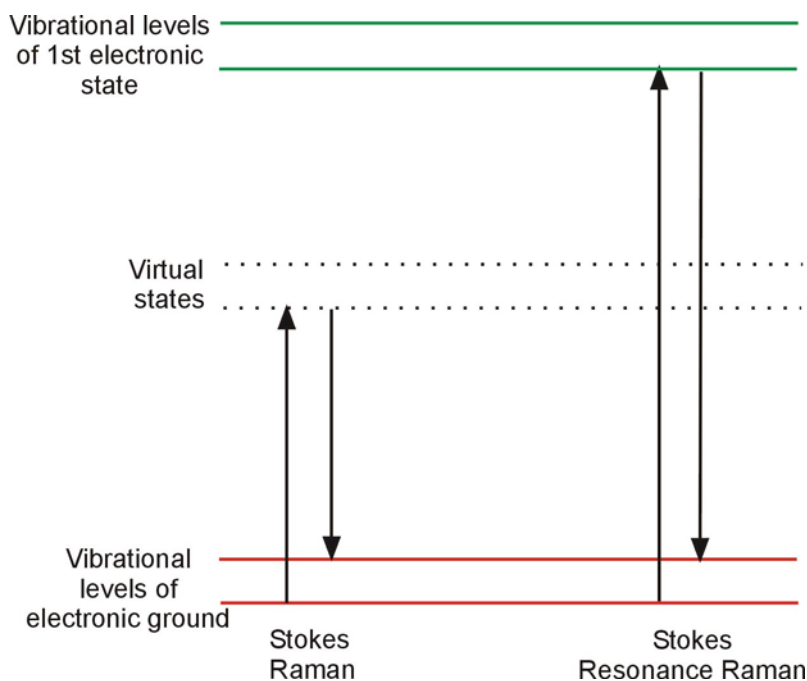


Figure 1.6. Diagram of resonant Raman scattering process. Comparison of Stoke shifted Raman (left) and resonance Raman (right). Unlike Raman scattering, the vibrational energy level that the molecule attains is real.

The Kramer Heisenberg Dirac equation, a method of determining a molecule's polarisability, can be used to gain an understanding of why the resonance Raman effect increases Raman scattering.<sup>85, 86</sup> The equation defines a molecule's polarisability as:

$$(\alpha_{\rho\sigma})_{GF} = \sum_I \left( \frac{\langle F|r_\rho|I\rangle\langle I|r_\sigma|G\rangle}{\omega_{GI} - \omega_L - i\Gamma_I} + \frac{\langle I|r_\rho|G\rangle\langle F|r_\sigma|I\rangle}{\omega_{IF} + \omega_L - i\Gamma_I} \right) \quad (1.15)$$

where  $\rho$  and  $\sigma$  are the incident and scattered polarisation directions,  $G$ ,  $I$  and  $F$  are the vibronic states of the initial electronic ground state, intermediate excited electronic state, and final electronic ground state respectively,  $r_{\rho/\sigma}$  is the dipole operator,  $\omega_{GI}$  is the frequency difference between the initial ground state and the excited state,  $\omega_{IF}$  is the frequency difference between the excited state and the final ground state,  $\omega_L$  is the frequency of the laser, and  $i\Gamma_I$  is a correction factor relating to the damping rate of the excited state.

The most important section of this expression, in relation to its description of the resonance Raman effect, is the denominator in the first term. When the frequency of the

exciting laser light,  $\omega_L$ , matches that of the difference between the ground and first electronic level of the molecule,  $\omega_{GI}$ , the denominator reduces to  $i\Gamma_I$ . Therefore, the polarisation of, and hence Raman scattering from, the molecule will be much higher than if the resonance condition had not been met. The correction factor,  $i\Gamma_I$ , ensures that the denominator does not equal zero, a condition which would result in infinite scattering. The expression also shows that the laser line need not exactly match the electronic transitional energy for some benefit to be gained, the closer the energy of the laser to the transition of the molecule, the smaller the denominator, hence the greater the polarisation.

Although this technique can provide a marked improvement over the intensity of normally Raman scattered light, it is not without its drawbacks. Matching the incident light to an electronic transitional energy within the molecule also causes significant levels of absorption to occur. This can in turn lead to rapid sample degradation and large fluorescence signals that drown out the Raman scattered light.

#### 1.4.4 Surface enhanced Raman scattering (SERS) by nanoparticle plasmonics

Localised surface plasmon resonances seen in nanoparticles and roughened metallic surfaces, can be used to significantly enhanced the Raman scattering from molecules absorbed onto, or situated very close to the resonating metal nano-structures. The effect is referred to as surface enhanced Raman scattering (SERS) and was first observed by Fleischmann *et al*<sup>16</sup> while studying the Raman spectra of pyridine adsorbed on a roughened silver electrode. Using this method in conjunction with the resonance Raman effect, a technique known as surface enhanced resonance Raman scattering (SERRS), has led to Raman scattering enhancements of  $10^{15}$ , facilitating single molecule detection.<sup>1,2</sup>

The large enhancements provided by optimised SERS and SERRS allow the techniques to compete with the sensitivity attainable using fluorescence, whilst also providing a higher level of functionality and versatility in structural studies. Unlike fluorescence spectra, which are spectrally very broad, Raman signals consist of many sharp peaks (each of which relate to a particular vibrational mode) which not only allow identification of the molecule under investigation, but also enable a level of multiplexing that is not possible using fluorescence. Furthermore, unlike fluorescence sensing the SERS technique does not require that analytes be tagged with a fluorophore. This makes SERS potentially label free, reducing the level of sample preparation required before measurement.

As described previously, interaction between a nanoparticle's oscillating surface charges and an incident light wave can lead to LSPR, which in turn amplifies the electromagnetic near field around the particle. These enhancements can be orders of magnitude larger than the incident field. The fluctuating plasmon interacts with the electrons in the molecule, increasing its polarisation (a molecule's polarisation is directly related to the magnitude of the local electric field, Equation 1.16).<sup>27</sup> Therefore, molecules located within the plasmonic near-field display greater Raman scattering intensities.

$$P = a E \tag{1.16}$$

where  $P$  is molecular polarisation,  $\alpha$  is the polarisability of the molecule and  $E$  is the magnitude of the local electric field.

The total scattering enhancement seen from molecules absorbed onto a nano-plasmonic metal surface, as opposed to those in solution, is proportional to the fourth power of the local e-field:<sup>87</sup>

$$\rho(r_m, \omega) = \left| \frac{E(r_m, \omega)}{E_{inc}(\omega)} \right|^4 \quad (1.17)$$

where  $\rho$  is the total Raman enhancement,  $E(r_m, \omega)$  is the total electric field at the molecular location  $r_m$ , and  $E_{inc}(\omega)$  is the electric field associated with the incident plane wave.

Although electromagnetic enhancement accounts for the majority of the SERS effect, another mechanism, referred to as chemical or charge transfer enhancement, also contributes to the overall signal increase. The level of understanding around this effect is less well developed when compared to electromagnetic enhancement, however, current theory suggests that the direct absorption of a molecule onto a metal surface facilitates the creation of new electronic states from which scattering can be enhanced.<sup>85, 86, 88, 89</sup> Bonding the molecule to the metal allows the transfer of electrons between the two, establishing electronic states that would not have been possible otherwise. Transfers between the Fermi level of the metal and the electronic states of the molecule (either from the highest occupied state to the Fermi level, or from the Fermi level to the lowest unoccupied state) increase the polarisation of the molecule, and hence its Raman scattering intensity, by the same mechanism as is seen in resonance Raman scattering. Therefore, the energy levels formed by the metal-molecule complex enable a resonance Raman effect at frequencies that would otherwise be forbidden (the molecule would normally require far greater energies to achieve resonance Raman scattering).

As well as the greatly increased scattering intensities, immobilising molecules on a metal surface has other benefits that can make a difference to the acquired Raman signal. From an experimental point of view, one of the major drawbacks of using resonance Raman is the large amount of fluorescence emitted from the molecules of interest. This can overwhelm the Raman scattered signal and make the peaks difficult to extract from the background. Since fluorescent dyes are commonly used as Raman active tags for molecules with zero or weak Raman activity that would otherwise be difficult to detect (DNA for instance), this excess fluorescence can severely limit the experimental sensitivity of resonance Raman. Fortunately, attaching the molecule to a metallic nanoparticle can quench the majority of this fluorescence. Interaction with the metal surface increases non-radiative decay through resonance energy transfer between the molecule and the metal, as well as decreasing radiative decay through destructive interference between the metal dipole and the molecular dipole (a consequence of a phase shift between the two, brought about by the complex dielectric function of the metal, which acts to decrease radiative decay channels).<sup>90-92</sup> The greatly reduced fluorescence (the total fluorescence reduction has been shown to be ~99% or more)<sup>90</sup> as well as the large contribution from the LSPR near-field, gives SERRS a great advantage over resonance Raman in terms of scattering efficiency and ease of signal collection.

Since the electromagnetic contribution to the SERS effect is far stronger, better understood and easier to manipulate than chemical enhancement, it is the optimisation of nanoparticle plasmonics that provides the most effective route toward fabricating SERS bio-sensors. The earliest SERS experiments were performed in the 1970's using chemically roughened electrodes,<sup>16, 93, 94</sup> but as time and fabrication methods have progressed, SERS substrates with specifically engineered LSPR frequencies and EM hot-spots have been realised. As described previously, plasmonic near-field coupling between two or more nanoparticles can provide significant enhancements of the localised electric field strength, which in turn result in Raman scattering enhancements of many orders of magnitude.

Perhaps the easiest and quickest way to produce such an effect is by drying a colloidal suspension of metallic nanoparticles onto a surface. Aggregated colloids and self assembled particulate films can provide good Raman enhancements due to interparticle plasmon coupling,<sup>56, 95-98</sup> but the random nature of their formation make the magnitude, frequency and location of their resonating electric fields difficult to predict or reproduce. Using lithographic techniques allows for finer control over such factors. Uniform arrays of close-packed structures, fabricated using nanosphere and electron-beam lithography, have also been shown to be effective SERS substrates, their Raman scattering efficiency dependent on interparticle array spacing.<sup>45</sup> Spatial manipulation of individual nanoparticles has also been used to induce large Raman scattering cross sections. Several groups have experimented with using atomic force microscopy (AFM)<sup>99</sup> and optical laser tweezing<sup>100</sup> to move single nanoparticles together, forming interacting dimers and particle chains. These methods, although somewhat complicated, can be used to tune (within a certain degree) the LSPR of the system, and generate strong Raman enhancements (in the order of  $10^7$ )<sup>99</sup> for molecules in the gaps between particles.

Near-field particle coupling, as demonstrated in Section 1.3.3, is not the only way to generate high electric fields. Single, non-interacting particles display lower electric fields at resonance so exhibit lower Raman enhancements (typically on the order of  $10^2$ - $10^3$ )<sup>87, 97</sup> when compared to coupled particles. However, recent advances in lithographic techniques have permitted greater control over particle morphology and allowed for the engineering of nanoparticles with sharp edges have also been used as effective SERS structures, generating Raman enhancements in the order of  $10^{10}$ .<sup>37</sup> Although these structures cannot compete with aggregated colloid or close-packed for overall SERS enhancement, the ability to tune their plasmons over a larger wavelength range and specifically engineer the location and magnitude of the electric field enhancement seen in their multiple resonances, make them appealing candidates for SERS structures.

### 1.5 Theoretical summary and preamble of experimental work described herein

In summary, the tunable plasmonic properties of metallic nano-structures enable a wide variety of highly sensitive, application specific, optical biosensors to be engineered. Molecular sensors which rely on the plasmonic activity of resonating nano-metallic structures have previously been shown to be capable of remarkably sensitive analytical detection and identification via surface enhanced resonance Raman spectroscopy (SERRS). Understanding and controlling the resonances of these nanostructures is essential for the engineering of biosensing

substrates tailored to a specific application or target molecule. However, many of these former studies use either aggregations of colloidal particulates, or directly engineered non-complex geometries, resulting in lower quality, non-specific resonances. These approaches are also restrictive in terms of the wavelength range over which they operate as the resonances cannot be tuned to specific values, or across a wide spectral range. This is most clearly illustrated in SERRS where the molecular resonance of a dye has to be tuned to the plasmon resonance, rather than the converse.

The research presented here represents a shift toward more functional plasmonic sensors, using advanced lithographic patterning to specifically engineer the sensor's resonance, so that it is tuned to the molecule's optical response (i.e. the sensor is constructed so that it performs specific sensory functions). The research concentrates on the fabrication of novel Au and Ag crescent shaped split-ring resonators for use as highly sensitive SERS substrates. Using the nanometer resolution afforded by the latest generation electron-beam lithography tools, these structures can be made small enough to exhibit resonances in the visible portion of the spectrum, enabling their use as visible wavelength SERRS structures. Characterising the plasmonic properties of these novel devices by measuring the absorption and scattering of light from the engineered particle arrays, the resonances are shown to be tunable over a wavelength range of several microns by altering the radius, arc-length, wall width, height, and metallic composition of the split-rings. The non-symmetrical geometries of the structures allow them to support multiple, polarisation dependent plasmon resonances, each of which have been identified and characterised using a combination of experimental data and finite difference time domain simulations.

Fine control over the geometry of 75 and 80 nm radius Ag split rings allows a single ring structure to support two, polarisation dependent, plasmon resonances corresponding to two common, commercially available, laser wavelengths (532 and 633 nm for the 75 nm radius split-ring sensor, 633 and 785 nm for the 80 nm radius split-ring sensor). The effectiveness of these devices to act as polarisation dependent (ie. dichroic) sensors is demonstrated in a series of sensing experiments; the multi-modal plasmonic properties of each sensor design used to independently perform SERS and SERRS at each of its resonant laser wavelengths. In achieving this, it is ultimately demonstrated how crescent-shaped nano split-ring resonators can be utilised as dichroic switch sensors for targeted, discrete biosensing of differently labeled oligonucleotide sequences bound complementarily to the modified sensor surface in a mixed population (the SERRS response of the device, and hence the particular type of DNA detected, altered by changing the orientation of the incident light with respect to structural geometry).

## Chapter 2 - Materials and Methods

### Abstract

A combination of numerical simulation, nano-scale fabrication and optical characterisation methods were used to engineer a range of nano-metallic split-ring resonators with different plasmonic properties for tailored, multifunctional biosensing applications. The surface of the sensors were modified with self-assembling monolayers of various biomolecules and utilised as highly functional biomolecular sensors for surface enhanced Raman spectroscopy.

### 2.1 Introduction

This chapter covers all of the experimental fabrication, characterisation and sensing methods used throughout the research, as well as a brief results and discussion section covering some of the fabrication problems encountered. A supplementary information section, including a more detailed discussion covering the theory, set-up and operation of the techniques, processes and tools employed throughout this research, can be found in the Appendix.

### 2.2 Materials

Cysteamine, 2-mercaptopyridine, 3-aminopropyltriethoxysilane and dithiothreitol were obtained from Sigma-Aldrich, UK. Cy5 N-Hydroxysuccinimide ester was obtained from Amersham Biosciences (now part of GE Healthcare), UK. Seven oligonucleotide sequence types were used throughout this research, some as probe strands, others as target strands, Table 2.1 (a detailed explanation of the sequence terminology can be found in Section A.1.14). All DNA was obtained from ATD Bio, University of Southampton:

	<i>3'-mod</i>	<i>Sequence</i>	<i>5'-mod</i>
Sequence A	THIOL	2TGCAGATAGATAGCAGT3	Cy5
Sequence B	THIOL	TGCAGATAGATAGCAGT3	–
Sequence C	–	2CTGCTATCTATCTGCA	Cy5
Sequence D	–	2CTGCTTTCTATCTGCA	Cy5
Sequence E	–	2CTTACCGATCGTATTC	Cy5
Sequence F	Cy5	CTGCTATCTATCTGCA3	–
Sequence G	–	CTGCTATCTATCTGCA	–
Sequence I	–	2CTGCTATCTATCTGCA	Cy7

500  $\mu\text{m}$  thick, 4 inch Pyrex wafers were obtained from University Wafer, Boston, USA. 500  $\mu\text{m}$  thick, 4 inch silicon wafers coated on both sides with ~200 nm of silicon nitride were obtained from the Scottish Microelectronics Centre, University of Edinburgh.

Ti and Ag wire used for resistive heating evaporation were purchased from Goodfellow Cambridge Limited, UK, and Testbourne Inc, UK, respectively. Au, Al and Ti used for electron beam evaporation were obtained from Pi-Kem, UK.

2010 and 2041 Elvacite Polymethyl Methacrylate (PMMA), with molecular weights of 80k and 345k respectively, was obtained from Lucite International Inc. S1818 photoresist, UV88 electron beam resist and Microposit Cd-26 developer were obtained from Shipley company Inc. Methyl isobutyl ketone was obtained from Merck Chemicals Ltd. Acetone was obtained from Fisher Scientific. Isopropyl alcohol and ethanol were obtained from Sigma-Aldrich.

## 2.3 Methods

### 2.3.1 Fabrication of Au and Ag split-ring structures

Figure 2.1 shows a schematic of the fabrication procedure. Details of each step can be found in the following sections (Sections 2.3.1.1-2.3.1.9). All devices used for plasmon characterisation and sensing purposes were fabricated on 500  $\mu\text{m}$  thick Pyrex wafers. Fabrication on Pyrex allowed the plasmon resonances of the structures to be easily determined by transmission spectroscopy.

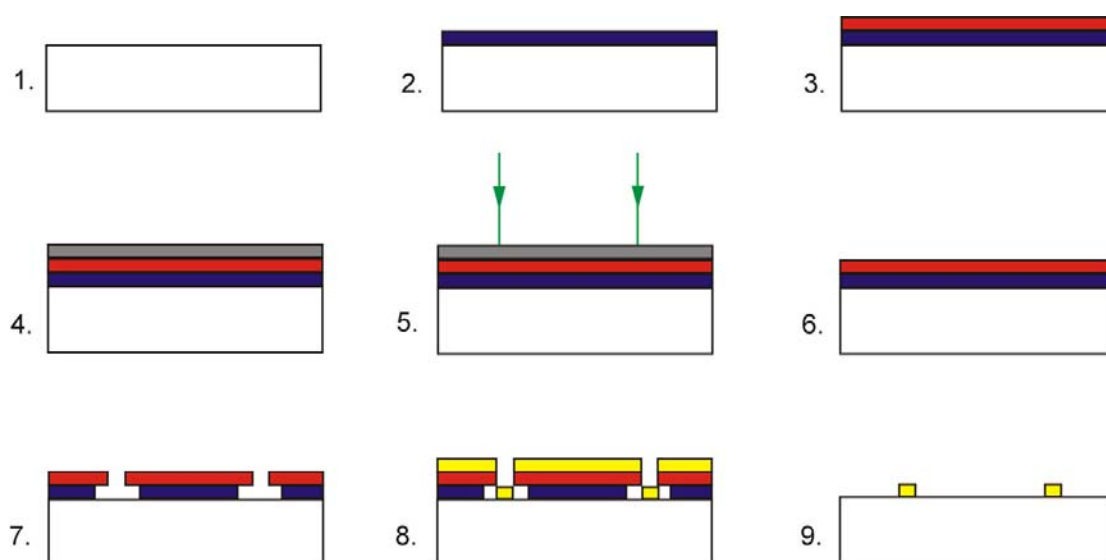


Figure 2.1. Schematic of fabrication procedure: 1- Cleaned Pyrex glass silde; 2&3- bi-layer of PMMA resist spun onto the glass substrate; 4- Evaporation of 30 nm Al onto the resist to act as charge conduction layer; 5- Exposure of pattern by electron beam tool; 6- Removal of Al layer; 7- Development of PMMA in MIBK, revealing patterned areas. The low molecular weight of the first resist layer, relative to the second layer, results in an undercut profile. At this point the patterned glass area may be modified with 3-aminopropyltriethoxysilane if necessary; 8- Evaporation of Au or Ag. 9- Sample is soaked in warm acetone, lifting-off the unwanted resist and metal.

#### 2.3.1.1 Cleaning

The wafers were divided into square segments measuring approximately 20 x 20mm. These segments were cleaned thoroughly to remove any organic contaminants as well as any large particles generated by wafer scribing. The samples were first sonicated in acetone for 10 minutes before being placed in pirhana solution (a 3:1 mix of sulphuric acid and hydrogen

peroxide) for a further 10 minutes at 80°C, then washed with de-ionised (DI) water and dried with nitrogen.

### 2.3.1.2 Resist Spinning

The electron beam resist used throughout for writing the ring structures was polymethyl-methacrylate (PMMA), a positive tone resist. Since the molecular weight and thickness of the resist can determine the size of the smallest patternable feature, resist dilution and molecular weight were optimised to ensure the highest level structural resolution possible. All structures were written in a bi-layer of PMMA, a low molecular weight resist deposited first, followed by a higher molecular weight layer. The lower molecular weight resist is more sensitive to chain-scission by the incident electron beam, thus a larger area of the resist receives the required clearing dose (through electron scattering), creating an undercut profile which promotes lift-off (Figure 2.1).

The samples were covered with a 2.5% dilution of 2010 PMMA in o-xylene, and spun at 5000rpm for 60 seconds using a vacuum spinner. The resulting layer of resist was approximately 40 nm thick. This was then baked at 180°C for 1 hour to drive off the solvent. This process was repeated, this time using 2.5% 2041 PMMA, a higher molecular weight resist, producing a second layer with a thickness of approximately 50 nm.

### 2.3.1.3 Charge Conduction Layer

Before exposure in the beam-writer, the resist was covered with a 30nm layer of aluminium. This was required when using a non-conducting substrate material like Pyrex glass. It acts as a charge conduction layer, preventing a build up of negative charge in the substrate that can adversely affect the positioning of the incident particle beam. Initially, nichrome (NiCr) was used for this step, but this process was changed in favour of aluminium because of problems with NiCr removal after exposure. The chrome etch (a mixture of ceric ammonium nitrate and nitric acid) was not removing all of the metal, possibly due to the alloy composition in the evaporator. The aluminium was deposited by electron beam evaporation in a Plassys MEB 400S (see Section 2.3.1.6 and Appendix A.1.2.1).

### 2.3.1.4 Patterning the resist using electron-beam lithography

The samples were then patterned using the Vistec VB6 UHR EWF electron beam tool. The pattern designs were defined using L-Edit CAD software, which exports the design as a graphical data system (GDS) file. In order for this representation of the design to be interpreted by the beam-writer it must be converted into geometries compatible with the lithography tool. CATS (Computer Aided Transcription System) software converts the GDS file into a series of trapezoids in a process known as fracturing. It is these trapezoidal shapes that the electron beam tool writes into the resist material. During the design process, the ring geometries were segmented into 4-sided polygons, ensuring compatibility with the trapezoidal fracturing processes required by the tool's software before exposure.

The dose for each particular shape was determined by performing a dose test on every new ring design. The dose tests were designed to write a small array of rings several times over,

each time using a different dose. Typical dose tests for PMMA were in the range from 200-3000  $\mu\text{C} / \text{cm}^{-1}$ , with smaller features requiring higher doses. The substrates were then studied by SEM to determine the correct clearing dose for a particular shape. Typical doses used for fabricating the structures found in Chapters 3-5 were 1700  $\mu\text{C}/\text{cm}^{-1}$  for the larger 135 nm radius rings and 2000  $\mu\text{C}/\text{cm}^{-1}$  for the smaller 75 nm radius rings. All of the nanostructures were written in  $1\text{mm}^2$  arrays using a 1 nA, 4 nm diameter beam, with a step size of 1.5 nm and a VRU of 3. More information on this technique can be found in Appendix A.1.1.

### 2.3.1.5 Development

Upon removal from the beam-writer, the substrate was placed in Microposit CD-26 chemical developer for 3 minutes to remove the 30nm Al charge conduction layer. Although it is a developer for some resists, CD-26 does not affect the PMMA. The sample was developed for 45 seconds in a 2.5:1 mix of isopropyl alcohol (IPA) : methyl isobutyl ketone (MIBK) at a temperature of 23°C, MIBK acting as the developer for the PMMA. PMMA is positive tone, so the exposed areas of the resist, having undergone polymer chain scission, are more soluble than unexposed areas when in contact with MIBK and are washed away. Rinsing with IPA for 1 minute stops development. The samples are then treated with oxygen plasma for 30 seconds at 30W in a Gala Plasma Prep 5 oxygen barrel asher. This step etches away approximately 1-2 nm of the resist layer, its primary purpose being to remove any un-developed resist residue at the bottom of the patterned features.

### 2.3.1.6 Au Metallisation and lift-off

The samples were metallised with a Ti/Au bi-layer in a Plassys MEB 400S electron beam evaporator. A 5 nm layer of Titanium was used as an adhesion layer, allowing Au to attach to the substrate. Using thin resist (~ 40nm for the first layer) limits the amount of metal that can be deposited on the substrate. If the metal is thicker than the first resist layer, the lift-off profile will be impaired and the resist may be hard to remove. In such cases it may require lengthy sonication in conjunction with the standard acetone lift-off soak, which may damage, or completely remove, the metallic features. Furthermore, if the metal is thicker than the total resist bi-layer, the resist may not lift-off at all. For these reasons, the chosen thickness of the evaporated Au was 20 nm. The unwanted resist and metal was then removed from the substrate by soaking in acetone at 50°C for 3 hours or more (samples are sonicated for 5 seconds if lift-off has not occurred by this point, a step which may be repeated several times if needed). AFM measurements (Section 2.3.3.3) show these crystal readings to be accurate and reproducible; the thickness of the Ti/Au measured over 10 separate samples being  $26 \pm 2$  nm. Further information on the evaporation tool can be found in Appendix A.1.2.

### 2.3.1.7 Ag Metallisation

Silver was not available in any of the electron-beam evaporation units in the JWNC, so all Ag evaporation was performed using an in-house built thermal evaporator. Unlike the Plassys systems, which have computer controlled recipes, shutters and evaporation rates, the thermal evaporator has entirely manual operation (see Appendix A.1.2 for further information). This can

make the thickness of the evaporated metal hard to control, especially if the deposition layer is very thin (<10 nm) or if there is more than one layer of metal to deposit. Furthermore, the pressure inside the bell-jar does not remain constant during the evaporation run, leading to inconsistent layer adhesion (see Section 2.4.3).

#### 2.3.1.8 Surface modification with 3-aminopropyltriethoxysilane

Chemical adhesion layers were used when it was not possible/practical to use metallic alternatives. In such cases, the developed substrate was modified with a self-assembled monolayer of 3-aminopropyltriethoxysilane. Samples were placed in a 4% solution of 3-aminopropyltriethoxysilane (in ethanol) for 1 hour. Hydroxyl groups in the glass displace the alkoxy groups on the silane, bonding the two covalently in a Si-O-Si formation. The result of this process is an amine-modified pattern, ready for metallisation with Ag.

#### 2.3.1.9 Ti/Ag evaporation

Although using a metal adhesion layer allowed the speed of the fabrication process to be increased it was not always used due to complications involving Ti evaporation using the resistive heating evaporator. The most important concern was the tendency for the boat holding the Ti to crack before evaporation had taken place. The temperature at which Ti evaporates is 1725 °C, and often the tungsten alumina boat holding the metal would fail before reaching this temperature (particularly if already subjected to several heating/cooling cycles), breaking the circuit and preventing evaporation. After many boat failures, and/or problems achieving a uniform, repeatable Ti/Ag layer, it was thought best to explore a chemical adhesion methods while these issues were being addressed. The crystal frequencies used for each layer were 20Hz for Ti and 1250 Hz for Ag, leading to an overall thickness of ~30 nm, ~2 nm of which is Ti (see Sections 4.4.3 and 4.4.4 for AFM characterisation study). Lift-off was performed in the same manner as before.

#### 2.3.2 Fabrication of a free standing, nanoporous membrane aligned to plasmonic split-ring structures.

A 500 µm Si wafer, covered on both sides with 200 nm of Si<sub>3</sub>N<sub>4</sub>, was used as the substrate for fabricating the free standing nano-porous Si<sub>3</sub>N<sub>4</sub> membrane device, with individual pores aligned to a plasmonic structure on the top-side of the membrane. The two main steps involved in the creation of such a device were patterning the wafer's topside with rings, aligning the pore pattern, and etching the pores through the Si<sub>3</sub>N<sub>4</sub>, Figure 2.3; and etching, both dry and wet, of the wafer's backside to produce a freestanding membrane, Figure 2.4. Each step was successfully performed in isolation, however, time restrictions meant that the two steps were never combined to produce the final device. The fabrication procedure for each of these steps is described below.

### 2.3.2.1 Patterning split-rings with alignment markers

Fabricating the rings and the pores involves two separate electron beam steps, one for patterning the rings, the other for patterning the pores. The first step was to fabricate the metallic rings. The rings were patterned in precisely the same way as before (Section 2.3.1.4) but with the addition of registration (or “alignment”) markers. These markers are small metal squares ( $20\ \mu\text{m}$  in size for the first alignment stage,  $6\ \mu\text{m}$  in size for the second alignment stage), four of which are positioned round the centre of the intended pattern area, allowing one lithographic layer to be aligned to the next (further information on this procedure can be found in Appendix A.1.1.2). In addition to these two marker sets, a  $200\ \mu\text{m}$  cross was patterned to the bottom left of the larger markers. The cross, which can be found easily by the operator, is related to the position of the two marker sets, allowing the operator of the tool to locate the first of the global markers. A 4” wafer was patterned with 32 sets of these alignment marks, each separated by 15 mm. Figure 2.2 shows a typical marker arrangement used to fabricate these devices.

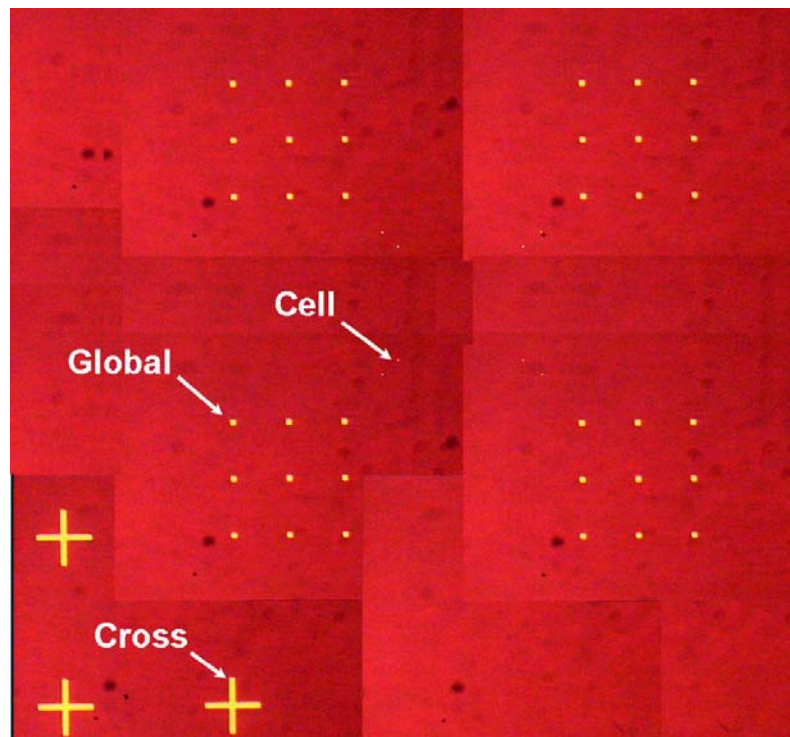


Figure 2.2. Composite image of typical alignment marker arrangement. This image is a composite and not to scale, the features in a scale image would be too small to see. The global markers were  $20\ \mu\text{m}$  large and were spaced  $600\ \mu\text{m}$  from the pattern’s centre. The cell markers (faintly visible in the figure) were  $6\ \mu\text{m}$  large and were spaced  $150\ \mu\text{m}$  from the pattern’s centre. The cross was  $200\ \mu\text{m}$  large and was located  $1650\ \mu\text{m}$  from the pattern’s centre. Since more than one lithographic alignment step may be needed, several groups of markers were patterned. This also ensured that if the alignment process fails due to defective markers, or the markers become damaged during the electron beam search, the procedure can be carried out again without loss of the sample. The distances quoted above relate to the spacing of the most commonly used markers, the other, reserve markers, were rarely utilised.

### 2.3.2.2 Patterning and etching of the nanopores

Figure 2.3 shows a schematic of the fabrication procedure for the production of nanopores through the silicon nitride layer.

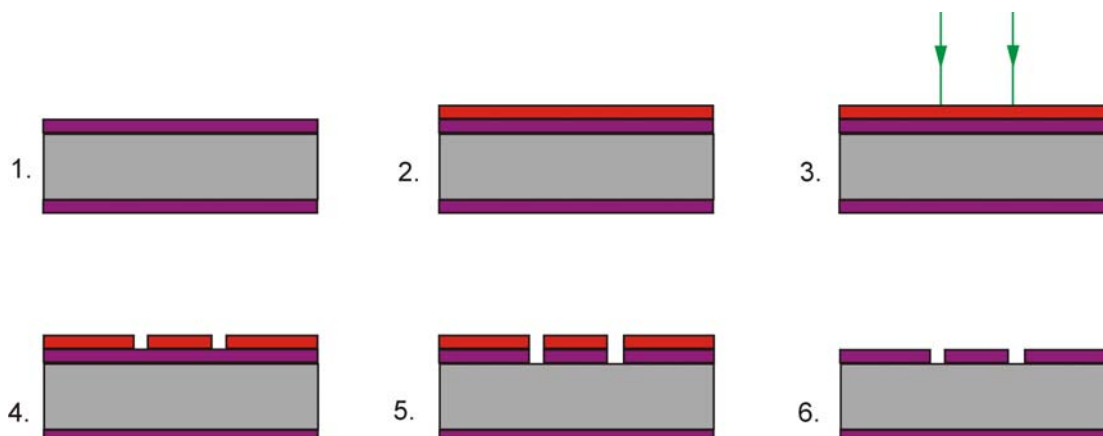


Figure 2.3. Schematic of nanopore fabrication procedure. 1-  $\text{Si}_3\text{N}_4$  / Si /  $\text{Si}_3\text{N}_4$  wafer cleaned by sonication in acetone for 5 mins. 2- 30% UVIII resist spun onto the topside at 3000rpm for 60secs. 3- Patterning of pores by electron beam lithography. 4- Post-bake and development of resist. 5- Dry-etch of the exposed  $\text{Si}_3\text{N}_4$  using  $\text{CHF}_3$  gas. 6- Removal of remaining resist layer by acetone soak.

After the rings had been patterned, developed and metallised, a layer of 30% UVIII resist was spun onto the sample at 3000 rpm for 60 seconds, before being baked on a hotplate at  $120^\circ\text{C}$  for 60 seconds. The resulting resist layer acted as an etch mask for the pores, whilst also protecting the metal rings. UVIII is a sensitive, chemically amplified, positive tone electron beam resist. After performing exposure tests to obtain the optimal dose, 120 nm diameter pores were written using  $315 \mu\text{C} / \text{cm}^{-1}$ .

As UVIII is a chemically amplified resist, the sample must be post-baked for a further 90 seconds at  $120^\circ\text{C}$  before development. The post bake process allows the additional chemicals, released during exposure, to diffuse throughout the surrounding resist, increasing its solubility (it is for this reason that chemically amplified resists are more sensitive). The sample was then developed for 60 seconds in Microposit CD-26, before washing with DI water for 60 seconds.

Dry-etching of the  $\text{Si}_3\text{N}_4$  was performed in an Oxford Instruments Plasmalab System 100 RIE (reactive ion etch). The sample was etched with  $\text{CHF}_3$  gas for 45 minutes, penetrating the entire 200 nm  $\text{Si}_3\text{N}_4$  layer. Soaking the sample in warm acetone for 1 hour removed residual resist material.

### 2.3.2.3 Fabricating nitride membrane

Figure 2.4 shows a schematic of the fabrication procedure for the production of the free standing silicon nitride membrane.

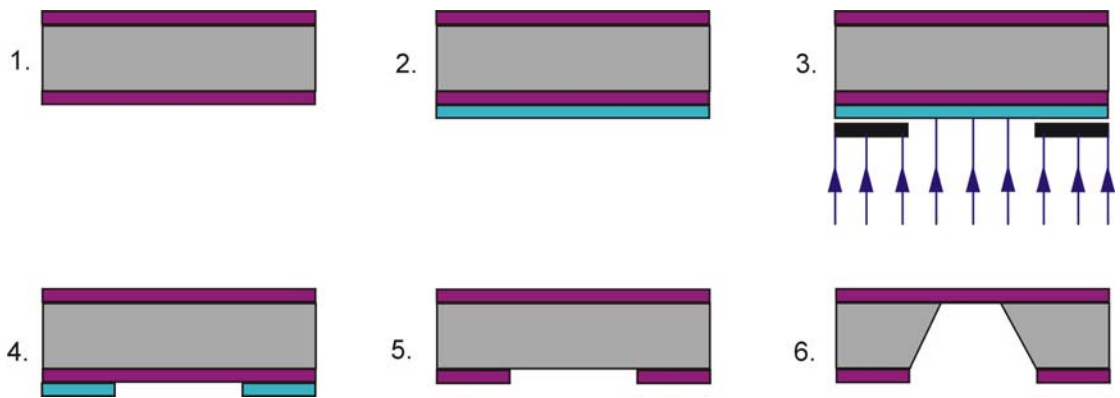


Figure 2.4. Schematic of membrane fabrication. 1-  $\text{Si}_3\text{N}_4$  / Si /  $\text{Si}_3\text{N}_4$  wafer cleaned by sonication in acetone for 5 mins. 2- S1818 resist spun onto the backside of the wafer. 3- Exposure of the resist through the pre-patterned chrome mask. 4- Development of the pattern. 5- Dry-etch of the exposed  $\text{Si}_3\text{N}_4$  using  $\text{CHF}_3$  gas, residual resist is removed with a warm acetone soak. 6- Wet-etching of the exposed Si using KOH at  $80^\circ\text{C}$ .

The same dry-etch process as described above was used to create a  $1692 \times 1692$  micron square in the backside of the wafer. These dimensions were chosen so that when the Si was etched with KOH the membrane dimensions would be  $1000 \mu\text{m} \times 1000 \mu\text{m}$ , the same size as a standard sensor array (anisotropic wet-etching of Si takes place at an angle of  $54.74$  degrees, the Si wafer is  $500 \mu\text{m}$  thick). This square was patterned by optical lithography in Shipley S1818 photo-resist using a  $4''$  chrome mask patterned by electron beam, its features designed to correspond to those on the topside.

Since the pattern on the topside of the wafer must align with the membrane etched from the backside, identical alignment marks were necessary on both sides of the wafer. These markers consist of a series of circles, of varying diameter, in a cross formation, Figure 2.5. The topside and backside patterns, including the backside alignment markers, were incorporated on the same CAD design, albeit on different layers, ensuring all features were correctly positioned, both rotationally and translationally, relative to one another. The backside alignment markers were patterned on the topside during the initial electron beam exposure, and were also included on the optical lithography mask used to pattern the backside of the wafer.

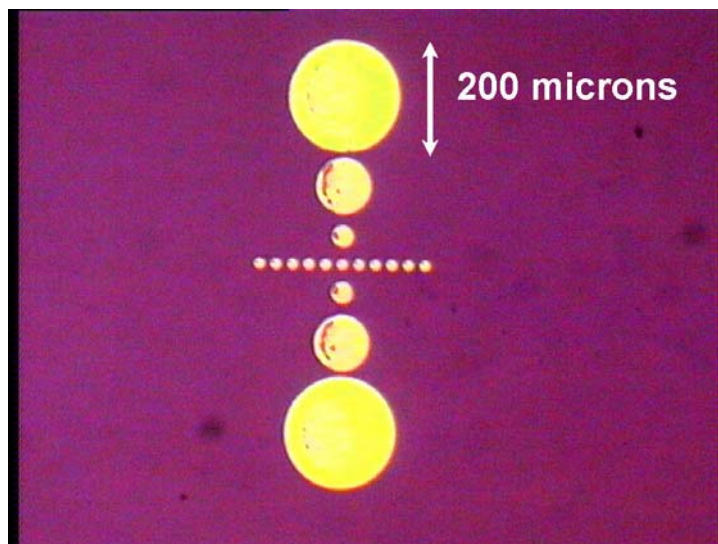


Figure 2.5. Markers used for backside alignment. Picture of circular Au markers fabricated on the wafer's topside. An identical pattern is included on the chrome mask used to pattern the backside, allowing the two patterns to align correctly.

S1818 resist was spun onto the wafer at 4000 rpm for 30 seconds, producing a resist layer of  $\sim 1.8 \mu\text{m}$ . The resist was exposed to UV radiation, through the chrome mask, for 4.5 seconds using a SUSS Microtec MA6 mask aligner. Cameras on both sides of the wafer enabled positional and rotational alignment of the top and backside markers.

Development of the S1818 resist took place for 60 seconds in a 1:1 mixture of water and Microposit developer at room temperature. The exposed  $\text{Si}_3\text{N}_4$  squares were then dry-etched away in identical fashion to that described in Section 2.3.2.2.

Potassium hydroxide (KOH) was used to etch away the Si layer exposed by the dry-etch process, producing the free standing  $\text{Si}_3\text{N}_4$  membrane. The samples were placed in a bath of KOH for approximately 12-16 hours (this etch was monitored every 2 hours and samples removed when etch is completed, so exact times will vary) at  $80^\circ\text{C}$ . The  $\text{Si}_3\text{N}_4$  is not effected by the KOH, the patterned backside acts to guide the etch process, while the topside layer acts as a natural etch stop.

### 2.3.3 Physical and optical characterisation

#### 2.3.3.1 Absorption spectroscopy

Characterisation of the nanostructured arrays was carried out using a Shimadzu UV3101PC absorption spectrometer and a linear thin film polariser (see Appendix A.1.3 for instrument set-up). Samples were mounted on a specially made holder with a 1 mm diameter pinhole through which light from the grating passed. Arrays were fabricated to be  $\sim 1 \text{ mm}^2$  and aligned to this pinhole. A piece of plain Pyrex glass was fixed to an identical holder and placed in the reference arm. The system was operated in the wavelength range of 400 - 2500 nm.

### 2.3.3.2 Scanning electron microscopy (SEM)

All scanning electron micrographs were taken using a Hitachi S-4700 SEM operating at 10kV. More information on this tool can be found in Appendix A.1.4. Before loading into the SEM the Pyrex glass samples were coated with Au/Pd using an in-house sputter coater operating at 15 mA for 2 minutes.

### 2.3.3.3 Atomic force microscopy (AFM)

Topographical characterisation of the fabricated structures was carried out using a JPK Nanowizard AFM, Appendix A.1.5. All AFM measurements referred to in this research were performed using Nanosensors SSS-NCH-10 Si cantilevers in tapping mode. These cantilevers had a tip radius of ~ 2 nm

### 2.3.4 Finite difference time domain (FDTD) simulations

FDTD simulations were performed using TEMPEST software. The x-y dimensions of the simulation space were chosen to reflect the periodicity of the fabricated structures (420 nm for the 135nm rings, 260 nm for the 75nm rings), whilst the z dimension remained fixed at 1  $\mu$ m for all simulations. The metal areas within the boundaries were specified in terms of their complex refractive index, values for which were taken from Palik<sup>50</sup>. In all cases, a resolution of one node per nanometre was used. Simulations were performed in increments of 100 nm over a wavelength range of 400 nm - 2500 nm, corresponding to the experimental range of the Shimadzu UV3101PC absorption spectrometer. Once the plasmon resonances had been identified a second set of simulations were performed to isolate the peaks. All of the simulations were run remotely on computer clusters located in the university's computer services department. More information on this simulation tool can be found in Appendix A.1.6.

### 2.3.5 Chemical and biological modification of sensor surface

#### 2.3.5.1 Modifying the Ag sensor surface with 2-mercaptopyridine

Samples were placed in 10 mM solutions of 2-mercaptopyridine (in 20 ml of ethanol) for 1 hour, before washing with DI water for 2 minutes to remove any non-specifically bound molecules. The sulphur in the molecule's thiol group bonds strongly to the Ag nanostructures, forming a SAM over time, see Appendix A.1.11 for more information.

#### 2.3.5.2 Modifying the Ag sensor surface with cysteamine/Cy5 NHS

Samples were placed in a 10 mM solution of cysteamine (in 20 ml of ethanol) for 1 hour, before washing with DI water for 2 minutes to remove any non-specifically bound molecules. The resulting monolayer of amine groups can be used to immobilise the Cy5 dye. The cysteamine modified samples were submerged in a 10 mM solution (in 20ml of PBS) of Cy5 NHS for 20 minutes, then washed for 2 minutes in DI water. The NHS ester attached to the Cy5 dye reacts with the amine group of the SAM, linking the dye to the sensor surface. More information on these molecules and their reactions can be found in Appendix A.1.13.

#### 2.3.5.3 Modifying the Ag sensor surface with thiolated oligonucleotides

A 0.02 M solution of dithiothreitol (DTT), in 0.1M Na<sub>2</sub>CO<sub>3</sub>, at pH 8.3 was used to reduce the disulphide group on the thiolated oligonucleotides (the acid dissociation constant of thiol groups is typically around pH 8.3). A 1:1 mixture of DTT:DNA was combined in an Eppendorf tube and placed in a vortex mixer for one hour. The subsequent thiol-disulphide exchanges effectively reduce the disulphide bonds on the DNA.<sup>101</sup> The unwanted DTT was removed in two stages: it was first extracted three times using ethyl acetate, before finally being passed through an Amersham Biotech NAP-10 column. The resulting solution contained 96% DNA (according to the NAP-10 column information sheet). The purified DNA was separated into small volumes (~100 µl), immediately frozen in liquid nitrogen, and transferred to a Thermo Scientific Powerdry LL3000 freeze dryer, thus preserving the reduction process. The freeze-dried samples can then be stored indefinitely and re-hydrated when required. As long as the re-hydrated sample was used immediately there was no need to repeat the reduction protocol. Modification of the Ag was achieved by spotting 20 µl of this solution onto the sensor surface (sealing it in a humidity rich container to reduce evaporation) and leaving to attach for 1 hour. More information on these molecules and their reactions can be found in Appendix A.1.14 - A.1.16.

#### 2.3.5.4 Hybridisation

After the thiolated sequence had been attached to the surface, it was hybridised with its complementary strand. This was performed by spotting 20 µl of target sequence onto the sensor immediately after attachment of the probe sequence. All hybridisation experiments were performed using target concentrations of 20 µM, and in all cases sequence B was used as the probe strand. More information on the hybridisation process can be found in Appendix A.1.14.

#### 2.3.6 Surface characterisation via X-ray photoelectron spectroscopy (XPS)

A Scienta ESCA300 XPS tool located in Daresbury laboratories was used to confirm the surface modification protocols. In all cases, samples were loaded into the ultra high vacuum chamber and adjusted to a take-off angle of 10°. Scan times and energies were chosen to correspond accordingly with the type and quantity of the element present on the sample. More information on the XPS technique can be found in Appendix A.1.7.

#### 2.3.7 Fluorescence microscopy

The Zeiss LSM 510 META confocal fluorescence microscope (Appendix A.1.8) was used as a method of confirming sample modification with a fluorescent probe, such as Cy5. Although designed for confocal microscopy, the system was used with the confocal hole set to infinity (i.e. non confocal). The system was equipped with a range of laser sources and excitation filters. Working primarily with Cy5 meant that the 633 nm HeNe laser and a low-pass 650 nm filter were used as excitation source and fluorescence filter set respectively. Scan times and sensitivities were chosen to correspond to the type and amount of material present on the sample.

### 2.3.8 Raman spectroscopy and surface enhanced Raman spectroscopy (SERS)

#### 2.3.8.1 Raman spectroscopy at 633 nm and 785 nm

A Horiba Jobin Yvon LabRam INV spectrometer attached to an Olympus IX70 microscope was used to perform Raman measurements at 633 and 785 nm. For all measurements, a 100x magnification, 0.75 NA objective lens was used in conjunction with a confocal hole diameter of 1000 $\mu$ m and a slit width of 150  $\mu$ m. The D1 neutral density filter (optical density of 1, corresponding to approximately 10% transmittance) was used in conjunction with the 633 nm laser, resulting in a beam power, measured at the objective, of 0.5mW. No filter was used in conjunction with the 785 nm laser, resulting in a beam power of 9.5 mW at the objective lens.

Samples were placed, face down, on the motorised stage (the sample edges bridging two microscope slides so that the patterned area was suspended above the objective) and aligned relative to the laser polarisation direction (confirmed for each laser using a linear thin film polariser). With the sample illuminated, the pattern was brought into focus using the microscope eyepiece. Once coarsely focused, the lamp was turned off and the laser turned on. Further, fine focusing was then performed using the intensity of the Raman scattering (from a short acquisition time of 1 - 2 seconds) as a guide. At this point a longer acquisition time was selected (e.g. 10 seconds) in order to obtain a well-defined, detailed Raman spectra. More information on this system can be found in Appendix A.1.9.

#### 2.3.8.2 Raman spectroscopy at 532 nm

In order to perform Raman spectroscopy at 532 nm, an Ocean Optics QE65000 spectrometer was used in conjunction with a Melles Griot 532 nm, 10 mW diode pumped solid state laser and a Zeiss Axiovert 40 CFL microscope. The laser was directed to the sample using the entrance port in the rear of the microscope, with the scattered light being collected at the front/camera port by a fibre optic cable and directed into the spectrometer. A 100x 0.75 NA objective lens and a D1 neutral density filter was used throughout (the laser power was measured to be 1mW at objective). More information on this system can be found in Appendix A.1.10.

## 2.4 Results and Discussion - Problems and solutions associated with nano split-ring fabrication

### 2.4.1 Effect that resist thickness has on high resolution patterns

As discussed later in Section 2.3.1.7 and Appendix A.1.2.2, manually operated evaporators can make metal deposition difficult to control, and it was often the case that, when using this equipment, slightly too much metal was evaporated onto the sample, thus preventing lift-off. In order to create a larger margin for error and increase device yield, the use of thicker resist layers was explored. However, the trade-off for increasing the resist thickness is a lower pattern resolution due to increased electron scatter. Figure 2.6 illustrates this point. On the left of the Figure is a 75 nm radius Au ring fabricated using the thin resist (~ 90 nm bi-layer), whereas the ring on the right has been fabricated using a thicker resist (~ 240 nm bi-layer). Although the design of the pattern was identical, there is a clear difference between final

structures, highlighting the need to use a resist as thin as possible when fabricating such high resolution patterns.

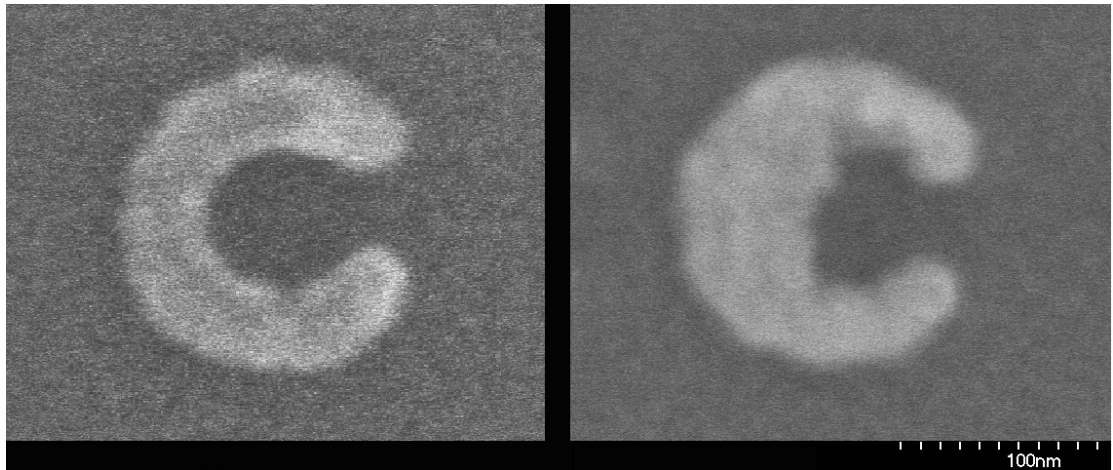


Figure 2.6. SEM comparison of identical patterns fabricated using thin (left) and thick (right) resist. Increased electron scatter caused by the extra resist material results in a less uniform structure with inconsistent feature sizes. As a result, the thinner of the resists was used throughout the research.

#### 2.4.2 Consequences of over and under exposure through incorrect choice of electron beam dose

The dose used to write each shape must be given careful consideration. If the dose is too high, the ring's features will "bulge" and lose definition. If the dose is too low the resist may not be cleared during development, resulting in incomplete, segmented features. Figure 2.7 shows the consequence of an excessively high and low dose respectively.

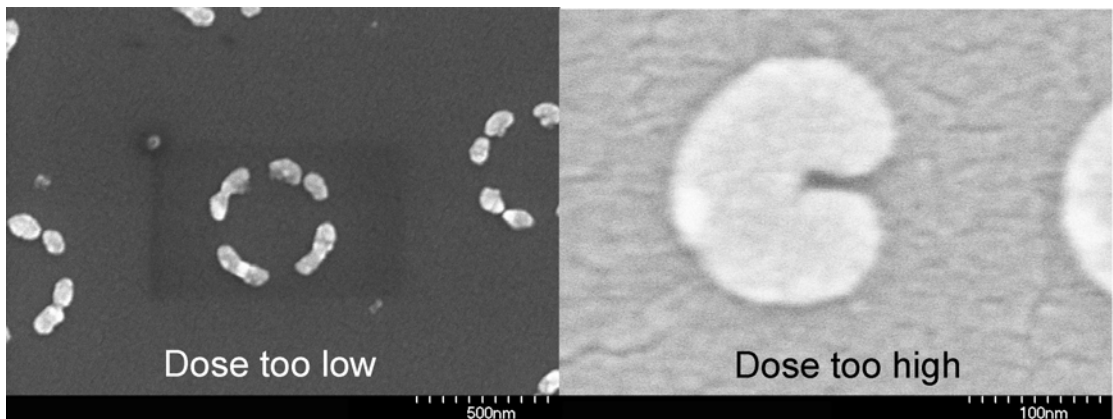


Figure 2.7. Influence of dose on structural geometry. SEMs displaying an under-exposed (left) and over-exposed (right) split-ring structure.

#### 2.4.3 Consequences of inconsistent Ti - Ag adhesion

Figure 2.8 shows the consequence of poor Ag adhesion to the initially evaporated Ti layer. Although Ti acts as an adhesion promoter, several factors, such as a low vacuum pressure

or unstable evaporation rate, can significantly reduce its effectiveness. The resulting geometric inhomogeneity makes plasmon tuning impossible and results in weak, broad resonance peaks.

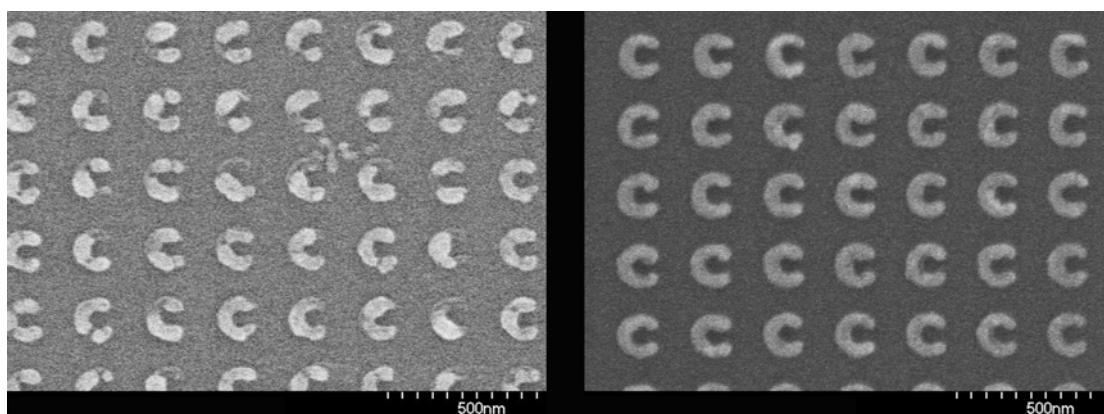


Figure 2.8. SEMs of poor (left) and good (right) Ag adhesion to Ti. The panel on the left of this Figure shows complete Ti rings, faintly visible below the Ag layer, with irregular Ag coverage. Inconsistent metal layer adhesion of this nature made a significant impact on device yield. On the right is an example of good adhesion; each ring is fully defined in Ag.

## 2.5 Conclusion

Methods for the successful fabrication, tuning and characterisation of multi-mode nano split-ring resonators have been demonstrated. Combination of FDTD simulation, electron beam lithography and absorption spectroscopy allow resonance wavelengths and the localised plasmonic activity of the ring arrays to be fully characterised, whilst minimising the need for costly iterative fabrication.

Techniques allowing molecular modification of the sensor surface have been described, along with the experimental set-up and operation of tools that allowed these modifications to be characterised and detected (more information can be found in the Appendix).

## Chapter 3 - Characterisation of Au split-ring resonators

### Abstract

Electron beam lithography was used to fabricate arrays of Au nano-split-ring resonators of various dimensions. The plasmonic activity of these structures was characterised using a combination of experimental transmission spectroscopy and FDTD software, allowing identification and assignment of the multiple, polarisation dependent resonances present in these structures. The ability to precisely engineer the optical properties of the rings is shown by altering the height, radius and arc-length of the ring geometry. In doing so it is demonstrated that the structure's multiple resonances can be tuned over several microns, and that those of higher order can exist within the visible spectrum, opening the way for these devices to be used in near-field biological sensing.

### 3.1 Introduction

Paramount to creating a versatile biosensing platform based on SER(R)S is the ability to tune the frequency and nature of the particle's plasmonic resonances. Metallic ring structures have been shown to produce highly tuneable resonances in the near infrared portion of the spectrum<sup>39</sup>, whilst at the same time generating a large, uniform field enhancement inside the ring cavity, thus having the potential to be exploited in the future for biosensing. It has also been shown, in both theoretical and experimental studies, that the introduction of a split into the ring geometry increases the structure's resonance frequency as well as the number of its supportable resonance modes.<sup>72, 75</sup> In this chapter the latest generation electron beam lithography tools were used to fabricate novel crescent shaped split-ring resonators. These unique structures were investigated with a view to understanding and harnessing their plasmonic properties for potential use as visible wavelength molecular sensors.

The quality and frequency of the resonances depends strongly on the size of the particle, its geometric and morphological properties and the uniformity of its fabrication over an array. Previously, split-ring resonator structures have not been used as SERS substrates, mainly due to problems associated with controllable fabrication on the nanometre scale required to produce structures small enough and uniform enough to generate tuneable optical resonances in the visible portion of the spectrum. As was discussed in detail in Sections 1.3.5 and 1.3.6, split-ring nanostructures fabricated by electron beam lithography have hitherto been square, and have been primarily used for the generation of metamaterials.<sup>72, 75</sup> Moving away from these square structures toward circular geometries was motivated principally by the problems associated with fabricating nano-scale right angles with electron beam lithography. Choosing a crescent shape eliminates this problem, allowing smaller structures to be fabricated with far greater array uniformity, which in turn leads to higher quality plasmonic resonance peaks. Unlike other crescent structures presented in the literature and used for SERS (those fabricated using nanosphere lithography and angled metal deposition),<sup>102</sup> these split-ring structures exhibit a uniform width along their entire arc length, are identical throughout the patterned array, and

have controllable, reproducible periodicity; all factors which contribute to the fine tuning and quality of their plasmon resonances.

There are a number of reasons why Au was the metal of choice for fabricating these initial structures. Foremost among these were its proven track record in creating nanoplasmonic devices, its stability and reduced reactivity in ionic and electrochemical environments, and its availability in the electron-beam evaporators in our fabrication facility. Although the use of Ag would be advantageous in generating high frequency resonance modes for visible wavelength SERS (due to Ag's higher bulk plasma frequency), the high level of plasmonic degradation experienced by Ag nanoparticles meant that the use of Au was seen as being the more practical for initial studies.

### 3.2 Materials

The substrates were cleaved from 500  $\mu\text{m}$  thick, 4 inch diameter, Pyrex (borosilicate) wafers purchased from University Wafer, USA. Resist material, Elvacite Polymethyl Methacrylate (PMMA) was obtained from Lucite International Inc. The Ti and Au sources used in the electron beam evaporator were obtained from Pi-Kem, UK.

### 3.3 Methods

A complete description of the fabrication and optical characterisation procedures used in this chapter can be found in Sections 2.3.

#### 3.3.1 Fabrication of 135 nm radius Au rings with varying arc-lengths

Four  $1\text{mm}^2$  arrays were fabricated (which shall be referred to as arrays A-D), each with a different arc length, but with the same 135 nm radius. The initial CAD designs had a 120 nm radius and wall width of 18 nm, dimensions which, once fabricated, produce a 135 nm radius ring with a wall width of  $\sim 50$  nm. These were chosen as a starting point as it was known that these dimensions were well within the capabilities of the electron beam tool and the resist material. The arc-lengths, as specified in the design file, were approximately 377 nm, 459 nm, 593 nm and 718 nm for arrays A, B, C and D respectively, see Figure 3.1. The plasmonic activity of each array was measured using a Shimadzu UV3101PC absorption spectrometer, as described in Sections 2.3.3.1. FDTD simulations were carried out on each of the ring geometries using TEMPST software for the experimental wavelength range of 400 nm - 2500 nm (see Section 2.3.4). Results and discussion relating to these arrays can be found in Section 3.4.1.

#### 3.3.2 Fabrication of Au split-rings with varying radius

Four  $1\text{mm}^2$  arrays of rings, each with a different radius (which shall be referred to as arrays E-H) were fabricated according to the procedure outlined in Section 2.3. Arrays E, F, G and H have a radius of 80 nm, 100 nm, 145 nm and 180 nm respectively. All other dimensions were identical from array to array, each displaying a wall width of  $\sim 50$  nm, a gap size of  $\sim 50$  nm a height of  $\sim 25$  nm and an interparticle spacing of 120 nm. Electron beam doses of  $1700\ \mu\text{C}/\text{cm}^{-1}$  were used for arrays E-G, a dose of  $2000\ \mu\text{C}/\text{cm}^{-1}$  was required for array H. The plasmonic response of each array was measured using a Shimadzu UV3101PC absorption spectrometer, as

described in Section 2.3.3.1. Results and discussion relating to these arrays can be found in Section 3.4.2.

### 3.3.3 Fabrication of 75 nm radius Au rings with varying arc-lengths

Three arrays of 75 nm radius Au split-rings were fabricated, each with a different arc-length (see section 2.3). The arc-lengths, as specified in the design file, were approximately 189 nm, 255 nm, and 316 nm for arrays I, J, and K respectively. A dose of  $2000 \mu\text{C}/\text{cm}^{-1}$  was used for each array. Results and discussion relating to these arrays can be found in Section 3.4.3.

### 3.3.4 Fabrication of split-rings with varying height/thickness of Au

Three arrays of identical structures were fabricated by electron beam lithography, onto which varying amounts of Au was evaporated. Each array contained rings with a radius of 75 nm, an arc length of  $\sim 430$  nm, a wall width of 50 nm and a gap size of  $\sim 30$  nm. The thickness of the evaporated Au layer was 10 nm, 15 nm and 20 nm respectively, with a 5 nm Ti layer used in each case to aid adhesion to the Pyrex substrate. Results and discussion relating to these arrays can be found in Section 3.4.4.

### 3.3.5 Fabrication of Au split-rings with varying periodicity

Three arrays of identical nanostructures were fabricated, each with a different interparticle periodicity. Each array contained rings with a radius of 75 nm, an arc length of  $\sim 430$  nm, a wall width of 50 nm and a gap size of  $\sim 30$  nm. The periodicity of the arrays was 260 nm, 230 nm and 200 nm respectively. These periods related to interparticle edge to edge spacing of 110 nm, 80 nm and 50 nm. Results and discussion relating to these arrays can be found in Section 3.4.5.

## 3.4 Results and discussion

### 3.4.1 Tuning and characterisation of 135 nm radius rings

The rings, making up the elements of the arrays A-D (Section 3.3.1), had a radius of 135 nm, a wall width of 50 nm and a period of 420 nm. The periodicity of the arrays was chosen to be small enough to provide good signal to noise ratios in spectroscopic measurements, yet large enough so to negate any interparticle near-field coupling.<sup>73, 75</sup> The final fabricated dimensions of the rings were larger than that of the CAD design due to electron scattering (Sections 2.4.1 and A.1.1). The measured arc lengths of the rings in each array were 450 nm, 510 nm, 670 nm and 765 nm for arrays A, B, C and D respectively. As shown in Figure 3.1, high resolution SEMs of the rings in each array show there was a high level of structural uniformity achieved using this lithographic technique. Each of the rings critical dimensions (its radius, wall width and gap-size) exhibited a variation of no more than  $\pm 5$  nm across the 1 mm x 1 mm device.

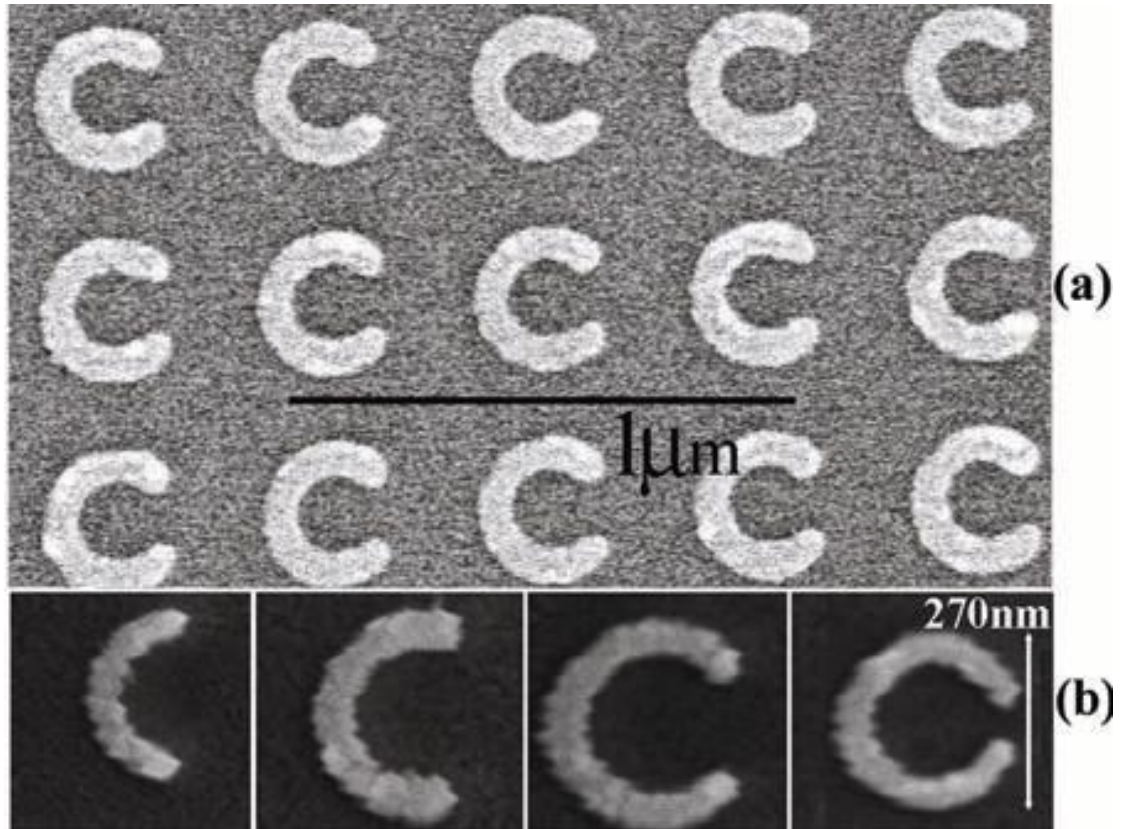


Figure 3.1. High resolution scanning electron micrographs of split ring arrays A-D. (a) shows an SEM of array C, illustrating the uniformity of fabrication; (b) shows high resolution SEMs of split ring crescents found in arrays A-D. The roughness of the edges seen in (b) is an artefact due to charging from the SEM, not the fabrication process.

Non-symmetrical nano-particles tend to display polarisation dependent plasmon resonances.<sup>38, 70, 75</sup> Figure 3.2 shows plots of transmission vs. wavelength for each array when the light incident on the structures is polarised both perpendicular and parallel to the split in the ring geometry. The optical restrictions of the Pyrex substrates along with the experimental limits of the spectrometer confined the spectral range of these measurements to 400 nm - 2500 nm. Also included in this figure is plasmonic activity of a ring structure that does not contain a split for comparison.

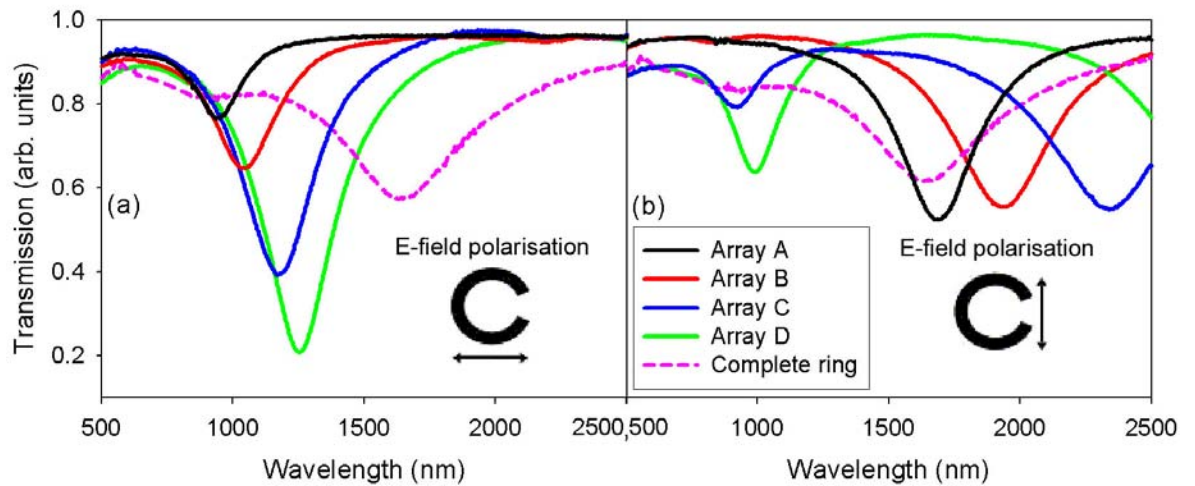


Figure 3.2. Resonant response of 135 nm radius split rings. Experimental transmission spectra of 135 nm radius split-rings with varying gaps (arrays A-D) as well as a complete 135 nm radius ring. Section (a) of the figure shows the resonances when the electric field is polarised perpendicular to the split, whereas section (b) shows the resonances when the electric field is polarised parallel to the split. The terminology “parallel” and “perpendicular” polarisation used from this point onwards in the Thesis refers to the geometric orientation specified in this figure.

As can be seen in Figure 3.2 (a), when the light is polarised perpendicular to the gap a single resonance is seen for each structure, its wavelength increasing with radius. Increasing the ring’s arc length from 450 nm to 765 nm (thereby decreasing the split size) red-shifts the peak resonance wavelength by 310 nm, from 944 nm to 1254 nm. The increase in arc length also increases the strength of the resonances. Both are expected consequences of increasing the quantity of Au present in each element.<sup>47, 48</sup>

However, when the light is polarised parallel to the split (Figure 3.2(b)) the relationship between the arc length and the resonance wavelength is not immediately apparent. Furthermore, more than one resonance can be seen for some arrays. As with the perpendicular polarisation (Figure 3.2 (a)), each resonance shows a red-shift in peak wavelength as the ring’s arc length is increased: Array A has a peak at 1688 nm, array B at 1936 nm, array C at 2338 nm (the corresponding peak for array D could not be measured experimentally as it lies out-with the 400-2500 nm experimental wavelength range). In contrast to the perpendicular polarisation, as discussed below, a second resonance appears as the arc length increases and the split becomes smaller (the peak appears in array B at 816 nm, array C at 918 nm and array D at 990 nm, becoming stronger and continuing to red-shift as the ring’s arc length is increased).

Note, when the gap in the ring geometry is removed, making an axially symmetric structure, as is the case for the complete ring, the structure no longer exhibits polarisation dependent resonances. Instead, a single, broad resonance, which can be excited at any incident polarisation angle, appears at 1630 nm.

Numerical simulations can be used to gain further insight into the behaviour of these resonances. Figure 3.3 shows a plot of transmission against wavelength for these simulations, along with the initial experimental data for comparison.

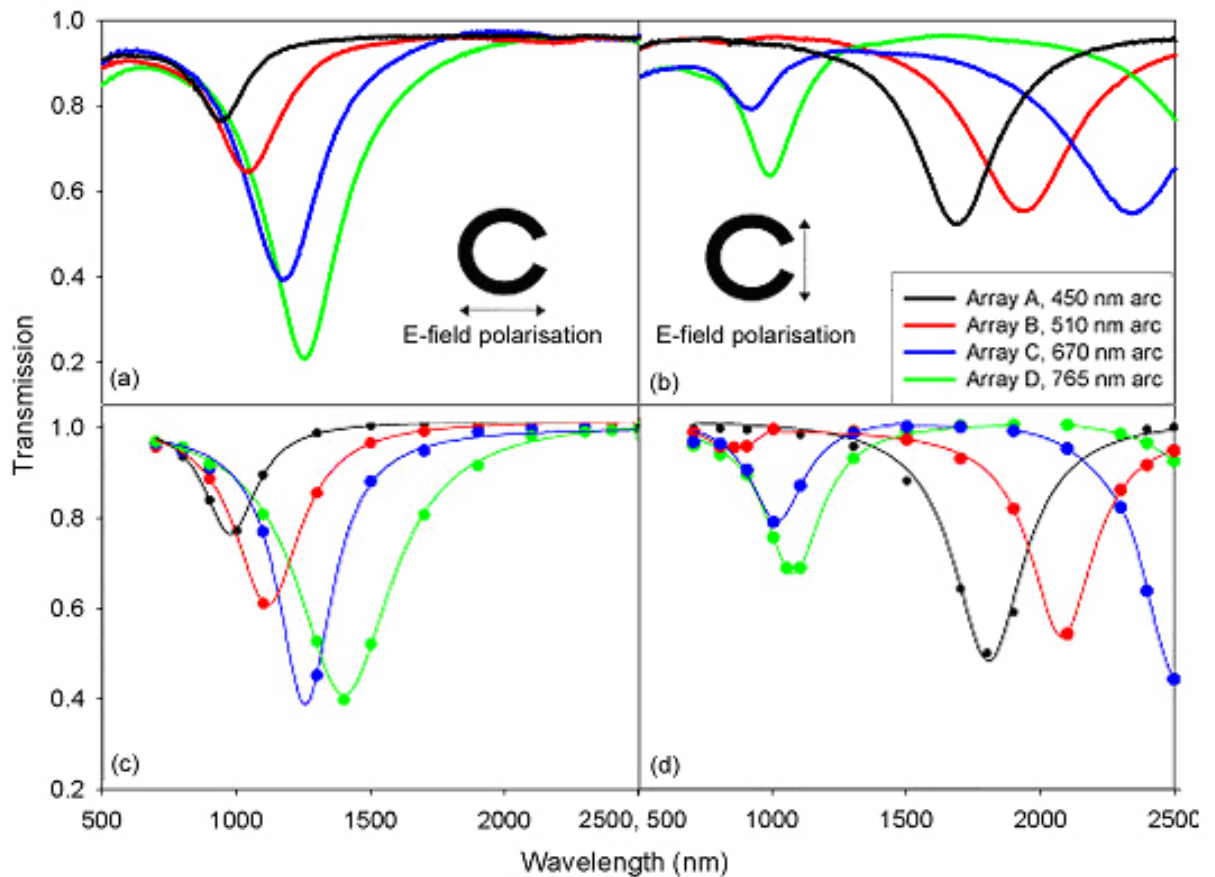


Figure 3.3. Comparing experimental (a) and (b) with simulated (c) and (d) data for 135nm radius split-rings. The simulated data points were fitted to Lorentzian curves using Sigma-plot software for a better visual representation of their peaks. The simulated data agrees very well with the experimental measurements. This correlation allows the plasmonic resonances of new structural designs to be tested first using FDTD, saving the need for expensive and time-consuming iterative electron beam fabrication.

The numerical data agrees extremely well with the experimental measurements, mimicking the trends of resonance red-shift and increasing strength with changing arc length. The peak resonance wavelengths do not match exactly; this is likely due to the morphologies of the fabricated rings and the numerical rings not being identical. Furthermore, values of complex dielectric constant for a particular metal can vary slightly due to deposition technique, and, more obviously, purity. Therefore the values quoted in Palik<sup>50</sup> that were used for simulation may not exactly reflect those of the fabricated structures.

FDTD can also provide an insight into the specific areas of EM enhancement. Such models allow us to visualise and identify the structural regions of excitation associated with the peaks observed in Figure 3.3. Figure 3.4 depicts the normalised electric field in the z-plane, at the surface of array A-D's ring structures, at each resonance frequency.

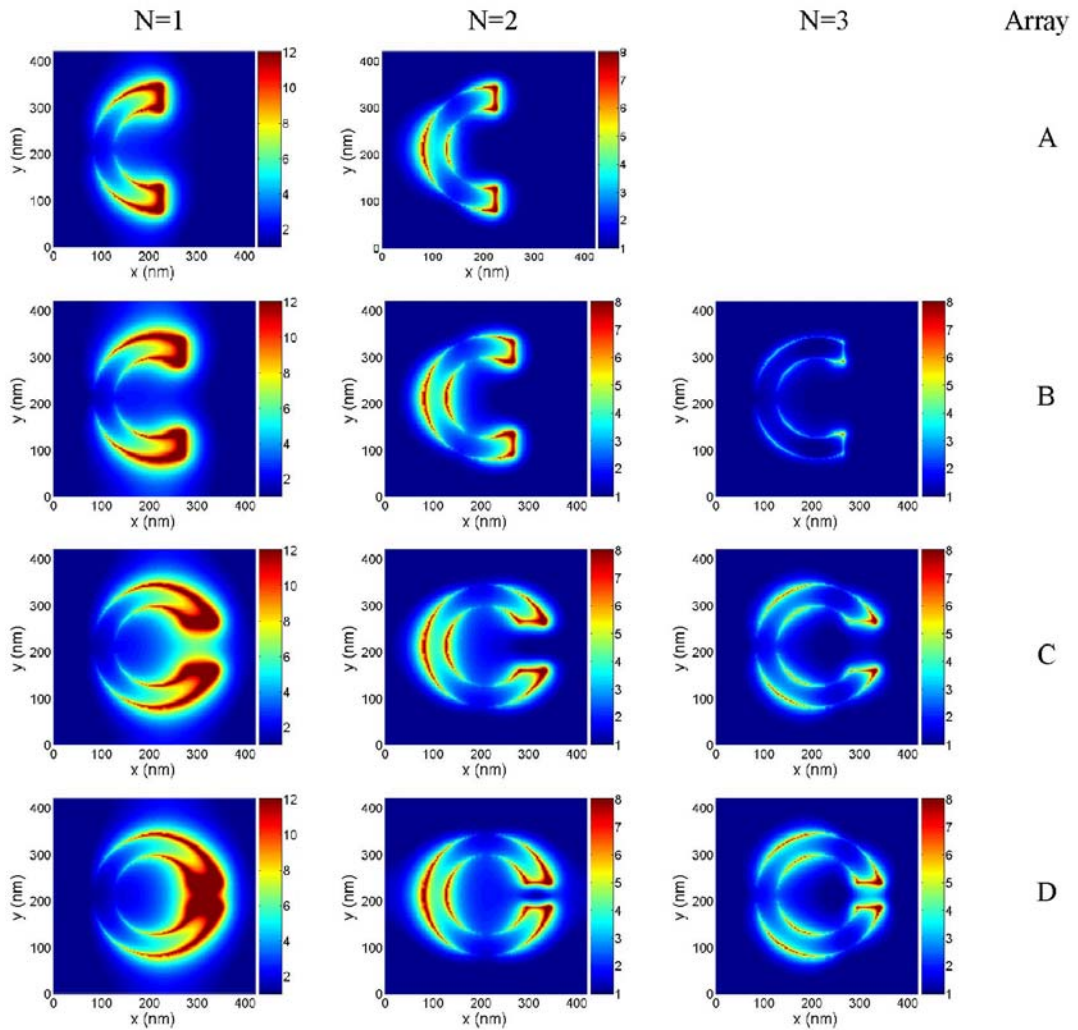


Figure 3.4. Localised electric field enhancement at resonance for 135 nm radius rings A-D. FDTD simulations of normalised electric field in the z-plane, at the surface of array A-D's ring structure, at each resonance frequency. The arc length of Array A is insufficient to support a third resonance. For N=1 & 3 the electric field of the exciting light was polarised along the y-axis, whereas for N=2 the polarisation was along the x-axis.

From Figure 3.4 it is possible to assign the mode order of the resonance peaks seen in Figures 3.2 and 3.3. The mode order is determined by the number of EM nodes supported around the structure (a node referring to a minima in EM activity), with odd modes generated when the electric field is polarised parallel to the split (in the y-axis), and even modes generated when the electric field is polarised perpendicular to the split (in the x-axis).<sup>72</sup> Thus the low frequency resonances seen in Figure 3.3 (b), when the light is polarised parallel to the split, were identified as the first resonance modes (or N=1), whilst the higher frequency resonances that appear in the arrays B, C and D, but not A, (Figure 3.3 (b)) were identified as the third resonance modes (or N=3). The resonances seen in Figure 3.3 (a), when the light is polarised perpendicular to the split, were identified as the second resonance modes (or N=2). Intuitively, the resonances with a higher mode order occur at higher resonance frequencies,

since a higher oscillatory frequency of light is required to support the plasmon's increased node number.

As illustrated in Figure 3.3, the direction of the electric field with respect to the structure has a direct effect on the field distribution around the ring. In fact, the dispersion of the EM field nodes in circular split-rings is analogous to that of square shaped split-rings used within the metamaterial community. It has long been popular to describe these resonances in electrical engineering terms, making a direct comparison between the split-rings and an LC resonator circuit.<sup>75, 83</sup> However, more recent theoretical and experimental studies have shown that it is not necessary to make such an analogy, since the resonances are plasmon oscillations of the entire ring structure,<sup>72, 84</sup> and are closer in nature to the response observed in nano-wire structures.<sup>103</sup> The gap-capacitive model is sufficient for understanding the fundamental modes of the structure,<sup>75, 83</sup> but are unable to describe the higher order resonances seen in this, and other, research.<sup>72, 73, 84</sup> In the case of the research presented in this thesis it is the higher order modes of the split-ring resonator that are of interest. The simulations presented here are in agreement with those published elsewhere in the literature for similarly shaped structures, displaying comparable field distributions and strengths for each plasmon mode.<sup>72, 73</sup>

Since the ring has only one plane of symmetry (in the x-axis, perpendicular to the split), the number of nodes the ring can support is directly related to the polarisation of the incident light. If the light is polarised along the axis of symmetry, the free electrons in the "arms" of the ring will be excited in-phase. Since the structure's plasmon can be thought of as a standing wave, and the plasmon field generated in the arms must remain in-phase, in this orientation there can only be an even number of nodes supported for any resonance mode order. If, on the other hand, the external electric field is polarised in the y-axis, parallel to the split (perpendicular to the axis of symmetry), the plasmon field in the each arm of the ring will be out of phase by  $\pi$ , therefore only an odd number of nodes can be supported.<sup>72</sup> This phenomenon can be seen in Figure 3.4. The location of these areas of enhancement become particularly important when considering the use of such structures as bio-molecular sensors, since only signals from molecules situated within these areas will undergo significant enhancement.

The colour scales used for the electric field values shown in Figure 3.4 were chosen to best represent visually the enhancement seen around the ring at resonance, but do not indicate relative field levels achieved between different modes, nor do they show the maximum levels of enhancement for individual modes. The largest enhancements occur in array D and are indicated by the simulation to be approximately 30, 9 and 9 for the first, second and third resonances respectively. In the context of biomolecular sensing via SERS, these field strengths would correspond to Raman enhancement factors of  $8.1 \times 10^5$ ,  $6.5 \times 10^3$  and  $6.5 \times 10^3$ , given that the Raman enhancement is equal to the fourth power of the field strength.<sup>87</sup> TEMPEST software is unable to accurately simulate the rounded edges seen at the tips of the ring "arms" on the fabricated structures, representing these are sharp right-angles (see Figure 3.4). As such, the field enhancements displayed here may be disproportionate when compared to the final fabricated structure, therefore the fields seen in the outermost nodes which make up these areas were discounted. It should be noted that the areas of the ring experiencing a large field enhancement cover a small proportion of the ring's surface itself, and that while the enhancement seen in the

first resonance mode may be the largest, the more even distribution (and hence greater surface coverage) of the enhanced electric field in the higher order modes, along with the higher frequency of their resonances, may make them more effective for SERS.

In the case of each array, the largest localised enhancement is experienced by the first order resonance mode. The majority of the induced field is concentrated at the end of the ring's "arms", and in the case of arrays C and D, where the gap is sufficiently small, the enhanced field fills the entire region of the split. In fact, the ring structure seen in array D displays a field enhancement of  $\sim 15\times$  in the centre of the split, 15 nm away from either arm. This is due to surface charge distribution leading to coupling of the fields in each tip, which in turn leads to an increased enhancement in the split, similar in fashion to the effect seen in coupled particle pairs. Returning briefly to the LC circuit analogy, this effect has also been explained as an increase in capacitance between the tips (or plates).<sup>75</sup> Such large enhancements covering a relatively large area could open up these structures to interesting sensor applications if it were possible to introduce, or trap, a molecule in the centre of the split. Unfortunately, the 135 nm radius Au split-rings shown above (and the smaller, 75 nm radius, rings described later in this chapter) exhibit first order resonances out with the visible spectrum, making them unsuitable for visible wavelength SERS.

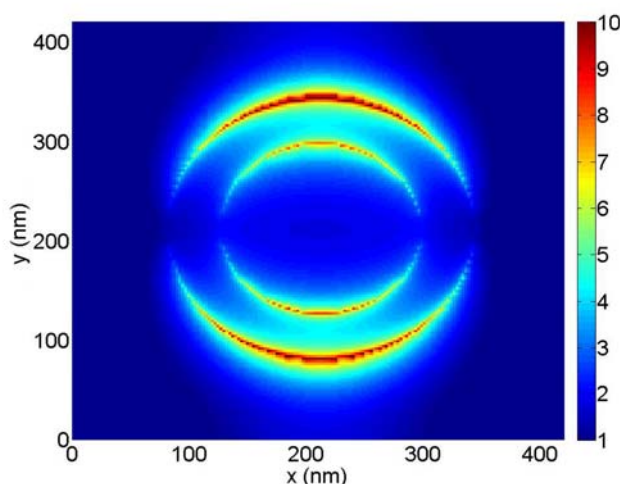


Figure 3.5. Localised electric field enhancement at resonance for a complete 135 nm radius ring. FDTD simulation of the normalised electric field in the z-plane, at the surface of the ring structure. The electric field component of the exciting wave was polarised in the y-direction. An identical distribution was observed when the electric field was polarised in the x-direction, except rotated through 90 degrees (with nodes appearing in the y-plane rather than the x-plane as seen above).

Figure 3.2 showed when the split in the ring is eliminated, the structure exhibits a single resonance in the near IR. This was confirmed by FDTD simulation, Figure 3.5. Unlike the complex field distribution of the split-ring structures, the resonant electric field distribution of the full ring is symmetrical, exhibiting two areas of field enhancement with positions determined by the polarisation of the exciting wave.

Figure 3.6 shows the dispersion relationship of the each plasmon mode identified in arrays A-D with respect to the arc length of the ring. The shift in resonance frequency with

increasing arc length is approximately the same for all supported surface plasmon modes. The simulated data shown on the graph correlates well with the experimental results, making it possible to accurately predict the resonance frequency of particular modes before fabrication.

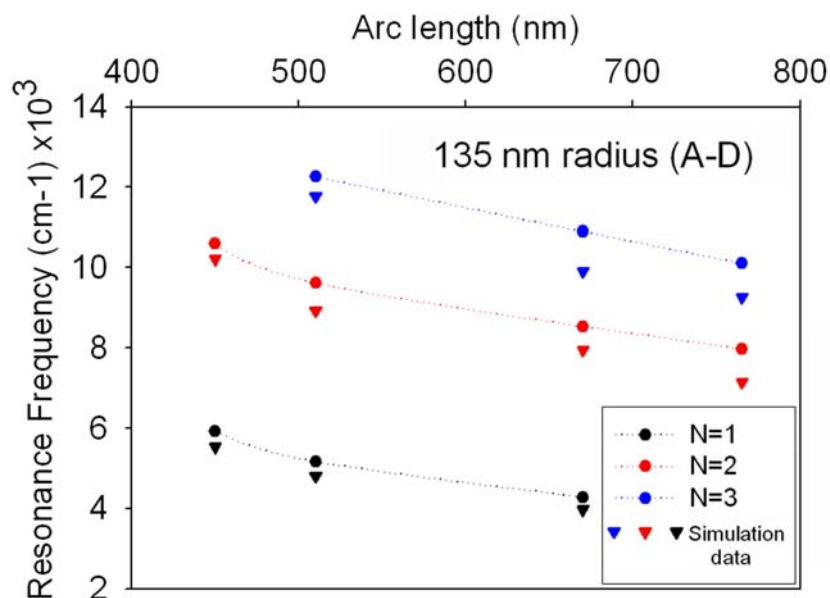


Figure 3.6. Dispersion of plasmon resonances with changing arc length for 135nm radius Au split-rings. Resonance frequency vs. Au arc-length for N=1, N=2 and N=3 plasmon modes in arrays A-D. Experimentally and numerically measured peaks show good correlation.

Although the resonances these 135 nm rings have been shown to be tuneable over a large wavelength range ( $> 1.5\mu\text{m}$ ), and exhibit field enhancements  $\sim 30\times$  the incident light, the lowest wavelength resonance achieved was 944 nm. In the context of performing bio-molecular SERRS, it is important for these resonances to appear in the visible portion of the spectrum. Not only does this region correspond to the absorption wavelength of many dyes and fluorophores commonly used in bioscience for the sensing and tracking of molecules and events, but also to the wavelength of lasers available within the laboratory. With this in mind, efforts were directed toward making the rings smaller, thereby increasing their resonance frequency.

### 3.4.2 Plasmonic effect of radius alteration in Au split-rings

Size is one of the most important factors in determining the plasmon resonance wavelength of a nano-structure, the smaller the structure, the lower the resonance wavelength. Figure 3.7 shows plots of transmission against wavelength for arrays E-H (Section 3.3.2) when the light incident on the structures is polarised both perpendicular and parallel to the split in the ring geometry.

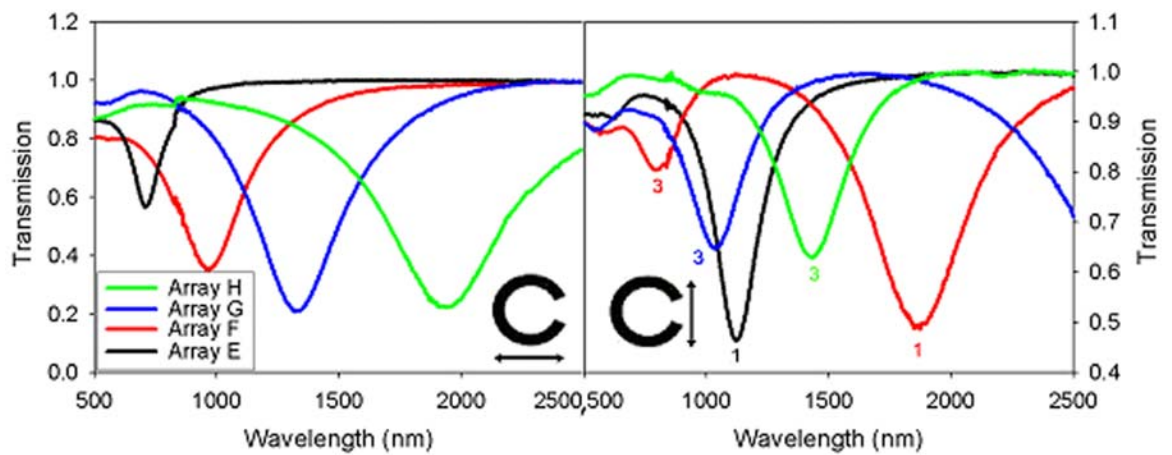


Figure 3.7. Plasmonic response of Au split-rings E-H with changing ring radius. Transmission spectra of arrays E-H at both polarisations. The even modes,  $N=2$ , are generated when the light is polarised parallel to the split (left), whereas odd modes,  $N=1$  and  $N=3$ , are generated when light is polarised parallel to the split (right). The mode numbers for the odd modes have been marked for clarity.

Figure 3.7 shows that the trend in resonance generation is similar to that seen in Figures 3.2 and 3.3, with resonances undergoing a “red-shift” as the ring radius, and with its arc-length, is increased.  $N=1$  resonances occur for array E at 1073nm and array F at 1870 nm. The first resonance modes of the two larger rings, arrays G and H, are out with the experimental spectroscopic measurement range, occurring above 2500 nm.  $N=2$  resonances occur for array E at 710 nm, F at 966 nm, G at 1330 nm and H at 1938 nm.  $N=3$  resonances occur for array F at 798 nm, G at 1036 nm and H at 1434 nm. The large difference that ring size has on the plasmon resonances can be observed in the odd resonance modes, with the 70nm radius rings experiencing their first resonance at a higher frequency than the 170nm radius rings experience their third resonance. As with the arc-length studies shown above, the resonance frequency of each mode can be tracked predictably with changing radius size (Figure 3.8). All three resonances shift by approximately the same amount as the ring radius is increased. From these results it is clear that should resonances in the visible portion of the spectrum be desired it is necessary to fabricate split-rings with a radius of  $\sim 70$ nm, at which point fine-tuning can be achieved by arc-length alteration.

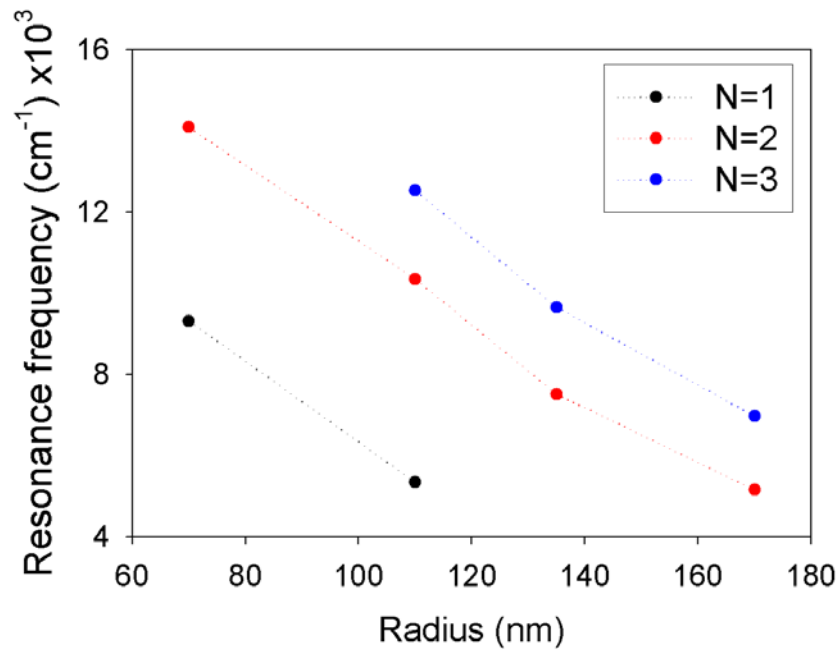


Figure 3.8. Dispersion of plasmon resonances with changing radius, showing resonance frequency vs. radius for N=1, N=2 and N=3 plasmon modes in arrays E-H. Plasmon resonance frequencies scale in an approximately linear fashion as the radius is increased - as was the case with the arc-length studies shown in Figure 3.5.

#### 3.4.3 Tuning and characterisation of 75 nm radius rings

Figure 3.9 shows high-resolution SEM images of the 75 nm radius elements that are contained within arrays I-K (Section 3.3.3). The fabricated elements of array I had an arc-length of 285 nm, array J 370 nm and array K 430 nm, all arrays had a periodicity of 260 nm. It is when fabricating structures of this size that the importance of choosing circular-shaped rings over the more traditional square-shaped rings becomes apparent. The most common problem encountered in the fabrication of nanoscale square split-rings is maintaining structural uniformity over a large array, since the nature of electron beam lithography does not lend itself to the creation of sharp right angles. This leads to unwanted bulging at the junction of the ring's base wire and its two arms, an effect that becomes more pronounced with decreasing radius.<sup>81</sup> Therefore, the wall width of the structures is not uniform along the entire length of the ring, making both fabrication and plasmonic characterisation studies of these shapes difficult. Circular shaped rings do not suffer from these same constraints, allowing much smaller rings with uniform wall width to be fabricated.

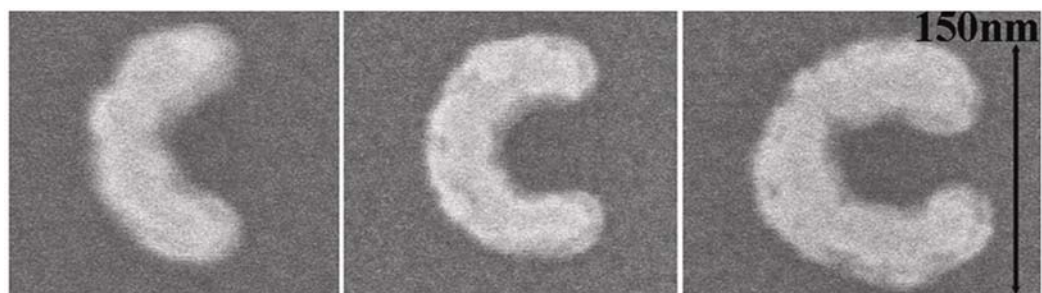


Figure 3.9. High resolution scanning electron micrographs of split ring arrays I-K (left-right).

Figure 3.10 shows both the experimentally measured and numerical calculated plasmonic activity of these arrays. The N=1 resonances occur for array I at 990 nm, J at 1290 nm and K at 1410 nm. N=2 resonances occur for array I at 650 nm, J at 754 nm and K at 765 nm. Array J shows a weak N=3 resonance (confirmed by simulation) at 605nm, while array K exhibits an N=3 resonance at 660 nm (Figures 3.10 (a) and (b)). The resonances match the trends seen in the study of the larger 135 nm radius rings. Once again the numerical values match the experimental values closely.

Figure 3.11 depicts the dispersion relationship of the each plasmon mode identified in arrays I-K with respect to the arc length of the ring. The shift in resonance frequency with increasing arc length is approximately the same for all supported surface plasmon modes, as was the case with the 135 nm radius rings.

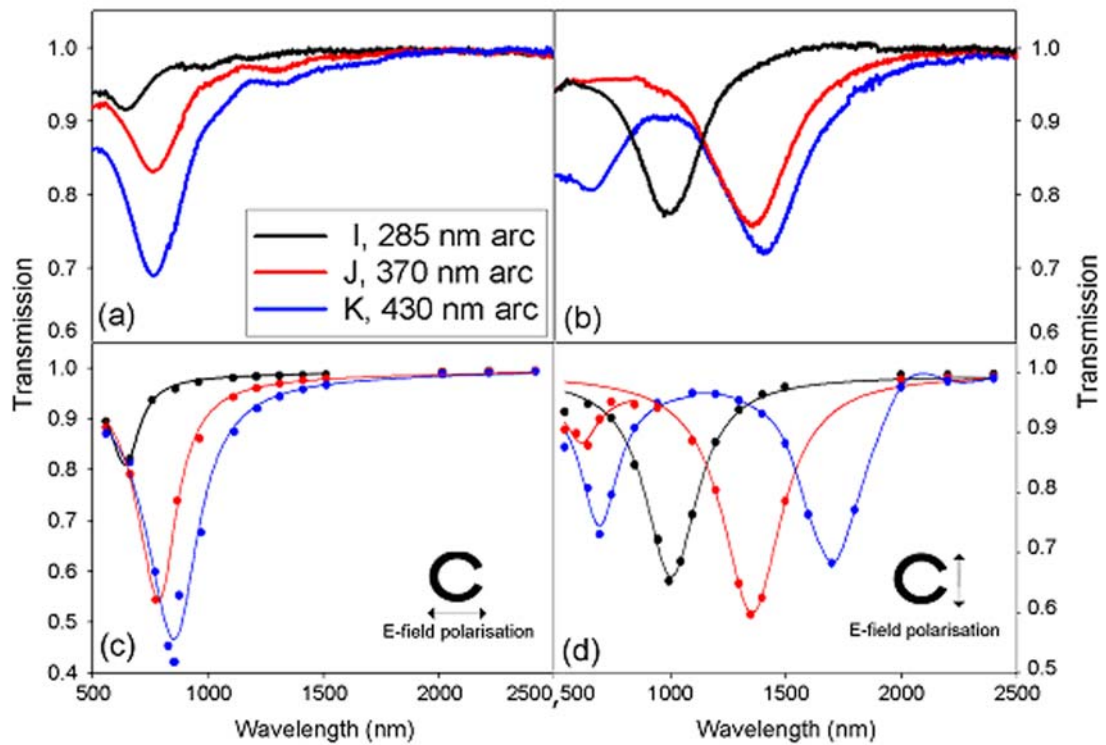


Figure 3.10. Plasmonic response of 75 nm radius split rings. Experimental (a,b) and simulated (c,d) transmission spectra of 75 nm radius split rings with varying gaps (arrays I-K). Figures a and c show the resonances when the electric field is polarised perpendicular to the split, whereas figures b and d show the resonances when the electric field is polarised parallel to the split. Good correlation is seen between the experimental and numerical data, although, as was the case in Figure 3.3, the experimental peak values are blue-shifted with respect to their numerical counterparts.

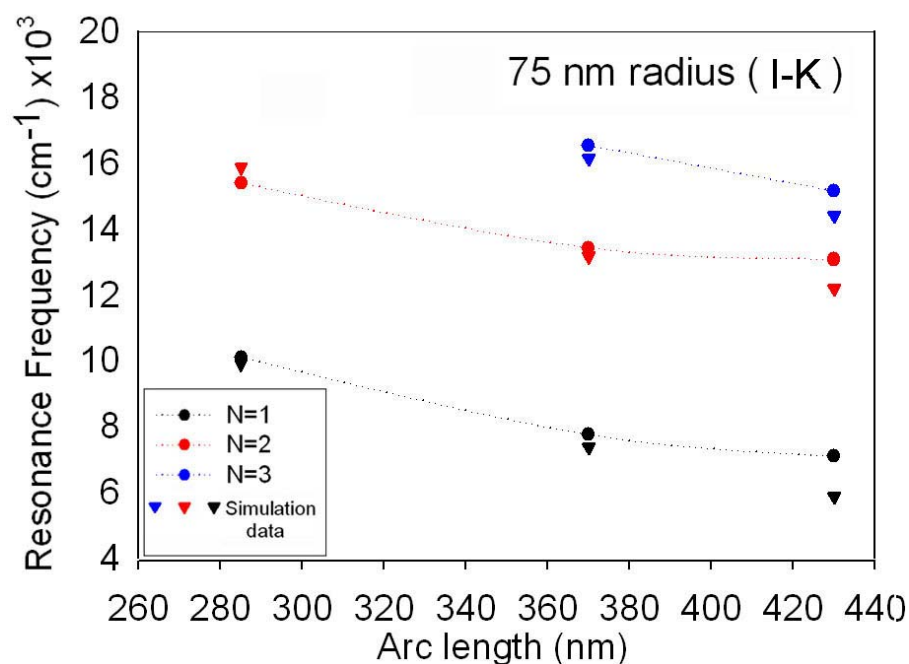


Figure 3.11 Plasmon resonance dispersion with changing arc length of the 75nm radius Au split-rings I-K. Experimental and numerically measured values for resonance frequency vs. Au arc-length for N=1, N=2 and N=3 show good correlation.

If these nano resonators are to be used for biosensing, it is important to maintain a high level of structural uniformity across an array of rings, as well as from one “identical” array to the next. Preserving this uniformity maximises the Q of the resonances whilst allowing repeatable readings to be obtained from separate sensors.

Excellent fabrication uniformity was achieved using the electron beam lithographic fabrication technique. Measuring the dimensions of ten structures, chosen at random, within array K, showed that the rings contained within had a radius of  $77 \pm 2$  nm, a wall width of  $50 \pm 2$  nm and a gap size of  $29 \pm 2$  nm. Good reproducibility of the plasmon resonances from sample to sample is also achieved. Measuring the plasmon resonances of multiple samples, fabricated using the designs employed in arrays I-K, shows the mean deviation to be 115, 40 and 16 nm for the first, second and third order resonances respectively (Array I exhibits resonances at  $1081 \pm 118$  nm and  $668 \pm 34$  nm for N=1 and N=2. Array J exhibits resonances occur at  $1135 \pm 92$  nm,  $774 \pm 29$  nm and  $623 \pm 18$  nm for N=1, N=2 and N=3. Array K shows resonances at  $1506 \pm 135$  nm,  $805 \pm 56$  nm and  $670 \pm 14$  nm for N=1, N=2 and N=3). As was the case for the larger rings in Section 3.4.1, the resonances associated with rings of longer arc-length are more numerous and of higher frequency.

Several of these resonances (namely the second resonance of array I and the third resonances of arrays J and K) fall within the desired range for visible wavelength sensing. Figure 3.12 depicts the normalised electric field at the surface of array I-K’s ring structures at each resonance frequency.

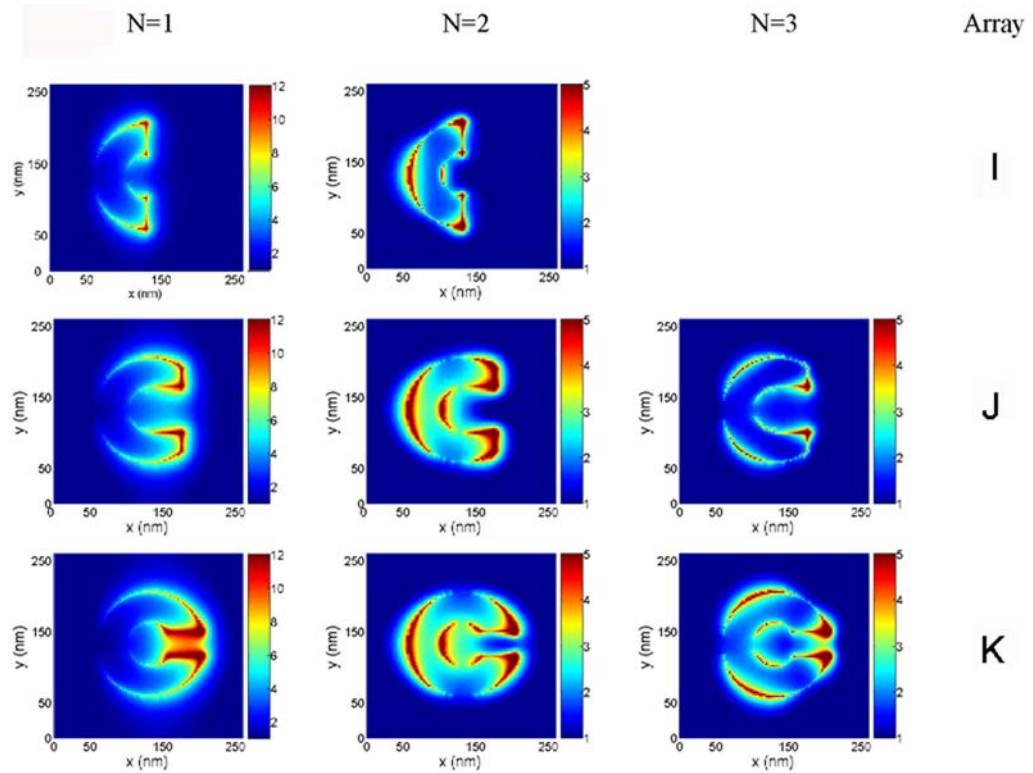


Figure 3.12 Electric field enhancement at resonance for 75 nm radius rings. FDTD simulations of the normalised electric field in the z-plane at the surface structures found in arrays I-K at each plasmonic resonance. Array E is not of sufficient arc-length to display an N=3 resonance. For N=1 & 3 the electric field of the exciting light was polarised along the y-axis, whereas for N=2 the polarisation was along the x-axis.

The localised electric field enhancements seen in the 75 nm radius rings are less than those seen in the 135 nm radius rings. Once again, the array containing the largest of the rings, array K, displays the highest field enhancements; approximately 16, 8 and 7 for the first, second and third resonances respectively. The resonances which fall within the visible region of the spectrum, N=2 in arrays I and J, and N=3 in array K, have maximum field enhancements of approximately 6, 7 and 7 respectively, theoretically providing Raman enhancements of  $1.3 \times 10^3$ ,  $2.4 \times 10^3$  and  $2.4 \times 10^3$ . As was the case with the larger rings, none of the N=1 resonance modes (which exhibit the largest localised field enhancements) fall within the visible spectrum. Since ring radii of  $\sim 70$ -75 nm are at the limit of what can be readily fabricated using the electron beam tool without losing structural uniformity and/or reproducibility, it has not been possible to achieve visible N=1 resonances using Au split-rings.

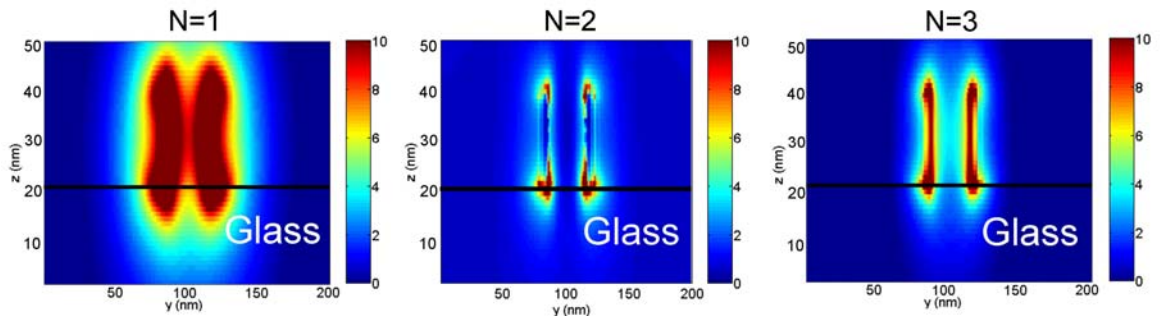


Figure 3.13. Electric field enhancement inside the split of a 75 nm radius Au split ring. FDTD simulations of the normalised electric field through the centre of the split (in the x-plane) at each resonance mode for the ring structure found in array K. Field enhancements of approximately 8 and 4 can be found in the centre of the split for the 1<sup>st</sup> and 3<sup>rd</sup> order resonances respectively. No enhancement is experienced in the centre of the split for the 2<sup>nd</sup> order resonance.

As was mentioned in Section 3.4.1, the ring structure, having only one plane of symmetry, supports different mode orders at different polarisation directions of the exciting light. Due to the charge distribution around the structure when driven by the external field, odd mode order exist when the field is polarised in the y-axis, parallel to the split, and even modes exist when the field is polarised in the x-axis, perpendicular to the split. This has a direct bearing on the localised field distribution around the structure at each resonance mode, as well as the enhancement experienced inside the split, Figure 3.13. For the odd modes, N=1 and N=3, the charges on either side of the split are opposite, leading to coupling between the ring arms and an enhanced field throughout the volume of the split. However, for the even mode, N=2, the charges on either side of the split are the same, so no enhancement is seen inside.

#### 3.4.4 Plasmonic effect of height/thickness alteration in Au split-rings

Along with geometric factors of particle size and shape, the height of a nanoparticle (i.e. the thickness of the evaporated metal layer) has also been shown to affect its plasmon resonance wavelength.<sup>33, 79, 104</sup> As described in Section 2.4.1, the PMMA resist thickness required to fabricate structures with feature sizes in the tens of nanometres restricts the height of the split-rings shown in this research to less than 40 nm. Figure 3.14 displays the plasmon resonances of three split-ring arrays, identical in every aspect but height (Section 3.3.4). The transmission of each array was measured when the electric field of the exciting light is polarised both parallel (odd resonance modes) and perpendicular (even resonance modes) to the split in the ring geometry.

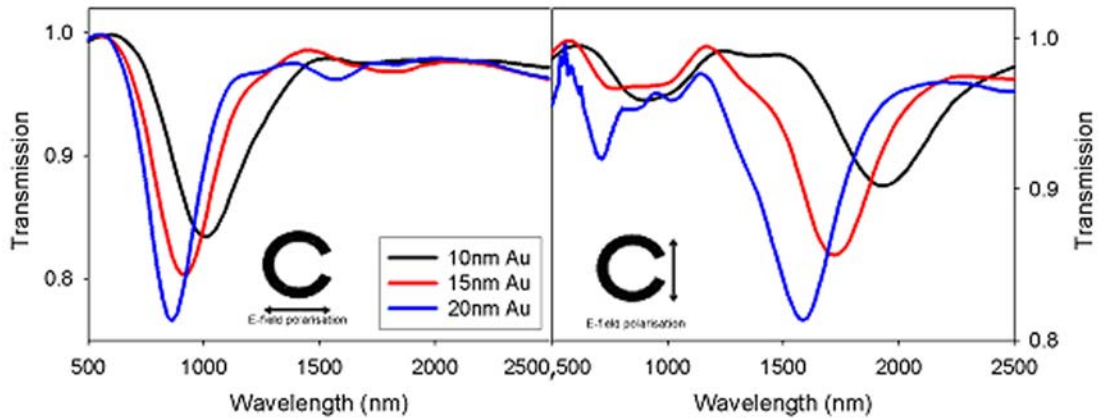


Figure 3.14. Plasmonic response of 75 nm radius rings fabricated with increasing thickness of Au. Resonances shift to higher frequencies and increase in intensity as the height of the rings increases from 10 nm - 20 nm. The third resonance mode, N=3, can only be resolved when 20nm of Au has been evaporated.

As the thickness of the Au layer was increased the resonances of the structure blue-shift to higher frequencies, a phenomenon that agrees well with other studies of this nature conducted on a variety of different shapes.<sup>33, 79, 104</sup> The resonances also become stronger and narrower with increasing Au thickness. The second order resonance, for example, exhibits a significant decrease in FWHM (~350 nm to ~230 nm) when the Au layer is increased from 10 nm to 20 nm. The N=1 resonance occurs at 1575 nm, 1715 nm and 1940 nm for 10 nm, 15 nm and 20 nm of Au respectively. The N=2 resonances occur at 850 nm, 900 nm and 1010 nm for 10 nm, 15 nm and 20 nm of Au respectively. The N=3 resonance is only apparent for an evaporation thickness of 20 nm, occurring at 740 nm. The dispersion of these resonances with changing Au thickness is shown in Figure 3.15.

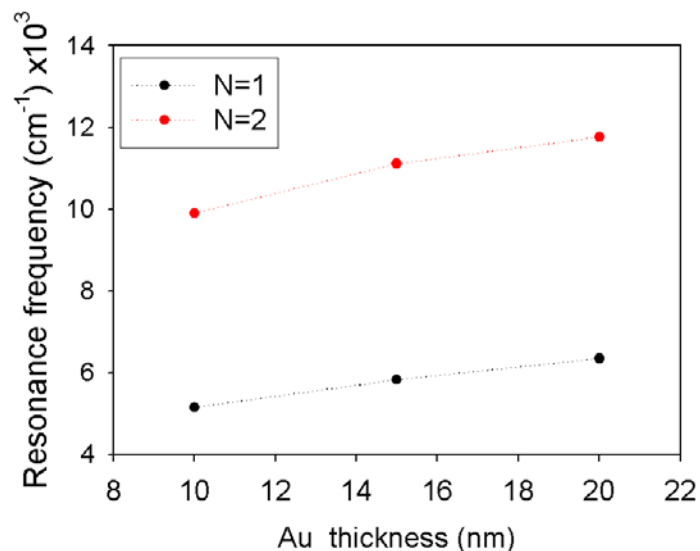


Figure 3.15 Dispersion of plasmon resonances with changing Au thickness, showing resonance frequency vs. Au thickness for N=1 and N=2 plasmon modes of 75nm radius rings. A linear frequency shift is observed for the increasing levels of Au. N=3 mode is not shown in the above Figure because only one array (20 nm thick Au) displays this resonance.

As described previously, the motivation of this research is the ability to fabricate structures capable of tuneable plasmonic resonances in the visible portion of the spectrum, corresponding to the absorption wavelength of many dyes and fluorophores commonly employed in the marking of biological samples. As such, Figures 3.14 and 3.15 demonstrate that should higher resonance frequencies be required, a thicker layer of metal should be evaporated onto the nano-patterned substrate.

### 3.4.5 Plasmonic effect of periodicity alteration in Au split-rings

It has been demonstrated that the periodicity of a regular nanoparticle array can have an effect on its plasmonic response<sup>45</sup>. In order to determine whether the plasmonic resonances observed for these particles were indeed resonances of the single geometries themselves and not due to interparticle coupling or grating effects, three arrays of identical particles were fabricated, each with a different periodicity (Section 3.3.5). Figure 3.16 shows the plasmonic activity of the three arrays.

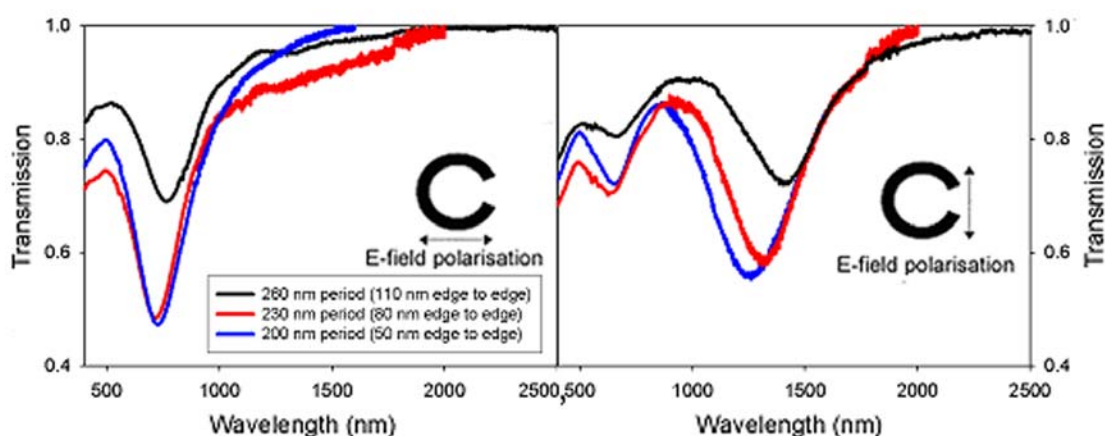


Figure 3.16. Plasmonic response of 75 nm radius rings fabricated with varying particle periodicity. No significant shift in resonance wavelengths is seen (the differences seen are within the expected standard deviation experienced due to the fabrication process), confirming that the resonances exhibited by these structures are due to geometry, not interparticle effects.

Figure 3.16 shows no significant change in the peak resonance wavelength of any of the structural modes when the particle period is decreased. Although  $N=1$  shows a blue-shifting trend as the period is decreased from 260 - 200 nm (an edge to edge spacing decrease of 110 - 50 nm),  $N=2$  and  $N=3$  show no such trend. In fact, the standard deviation of each resonance is either within that of the sample to sample reproducibility demonstrated in Section 3.4.3, or sufficiently similar as to be considered as such (the standard deviations in this case being  $\pm 79$  nm,  $\pm 25$  nm and  $\pm 21$  nm for the first, second and third modes respectively, compared to values of  $\pm 135$  nm,  $\pm 56$  nm and  $\pm 14$  shown in Section 3.4.3). Therefore, it can be concluded that the lateral spacing of the structures had no effect on the peak positions of the plasmonic resonances, and that these resonances were indeed plasmonic effects of individual structures and not an array effect. This is confirmed by the research of S. Linden et al.<sup>75</sup> and C. Rockstuhl et al.<sup>73</sup>, who show this to be true for particle spacing far smaller than those shown here.

### 3.5 Conclusion

Previous studies have shown the plasmonic behaviour of square shaped nano split-rings is similar to that of nanowires, with the resonance frequency of the structure determined by the ratio of its arc length to its height (although red-shifted in comparison with wires of the same length due to interaction at split effecting plasmon oscillation).<sup>79</sup> The results demonstrated in this Chapter concur with those findings. What can be inferred from these studies is that the highest frequency resonances are achieved when the ring radius and arc-length are kept to a minimum, while the height of the rings is as large as possible. The sharpest, most intense resonance peaks occurred when the volume of Au present in the structure is maximised. 75 nm radius rings were required to produce visible resonance wavelengths, but these were of relatively low quality, occurring as they did at either the third resonance mode of a larger arc-length ring, or the second resonance mode of shorter arc-length rings. Issues with fabrication uniformity below ~70-75 nm radius dictate that in order to produce high quality, high frequency plasmonic resonances using nano split-ring resonators, a metal other than Au must be used (as is covered in the following chapter).

In conclusion, the ability to predictably tune the surface plasmon resonance wavelength of Au crescent shaped nano split-ring resonators has been shown. Importantly, the polarisation dependent nature of these resonances enables a single homogeneous array of nano-scale split-rings to support multiple spectroscopic resonance modes with wavelengths ranging over several microns depending on the structure's feature sizes. The high resolution afforded by the VB-6 electron-beam lithography tool allows these resonances to be shifted into the visible portion of the spectrum by fabricating 75 nm radius split-rings, opening up possibilities for the creation of ultra-small biosensors, with scales of an appropriate size for single molecule detection and-or nanofluidics.

## Chapter 4 - Ag split-ring resonators as molecular sensors

### Abstract

The application of tuned silver split-ring resonators as dichroic sensors for multi-purpose visible wavelength molecular spectroscopy is described. By producing arrays of these identical nanostructured elements, with critical dimensions of 30-150 nm, the controllable generation of plasmonic resonances at two common visible laser wavelengths is demonstrated, produced as a consequence of the polarisation of the light with respect to structural geometry. The engineered dichroic response of the single geometry structures is used to carry out surface enhanced Raman spectroscopy (SERS) on a self-assembled monolayer of 2-mercaptopyridine. By utilising the multi-modal plasmonic resonances exhibited by the split-rings, molecular sensing is performed at both 532 nm and 633 nm.

### 4.1 Introduction

As was demonstrated in the previous chapter, the multiple plasmonic resonances of Au crescent shaped nano split-ring resonators can be specifically tuned over a wide spectral range. However, the need for these resonances to exist in the visible portion of the spectrum for biomolecular SERRS studies requires that the rings themselves be small. Not only does this provide significant fabrication challenges, but also the smaller rings exhibit weaker, lower quality resonances. These problems can be overcome by fabricating the same structures using a metal with a higher plasma frequency, such as silver. Not only would this allow higher frequency resonances to be achieved, but, in accordance with the results seen in Chapter 3, these resonances would also be stronger since the relative volume of metal used to achieve the resonance would be greater (i.e. a larger arc-length or radius). It would also allow resonances to be supported and tuned throughout the entire visible spectrum, increasing the functionality of the structures. Although simple SERS substrates have been constructed previously using metallic nanocrescents as a template,<sup>102</sup> the potential of such structures as tuneable, multi-wavelength biological sensors with discretely engineered plasmonic hot-spots has not been realised.

This chapter demonstrates the fabrication and characterisation of silver split-ring resonators, showing their plasmonic response to be similar in nature to the gold rings but at a significantly higher frequency. It is shown that a single structure is capable of supporting two polarisation independent resonances within the visible spectrum and that these resonances can be tuned to correspond to the wavelength of visible lasers commonly used in biomolecular detection. Finally, the potential of these structures as novel, multi-wavelength SERS substrates is demonstrated by using their polarisation dependent resonances to perform molecular sensing of 2-mercaptopyridine at two separate excitation wavelengths. The structures are shown to act as plasmonic dichroics, their sensory response dependent on both the polarisation and the wavelength of the exciting radiation.

## 4.2 Materials

The substrates were cleaved from 500  $\mu\text{m}$  thick, 4 inch diameter, Pyrex (borosilicate) wafers purchased from University Wafer, Boston. Resist material, Elvacite Polymethyl Methacrylate (PMMA) was obtained from Lucite International Inc. The 2-mercaptopyridine and 3-aminopropyltriethoxysilane were purchased from Sigma Aldrich, UK. The Ti and Ag wire, used in the resistive heating evaporator, were purchased from Goodfellow Cambridge Limited, UK, and Testbourne Inc, UK, respectively.

## 4.3 Methods

The nanostructures were designed, written and developed in accordance with the protocol detailed in Section 2.3.1. Ag metallisation using the resistive heating evaporator is described in Section 2.3.1.7. Fabrication of Ag structures was initially far more problematic than fabrication of Au structures had been. Since Ag was not available in the clean-room's electronically-controlled Plassys electron-beam evaporators, an in-house resistive heating evaporator was used to deposit the Ag (the problems associated with which are discussed in more detail in Sections 2.3.1.7 and A.1.2.2). As was the case with the electron beam evaporation performed in the previous chapter, Ti was used as an adhesion layer for the Ag. However, due to a combination of inconsistent evaporation thickness and poor bi-layer adhesion (see Section 2.4.3) this method was abandoned in favour of a chemical adhesion solution. In such cases the developed pattern was modified with a self-assembled monolayer of 3-aminopropyltriethoxysilane (Section 2.3.1.8), which acted as an adhesion promoter for the Ag.

XPS measurements were performed using Daresbury Laboratoire's Scienta ESCA300 XPS tool. Background information and on this technique and operational details of this tool can be found in Section A.1.7.

AFM measurements were carried out using a JPK Nanowizard. Further detail can be found in Section 2.3.3.3 and A.1.5.

### 4.3.1 Fabrication of 75 nm radius Ag split-rings

Three arrays of 75 nm Ag split-rings were fabricated (using 3-aminopropyltriethoxysilane as an adhesion promoter), each with a different arc-length. These arrays (which shall be referred to as L, M and N) were identical to arrays I-K (see Section 3.3.3), having arc-lengths of 285 nm, 370 nm and 430 nm respectively. The plasmonic activity of each array was measured using a Shimadzu UV3101PC absorption spectrometer, as described in Sections 2.3.3.1 and A.1.3. Results and discussion relating to these arrays can be found in Section 4.4.1.

### 4.3.2 Fabrication of 80 nm radius Ag split-rings

A design with a radius of 65 nm, a wall width of 12 nm and an arc length of  $\sim 388$  nm was written using a dose of  $2044 \mu\text{C}/\text{cm}^2$ . Once developed and metallised the split-ring, which shall be referred to as array O, exhibited an 80 nm radius, a 50 nm wall width and a 10 nm gap size. The plasmonic activity of each array was measured using a Shimadzu UV3101PC absorption spectrometer, as described in Sections 2.3.3.1 and A.1.3. Results and discussion relating to these arrays can be found in Section 4.4.2.

#### 4.3.3 SERS of 2-mercaptopyridine using 532 nm and 633 nm lasers

A self-assembled monolayer of 2-mercaptopyridine was attached to an array of split-rings matching the structure of array N (Sections 4.3.1 and 4.4.1). The sensor was modified according to the procedure outlined in Section 2.3.5.1. The surface enhanced Raman spectra from this resonance were collected using both a Horiba Jobin Yvon LabRam INV spectrometer, and an Ocean Optics QE65000 spectrometer, using a 633 nm and a 532 nm laser respectively, according to the procedure detailed in Sections 2.3.8.1. and 2.3.8.2. Rotating the sample through 90 degrees also allows collection of the Raman scatter from the “off-resonance” condition. In addition to the measurements made using the rings, a 10mM solution of the molecule in water was measured using both the 633 nm laser and the 532 nm laser. Results and discussion relating to these arrays can be found in Section 4.4.5.1.

#### 4.3.4 SERS of 2-mercaptopyridine using 633 nm and 785 nm lasers

An array identical to the that of array O (Section 4.3.2 and 4.4.2) was modified with a SAM of 2-mercaptopyridine (Section 2.3.5.1) before SERS spectra were taken using both 785 and 633 nm lasers and a Horiba Jobin Yvon LabRam INV Raman spectrometer (in accordance with Section 2.3.8.1). Results and discussion relating to these arrays can be found in Section 4.4.5.2.

#### 4.3.5 SERS of 2-mercaptopyridine immobilised on split-ring arrays with varying second order resonance peak wavelengths using a 633 nm laser

Four Ag ring arrays were fabricated following the designs of arrays L-O (Section 4.4.1 and 4.4.2), each of which has a different second order resonance wavelength (~ 545 nm, 600 nm, 655 nm and 794 nm respectively). Each array was modified with a SAM of 2-mercaptopyridine before SERS was carried out using a 633 nm laser polarised perpendicular to the split. Results and discussion relating to these arrays can be found in Section 4.4.5.3.

#### 4.3.6 Storage of Ag and Au capped Ag rings in PBS

An array of 75 nm radius Ag split-rings (following the geometry described in array N, Section 4.4.1) was stored in PBS over a period of 84 hours. An array of Ag rings with identical geometry and Ag thickness, but with the addition of approximately 2 nm of Au evaporated on top of the Ag layer, was then fabricated. This second array was also subjected to PBS storage for 84 hours. Taking the second resonance mode as a reference, the plasmonic activity of both arrays was measured using a Shimadzu UV3101PC absorption spectrometer, as described in Sections 2.3.3.1 and A.1.3.

### 4.4 Results and discussion

#### 4.4.1 Plasmonic comparison of 75 nm Au and Ag rings with changing arc-length

Figure 4.1 shows experimental and simulated plasmonic activity of Ag ring arrays L-N (Section 4.3.1) when the incident light was polarised both parallel and perpendicular to the

split. The resonant behaviour was identical to the trends seen in the 75 nm radius Au split-rings, only with each resonance occurring at a higher frequency.

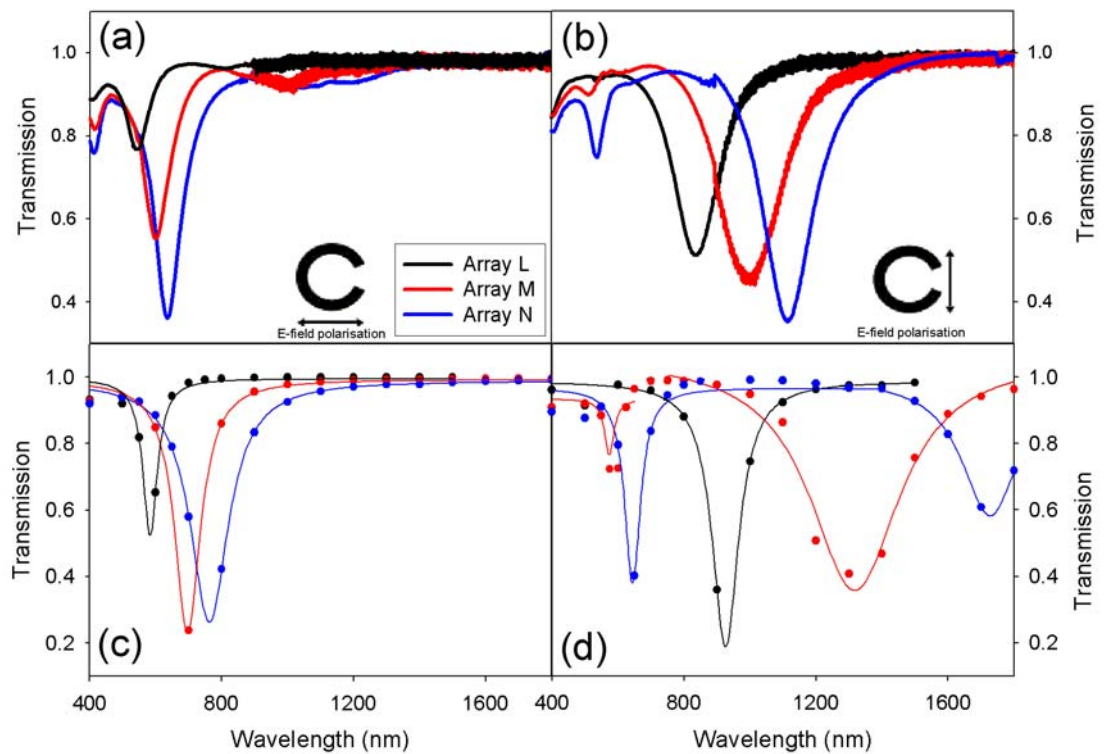


Figure 4.1. Experimental, (a) and (b), and simulated, (c) and (d), transmission spectra of 75 nm radius Ag split-rings with varying arc-lengths. The simulated data points were fitted to Lorentzian curves using Sigma-plot software for a better visual representation of their peaks. This Figure shows the plasmonic activity of rings at both polarisation states, with (a) and (c) displaying even resonance modes ( $N=2$ ), and (b) and (d) displaying odd resonance modes ( $N=1$  &  $3$ ). The trend of plasmonic red-shifting with increased particle length is seen in both experimental and simulated data, agreeing well with the trend seen in Chapter 3 for Au rings. The peak positions of the experimental and numerical curves do not match exactly, the reasons for this have been previously mentioned in Section 3.4.1.

$N=1$  modes occur for array L at 838 nm, M at 996 nm and N at 1116 nm.  $N=2$  modes occur for array L at 543 nm, M at 600 nm and N at 635 nm, while only arrays M and N exhibit  $N=3$  modes, occurring at 512 nm and 538 nm respectively. With the exception of the first order modes, all of Ag split-ring resonances occur in the visible portion of the spectrum. Figure 4.2 shows a plot of the resonance dispersion in the Ag rings for each mode, together with those for the same shapes fabricated in Au. The trends of resonance position with arc-length are almost identical for each metal, however, the average wavelength of the Ag resonances are blue-shifted from the Au resonances by an average of 248 nm for  $N=1$ , 125 nm for  $N=2$  and 103 nm for  $N=3$ .

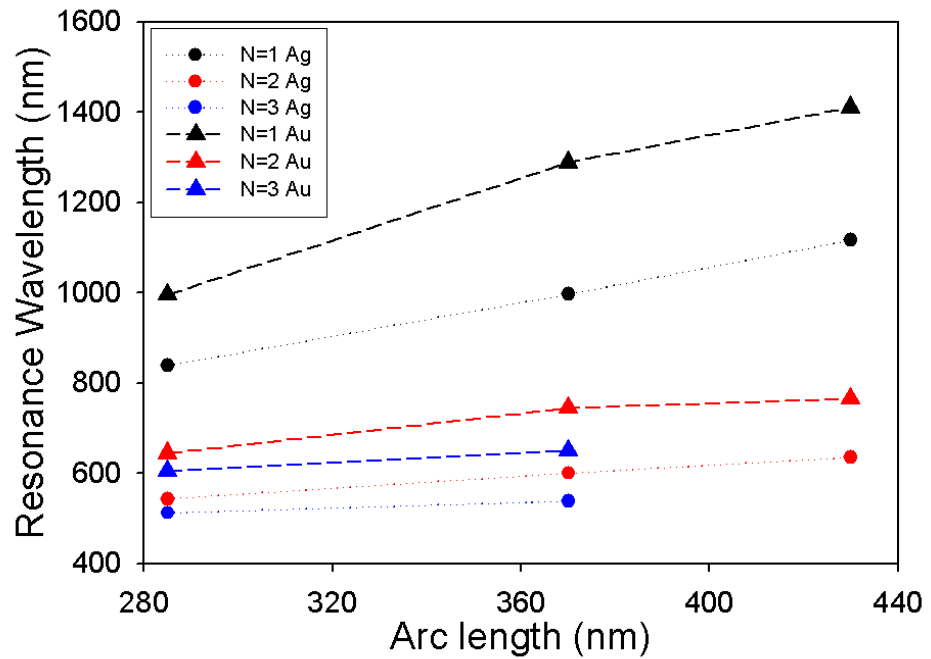


Figure 4.2. Resonance dispersion for all modes of identical Ag and Au rings with varying arc-lengths. The Ag structures behave in the same manner as the Au structures, their resonances red-shifting in a predictable fashion with increasing arc length. However, the resonance frequency of the Ag rings is higher than the Au rings for each comparable mode.

Figure 4.3 shows high resolution SEMs of the Ag structures. These structures exhibit slightly less uniform arcs than those seen for the same shapes fabricated using Ti as an adhesion layer (see Figure 3.9). This is most likely due to the chemical adhesion method employed in this case. SAM coverage may not be perfect around the extremities of the pattern, leading to rougher Ag coverage in these areas. The effect of this is further explored in Section 4.4.3.

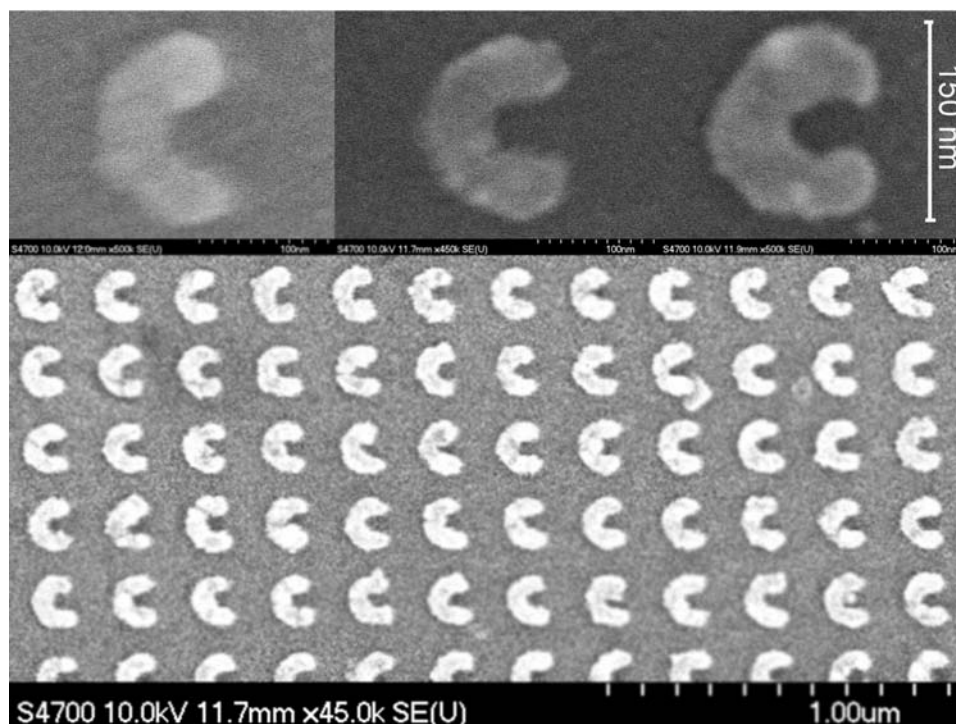


Figure 4.3. Scanning electron micrographs of Ag split rings. High resolution SEMs of arrays L-N (top) and a wide area SEM of array M (bottom). As seen in this figure, chemical adhesion can occasionally lead to structures with rougher features than those previously fabricated using Ti as an adhesion layer. This is most likely due to varying 3-aminopropyltriethoxysilane SAM coverage from sample to sample. Although the samples are slightly less uniform throughout the length of their arc, the variation in feature size does not exceed  $\pm 5$  nm (Section 4.4.3).

#### 4.4.2 Tuning the dichroic resonances of Ag split-rings to common laser wavelengths

Of the arrays detailed above, array N is of most interest since it was designed so that its second and third resonances were tuned to encompass the common laser wavelengths of 633 and 532 nm respectively. This, as will be detailed later (Section 4.4.5), would allow such a structure to act as a SERS based molecular sensor at both of these wavelengths. In an effort to fabricate an additional multi-functional resonator, a second structure was made in which the geometry of the ring was tuned such that it exhibited second and third resonances at 785 and 633 nm respectively. Along with 532 nm and 633 nm, 785 nm lasers are also frequently used in Raman and fluorescence spectroscopy.

As has been demonstrated in Sections 3.4.1, 3.4.3 and 4.4.1, the ring's resonances can be red-shifted by maintaining a constant radius and increasing the arc-length, or by increasing its radius. Increasing the arc-length of the 75 nm radius rings was not sufficient to achieve the desired resonances, so a larger, 80 nm radius ring array was fabricated with a gap size of  $\sim 10$  nm (Section 4.3.2). Figure 4.4 shows the plasmonic response from this array, which shall be referred to as array O.

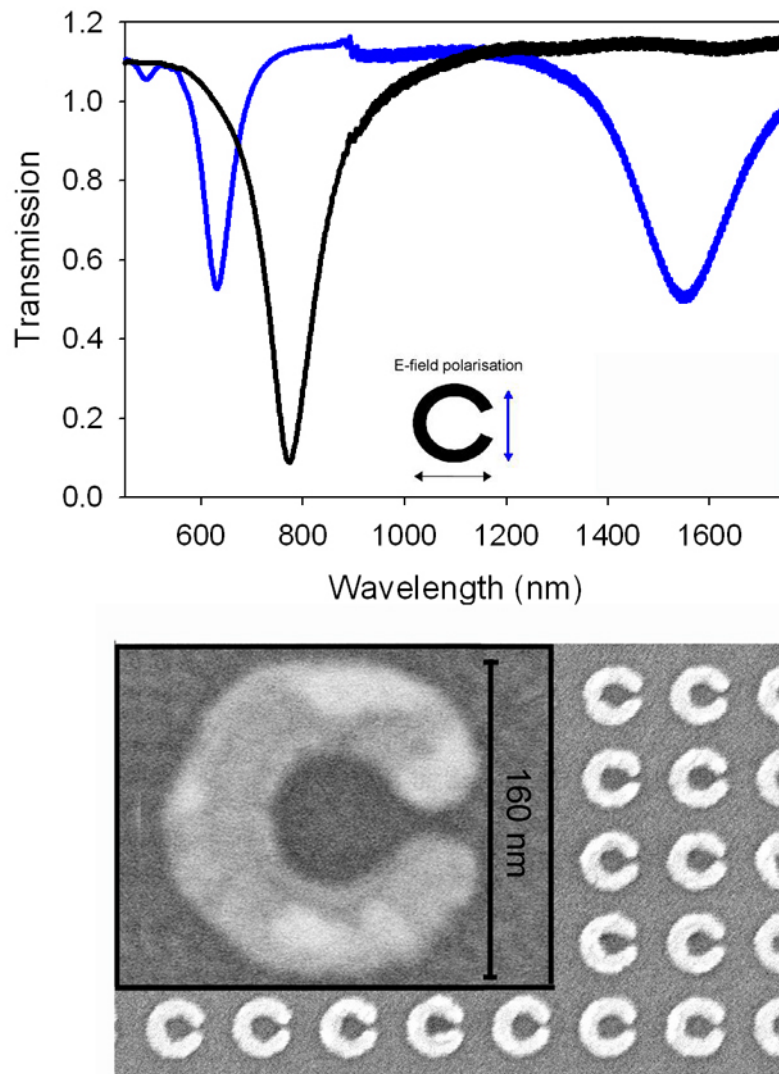


Figure 4.4. Plasmonic response (top) and high resolution SEM (bottom) of 80 nm radius, 10 nm gap Ag split-rings. Rings display second and third resonances at 774 and 631 nm respectively, resonances corresponding to common laser wavelengths of 785 and 633 nm.

Array O exhibits first, second and third resonance peaks at 1551 nm, 774 nm and 631 nm respectively, matching the requirements for a dichroic resonator with modes encompassing 785 and 633 nm.

#### 4.4.3 Reproducibility of resonances using chemically adhered Ag

As Figure 4.3 illustrates, the Ag ring structures are rougher and less uniform than their Au counter-parts (Figures 3.1 and 3.8). This would appear to be due to the chemical adhesion method employed to fabricate the Ag rings. Array N was used to determine the structural error caused by this fabrication method. The rings contained within this array had a radius of  $75 \pm 2$  nm, a wall width of  $53 \pm 4$  nm and a gap size of  $33 \pm 5$  nm (measured from a random sample of 10 structures). This structural deviation is only marginally worse than exhibited by identical designs fabricated using electron-beam evaporation of Ti/Au (Section 3.4.3 showed that for this

design the dimensions were  $77 \pm 2$  nm,  $50 \pm 2$  nm and  $29 \pm 2$  nm for radius, wall width and gap size).

In order to determine whether the slightly decreased uniformity substantially affected the reproducibility of the rings; four arrays with identical patterns (using the pattern from array N) were fabricated. The plasmonic response of each array was measured. The mean peak wavelength and standard deviation of each mode was  $1129 \pm 91$  nm,  $655 \pm 24$  nm and  $525 \pm 9$  nm for N=1, N=2 and N=3 respectively. This would suggest that, like the Au rings in Chapter 3, the resonances become less sensitive to morphological changes with increasing mode order. Importantly, since they fall within the desired visible spectral range, the second and third resonances showed good reproducibility across several arrays, showing deviations of 24 nm and 9 nm respectively.

When this process was repeated for the structures detailed in array O, the outcome was similar. Measurements over several samples show the radius to be  $79 \pm 2$  nm, the wall width to be  $48 \pm 2$  nm and the gap size to be  $10 \pm 2$  nm. The mean peak wavelength and standard deviation of each mode was  $1488 \pm 68$  nm,  $772 \pm 14$  nm and  $631 \pm 3$  nm for N=1, N=2 and N=3 respectively. Once again, the first resonance mode appears to be the most sensitive to slight array inhomogeneity, while the second and third resonances show little deviation across several samples. The deviations seen here are comparable to those exhibited in Section 3.4.3.

Along with slight deviation in structural uniformity as a consequence of chemical adhesion, the resonance wavelength of the rings may also be affected by inconsistent Ag thickness as a consequence of the manually operated evaporation shutter (see Section A.1.2.2). In order to test this, each of the 8 samples used for determining the reproducibility of arrays N and O were subject to interrogation by AFM. The drop in crystal frequency that yielded the best lift-off results was 1300 Hz, which, according to measurements made by AFM, relates to  $31 \pm 3$  nm of Ag. This proves that the manual operation of the shutter does not significantly affect the thickness of the fabricated structures, and hence their plasmon resonance.

AFM can also be used to determine the roughness of the structures surface, a factor that may not have a large influence on the plasmonic response of the ring, but will certainly affect its SERS response. In the case of all adhesion methods and metals, the root mean squared roughness of the rings varied from  $\sim 2$  nm in the majority of cases, to  $\sim 4$  nm in a small proportion of structures.

#### 4.4.4 Ti as an adhesion layer

In order to determine whether the more uniform shapes fabricated by Ti adhesion provide any advantage (be it in plasmonic response or reproducibility) over the chemically adhered Ag, or whether the addition of the Ti influences the resonance frequency, an array containing structures identical to those found in array O was fabricated using a Ti/Ag bi-layer. The thickness of the Ti/Ag layer, measured by AFM, was  $29 \pm 5$  nm (the Ti layer contributing between 2 and 5 nm of the overall thickness; relating to a drop of 20Hz in crystal frequency), which compares well with both the silane adhesion method and the Ti/Au evaporation in Chapter 3. The device yield using this fabrication method was approximately 50% (many arrays did not lift-off, while others suffered from poor Ti -Ag adhesion).

Four identical arrays were fabricated with Ti as an adhesion layer (using the pattern from array O) to determine the reproducibility of the resonances from sample to sample. The mean peak wavelength and standard deviation of each mode was  $1524 \pm 61$  nm,  $794 \pm 15$  nm and  $649 \pm 4$  nm for N=1, N=2 and N=3 respectively. These compare well with the standard deviations of the chemically adhered Ag rings of the same pattern, the standard deviations of which were 68 nm, 14 nm and 3 nm for N=1, N=2 and N=3. The peak resonance wavelengths and associated errors for both fabrication methods are displayed in Figure 4.5.

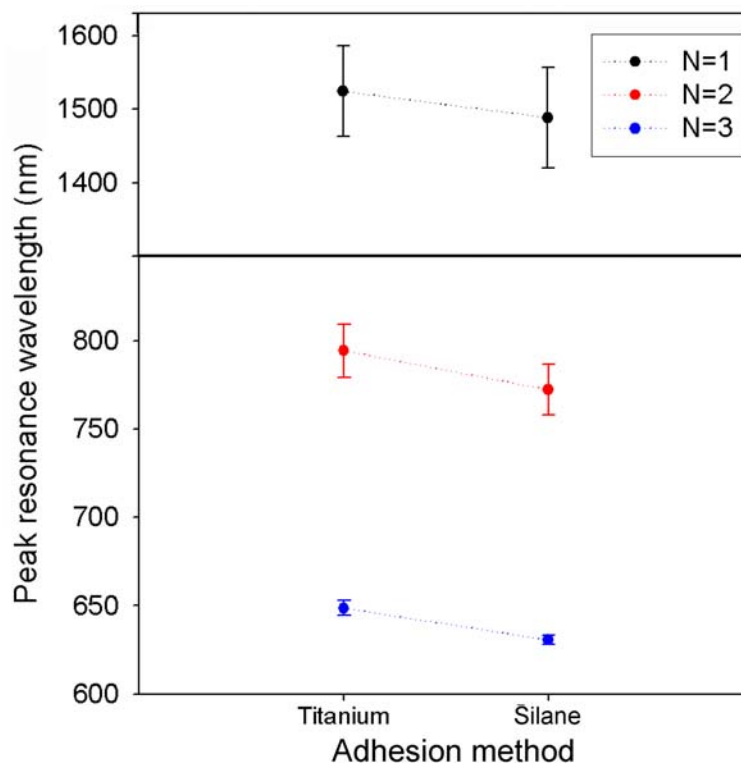


Figure 4.5. Peak resonance wavelengths and standard deviation of 80 nm Ag split-rings fabricated using separate adhesion methods. The rings fabricated using the Ti adhesion method exhibit higher resonance wavelengths, yet do not show improved sample to sample resonance reproducibility.

The Ti adhered samples, although seemingly more uniform across the length of their arc, do not provide for better plasmon reproducibility than can be achieved using 3-aminopropyltriethoxysilane as the adhesion layer. The very small fluctuations in geometry seen for the chemical adhesion do not make the plasmonic behaviour unpredictable, nor do they affect their reproducibility (the deviation of the resonances in either method is almost identical). However, the addition of Ti does have an adverse effect on the position of the resonances. For duplicate patterns, the resonance wavelength of the Ti/Ag rings are, on average, 36 nm, 22 nm and 18 nm higher than the N=1, 2 and 3 modes of the chemically adhered Ag rings. Since the height of the rings was restricted due to the thickness of the resist, the addition of a Ti layer effectively decreased the amount of Ag that can be evaporated onto the sample, which, in line with the results seen in Section 4.4.4, red-shifts its plasmon modes.

Considering these results, (along with the apparent lack of inhomogeneous broadening for the resonances in Figure 4.1 and the consistent dispersion of the Ag resonances relative their Au counterparts in Figure 4.2) there seems no distinct disadvantage in using a metallic adhesion method over a chemical one, especially considering the lower frequency resonances and the poor device yield that accompanies the use of Ti. As such the Ti method was rarely employed.

#### 4.4.5 Ag split-rings as molecular sensors

The plasmonic properties of metallic nanoparticles can be used in a variety of ways to facilitate biosensing. These can include using nanoparticles as labels,<sup>8, 9, 13</sup> monitoring changes in their plasmon due to the presence of an analyte,<sup>14, 15</sup> or by using the amplified fields around resonant particles to enhance existing spectroscopic sensing techniques.<sup>4, 5, 105, 106</sup> SERS and SERRS fall into this latter category. SERS is a powerful sensing tool that can not only detect very small quantities of molecules, but can also provide diagnostic structural information based on the chemical bond vibrations within those molecules, hence it is a potentially label-free technique (see Section 1.4.4 for further detail).

The highly tuneable nature of the visible plasmon resonances exhibited by Ag split-rings makes them ideal candidates for the creation of application specific sensing surfaces based on SERS. Furthermore, the ring's dichroic function provides the possibility of their use as multiple wavelength sensors, the sensory response of each resonance dependent on the polarisation of the incident light.

As described in Section 4.4.1, a 75 nm radius Ag split-ring with an arc-length of ~ 430 nm (based on array N) can support two polarisation independent resonances in the visible region, N=2 at  $655 \pm 24$  nm and N=3 at  $525 \pm 9$  nm. Significantly, these resonance wavelengths corresponded to two common laser wavelengths of 633 nm and 532 nm. Even though the resonances were densely packed, they did not significantly overlap, allowing each mode to maintain its polarisation independence. The dichroic function of the rings allowed the resonances to be spaced more closely (in this case just over 100 nm apart) than would be possible in a symmetrical nanoparticle resonator, even if it were multi-modal.

##### 4.4.5.1 Ag split-rings as dichroics for molecular spectroscopy at 633 and 532 nm

Mercaptopyridine was chosen as the analyte for the SERS characterisation experiments because of its favourable chemical properties. The molecule consists of a thiol group attached to a Raman active pyridine ring (Figure A.16). The thiol group ensured the molecules attach to the surface of the Ag structures, forming a SAM. Figure 4.6 shows high resolution XPS spectra of 2-mercaptopyridine attached to planar Au evaporated on a glass slide, confirming the attachment protocol detailed in Section 4.3.3. The presence of sulphur confirms the thiol attachment, while comparison of carbon to nitrogen quantities on the surface confirms the presence of the pyridine ring.

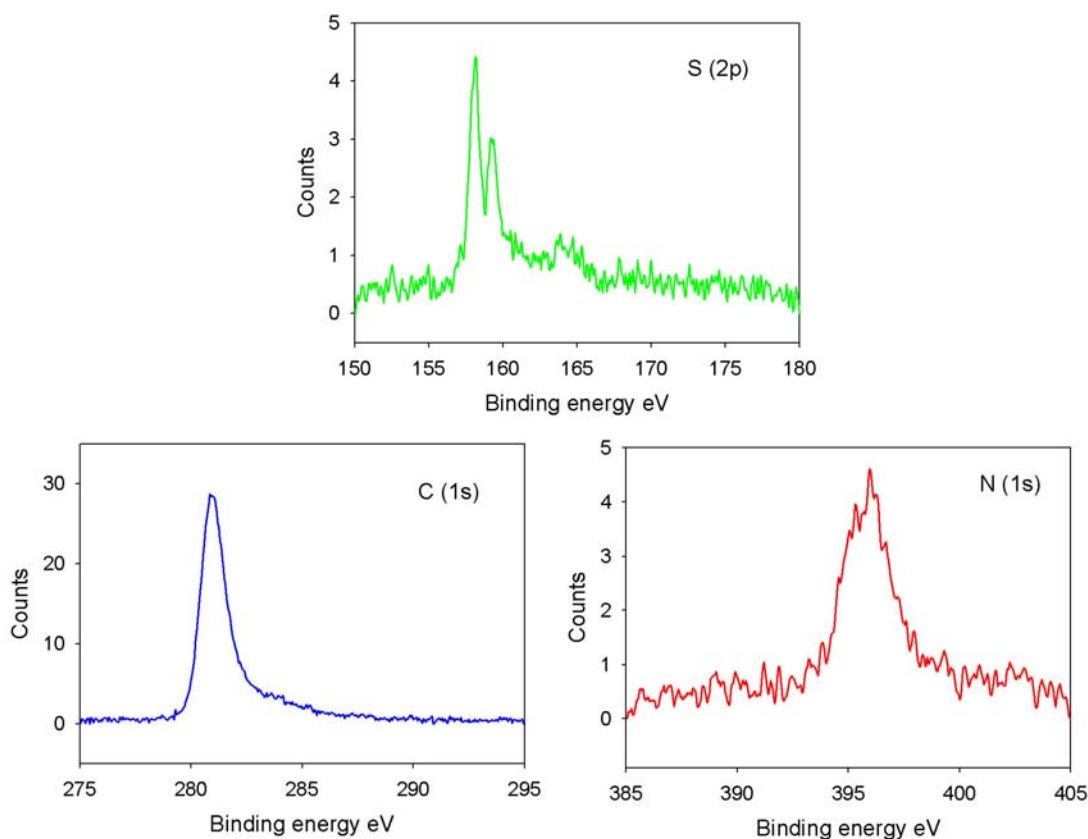


Figure 4.6. High resolution XPS spectra of 2-Mercaptopyridine attached to metallic surface via thiol linkage. The ratio of C to N in mercaptopyridine is 5:1, approximately the ratio exhibited in this spectra. Along with the presence of S, this confirms the modification procedure. The use of Au for this experiment is irrelevant, as it is merely to confirm the attachment protocol.

Since the molecule does not absorb near the laser wavelengths used in these experiments (532, 633 and 785 nm), no resonance Raman takes place, so the SERS intensities recorded are solely due to the EM enhancements of the structures plasmon, allowing for simpler characterisation of the sensor. Furthermore, it makes the signal easier to collect since it will not suffer from excessive bleaching and there is no background fluorescence for it to compete with.

Using a 633 nm 5mW HeNe laser (beam power measured at the objective without the use of a neutral density filter), and taking into account the samples orientation with respect to the polarisation of the beam, the ring's second order resonance can be excited.

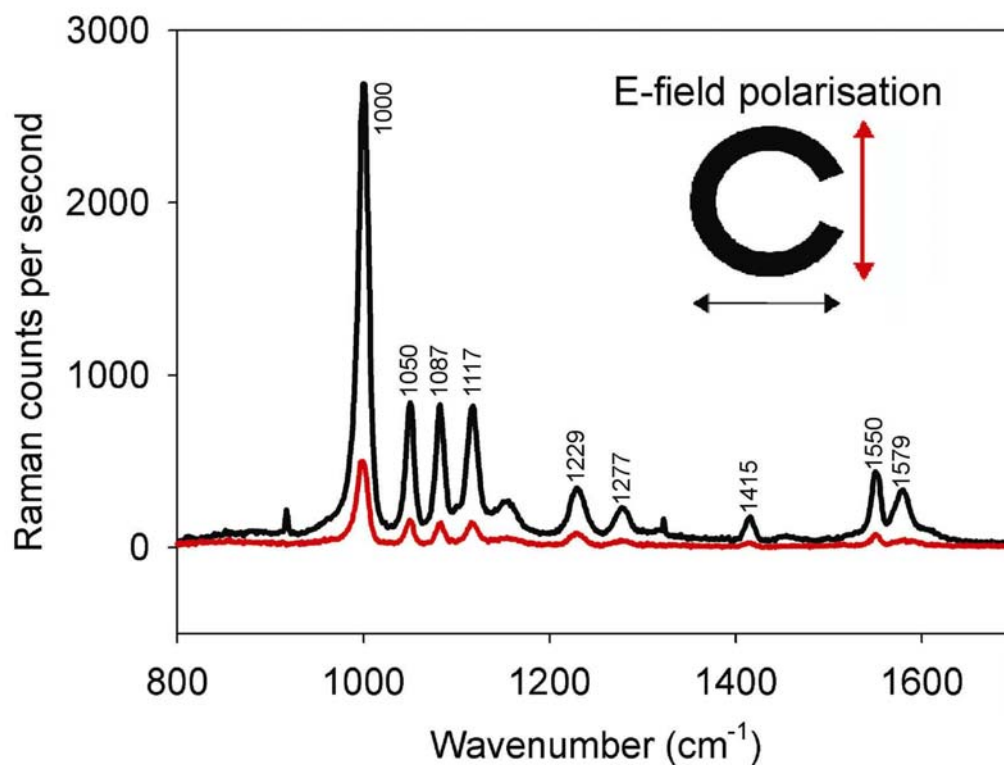


Figure 4.7. SERS spectra of 2-mercaptopyridine attached to an array of Ag split rings and excited with 633 nm laser light. Raman scatter was collected at both polarisation states. The N=2 mode (excited when the external electric field is polarised perpendicular to the split in the ring geometry) provides the largest scattering intensity, over 5x greater than when the “off-resonance” condition (using the 1000cm<sup>-1</sup> band as a reference). Spectra were collected over 20 seconds using a 5mW laser and a Horiba Jobin Yvon LabRam INV Raman spectrometer. Spectra calibrated using the 520cm<sup>-1</sup> band of Silicon.

Figure 4.7 shows the SERS spectra of Mercaptopyridine attached to a sensor array identical to that of array N in Section 4.4.1. As expected, the Raman scattering from the N=2 mode, when the light is polarised perpendicular to the split (black trace in Figure 4.7), is far greater than the scattering seen in the “off-resonance” condition when the light is polarised parallel to the split (red trace in Figure 4.7). The strongest band was at 1000cm<sup>-1</sup> and can be attributed to the pyridine-ring breathing mode<sup>98</sup>. Using this band as a reference, scattering from the N=2 mode is over 5x more intense. This difference was a consequence of greatly increased field strengths around the structure when it meets its N=2 resonance condition, fields which all but disappear when the orientation of the exciting light is changed. Figure 4.8 shows the simulated electromagnetic field distribution around the ring at its N=2 resonance wavelength when the incident light is polarised both parallel (black spectra) and perpendicular (red spectra) to the split.

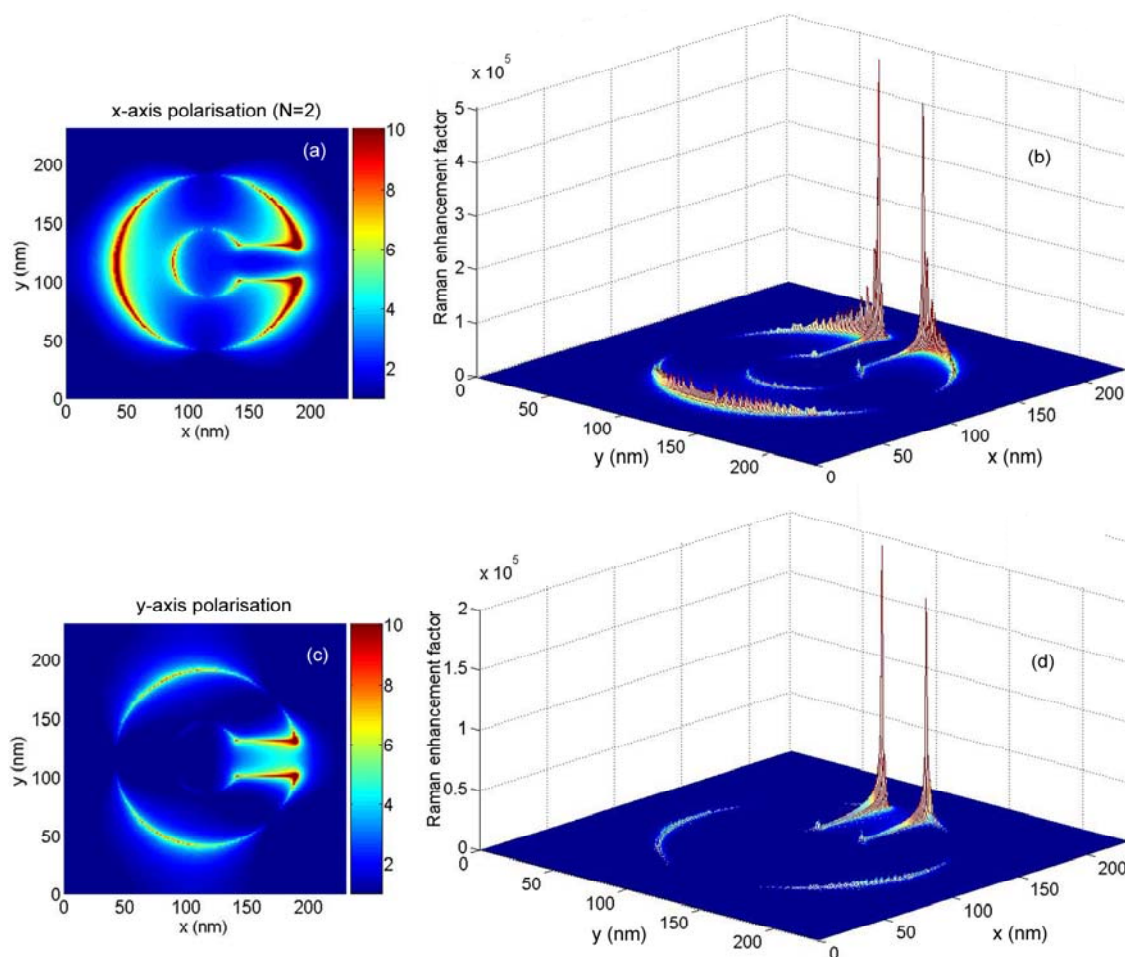


Figure 4.8. FDTD simulations showing the electric field enhancement, as well as the predicted Raman enhancement factor at resonant (a) & (b) and non-resonant (c) & (d) polarisation directions for the second order resonance of the 75 nm radius Ag rings. FDTD simulation of the normalised electric field in the z-plane at the surface the ring structure shows a significant decrease in the enhanced field's surface coverage from (a) to (c). This is reflected in plots of the Raman enhancement factor (Equation 1.17) over the ring's surface in (b) and (d), where the predicted enhancement is greater and more widespread over the surface of the structure when the incident radiation is polarised to excite the second order plasmon resonance ( $N=2$ ). Therefore, more molecules will experience an enhanced field when the exciting radiation is polarised perpendicular to the split in the ring geometry (in the x-axis), accounting for the increasing the Raman scattering seen in Figure 4.7.

As Figure 4.8 demonstrates, the area of the ring's surface experiencing localised field enhancement reduced significantly when the ring is in its "off-resonance" condition. The magnitude of the field at its most intense points also diminishes slightly, dropping from  $>20$  in (a), to approximately 14 in (b). Although the field enhancement provided by the "off-resonance" condition is more confined and less intense than the  $N=2$  resonant condition, it is not zero. Along with any contributions from chemical (or charge transfer) enhancement, this minimal field activity accounts for the Raman scattering exhibited from this orientation in Figure 4.7.

To determine an enhancement factor for this mode it was necessary to establish the intensity of the Raman scattering from 2-mercaptopyridine without any surface enhancement.

This was achieved by recording the Raman scattering of the molecule whilst in solution and comparing the intensity of the scattering to that from the rings (Section 4.3.3). Figure 4.9 shows this spectra, comparing it to the enhanced spectra collected from the rings.

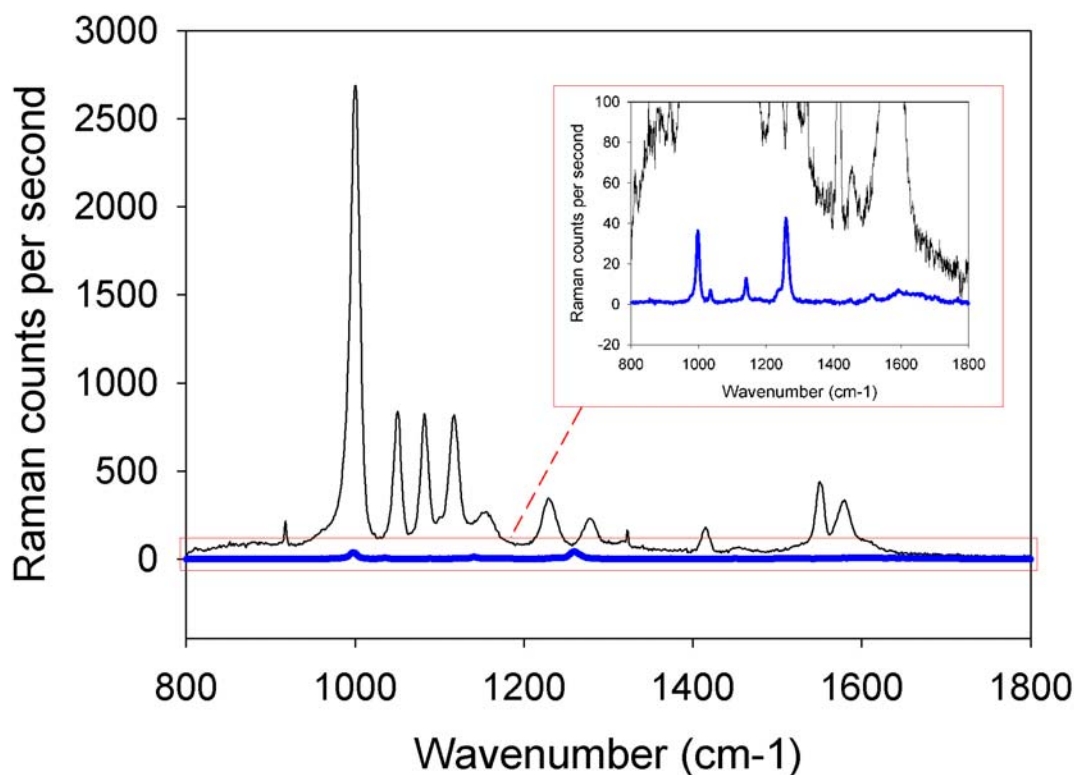


Figure 4.9. SERS and Raman spectra of 2-mercaptopyridine. Spectra collected using a 633 nm laser. This Figure shows SERS from a monolayer of 2-mercaptopyridine attached to a Ag sensor array (black line) as well as Raman spectra of a 10mM 2-mercaptopyridine solution (blue line).

The estimated probe volume of the Raman system, that is to say the volume of the sample irradiated with a power density expected to provide detectable Raman scattering,<sup>85</sup> at 633 nm using the 100x 0.75 NA Leica objective lens, is approximately  $4.4 \times 10^{-18} \text{ m}^3$ , which corresponds to approximately  $2.65 \times 10^7$  molecules for a 10mM solution. At  $1000 \text{ cm}^{-1}$  the intensity of the Raman scattering is  $\sim 37$  counts per second, which relates to  $1.4 \times 10^{-6}$  counts per molecule per second. In the case of the Ag ring array, it can be assumed that for a perfect SAM coverage<sup>107</sup> there are approximately  $1.6 \times 10^4$  molecules per ring, assuming a ring area of  $\sim 1.4 \times 10^{-14} \text{ m}^2$ . Since there are approximately 12.3 rings under the focused laser spot (considering an array periodicity of 260 nm) this corresponds to  $\sim 1.97 \times 10^5$  molecules, and a Raman intensity, at  $1000 \text{ cm}^{-1}$ , of  $1.36 \times 10^{-2}$  counts per molecule per second. Therefore, through comparison of the Raman scattering from the sensor and the bulk solution, the enhancement factor of this mode is  $\sim 9.7 \times 10^3$ .

However, this assumes a perfect SAM, and although every effort was made to minimise the time between evaporation and thiol attachment (approximately 1hr), surface oxidation of the Ag during this time will reduce the number of available binding sites. Furthermore, this value

represents an average enhancement over the entire ring structure. It can clearly be seen from the simulations represented in Figure 4.8 that only a small proportion of the ring's structure, and hence its bound molecules, experience a significant localised field enhancement, therefore contributing to the SERS signal. Indeed, at resonance, the areas of maximum enhancement reach values  $>20$ . Since Raman enhancement can be assumed to be proportional to the fourth power of the localised electromagnetic field enhancement,<sup>87</sup> it would indicate that enhancements of  $\sim 10^5$  are occurring for the molecules bound to these areas of the ring.

Since these ring structures have a dichroic functionality at two visible laser wavelengths, it is also possible to use this array as a polarisation dependent molecular sensor at 532 nm. To demonstrate this the same array was excited with a 1mW 532 nm laser and the Raman scattered light collected using an Ocean Optics QE65000 spectrometer (see Sections 2.3.8.2 and A.1.10 for details). As before, the Raman scattering was collected at both polarisations (perpendicular and parallel to the split in the ring geometry). Figure 4.10 shows these spectra.

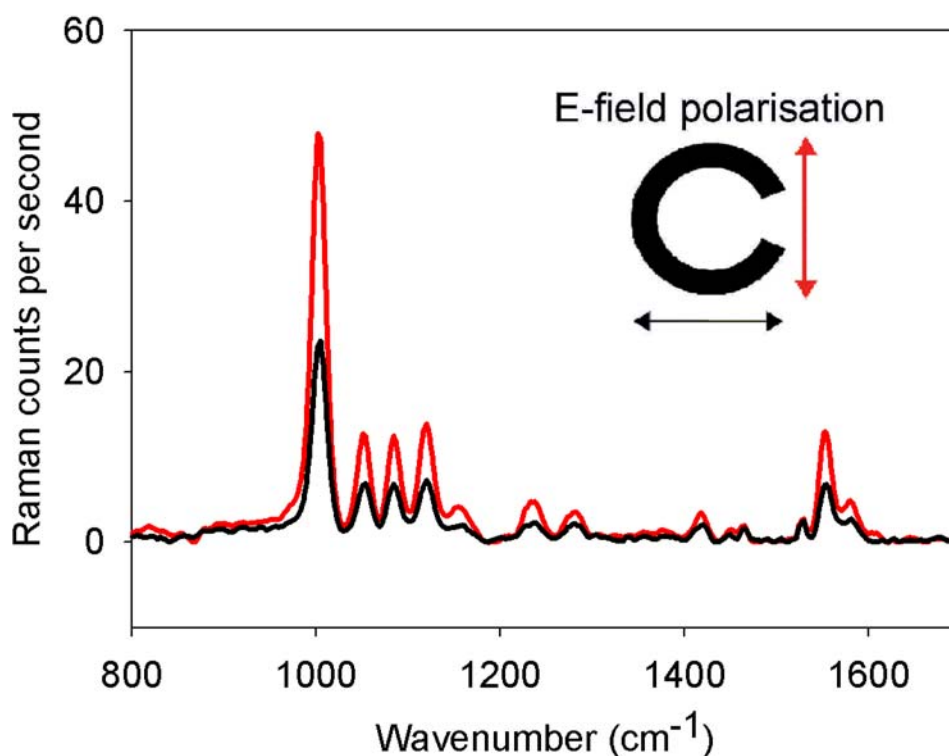


Figure 4.10. SERS spectra of 2-mercaptopyridine attached to an array of Ag split rings and excited with 532 nm laser light. Raman scatter was collected at both polarisation states. The N=3 mode (excited when the external electric field is polarised parallel to the split in the ring geometry) provides the largest scattering intensity,  $\sim 2x$  greater than when the “off-resonance” condition (using the  $1000\text{cm}^{-1}$  band as a reference). Spectra were collected over 20 seconds using a 1mW laser and an Ocean Optics QE65000 Raman spectrometer. Spectra calibrated using the  $520\text{cm}^{-1}$  band of Silicon.

The Raman scattering was most intense when the electric field of the 532 nm laser was orientated parallel to the split, exciting the ring's third resonance mode. Using the  $1000\text{cm}^{-1}$  band once again as a reference, the scattering from the N=3 mode was  $2x$  more intense than

from the “off-resonance” condition. As expected, due to the relative weakness of the N=3 mode, (Figure 4.1 (b) array N), the polarisation dependence was not as pronounced as for the N=2 resonance. This was further emphasised by its averaged Raman enhancement;  $-5.6 \times 10^2$  compared to  $-9.7 \times 10^3$  for N=2 (as with N=2, this was determined by comparing the scattering from a 10mM 2-mercaptopyridine solution with that from the ring array; 8.7 rings under the focused 532 nm laser spot gave a Raman signal of 48 counts per second, while the solution gave a Raman signal of 10 counts per second for a sample volume containing  $-1.57 \times 10^7$  molecules).

As before, we see a significant increase in localised field around the ring at this wavelength when the light is polarised so to excite the N=3 mode (Figure 4.11).

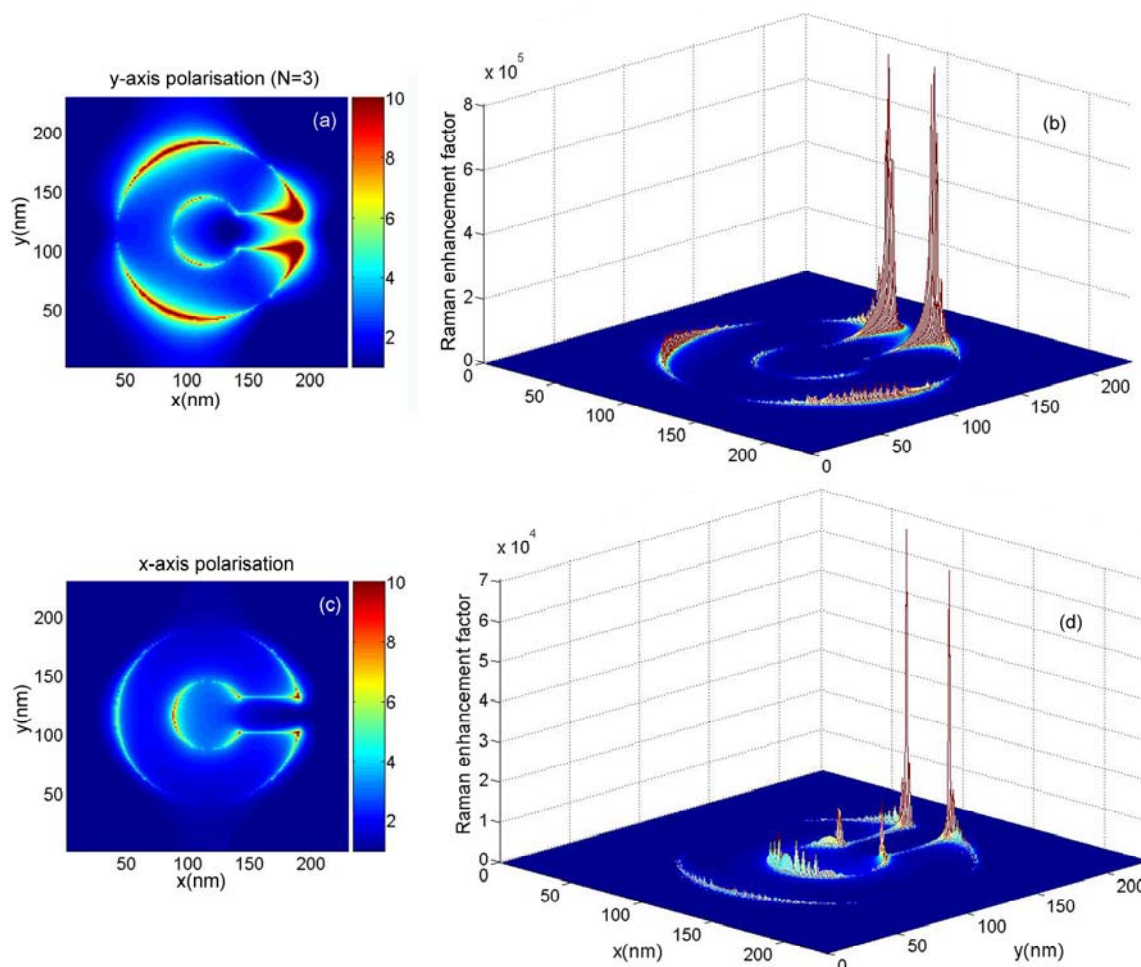


Figure 4.11. FDTD simulations showing the electric field enhancement, as well as the predicted Raman enhancement factor at resonant (a) & (b) and non-resonant (c) & (d) at resonant polarisation directions for the third order resonance of the 75 nm radius Ag rings. The N=3 mode, excited when the incident field is polarised parallel to the split (y-axis), shows considerably higher localised field strengths ( $>20$ ) than when the incident field is polarised perpendicular to the split, the “off-resonance” condition ( $\sim 7-8$ ). As was the case for the second order resonance (Figure 4.8), this is reflected in plots of the Raman enhancement factor (Equation 1.17) over the ring’s surface in (b) and (d), where the predicted enhancement is greater and more widespread over the surface of the structure when the incident radiation is polarised in the y-axis, exciting the ring’s third order plasmon resonance (N=3).

Although generally weaker than the second resonance mode (Figure 4.1), simulations indicate maximum field enhancements larger than 20, comparable to  $N=2$ , and suggesting Raman enhancements of  $\sim 10^5$  from molecules situated within these areas.

#### 4.4.5.2 Ag split-rings as dichroics for molecular spectroscopy at 785 and 633 nm

Section 4.4.5.1 showed that a 75 nm Ag split-ring can be used as a dichroic molecular sensor at both 633 and 532 nm. This multi-modal sensing capability can also be demonstrated at longer wavelengths by altering the geometry of the structures that comprise the sensing surface. Fabricating sensors based on the pattern seen in array O (Figure 4.4), permits an 80 nm radius Ag split-ring to be used as a multi-wavelength dichroic sensor at 785 and 633 nm. As was the case in the previous section, the multi-modal sensing of these structures is enabled by the sharp, closely-packed, polarisation dependent resonances of the Ag split-ring's second and third resonance modes, this time occurring at  $772 \pm 14$  nm and  $631 \pm 3$  nm respectively. Figure 4.12 shows the Raman spectra of mercaptopyridine collected from such a ring using both 785 nm and 633 nm lasers (Section 4.3.4).

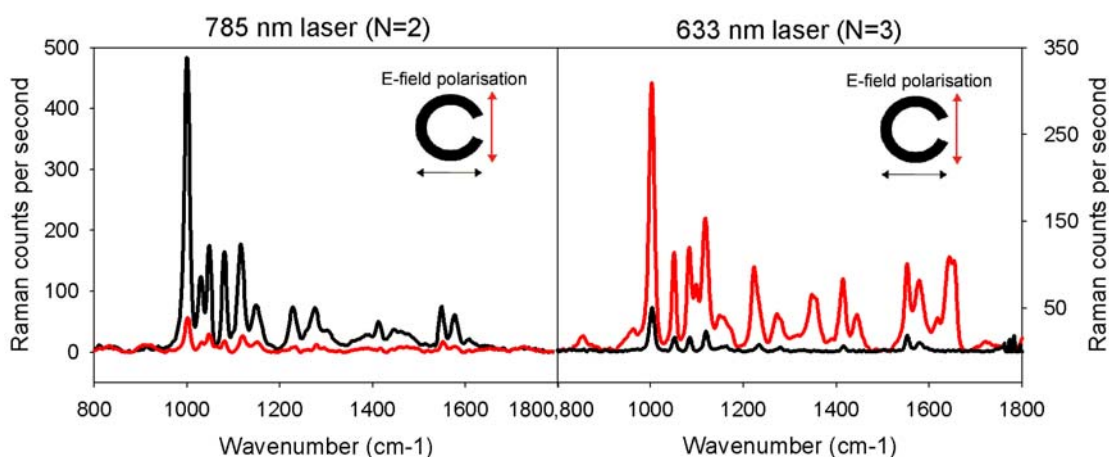


Figure 4.12. SERS spectra of 2-mercaptopyridine attached to an array of Ag split rings and excited, in turn, with 785nm and 633 nm laser light. Raman scattering for each lasers was collected at both polarisation states. The  $N=2$  and  $N=3$  modes provide scattering intensities of  $\sim 9x$  and  $\sim 6x$  greater than when in their “off-resonance” condition (taken over several measurements using the  $1000\text{cm}^{-1}$  band as a reference). Spectra were collected over 20 seconds using a Horiba Jobin Yvon LabRam INV Raman spectrometer, and calibrated using the  $520\text{cm}^{-1}$  band of Silicon.

As expected, the rings show significantly increased Raman scattering when the laser's electric field was orientated to excite either the second or third resonance mode. Averaged over several measurements the  $N=2$  mode at 785 nm shows  $\sim 9x$  greater Raman scatter when compared to the “off-resonance” condition, while the  $N=3$  mode at 633 nm exhibits  $\sim 6x$  greater Raman scatter than its “off-resonance” condition. These values, particularly that of the  $N=3$  mode, were notably larger than those seen for the corresponding resonances of the smaller 75 nm radius ring. This was due, in part, to the stronger  $N=3$  resonance displayed by the 80 nm radius ring, a product of this ring's larger arc-length relative to its radius. However, contributing most

significantly to the increase in resonance strength, and hence Raman scattering, of both modes was the overall increase in Ag volume these rings display, as a product of their larger radius and arc-length. Experimental results indicated averaged Raman enhancement factors of  $\sim 1 \times 10^5$  and  $\sim 1 \times 10^4$  for the N=2 and N=3 modes respectively (measured using the same method employed in Section 4.4.5.1), again, slightly greater than the enhancement from the smaller ring's corresponding modes. This was reflected in Figure 4.13, a graphical representation of the EM field and associated Raman enhancement factor around a single structure at both N=2 and N=3 resonance modes. Although the maximum field values were equivalent to those exhibited by the smaller ring (albeit slightly higher;  $>20$  for N=2,  $\sim 25$  for N=3), the major contributor to the larger experimental enhancements are likely due to the increased proportion of the structure's surface experiencing mid-level enhancement (enhancements of  $\sim 5$  can be seen covering the majority of the ring at both modes). As can be seen in sections (b) and (d) of this figure, the large electric fields enable Raman enhancement factors of  $10^5$  to be generated over a more substantial portion of the ring than was seen in the 75 nm radius structures (Figures 4.8 and 4.11).

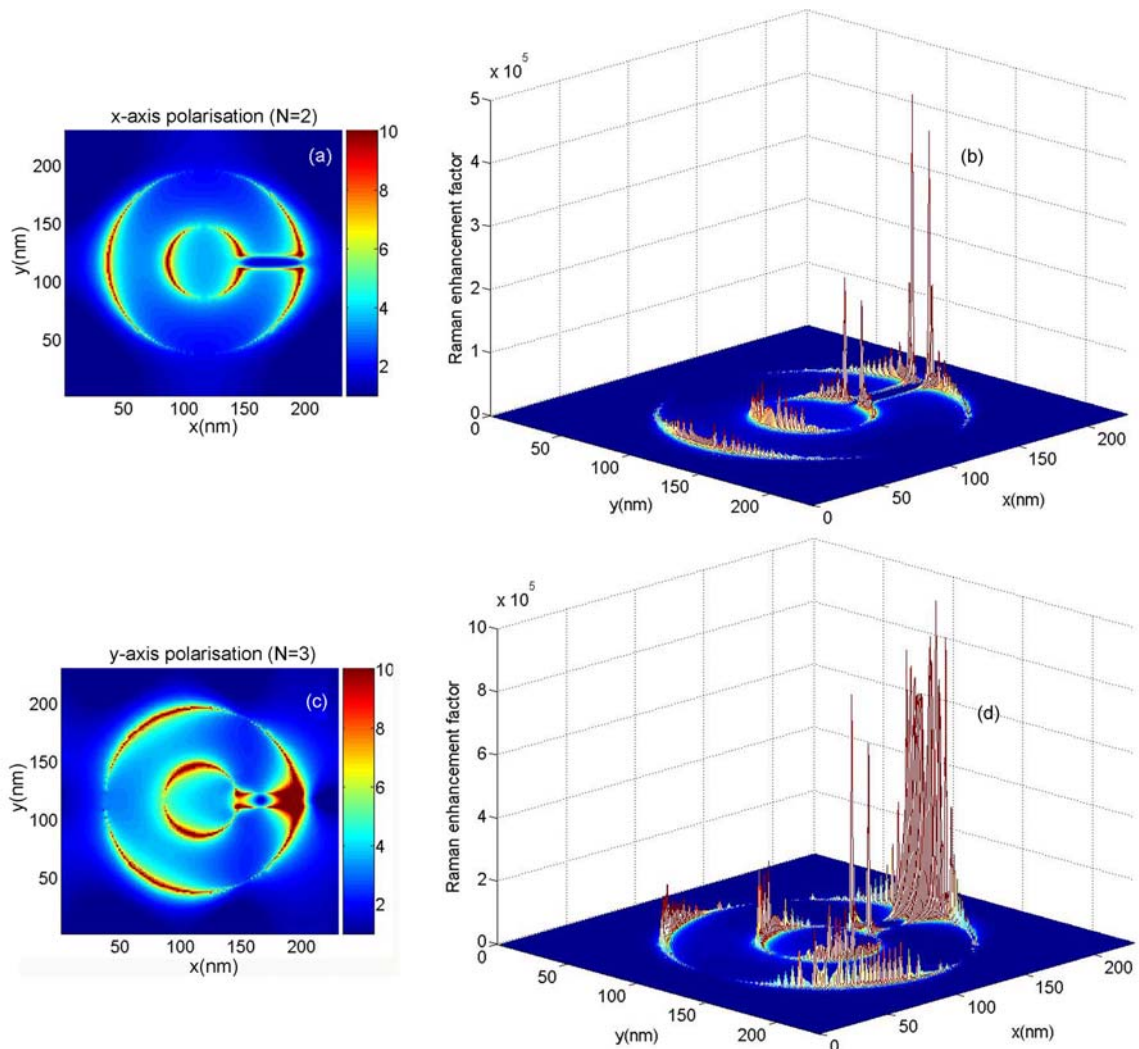


Figure 4.13. FDTD simulations of the enhanced electric fields, (a) & (c), and their associated Raman enhancement factors, (b) & (d), for the second and third order resonances of an 80nm radius Ag ring. Areas of electric field enhancement, and as a result the expected Raman enhancement factor, are

proportionally larger than seen in the 75 nm radius ring at resonance. Furthermore, the maximum values of electric field enhancement are larger for the N=3 mode;  $\sim 25$ , resulting in larger Raman enhancement for this mode. This is likely due, in part, to increased coupling between the ring arms due to the smaller, 10 nm, gap.

#### 4.4.5.3 Demonstrating the significance of specifically tuned resonances

The advantage of a specifically engineered plasmonic surface over a generally rough Ag surface (which has also been shown to provide some SERS enhancement<sup>16</sup>) can be seen in Figure 4.14. This figure contains the Raman spectra collected from three areas of the same substrate, all of which were submerged in the 2-mercaptopyridine solution. These areas included the split-ring array (positioned to excite the N=2 mode), an area of plain Ag deposited adjacent to the rings (with a root mean squared roughness of  $\sim 4$ nm), and a section of the plain glass substrate itself.

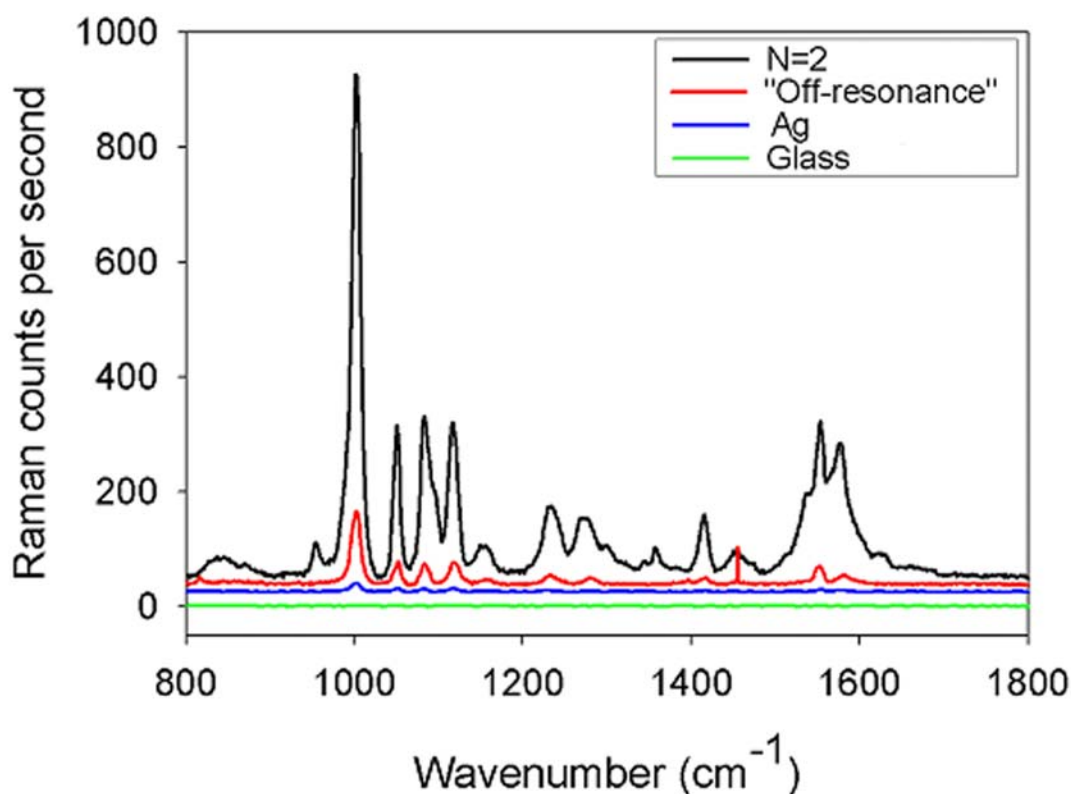


Figure 4.14. Comparison of Raman scattering from engineered structures, an area of plain Ag and glass. The intensity of the Raman signal from the resonating rings was  $\sim 60$ x greater than the Ag area, even though there were  $\sim 4$ x less molecules underneath the focused laser (due to the fill factor of the rings). No signal was recorded from the glass substrate.

Although the samples were washed thoroughly after thiol attachment, there was still the possibility that some molecules will remain present on the glass areas between the rings. As Figure 4.14 shows, the plain glass exhibits zero Raman scattering, indicating that any non-specific absorption of molecules to the glass between the rings does not make a contribution to the Raman scattering seen from the array, and that the signal was solely from the molecules

thiol-bonded to the Ag. The plain Ag (exhibiting a root mean squared roughness of 4nm) does provide some SERS enhancement, but at  $\sim 1.2 \times 10^2$ , this was significantly less than the enhancement seen from the engineered plasmon of the ring array.

As illustrated in Figure 4.7, generating a plasmonic resonance within the nanostructure leads to significantly improved Raman scattering, which, in this case, was controlled by modifying the polarisation state of the exciting radiation. When the laser light was polarised parallel to the split, the second resonance mode was no longer supported and the localised field diminishes. The same was true if the polarisation state does not change, but the resonance wavelength of the N=2 mode does. Figure 4.15 shows a plot of the Raman spectra collected from four arrays of plasmonic split-rings, each with a different second order peak resonance wavelength (a), as well as a plot of the mean scattering intensity from each array for the  $1000\text{cm}^{-1}$  band (each corrected to account for the geometry variation between designs) (b) (experimental details can be found in Section 4.3.5)

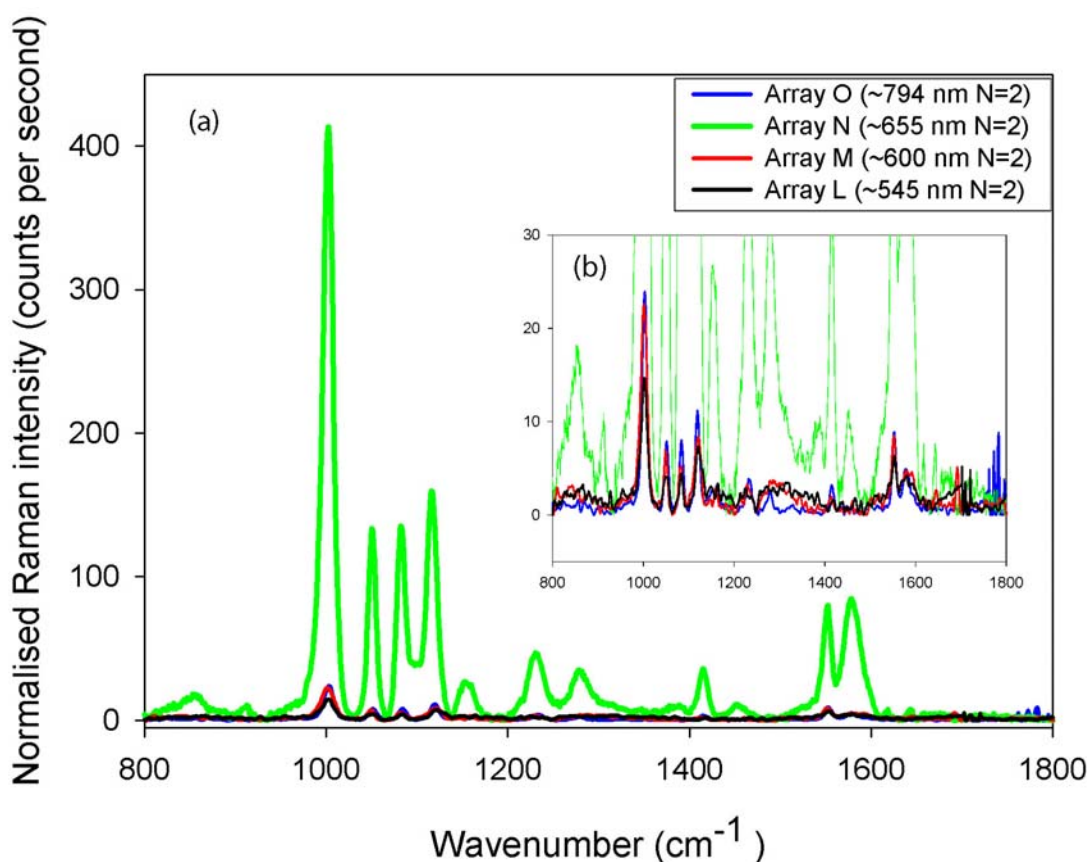


Figure 4.15. Normalised Raman spectra of 2-Mercaptopyridine attached to 4 arrays with different second order peak resonance wavelengths. Section (a) of the figure shows the spectra from all 4 arrays, whereas section (b) focuses on the smaller spectra obtained from arrays O, M and L. All arrays were excited with a 633 nm laser polarised perpendicular to the split. Scattering is significantly greater ( $\sim 21\times$ ) from array N, since this array's resonance is the only one to encompass the 633 nm laser excitation wavelength.

The structure with an N=2 resonance peak closest to (and encompassing) 633 nm was array N, and, as expected, it was this array which exhibits the strongest Raman signal. As the resonance wavelength of the nanostructures moves away, in either direction, from the

wavelength of the exciting laser (arrays L, M and O), the intensity of the Raman scattering was significantly lowered. The scattering from array N is approximately 21x more intense than from any other array, further illustrating the need for precise resonance engineering if these structures were to be used for low concentration molecular sensing.

#### 4.4.6 Curbing the degradation of plasmonic response in Ag rings using Au capping

The primary disadvantage of working with Ag, rather than Au, was the steady degradation of the nanostructure's plasmonic activity over time as a consequence of Ag oxidation. Loss of free electrons due to this surface tarnishing can have a significant impact on the frequency and strength of a structure's plasmon. Since the oxidation is promoted by direct contact with ozone and sulphur compounds, the local environment of the Ag structures determines the speed of the plasmonic deterioration (the only way to ensure the stability of the silver is to store the devices in a high vacuum environment, an impractical solution). As these structures are to be used as biomolecular sensors, the analytes will most likely be introduced via aqueous, biocompatible buffer solutions. Whether this is done simply by dropping microlitre quantities onto the sensing surface, or by more complex micro and nano-fluidic methods, the Ag structures will spend a significant period of time submerged in an environment that will increase their rate of oxidation. Figure 4.16 shows the plasmonic activity of the N=2 mode of an array identical to that of array N (Section 4.4.1) at a series of intervals over the 84-hour time frame (Section 4.3.6). The figure also displays the plasmonic activity of an identical ring geometry that has been capped with ~ 2 nm of Au and undergone the same storage conditions.

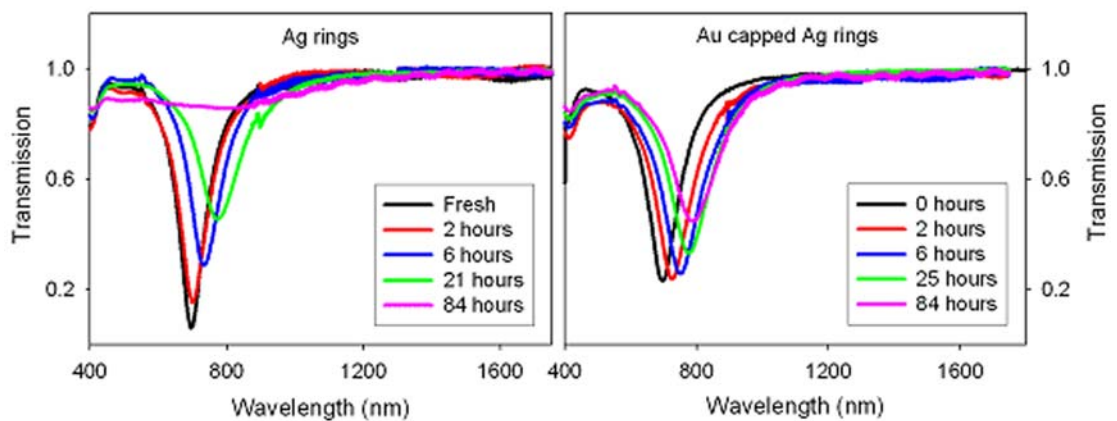


Figure 4.16. Transmission spectra taken over a series of time intervals for a Ag split-ring array and a Au capped Ag split-ring array kept in PBS for 84 hours. Steady degradation of the resonance can be seen over the 84 hour period for the Ag rings. Oxidation of the Ag surface leads to the damping of the structures plasmon, until, after the full 84 hours have elapsed, the ring displays no plasmonic activity. The Au capped sample also shows some plasmonic degradation over time, but the results are far less pronounced. After 84 hours the array retains a plasmonic response, albeit red-shifted by approximately 93 nm.

After 21 hours, the resonance showed a peak red-shift of 81 nm, from 696nm to 777nm. During this time the resonance became progressively broader and weaker, and after 84 hours has all but disappeared. If nano-structures of this nature were indeed to be used in as tuneable,

targeted biosensors, it is clear that this resonance shift, and eventual disappearance, would not be ideal. In order to prevent, or at least retard, this process, the rings were capped with ~2 nm of Au, a non-reactive metal which shields the Ag and inhibits oxidation. The same experiment was performed using these Au capped rings, once again the plasmonic activity of the array was taken at several time intervals. Figure 4.17 shows the degradation of the plasmonic resonance's sharpness (a) and peak strength (b) over an 84 hour time frame.

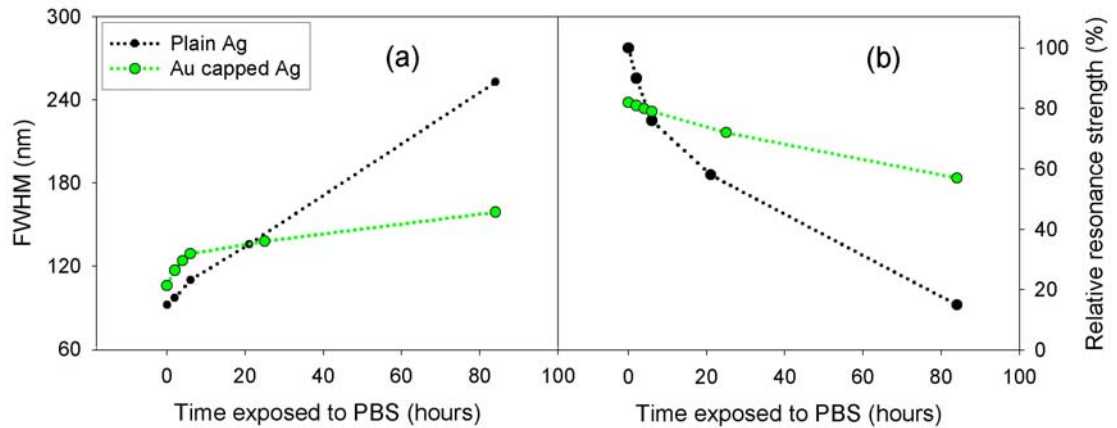


Figure 4.17. Plasmonic degradation of the second order resonance mode of plain Ag structures and Au capped Ag structures. (a) is a plot of each array's FWHM values vs. time, (b) is a plot of the relative strength of the Plasmon peak vs. time (100% being the strength of the plain Ag peak at 0 hours). Although the plain Ag resonance shows a significant drop in strength (decreasing to 15% of the resonance's original value) and an increase in breadth (the FWHM increases from 92nm - 253nm), the Au capped structures remain strong (dropping to 70% of its initial value) and sharp (the FWHM increases from 106nm - 159nm) over the same time frame.

The addition of a Au capping layer significantly retards the plasmonic degradation of the sample when stored in the buffer solution. At 0 hours, the Au capped sample is approximately 80% the strength of the plain Ag ring, whilst having a slightly broader resonance (FWHM of 106 nm compared to 92 nm). However, the Au capped sample retains much of its sharpness and strength over the 84 hour period, whereas the plain Ag sample shows almost no activity after this time. Since the Au layer is so thin, it does not impact significantly on the resonance frequency of the structure ( $N=2$  occurred at 696 nm for both arrays). A red-shift in peak resonance wavelength is once again observed for the Au capped rings, although this shift is not as pronounced as for the plain Ag structures, after 84 hours the peak has shifted 93 nm. It can be concluded that capping of the Ag ring with a Au layer provides significantly improved stability, enabling these devices to function as biosensors for longer periods in ambient, aqueous conditions.

#### 4.5 Conclusion

It has been demonstrated that a homogenous array of Ag split-ring resonators can support multiple, polarisation dependent plasmon resonances in the visible portion of the spectrum. Fabrication by electron-beam lithography provides sufficient control over the ring's

nanometre scale geometry that their multi-modal plasmonic activity can be tuned to separate excitation wavelengths commonly used in both Raman and fluorescence spectroscopy (532 nm, 633 nm and 785 nm).

Two types of multi-functional ring were fabricated, the first with resonances at 532 and 633 nm, the second with resonances at 633 and 785 nm. The use of these structures as multi-wavelength molecular sensors based on SERS has been demonstrated by sensing a monolayer of 2-mercaptopyridine. The separate modes of each ring type have been shown to exhibit a dichroic SERS response, an attribute that allows a single structure to perform dual sensing roles. Each resonance mode has been shown to produce intense, highly isolated electromagnetic fields that in turn yield significant Raman enhancement factors for the molecules situated within ( $\sim 10^5$  in areas of maximum field strength). The ability to create structures with multiple plasmonic characteristics, each of which suit specific applications, provides exciting future opportunities in molecular spectroscopy.

## Chapter 5 - Plasmonic Split-Ring Resonators as Dichroic Nanophotonic DNA Biosensors

### Abstract

In this chapter, specifically tuned, single-geometry split-ring-resonators are demonstrated as highly functional nanophotonic DNA biosensors with targeted dichroic properties. By tuning these nanostructures to exhibit two independently addressable plasmon resonances for SERRS, it is shown that each resonance can be used for tailored, multiplexed biosensing to detect specific DNA sequences from within a mixture of oligonucleotides. The ability to independently excite each engineered plasmon resonance allows the split-rings to act as discriminating sensors, specifically sensing Cy7 and Cy5 labelled target oligonucleotide sequences bound to the sensor surface, modified with complementary probes.

### 5.1 Introduction

The detection of single stranded DNA sequences is one of the fundamentals of biomolecular diagnostics. Complementary strands can be used to “sense” particular DNA sequences, and, to date, a number of nanotechnologies based on the complementary binding of target and probe DNA sequences have been successfully demonstrated.<sup>12, 108-110</sup> Since these molecular recognition events occur on a nanometre length scale, and there may be extremely low numbers of the target sequences present in the sample volume, sensor sensitivity is of paramount importance for their detection. As nanotechnology has progressed, engineered sensors on the same scale as these events (i.e. plasmonic nanoparticles) have allowed extreme levels of sensitivity to be achieved, without the need for time consuming and potentially costly amplification techniques such as polymerase chain reaction (PCR). In concert with advancing micro and nanofluidic delivery techniques, these systems have the potential to enable rapid, low cost sensing of low concentrations of analyte within small sample volumes. Chapter 4 demonstrated that nanophotonic split-ring resonators could be used as dual-wavelength dichroics for molecular detection via SERS. This chapter demonstrates that by tuning the individual resonances of the split-rings to match the electronic absorption wavelengths of different Raman dyes, the structures can act as targeted, multifunctional SERRS biosensors.

As stated in Chapter 1, the SERRS process can compete with fluorescence in terms of sensitivity (e.g. enabling “single” molecule detection).<sup>2</sup> However, unlike fluorescence, SERRS also provides structural information based on the vibrational modes of the molecule’s chemical bonds, allowing a level of multiplexing functionality that cannot be matched by the spectrally broad signatures obtained using fluorescence spectroscopy. SERRS relies on the frequency of both the exciting radiation and the particle plasmon matching the electronic absorption of the analyte. Controlling the number and nature of a nanoparticle’s plasmon resonances, by engineering of the nanostructure’s geometry, is therefore essential for the development of photonic biosensors capable of performing SERRS measurements at a variety of wavelengths. Many nanostructured substrates described in the literature for surface enhanced Raman sensing have used either aggregations of colloidal particulates,<sup>97</sup> or simple engineering of non-complex

geometries such as pillars or discs.<sup>45</sup> However, these approaches can restrict the functionality of the sensor as it is difficult to tune the resonances over a wide spectral range, or, in the case of colloidal aggregates, to a specific, reproducible wavelength. In addition, poor geometric constraint and/or periodicity of the nanoparticles can lead to spectral broadening and diminish resonance Raman scatter from those structures with peak wavelengths shifted from that of the laser. As an alternative to such systems, multi-modal structures which exhibit distinct resonances at different polarisation angles, such as non-symmetrical particles or coupled particle pairs, have been shown to produce multiple high frequency resonances and have the potential to be employed as multi-functional plasmonic biosensors.<sup>45, 58, 65, 70</sup> However, due to the weakness of the resonances in these simple non-symmetrical particles,<sup>65, 70</sup> and the greatly increased plasmonic damping seen in coupled particle pairs,<sup>58</sup> the multiple resonances are not ideal for independent SERRS use.

Since nano split-rings exhibit several, closely packed, polarisation dependent resonances which can be tuned accurately over several microns, these structures are ideal candidates for multi-analyte SERRS biosensors. Strict geometric control over the dimensions of Ag split-ring resonators allows the engineering of the nanostructure's geometry to precisely control both the number and nature of plasmon resonances generated, matching them to the electronic absorptions of already synthesised dye molecules. This allows the SERRS effect (which can provide enhancements several orders of magnitude greater than SERS) to be exploited at two distinct wavelengths for a geometrically defined nanophotonic structure. Not only does this greatly increase the sensitivity of the device over a range of excitation wavelengths when compared to a single resonance structure, but also increases multiplexing capability, as molecules labelled with a variety of existing Raman-active labels can be detected with equal fidelity at appropriate absorption wavelengths. By tuning the devices to have characteristic optical dichroic resonances at 785 and 633 nm, their use as a dichroic switch sensor for multiple-analyte biosensing is demonstrated via SERRS of Cy7 and Cy5 labelled target oligonucleotide sequences bound complementarily to the modified sensor surface. The ability of each of the two resonances to independently sense single DNA sequences from within a mixed population of oligonucleotides is shown, using the polarisation-dependence of the structure's plasmon to create sensory "on" and "off" states at particular wavelengths, providing a unique level of molecular SERRS selectivity.

## 5.2 Materials

All oligonucleotides were purchased from ATD Bio, Southampton. Cy5 NHS (N-hydroxysuccinimide) ester was obtained from Amersham Biosciences, UK (now part of GE Healthcare). Cysteamine was purchased from Sigma Aldrich, UK.

## 5.3 Methods

The nanostructures were designed, written and developed in accordance with the protocol detailed in Section 2.3. Metallisation using the resistive heating evaporator is described in Section 2.3.1.7.

Raman spectroscopy was carried out using the Horiba Jobin Yvon LabRam INV spectrometer in conjunction with a 633 nm and a 785 nm laser source (Section 2.3.8.1).

XPS measurements were performed in Daresbury laboratories. More information on this technique can be found in Section 2.3.6.

### 5.3.1 Modification of sensor with thiolated, Cy5 labelled oligonucleotides and Cy5 N-Hydroxysuccinimide ester

A 17-mer oligonucleotide was attached to a sensor array with a second order resonance at ~ 633 nm (Array N, Chapter 4). The oligonucleotide sequence (2TGCAGATAGATAGCAGT3) was 3' modified with a thiol group and 5' labelled with the cyanine derived Cy5 fluorescent dye.

An identical array was modified with Cy5 N-Hydroxysuccinimide ester according to the procedure in Section 2.3.5.2. Results and discussion relating to this experiment can be found in Section 5.4.1.

### 5.3.2 Hybridisation of fully, partially and non-complementary sequences to probe oligonucleotides immobilised on the sensor

Three identical arrays (of the type matching array N, Chapter 4) were modified with a SAM of 3'-thiolated oligonucleotide (TGCAGATAGATAGCAGT3). Each array was then spotted with one of three 5'-Cy5 labelled strands, one of which was exactly complementary to the sequence attached to the sensor (2CTGCTATCTATCTGCA), one which was a complementary strand differing by one base (2CTGCTTTCTATCTGCA), and one which was a complete mismatch (2CTTACCGATCGTATTC). All hybridisation experiments are described in Section 2.3.5.4, and a schematic of the hybridisation orientation can be seen in Figure 5.1(b). Raman spectroscopy was carried out on both substrates using a 633 nm laser orientated such that it excited the N=2 resonance of the split-rings at  $655 \pm 24$  nm. Results and discussion relating to this experiment can be found in Section 5.4.2.

### 5.3.3 Hybridisation of oligonucleotides with different dye arrangements (Cy5 located at either the 3' or 5' position) to a probe sequence immobilised on the sensor

Two separate arrays of split-rings (identical to array N, Chapter 4) were modified with a SAM of 3'-thiolated oligonucleotide (TGCAGATAGATAGCAGT3). Onto these arrays were spotted one of two complementary sequences, one of which was 5'- modified with Cy5 (2CTGCTATCTATCTGCA), the other of which was 3'- modified with Cy5 (CTGCTATCTATCTGCA3) (the hybridisation orientation of these two strands can be found in Figure 5.1(b) and (c)). Due to the nature of the hybridisation process, the sequence order of the strands dictates that, when bound, the dye on the 5'-modified oligonucleotide will be <1 nm from the sensor surface, whereas the dye on the 3'-modified oligonucleotide will be spaced ~ 6nm from the sensor surface (assuming they are orientated perpendicular to the sensor). Raman spectroscopy was carried out on both substrates using a 633 nm laser orientated such that it excited the N=2 resonance. Fluorescence measurements were also taken using a Zeiss LSM 510 META confocal fluorescence microscope (Section 2.3.7). Results and discussion relating to this experiment can be found in Section 5.4.3.

#### 5.3.4 Competitive hybridisation of labelled and non-labelled oligonucleotides

Five oligonucleotide mixtures were prepared, each containing a different ratio of Cy5 labelled (2CTGCTATCTATCTGCA) to control (CTGCTATCTATCTGCA) sequences (3:1, 1:1, 1:3, 1:9 and 1:19). These mixed populations were then spotted onto five identical sensor surfaces (identical to that of array N, Chapter 4; N=2 at  $655 \pm 24$  nm) that had been modified with a SAM of complementary 3'-thiolated oligonucleotide (TGCAGATAGATAGCAGT3). Since both sequences are complementary to those attached to the sensor surface, the labelled and unlabelled sequences have to compete for a limited number of binding sites on the split-rings. It is assumed that the sequences hybridise to the surface according to their ratios within the sample volume, therefore the percentage of bound strands on each array which contain the Cy5 dye is approximately 75%, 50%, 25%, 10% and 5% for arrays 1, 2, 3, 4 and 5 respectively. Raman spectroscopy was performed at both polarisation states using a 633 nm laser (Section A.1.9). All measurements were performed in triplicate. Results and discussion relating to this experiment can be found in Section 5.4.4.

#### 5.3.5 Hybridisation of Cy7 labelled oligonucleotides to probe strands immobilised on the sensor

An array identical to that of array O, Section 4.4.2, exhibiting second and third order resonances at  $772 \pm 14$  nm and  $631 \pm 3$  nm respectively, was modified with a SAM of 3'-thiolated sequence (TGCAGATAGATAGCAGT3) before being hybridised with a complementary oligonucleotide sequence 5'-labelled with Cy7 (2CTGCTATCTATCTGCA). Raman scattering was collected at both polarisation states using a 785 nm diode laser excitation source (Section 2.3.8.1). Results and discussion relating to this experiment can be found in Section 5.4.5.

#### 5.3.6 Competitive hybridisation of Cy5 and Cy7 labelled oligonucleotides to a probe sequence immobilised on the sensor - 1:1 ratio

An 80 nm radius split ring array identical to that of array O, Section 4.4.2, was modified with a SAM of a 3'-thiolated oligonucleotide sequence (TGCAGATAGATAGCAGT3), at a density which was assumed to be  $\sim 3 \times 10^{13}$  molecules per  $\text{cm}^2$ .<sup>111, 112</sup> An equimolar mixture of two differently labelled complementary sequences (5'-labelled with Cy5 or Cy7) was prepared and hybridised to the sensor. In all assays the total concentration of oligonucleotide was a constant 25  $\mu\text{M}$ . Raman measurements were carried out with a Horiba Jobin Yvon LabRam INV spectrometer using both a 0.5 mW 633 nm HeNe laser and a 9.5 mW 785 nm diode laser (Section 2.3.8.1). Data was collected when the electric field vector of each laser was both parallel (N=3 resonance, 633 nm) and perpendicular (N=2 resonance at 785 nm) to the split in the ring geometry. Results and discussion relating to this experiment can be found in Section 5.4.5.

#### 5.3.7 Competitive hybridisation of different ratios of Cy5: Cy7 labelled oligonucleotides to a probe sequence immobilised on the sensor

Four oligonucleotide mixtures containing different ratios of the two labelled sequences were prepared (these will be referred to in terms of the percentage of Cy5 labelled sequences

that constitute their volume - mixtures contain 75, 50, 25 and 10% Cy5 labelled oligonucleotide). These sample volumes were hybridised against a number of separate arrays modified with complementary strands - such that the mixed populations compete for a limited number of binding sites, leading to each array exhibiting a mixed monolayer with a different dye ratio. Results and discussion relating to this experiment can be found in Section 5.4.5.

## 5.4 Results and Discussion

### 5.4.1 Nano Split-ring resonators as sensors for labelled DNA detection

The tagging of oligonucleotide sequences with fluorescent, Raman active dye labels is a common way to improve the detection and identification of target DNA analytes. As previously stated, the combination of plasmonic surface enhancement with the resonance Raman effect can yield sensitivities to rival those of fluorescence techniques,<sup>2</sup> whilst also providing sharp, molecularly specific bands based that can be used to discriminate between many different dyes/sequences in a mixed population (even if the fluorescence signature of the dyes is identical). In this chapter, the cyanine derived dyes Cy5 and Cy7 are used as tags for the identification of DNA. Although it is possible to detect large quantities of DNA using Raman scattering, the addition of such a tag significantly improves the limit of detection, allowing small numbers of molecules to be sensed and identified. Cy5 and Cy7 were chosen for the following experiments due to their respective absorption wavelengths matching the resonances of the split-ring shown in Figure 4.4 (633 and 785 nm respectively), thus allowing their detection via SERRS.

In order to demonstrate the effective use of nano-split-ring resonators as DNA biosensors, a 17-mer oligonucleotide was attached to an array of Ag split-rings of the design found in array N (Section 5.3.1). Figure 5.1 (a) shows the location of the dye with respect to the sensor when attached to the surface. Also displayed in Figure 5.1 are the dye locations when 5' (b) and 3' (c) labelled complementary strands are hybridised against a 3'-thiol modified oligonucleotide. Only Figure 5.1 (a) is relevant in this section, (b) and (c) relate to experiments performed in Section 5.4.2 - 5.4.5.

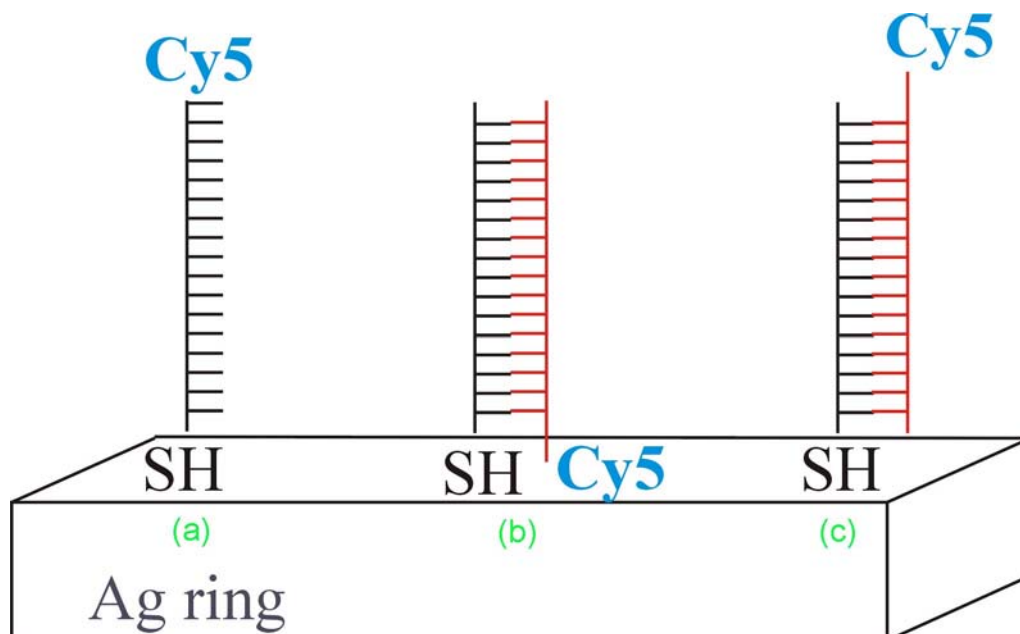


Figure 5.1. Attachment and hybridisation arrangement of Cy5 labelled oligonucleotides. (a) represents sequence A; (b) represents sequences B & C; (c) represents sequences B & F (see Section 2.2 and text below for details). SH represents the thiol group present on the oligonucleotides, enabling their attachment to metal.

XPS measurements (Section 2.3.6) confirm the success of the thiol-reduction/attachment protocol detailed in Section 2.3.5.3 and used here. Figure 5.2 shows high resolution XPS spectra of thiolated DNA attached to plain Au. Comparison of P to N levels on the surface confirms the presence of oligonucleotides, while S confirms attachment by Au-thiol linkage.

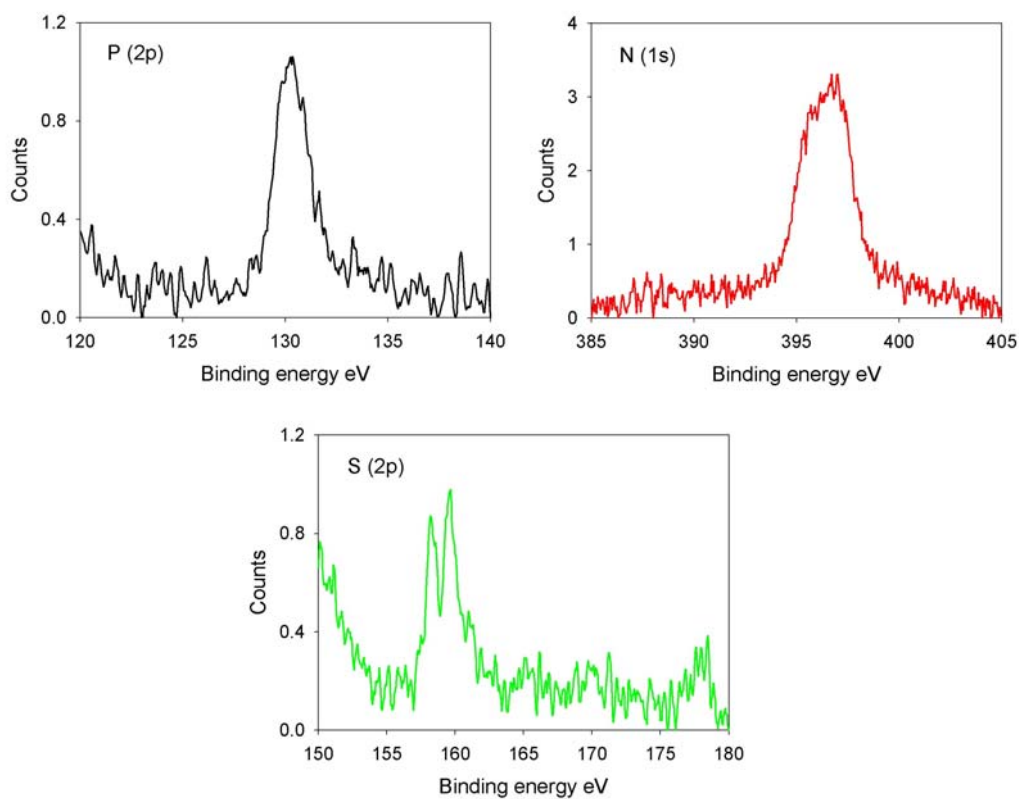


Figure 5.2. High resolution XPS spectra of oligonucleotides attached to metallic surface via thiol linkage. The ratio of P to N in an oligonucleotide strand is approximately 1:4, a ratio present in this spectra. The presence of S confirms the reduction chemistry was successful and that the oligonucleotide is specifically bound to the surface. The use of Au for this experiment is irrelevant, as it is merely to confirm the reduction and attachment protocol of the oligonucleotide.

Figure 5.3 shows Raman spectra obtained using the Horiba Jobin Yvon LabRam INV spectrometer in conjunction with a 0.5 mW 633 nm HeNe laser (Section 2.3.8.1). The excitation laser wavelength and absorption maximum of the Cy5 label (649 nm) were carefully chosen to match the second order resonance of this particular ring geometry ( $655 \pm 24$  nm), factors critical for optimisation of the SERRS effect.<sup>2, 85, 113</sup>

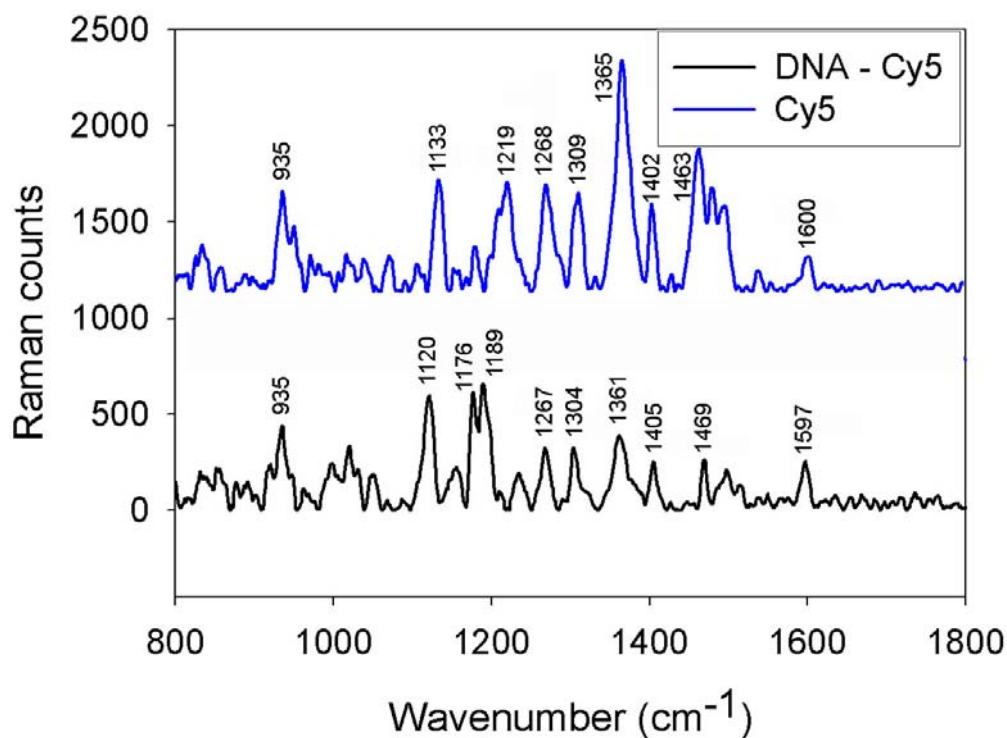


Figure 5.3. Raman spectra of both Cy5 modified DNA and Cy5 dye immobilised on sensor surface. The 633 nm laser line excites the N=2 mode of the ring. The two Raman spectra agree well, exhibiting only slight wavenumber variations, most likely due to the different dye attachment arrangements.

Figure 5.3 shows the Raman scattering from DNA modified array, together with the scattering from an array modified solely with Cy5 dye. Since the wavelength of the laser closely matches the absorption of maximum of the dye, a broadband fluorescence signature is present on the gathered spectra (removed using ACD/Labs software), a feature not observed when sensing 2-mercaptopyridine (Section 4.4). However, the proximity of the dye to the metal surface acts to quench the majority of the fluorescence, allowing the Raman scattered peaks to be easily identified. The spectral bands exhibited by both arrays agree well with each other and those previously reported for Cy5 dye and Cy5 labelled DNA.<sup>114-117</sup> Slight wavenumber variations seen between the corresponding bands of each array are likely due to the different attachment schemes affecting the vibrational modes of the dye. Although labelling DNA with a Raman active probe greatly increases the sensitivity of detection, studies have shown that the DNA bases themselves have the requisite vibrational modes to induce Raman scattering, enabling label-free detection.<sup>118-120</sup> However, these bands are not present in these experiments.

#### 5.4.2 Detection via hybridisation

In practical sensor applications, target sequences are detected when they bind to complementary sequences immobilised on the sensing apparatus, which in this case would be a nanoplasmonic split-ring resonator. Since only the complementary strand will bind, this system can be used to specifically sense one particular DNA sequence from a sample volume which may contain countless others. This is demonstrated in Figure 5.4, which shows SERS spectra collected

from three sequences, one fully complementary to the probe strand, one with a single base pair mismatch and one fully non-complementary.

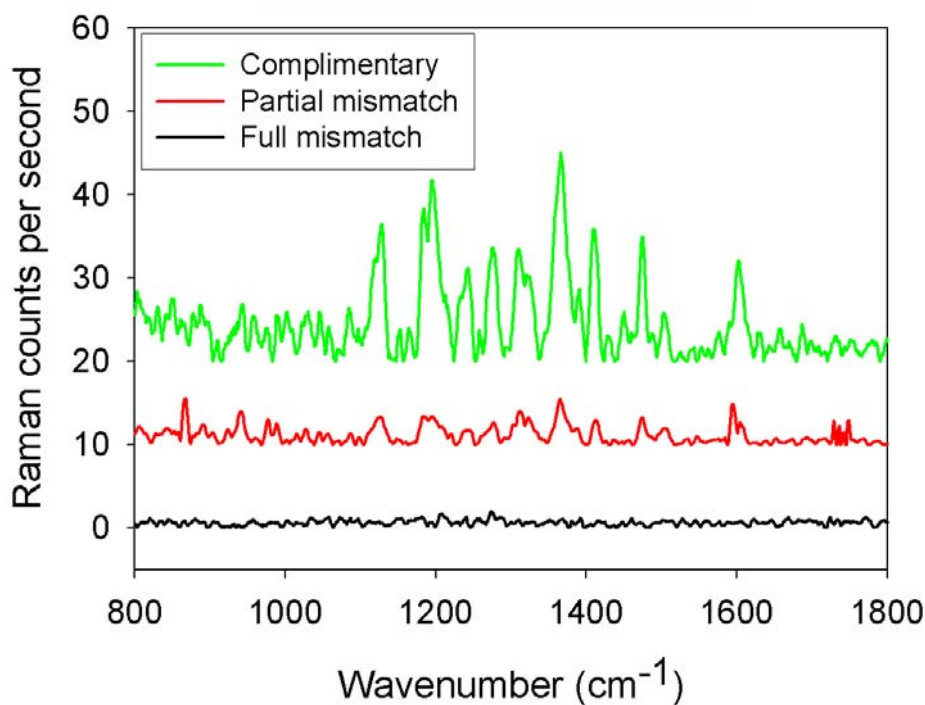


Figure 5.4. SERRS spectra of differently sequenced oligonucleotides hybridising to probe DNA attached to the sensor surface. The complementary sequence exhibits the greatest hybridisation efficiency, producing the strongest Raman signal. A weak signal is displayed by partially mismatched sequence, while the signal from the fully mismatched sequence is indistinguishable from the system noise.

As is clear from Figure 5.4, the perfectly complementary sequence binds strongly to the sequence present sensor surface, resulting in a Raman signature of Cy5. The arrangement of the oligonucleotide sequences ensures that for the complementary sequence the dye is proximal to the metallic surface, maximising the Raman enhanced scattering and minimising background fluorescence. The partially mismatched sequence, differing by one base, exhibits a Cy5 Raman signal ~5x less intense than that of the perfectly complementary strand. The strong band at  $1360\text{cm}^{-1}$ , which is associated with a stretch vibration of the molecule's methane chain, was used as a reference.<sup>114, 116</sup> The base mismatch causes less efficient binding, lowering the number of strands bound to the sensor. No Raman scattering is observed from the array spotted with the completely mismatched sequence, the nature of this sequence dictates that it cannot bind to the modified surface. The lack of any Raman scattering, or indeed any background fluorescence, on the signal from this array proves that levels of non-specific absorption are very low, and any that is occurring does not provide a reading that may be confused with complementary binding.

### 5.4.3 Impact of label proximity to sensor surface

The localised electromagnetic enhancement provided by the resonant plasmon condition of the structures is closely confined to the metallic surface, falling exponentially with respect to distance away from this surface. This effect becomes particularly important for the detection of molecules immobilised onto these nano-structured surfaces, as the length and orientation of the molecule will have a significant effect on the intensity of the Raman scattered signal. In Chapter 4 where 2-mercaptopyridine was used as an analyte, this effect was negligible. The size of the molecule ( $< 1$  nm) suggests that it would be located at the Ag surface, entirely enveloped by the strongest EM field. However, in experiments with DNA, which has a molecular chain length that can range from a few nanometres to several hundred in length, this distance dependence must be taken into consideration.

The oligonucleotide sequences used throughout these experiments have 17 base pairs, corresponding to a length of approximately 5.8 nm. The sequence orders, length and label modifications of the target and probe strands, play a vital role in determining the intensity of the Raman signal, and therefore the sensitivity of the nanosensor. Figure 5.5 shows Raman and fluorescence spectra from an array of split-ring resonators modified with 3' and 5' Cy5 labelled oligonucleotides (Section 5.3.3). Due to the nature of the hybridisation process, the sequence order of the strands dictates that, when bound, the dye on the 5'-modified oligonucleotide will be  $< 1$  nm from the sensor surface, whereas the dye on the 3'-modified oligonucleotide will be spaced  $\sim 6$  nm from the sensor surface (assuming the strands are perpendicular to the surface).

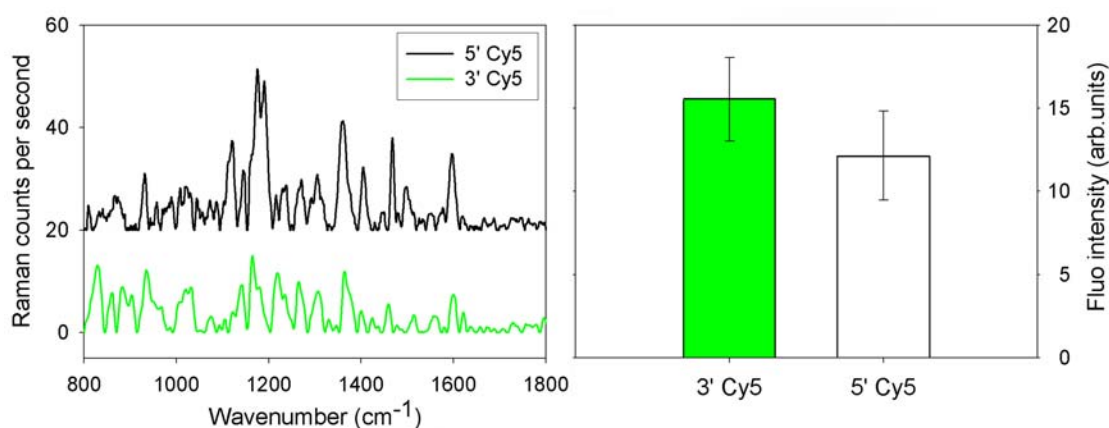


Figure 5.5. Influence of dye position on Raman and fluorescence signal quality. The sequence modified such that when hybridised the dye is spaced proximal to the surface, exhibits approximately twice the Raman scatter (a)-left, and 22% less fluorescence, (b)-right, than the sequence modified such that the dye is spaced several nm away from the surface.

Figure 5.5 highlights how critical it is, from the perspective of SERRS, that target molecules be located as close to the surface of the structure as possible. Molecules in this region experience a stronger EM field, increasing the polarisation around the molecule and therefore increasing their Raman scattering. The localised EM field also acts to quench background fluorescence, making peaks easier to distinguish. The intensity of the Raman band at  $1360\text{cm}^{-1}$  was  $\sim 2\times$  greater for the 5'-modified sequence than it was for the 3'-modified sequence. In

contrast, the fluorescence signal from the 5'-modified sequence was 22% weaker than its 3'-modified counterpart. This highlights the importance of both sequence coding when engineering the probe oligonucleotide, as well as the position of the dye on the target oligonucleotide. In the context of practical, real-world sensing applications, this effect could prove significant. Should a particular target molecule exhibit only weak Raman scattering, the identifying bands may be obscured by the background fluorescence, rendering them unobservable. Therefore, the location of the analyte from the plasmonic sensor surface could be the critical factor in determining whether the molecule is detected or not.

FDTD simulations can be used to gain a better understanding of this effect in the nanostructures studied. Figure 5.6 shows the normalised EM field as a vertical slice through the y-plane of the split in the ring. Close to the surface of the metal, where the dye was located on the short chain spacer between the DNA and the thiol group, the EM enhancement is  $>10$ . At a distance of 5.4 nm, the location of the dye on the long chain spacer, the EM enhancement has more than halved, dropping to  $\sim 4$ .

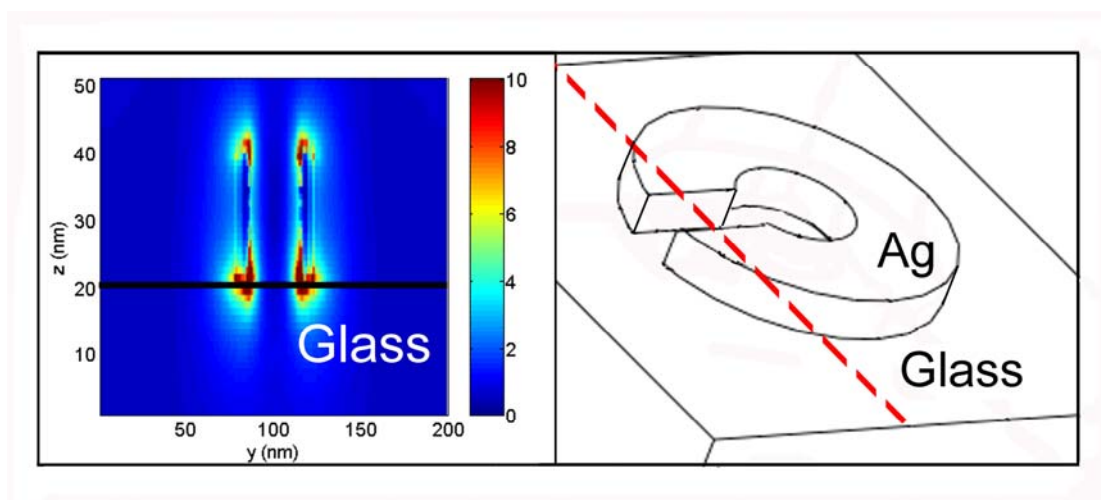


Figure 5.6. FDTD simulation displaying the electromagnetic decay at the surface of the resonant split-ring structure. EM enhancement in the z-plane at  $N=2$  (excited by a 633nm laser), taken as a slice through the split in the ring (dotted line).

#### 5.4.4 Competitive hybridisation assay using labelled and unlabelled sequences

The limit of detection (LOD) for the hybridisation based sensing method can be determined for the array's second order resonance by performing a competitive hybridisation assay using identical labelled and unlabelled target sequences. Five oligonucleotide mixtures, each containing a different ratio of Cy5 labelled to non-labelled sequences were prepared and hybridised against probe strands immobilised on five separate sensor arrays (Section 5.3.4).

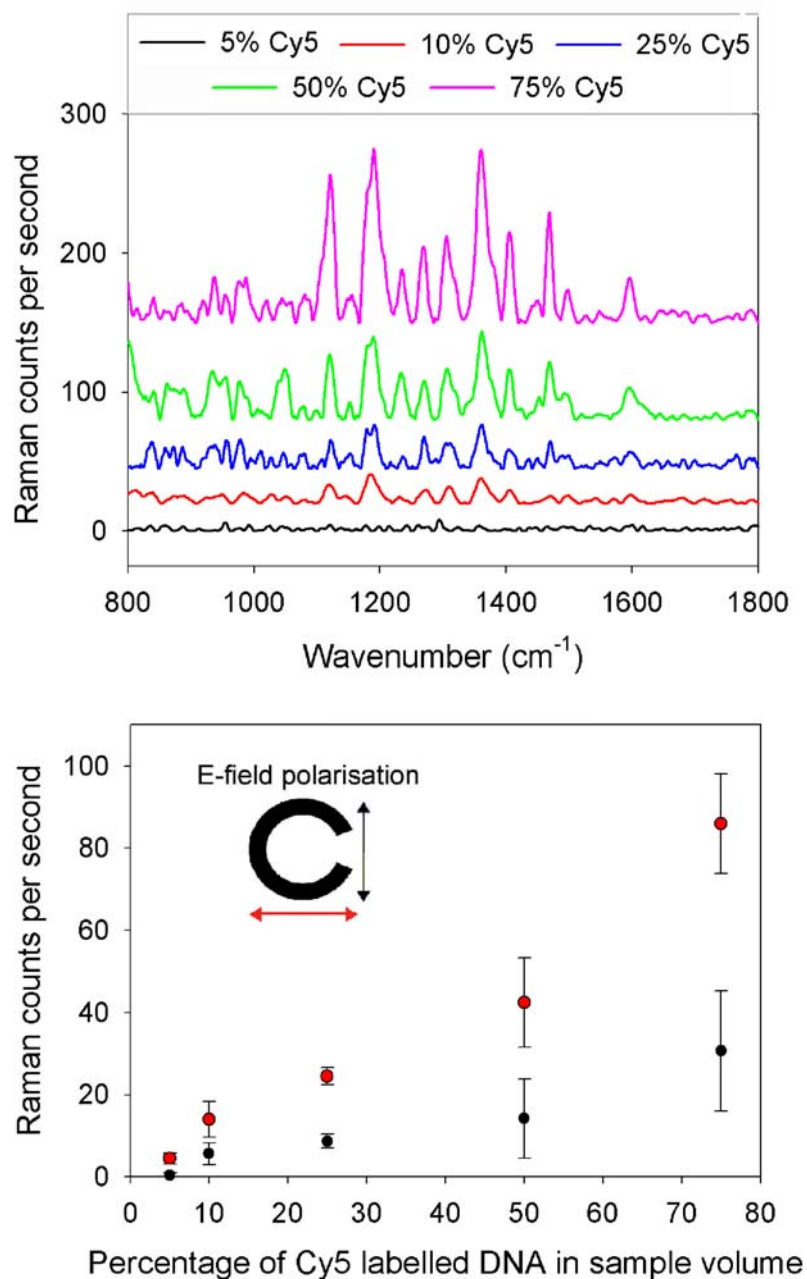


Figure 5.7. Competitive hybridisation of labelled and unlabelled sequences to the sensor surface. A steady decline in the intensity of the  $1360\text{cm}^{-1}$  band was observed at both polarisations (N=2 readings are shown in red, “off-resonance” readings in black). At 5% (200 molecules per ring) the sensor was only effective in its resonant state, the scattering from the “off-resonance” condition is undetectable. Therefore, the sensor acts as a dichroic switch.

Figure 5.7 shows a decline in the Raman signal associated with Cy5 as the percentage of Cy5 labelled sequence decreases in the sample volume. Using the strong band at  $1360\text{cm}^{-1}$  for comparison, the lowest detectable level of labelled DNA was 5% (the signal was defined as a value which was greater than 3 times the standard deviation of the mean of the noise - which in this case is approximately 1 count per second). This figure corresponds to  $\sim 200$  labelled molecules per ring, assuming a surface coverage of  $\sim 3 \times 10^{13}$  molecules per  $\text{cm}^2$  (in accordance with previous studies of thiolated oligonucleotides of approximate length)<sup>111, 112</sup> and a ring area

of  $\sim 1.4 \times 10^{-14} \text{ m}^2$ . Only those rings located under the focused spot of the 633 nm laser contribute toward the Raman signals found in Figure 5.7. Using a 0.75 NA objective lens this spot size will be  $\sim 1.03 \text{ }\mu\text{m}$  in diameter, which, considering an array periodicity of 260 nm, relates to  $\sim 12$  nanostructures. Therefore the limit of detection for this array's second order resonance is approximately 2400 Cy5 labelled oligonucleotides.

No response was seen from the "off resonance" condition at this concentration, demonstrating the sensors use as a dichroic switch. However, the above calculation assumes not only perfect monolayer coverage of the thiolated strand, but also 100% hybridisation of these strands with the mixed sequence population. This of course will not be the case. Although every effort was made to minimise the time from metallisation to thiol attachment, this time spent exposed to oxidising agents will have reduced the number of available binding sites for the thiol-terminated oligonucleotide on the sensor surface. Furthermore, the FDTD simulations shown in Chapters 3 and 4 have shown the localised EM field at resonance to inhabit only a small proportion of the structure's surface, hence only a fraction of the molecule numbers quoted above will actually be contributing to the SERRS signal. Therefore the minimum number of DNA molecules detectable using this method is likely far smaller than the approximate values stated above.

#### 5.4.5 Dichroic plasmonic split-rings as multiple-analyte optical nanosensors

Section 5.4.1 showed that split-ring resonators could be used as effective nanosensors for DNA analyses. It is possible to extend the sensing functionality of these structures by exploiting their multiple resonances, using each one to independently sense a different type of DNA. Section 4.4.2 described a split-ring resonator with second and third order plasmonic resonances at  $772 \pm 14 \text{ nm}$  and  $631 \pm 3 \text{ nm}$  respectively, resonances which encompass the excitation wavelengths of the Raman active dyes Cy7 and Cy5 (excitation maximums at 649 nm and 743 nm). By employing these dyes as oligonucleotide labels, the split-ring resonator array can be utilised as a selective multi-analyte DNA sensor. The dichroic nature of the resonances permits each to be excited separately, allowing each resonance to exclusively sense a particular DNA strand from within a sample volume of mixed population.

Sections 5.4.1 - 5.4.4 detailed the use of the second order resonance of a 75 nm split-ring, at  $655 \pm 24 \text{ nm}$ , to detect Cy5 labelled oligonucleotide strands attached to the sensor surface. Using, instead, the geometry detailed in Section 4.4.2, the second order resonance at  $772 \pm 14 \text{ nm}$  now enables SERRS to be performed using Cy7 labelled oligonucleotides. Cy7 shares much of its molecular structure with Cy5 (Section A.1.13), yet possesses a unique vibrational spectra that makes it easily identifiable.

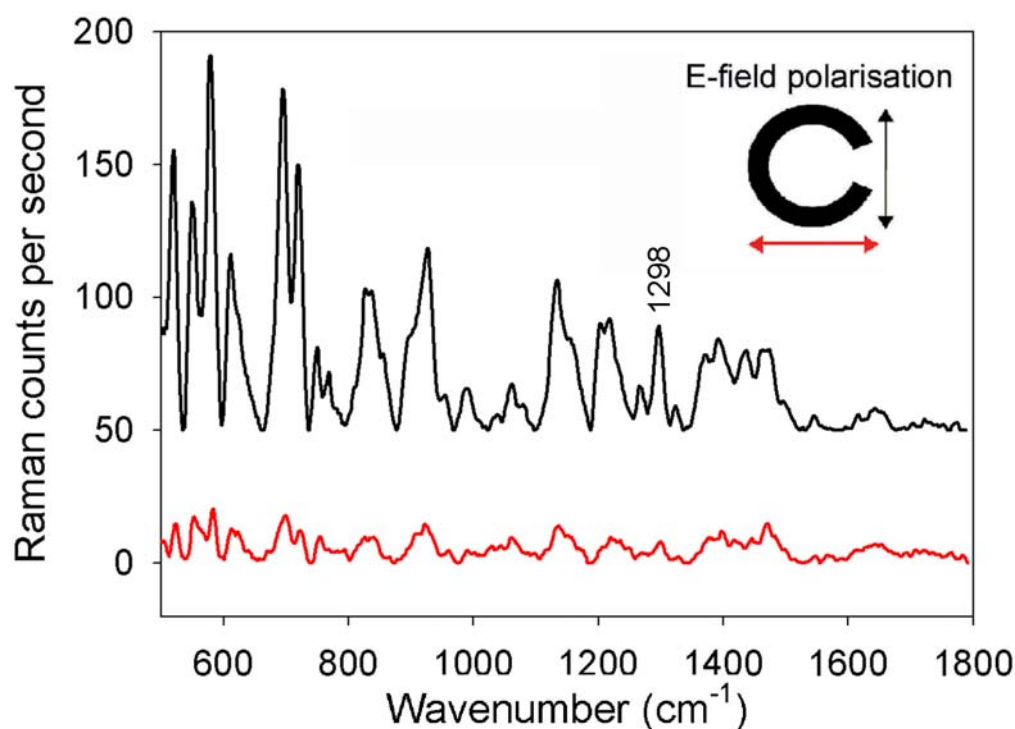


Figure 5.8. Raman spectra of a Cy7 modified oligonucleotide hybridised to the sensor. The second order resonance mode provides 5x greater scattering than the “off-resonance” condition.

Figure 5.8 shows Raman spectra from a Cy7 labelled oligonucleotide hybridised to the sensor surface (Section 5.3.5). The measured Raman spectra agrees with those previously reported for Cy7.<sup>114, 121</sup> As was the case in Section 5.4.4, the Raman scattering observed when exciting the N=2 resonance is significantly greater (~5x, using the band at 1298cm<sup>-1</sup> as a reference - a band related to the molecule’s methine chain motion<sup>114</sup>) than when the sensor is orientated in the “off-resonance” position.

It has been demonstrated in Chapter 4 that structures of this kind have the capability to act as sensors at two separate wavelengths (Section 4.4.5.1). Using SERRS, this functionality can be applied in order to engineer a sensor capable of discriminating between different molecules attached to the surface. The inherent dichroism of the resonances allows them to exhibit “on” and “off” sensing states dependent on the sensor’s orientation with respect to the polarised laser beam. This feature would not be possible using traditional plasmonic sensor arrays comprising of symmetrical nanostructures that exhibit a single resonance irrespective of excitation polarisation.

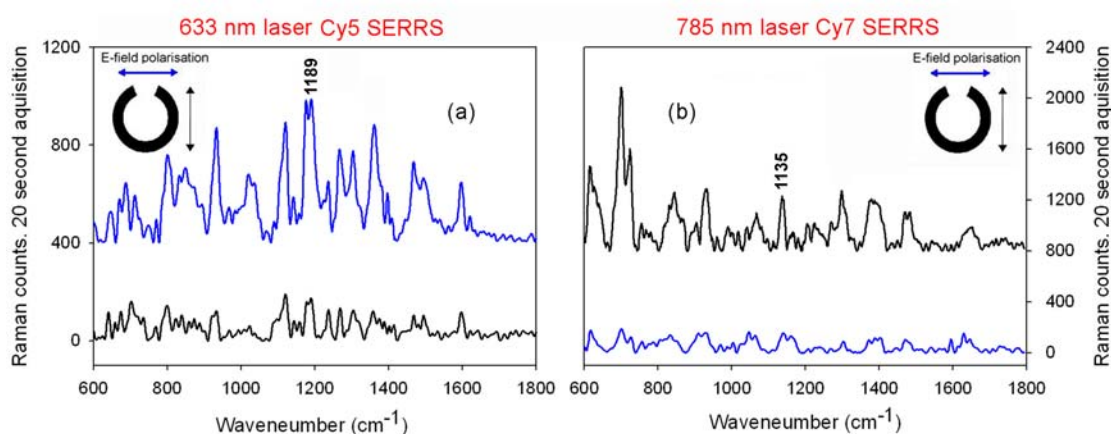


Figure 5.9. Raman scattering from single array modified with sequences of Cy5 and Cy7 labelled oligonucleotide sequences hybridised to thiolated oligonucleotide strand (detailed in the text). Spectra were collected using a 633 nm laser (a) (exciting N=3) and a 785 nm laser (b) (exciting N=2) for the electric field polarised both parallel and perpendicular to the split in the ring geometry. SERRS dominates both graphs, (a) shows scattering from the Cy5 dye labelled sequence, whereas (b) shows scattering from the Cy7 dye labelled sequence. The Raman scattering intensity of each dye is far greater when the ring is in a resonant condition compared to when the electromagnetic field is polarised in the ‘off’ direction (4 times greater at N=3 and 6 times greater at N=2).

Figure 5.9 shows Raman spectra collected from a sensor modified with 50:50 Cy5: Cy7 oligonucleotide strands (Section 5.3.6) Although similar in structure, the SERRS spectra of Cy5 and Cy7 possess enough unique vibrational bands to allow easy identification of either dye. The spectral bands used here for identification were  $1189\text{ cm}^{-1}$  for Cy5 and  $1135\text{ cm}^{-1}$  for Cy7, in accordance with previous studies of Raman scattering from cyanine dyes.<sup>114-116</sup> Figure 5.9 shows that the resonance Raman signal dominates at either wavelength. Using a 633 nm excitation source scattering was collected from the Cy5 labelled sequence, whereas scattering from the Cy7 labelled DNA was collected using a 785 nm excitation source.

A strong signal is observed for both resonances when the exciting laser light is polarised in the correct direction (parallel to the split for N=3, perpendicular to the split for N=2). Rotating either device through 90 degrees resulted in a significant drop in signal strength (~ 4x for N=3, ~ 6x for N=2) due to the disappearance of the plasmonic resonances at these polarisations. Note that in their ‘‘off’’ resonance states, the structures still provide some enhancement (seen in the very weak signals of Figure 5.9) due either to the lightning rod effect from the structure’s areas of high curvature,<sup>53, 54</sup> or to contributions from chemical enhancement (charge transfer) effects.<sup>88, 89</sup>

The presence of strong, independent plasmonic resonances at N=2 and N=3 becomes particularly important as the quantity of the target molecule is reduced. Figure 5.10 shows the Raman peak intensity of the  $1189\text{ cm}^{-1}$  band of Cy5 and the  $1135\text{ cm}^{-1}$  band of Cy7 on four separate sensor arrays, each modified with a different ratio of Cy5: Cy7 labelled oligonucleotide (Section 5.3.7).

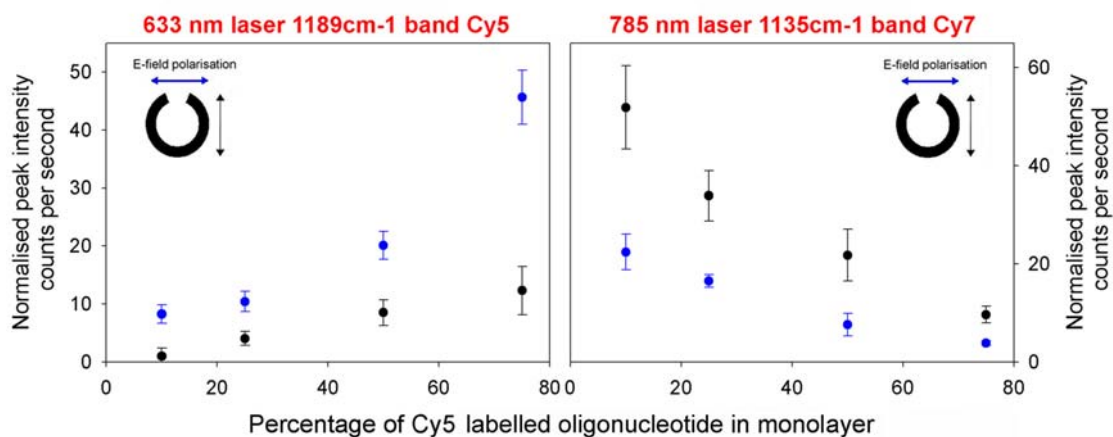


Figure 5.10. Raman spectra collected from arrays of Ag split-rings modified with varying ratios of the two sequences: Excitation was at 633 nm and 785 nm for both polarisations. The resonance Raman signals dominate at each wavelength, so that for the concentrations stated above, only Cy5 is detected at 633 nm and only Cy7 at 785 nm. The limit of detection for N=3 was 10% Cy5 coverage, and for N=2 was 25 % Cy7 coverage.

As the percentage of the Cy5 labelled sequence increased, the intensity of the Raman scattered Cy5 signal from the N=3 resonance also increased, whilst, when exciting the N=2 resonance at 785nm, the Raman scattered Cy7 signal decreased. Consistent with the observations made in Figure 5.9, the Raman scattered bands collected in the “off-resonance” condition (black data points, Fig.5.10), are less intense but exhibit a similar intensity trend with changing monolayer population.

As the relative concentration of either labelled sequence lowered, the Raman signal from the “off-resonance” condition start to become indistinguishable from the noise, whilst the resonant states continue to display an observable signal, demonstrating the structure is acting as a dichroic switch, sensing a particular analyte at one polarisation but not another, irrespective of laser excitation wavelength. Importantly, this demonstrated that the engineered resonances of the nanostructure dictate the sequence that is detected, and that changing the excitation wavelength alone is not enough to induce a SERRS response from a different sequence, maintaining molecular selectivity.

The minimum detectable DNA levels achieved were 10% Cy5 (in the assay) for the N=3 mode at 633 nm, and 25% Cy7 coverage for the N=2 mode at 785 nm, which corresponds to limits of detection of approximately 5760 Cy5 labelled and 22800 Cy7 labelled molecules (considering the number of structures present in the focused laser spots and assuming a surface coverage of  $\sim 3 \times 10^{13}$  molecules/cm<sup>2</sup>).<sup>111, 112</sup> However, as stated in Section 5.2.4, FDTD studies have shown the localised EM field at resonance to inhabit only a small proportion of the structure’s surface, hence only a fraction of the molecule numbers quoted above will actually be contributing to the SERRS signal.

It was noted that the limit of detection was lower at the N=3 resonance than the N=2 resonance, despite the fact the N=2 resonance was stronger, Figure 4.4. This is explained, not by the magnitude of the resonance itself, but by the fact that efficiency of Raman scatter is

related to the wavelength of the exciting light by  $1/\lambda^4$  (i.e. the lower the exciting laser wavelength, the greater the Raman scattering). Thus at 633 nm the response would be expected to be ~2.4 times greater than the scattering from the 785 nm laser, allowing lower concentrations of the Cy5 labelled DNA to be detected with SERRS than the Cy7 labelled DNA.

## 5.5 Conclusion

In conclusion, it has been demonstrated that a homogeneous array of single-geometry nanophotonic particles can act as plasmonic sensors for DNA analyses. Exploiting the dichroic character of the split-ring resonances allows the engineering of a discriminating SERRS substrate for the detection of two differently labelled DNA strands at two separate plasmonic wavelengths. The polarisation dependence of the ring's plasmon allows two closely spaced, distinct resonances, each exhibiting a narrow spectral range, to be used independently for bio-molecular sensing. This allows for a strict level of molecular SERRS selectivity previously unseen in single geometry, homogeneous nanoparticle arrays. The importance that the exciting radiation's polarisation state, and hence the engineered plasmonic resonance, has on the sensing functionality of the rings has been illustrated, providing a dichroic sensor switch between two target analytes in a mixed population.

## Chapter 6 - Future Work

### Abstract

The future direction of the research presented in Chapters 3-5 is discussed. Progress made toward these future goals throughout the course of the PhD research period is also presented.

### 6.1 Introduction

This thesis shows that nano-metallic split-ring resonators have multiple, tuneable plasmon resonances and can be employed as low concentration, multiple analyte biosensors. Through further refinement of geometric considerations it may be possible to generate larger localised electric fields as a consequence of plasmon activity, thus increasing device sensitivity. Furthermore, integrating sensors of this type into micro and nanofluidic membrane platforms opens the possibility of creating flow-through sensors capable of sensitive, real-time molecular detection. As such, there is considerable scope for this research to be taken forward, with improvements in both sensitivity and functionality possible. This chapter will briefly discuss the work completed to date towards such goals, and describe how this research could be pushed forward in the future.

### 6.2 Materials

4-inch diameter silicon wafers coated on either side with approximately 200 nm of silicon nitride were obtained from the Scottish Microelectronics Centre at the University of Edinburgh.

### 6.3 Methods

#### 6.3.1 Fabrication of nanoporous membrane aligned a plasmonic split-ring resonator array

Au split rings of 240 nm radius were fabricated on a silicon nitride - silicon - silicon nitride wafer according to the procedure described in Section 2.3. Using alignment markers defined during the first lithography step, a 120 nm diameter circle was patterned in UVIII resist in the centre of each ring in the array. The resist acted as a dry etch mask for the fabrication of the pores through the thin silicon nitride layer (Section 2.3.2).

Optical lithography was used to define 1.7 mm squares in the backside of the wafer. Using the resist as a mask the silicon nitride inside these squares was removed by dry etch. KOH wet etch was used to remove the silicon in those areas, leaving a free standing silicon nitride membrane. A full description of this process can be found in Section 2.3.2.

The two component sections of the device (the first being a free standing  $\text{Si}_3\text{N}_4$  membrane, the second an array of nanopores aligned to Au split-ring resonators) were fabricated separately but not combined, due to time restraints and fabrication challenges. Results and discussion relating to this device can be found in Section 6.4.1.

### 6.3.2 Fabrication of a 60 nm radius Au split-ring resonator array

An exposure test containing several split ring geometries designed with a radius of less than 60 nm was performed in accordance with the procedure detailed in Section 2.3. Following examination by SEM, an array containing elements designed with a radius of 50 nm, a wall width of 12 nm and an arc length of 240 nm was exposed using an electron beam dose of  $986 \mu\text{C} / \text{cm}^{-1}$ . Once developed and metallised the geometry of the structures had a radius of 60 nm, a wall width of 40 nm and an arc length of approximately 265 nm. Results and discussion relating to this array can be found in Section 6.4.2.

### 6.3.3 Fabrication of an 80 nm radius Au split-ring resonator array with split sizes of 2-3 nm

An exposure test containing several split ring geometries designed with split sizes of less than 20 nm was performed in accordance with the procedure detailed in Section 2.3. Following examination by SEM, an array containing elements designed with a radius of 65 nm, a wall width of 12 nm and a split size of 16 nm was exposed using an electron beam dose of  $2009 \mu\text{C} / \text{cm}^{-1}$ . Once developed and metallised the geometry of the structures had a radius of 80 nm, a wall width of 50 nm and a split size of approximately 2-3 nm. Results and discussion relating to this array can be found in Section 6.4.2.

## 6.4 Results and discussion

### 6.4.1 Nanofluidic delivery system for real-time molecular detection

Nanofluidics refers to the confinement and/or manipulation of fluids on a nanometre scale. Wide-ranging techniques based on these principals are gaining momentum in the field of bio-technological research as they allow exceptionally small sample volumes to be probed and have been used for the label-free isolation and detection single DNA strands<sup>122-124</sup>. This section describes the design and fabrication of a nanofluidic device that incorporates the sensing technology described in the previous chapters. Although fabricated, this device has not been tested in a fluidic or sensing capacity.

It has been demonstrated that the areas of localised field enhancement generated as a consequence of LSPR in nano split-ring resonators can be located and quantified using FDTD software. With this in mind, it may be possible to specifically introduce molecules into these areas, and these areas only, through the use of nano-fluidics. Nano-pores positioned directly beneath the ring cavity (or any area exhibiting an enhanced e-field, such as between the split when the first resonance mode condition is satisfied) would allow molecules to pass directly through these areas. As the molecules enter these regions their polarisability will be sufficiently increased to enable a Raman scattered signal to be briefly detected. Monitoring individual pores in this fashion would allow real-time detection and characterisation of molecules within low concentration sample volumes, without the need for prior labelling (as would be the case if molecules were to be detected via fluorescence signals), as they pass through the nanofluidic system.

Such a device requires that both the plasmonic nanostructures and the pores be fabricated on a suspended membrane. The molecular solution would approach the back-side of this membrane and could be transported through the pores by capillary forces, a pressure

difference, or electro-osmosis, while the topside, inhabited by the nanoparticle array, is probed using Raman spectroscopy.

The area of the  $\text{Si}_3\text{N}_4$  membrane was  $\sim 1\text{mm}^2$ , making the devices exceedingly fragile and prone to shattering. Should these devices be used in fluidic applications it is clear that this area would have to be made considerably smaller, increasing the stability of the membrane. This fragility may also dictate the order of the final fabrication procedure, as it is unlikely to survive the processing steps required to pattern the nano features on the wafer's topside (particularly the resist spinning).

Figure 6.1 shows high resolution SEMs of the wafer's top-side, detailing the feature sizes involved and the excellent lithographic alignment afforded by the Vistec VB6 e-beam tool.

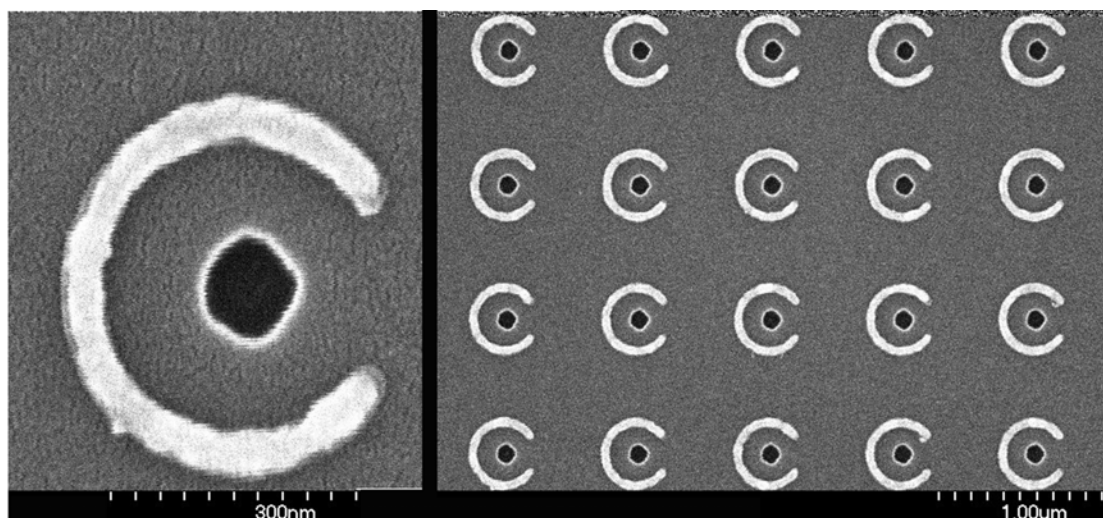


Figure 6.1. High resolution SEMs of engineered nanoporous  $\text{Si}_3\text{N}_4$  etched through the centre of Au splitting structures. Ring radius is  $\sim 240$  nm, pore radius is  $\sim 80$  nm. The membrane is  $\sim 1\text{mm}^2$  and 200 nm thick.

As Figure 6.1 shows, pores have been etched through the centre of each and every ring in the 1 mm square array. The rings used in this device, at 240 nm radius, were larger than those seen in the previous chapters, in order to give the greatest margin of error when performing the first e-beam alignment experiments. The pores have a radius of 80 nm and a depth of 200 nm (the thickness of the  $\text{Si}_3\text{N}_4$ ). In this instance the dimension of the pores and rings, as well as their relative positioning, is for proof of concept only, and if required the size of these features could be significantly reduced.

Figure 6.2 shows a picture of the patterning on the wafer's backside before the KOH wet-etch. Once etched, the area of the  $\text{Si}_3\text{N}_4$  membrane was  $\sim 1\text{mm}^2$ , making the devices exceedingly fragile and prone to shattering. Should these devices be used in fluidic applications it is clear that this area would have to be made considerably smaller, increasing the stability of the membrane. This fragility may also dictate the order of the final fabrication procedure, as it is unlikely to survive the processing steps required to pattern the nano features on the wafer's topside (particularly the resist spinning).

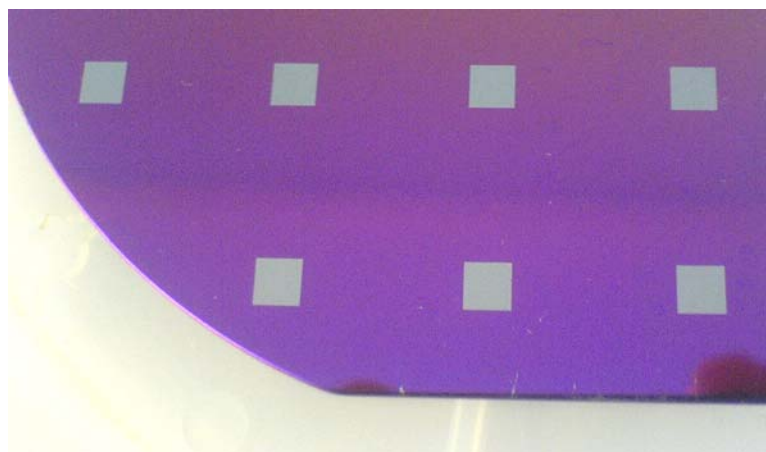


Figure 6.2. Backside wafer patterning before the KOH wet-etch step. Windows created in the silicon nitride by the  $\text{CHF}_3$  dry-etch process, expose the underlying Si in preparation for selective wet-etching.

This system need not only apply to split-ring structures, indeed it may prove more feasible to use other geometries or groups of particles capable of producing higher field enhancements. However, the ability to specifically flow atto-litre solutions to the most efficient areas of a plasmonic nanostructure would provide exciting opportunities for real-time single molecule detection.

#### 6.4.2 Reducing feature size for greater sensitivity

It was demonstrated in Sections 3.4.1 and 3.4.3 that the most intense field enhancements displayed by the split-rings occur between the split itself when the first order resonance condition is satisfied. Unfortunately, for the ring dimensions explored in Chapters 3 and 4, this  $N=1$  mode does not occur in the biologically relevant, visible spectrum. One solution to this problem, as demonstrated in Section 3.4.2, would be to significantly reduce the radius of the rings whilst preserving a large arc length relative to this radius. A large arc length, and hence a small gap, produces higher quality resonances, and, crucially, provides the level of asymmetry necessary to generate the particle's plasmonic dichroism.

The smallest rings successfully produced had a radius of  $\sim 60$  nm, but did not have their plasmonic properties tested, Figure 6.3. However, from the trends exhibited in Chapters 3 and 4, it is unlikely that this radius would be sufficient to produce a large arc-length structure with a first order resonance mode below 800 nm. Although problematic, it may be possible to further decrease the size of these structures through more rigorous investigation of ring CAD, e-beam dose, development technique and resist material.

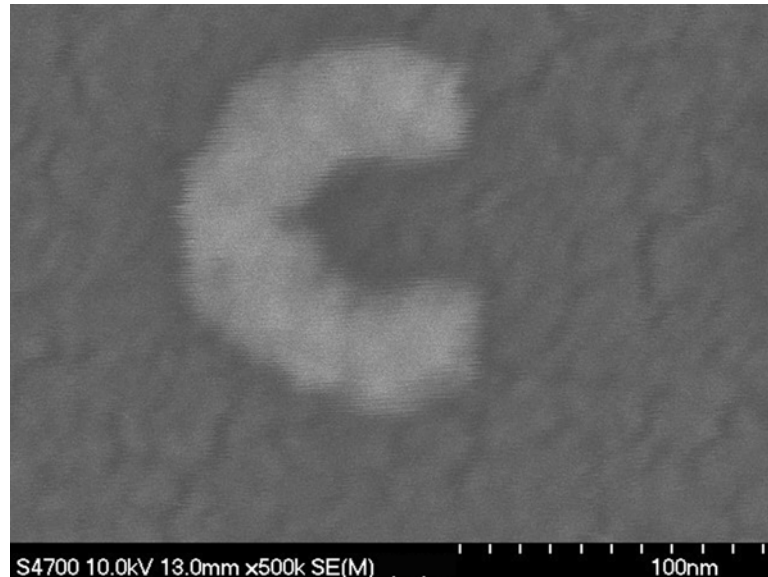


Figure 6.3. SEM of 60 nm radius split-ring. Ring has a radius of 60 nm and a wall width of 40 nm, demonstrating that it is possible to produce feature sizes smaller than those demonstrated in the previous chapters.

Disregarding, for a moment, the need for a plasmonic dichroism, altering the ring's basic geometry may yield higher field enhancements than have thus far been achieved. Fabricating a ring structure containing multiple splits, each no more than a nanometre large, should allow the generation of the extraordinarily high fields, similar to those seen in coupled particles<sup>61, 62</sup>. The Vistec VB6 e-beam tool has shown that it is capable of patterning features with gaps on this scale, Figure 6.4. Although exhibiting only a single split, the size of this split is ~2-3 nm, illustrating the potential of the tool for controllably patterning structures packed extremely close together (Section 6.3.3).

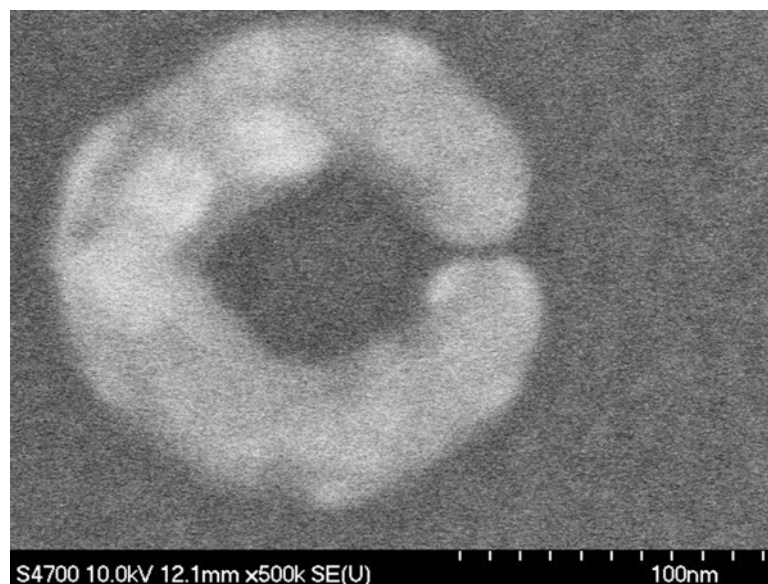


Figure 6.4. SEM of 80 nm radius split ring with ~2-3 nm gap size. Although nanometre sized gaps are possible, fabricating features of this size leads to higher levels of array irregularities than have previously been seen.

However, fabrication of features this small can significantly affect the reproducibility of the rings throughout the array. It was seen in Chapters 3 and 4 that the geometric variation from ring to ring is on the order of  $\pm 2-4$  nm. In the case of the ring displayed in Figure 6.4, this slight variation can lead to the gap in the ring disappearing in a significant proportion of the fabricated structures (approximately 20% of the rings examined by SEM had no split in their geometry).

Another method which may generate higher localised fields whilst retaining the ring's inherent tuneability and multiple plasmon mode generation are rings with more than one split in their geometry. It has been shown that resonances of single split-rings can be tuned over several microns by altering their radius (Section 3.4.2), and the same should be true for rings with multiple splits. Using the e-beam tool to fabricate large arrays of tuned plasmonic particles, electromagnetically coupled due to their nanometre proximity, would give this system a distinct advantage over other plasmonic systems which rely on coupled nanoparticles (a greater degree of field control, in terms of location, strength and reproducibility, than is offered by aggregated colloid, and a larger range of tuneable wavelengths than is possible using coupled particle pairs).

## 6.5 Conclusion

It has been shown that several stages of electron beam lithography can be used to align individual plasmonic split-rings with nanopores on a silicon nitride substrate. It has also been shown that these nanoporous regions can be aligned to etch windows on the backside of the wafer. Although the component parts of the device were fabricated separately and a stable membrane was never achieved, a smaller etch window (which would produce a smaller membrane) and more careful processing and etch steps (to minimise damage of the silicon nitride in the areas that will become the membrane) should enable the complete device to be realised.

Separately, it has been demonstrated that the dimensions of the nano rings can be made smaller than those seen in Chapters 3-5. Moving to a smaller radius, as well as introducing more than one split into the geometry, may enable the generation of first order modes in the visible spectrum. As was demonstrated in Chapter 3, this would allow significantly larger field to be generated and enable a higher degree of sensitivity. As well as applications in biosensing, these smaller structures may prove significant in generating visible wavelength metamaterials.

## Appendix

### A.1 Supplementary device and process information

#### A.1.1 Electron beam lithography using the Vistec VB6 UHR EWF

##### A.1.1.1 Electron beam lithography

In the context of micro and nano fabrication, the term lithography refers to patterning a substrate material with geometries with dimensions on the order of micrometers (micro-fabrication) or nanometers (nano-fabrication). An organic resist material, sensitive to electromagnetic radiation or charged particles, is used to facilitate this pattern transfer. Once exposed, unwanted resist can be removed by chemical development while the desired pattern remains. The patterned resist can then be used as a mask for metallisation or etching of the substrate material.

Electron beam lithography tools use a focused beam of electrons to write a pattern in a charge sensitive resist material. Although photolithography is of more widespread industrial use due to its speed and low cost, electron beam lithography is capable of patterning much smaller features (<10 nm vs. >100 nm). Compared to light, electrons have considerably shorter wavelengths ( $\sim 10^{-12}$  nm), easily surpassing the diffraction limit of light. Beam widths of the order of nanometres are routine, allowing for feature sizes of less than 10nm to be patterned. Unlike optical lithographic methods, which use a patterned mask to selectively transmit light onto a photosensitive resist, electron beam is a direct-write, serial process. Most high-resolution electron beam tools use a writing method known as vector scanning. In this process, the focused electron beam forms a Gaussian profile that scans the substrate surface, writing geometries pre-determined by the user in a computer aided design (CAD) package. This method of direct writing, where each pixel is exposed one-by-one, can be time consuming and therefore costly, especially if a large area is to be written. Electron beam tools based on raster scanning are also available. These tools constantly scan the beam over the substrate, in a similar fashion to a scanning electron microscope (SEM), using a shutter to block and unblock the beam in the areas required to generate a desired pattern. Although faster, this process suffers from poor resolution and shape definition when compared with vector scan tools.

The level of charge per unit area required to fully expose the resist is referred to as the exposure dose and is measured in  $\mu\text{C} / \text{cm}^2$ . When the electrons enter the resist, they do not distribute themselves in an even manner. Scattering of electrons within the resist can significantly alter the exposure levels, as well as the area of resist exposed, so must be taken into consideration when fabricating with electron beam tools. Both forward scattering and back scattering can occur, terms relating to scattering angles of <90 degrees and >90 degrees respectively. Both processes can result in electrons travelling laterally through the resist, exposing unwanted areas. This effect dictates that line widths and feature sizes are not simply defined by the beam spot-size, and in fact the ultimate size of the final features will be larger than the written pattern. Scatter induced over-exposure can become particularly problematic when writing high-density patterns. Scattered electrons from one feature can encroach on the area of a previously written feature. This so called "proximity effect" can lead to a distortion of

closely packed structures. The unwanted effects of electron scattering can be countered by using a higher beam energy and thinner resist layers, both of which minimize the possibility of excessive scatter.

To avoid excessive build up of surface charge when writing on non-conducting substrates, such as glass, a thin conduction layer must be placed either above or below the resist material. Failure to use such a layer can lead to unwanted exposure levels and erratic patterning due to repulsive interaction with the incident beam. This layer typically consists of a few tens of nanometres of metal (Al and NiCr are common because they can easily be removed after exposure) and allows the unwanted charge to dissipate.

#### A.1.1.2 Vistec VB6 UHR EWF tool

The electron beam lithography tool used throughout this research was the Vistec VB6 UHR EWF located in the James Watt Nanofabrication Centre. This tool is capable of a minimum spot size of approximately 4nm, a writing speed of 50MHz, a stitch accuracy of 15nm, and can write fields of 1.2mm at 100kV operation. The patterns written by the beam are determined using CAD software and subsequently “fractured” into a series of trapezoids. The beam-writer exposes these trapezoids in a pixel-by-pixel fashion, with the dimensions of each pixel being determined by the beam spot size (the minimum being 4 nm). The beam step size (BSS) is the distance between each pixel and is determined by Equation 2.1, and can be altered by changing the resolution of the trapezoidal fracture and/or the variable resolution factor (VRU), a multiple of the resolution.

$$BSS = Resolution \times VRU \quad (A.1)$$

For cases where alignment of one lithographic layer to another is required, the tool scans over a user-defined area, searching for the metallic markers by monitoring changes in reflection from the substrate. Two stages of alignment take place, each correcting for position and rotation of the sample. The first stage of alignment (specified as “global alignment” by the software) alignment takes place once and uses a set of four larger squares (20 μm) spaced several hundred microns from the pattern. The second alignment stage (specified as “cell alignment” by the software) uses a group of far smaller markers (6 μm) located close to the pattern’s centre, and may be performed several times, typically once for the exposure of every new pattern. The use of these two marker sets allows multi-level alignment of 10 nm or better.

#### A.1.1.3 Electron beam resist

Resists used for electron beam patterning are polymer-based materials and come in two types; positive tone resists and negative tone. The resist responds to charged particles in one of two ways, becoming either more soluble (positive tone) or less soluble (negative tone) to chemical developer after electron beam exposure. In positive tone resist the electrons are of high enough energy to break the bonds in the polymer chains, creating lower molecular weight molecules that are quicker to solvate than the longer chain polymers. In negative tone resist the electrons

promote cross linkage of the polymer chains, resulting in higher molecular weight molecules that are less soluble in developer than the surrounding, un-exposed resist.

### A.1.2 Metal Evaporation

Metallisation was carried out using two separate evaporators. Sections A.1.2.1 and A.1.2.2 detail the operation of these systems.

#### A.1.2.1 Plassys MEB 400S electron-beam evaporator

The main evaporator used throughout the research for gold, titanium and aluminium evaporation was the Plassys MEB 400S electron-beam evaporator. The system operates by directing a high-energy electron beam into a crucible containing the target metal, which heats up to the point of evaporating and travels upward toward the sample. Figure A.9 shows a schematic of the system. The sample chamber is evacuated to  $\sim 10^{-6}$  Torr in turn by a rotary (low vacuum) and cryogenic pump (high vacuum). A high vacuum is required to maximise the mean free path of the particles, ensuring the metal vapour's path to the sample is unobstructed, and also helps minimise contaminant formation on the freshly evaporated layer (crucial if multiple layers are to be deposited in a single run). The sample is located approximately 30 cm from the crucible on a rotating holder, ensuring even vapour coverage. The 10kW beam source is located underneath the crucible and is directed toward its target magnetically. Before deposition begins, the metal must reach a steady evaporation rate of  $0.30 \text{ nm s}^{-1}$ . The rate is monitored using an oscillating quartz crystal device. During this period a shutter masks the sample from unwanted deposition. Once a steady evaporation rate has been reached the shutter is removed, exposing the sample to the metal vapour. Beam current, evaporation rate, deposition thickness and shutter timings are all software controlled, ensuring repeatable layer thicknesses from one run to the next.

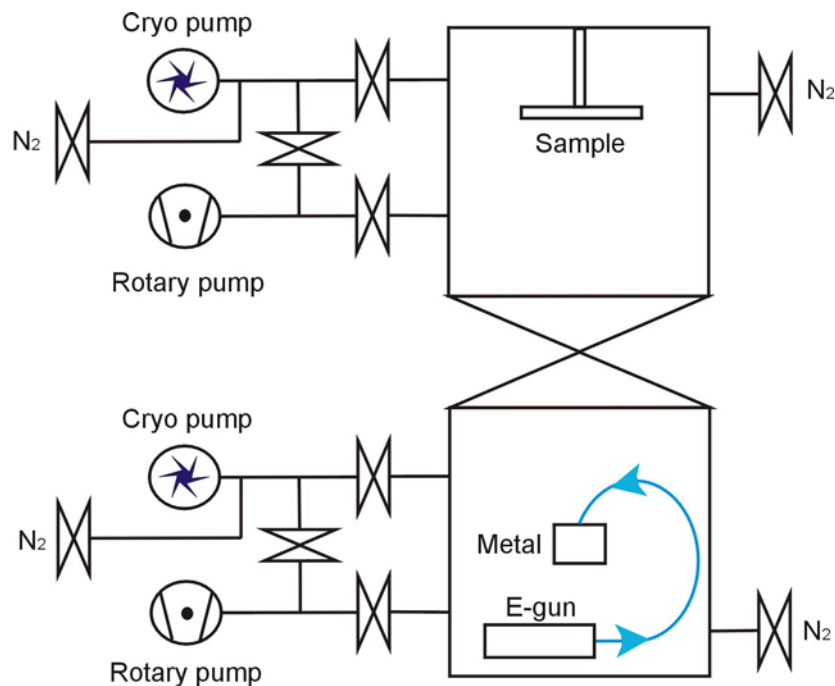


Figure A.9. Schematic of Plassys MEB 400S electron-beam evaporator. A valve separates the sample chamber from the metal crucibles, which remain permanently at high vacuum. The details of this schematic were obtained from the Plassys MEB 400S' operation software.

#### A.1.2.2 Resistive heating evaporator

An in-house resistive heating evaporator was used for metals not available in the JWNC's electron-beam evaporation systems. The system has space for 6 evaporation boats (tungsten, alumina or ceramic) contained within a high-pressure bell-jar, evacuated by a rotary pump and a diffusion pump in turn to  $10^{-6}$  Torr. High currents are passed through the boats, heating up any metals contained within. When the temperature of the boat becomes high enough, the metal evaporates onto the sample situated above. A schematic of the system is shown in Figure A.10.

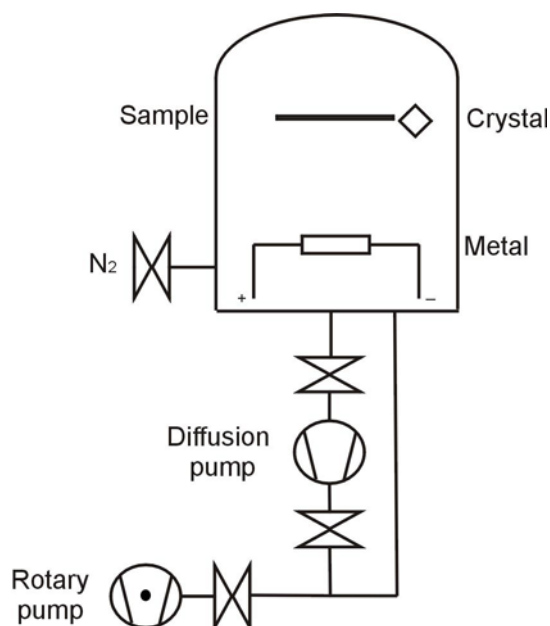


Figure A.10. Schematic of modified evaporator. All valves are manually operated.

Although resistive evaporators of this type are far simpler and less costly than their electron-beam counterparts, they are not without their problems. If using a metallic boat, evaporation of contaminants formed on the boat itself can contaminate the deposition layer. The boats themselves are small, limiting the thickness of the evaporated layer on the sample. Also, constant heating and cooling cycles put the boats under a large amount of stress, making them prone to cracking, breaking the circuit and preventing further evaporation.

As stated, the thickness of the metal film accumulating on the sample is measured using an oscillating quartz crystal sensor situated next to the sample. A read out of the crystal's oscillatory frequency is monitored as metal is evaporated, its frequency damped by the additional mass. The drop in frequency is directly related to the thickness of the metal film on the sample. Since different metals have different densities, each affects the crystal frequency by a different amount. Calibration graphs of thickness against frequency must be consulted to ensure the correct layer thickness is reached.

This system is completely manual, so boat current, evaporation rate and shutter operation are reliant on the user. Once the correct boat has been selected, the current must be turned up gradually until a frequency change is observed in the quartz crystal, indicating evaporation has started. When a steady rate has been reached the manual shutter can be opened, exposing the sample to the evaporating metal. The shutter is closed again when the frequency corresponding to the desired thickness has been reached.

### A.1.3 Optical characterisation using a Shimadzu UV3101PC absorption spectrometer

Figure A.11 shows the set-up of the Shimadzu UV3101PC absorption spectrometer. Recording the transmission of light through the sample allows for an accurate measurement of the structure's plasmon to be made since it accounts for losses due to both absorption and reflection. Measurements of this type are commonly referred to as “extinction” and allow an extinction cross section to be calculated using either of the following methods<sup>29</sup>:

$$E = 1 - T \quad (\text{A.2})$$

where T is transmittance, and E is expressed as a percentage.

$$E = \log\left(\frac{I}{I_0}\right) \quad (\text{A.3})$$

where I is the incident light intensity and  $I_0$  is the transmitted light intensity and E is expressed as a dimensionless property.

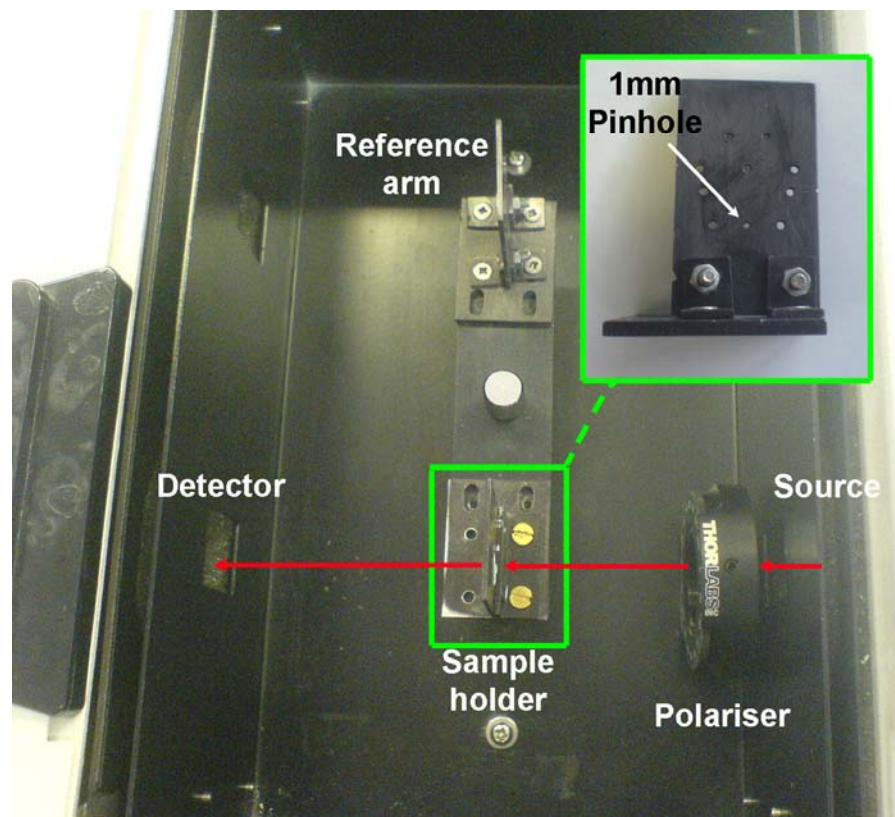


Figure A.11. Experimental layout of the Shimadzu UV3101PC absorption spectrometer. A Thor Labs linear thin film polariser is used to control the electric field orientation of the radiation passing through the sample. The sections marked “sample holder” and “reference arm” consist of home built metal holders

with a variety of pinhole sizes drilled through them. The sensor arrays are aligned to the pinhole in the “sample holder” before measurement and held in place using Blu-Tack adhesive (only the 1 mm pinhole is used in measurements as this corresponds to the size of the square arrays being tested). A clean piece of Pyrex glass was placed over the pinhole on the reference arm. The pinholes were then aligned to the narrow beam emitted from the spectrometer light source through a 5 mm slit. Transmission measurements were taken from 400 nm to 2500 nm.

#### A.1.4 Hitachi S-4700 Scanning electron microscopy (SEM)

All scanning electron micrographs were taken using a Hitachi S-4700 SEM. Having a substantially shorter wavelength than light, electrons can be used to resolve features on a nanometre scale. The electrons, produced by applying voltage to a sharpened tungsten tip, are focused by a series of electromagnetic lenses and scanned in a raster fashion over the sample using electromagnetic deflection coils (all of which is performed in a high vacuum environment). Two detectors, one positioned adjacent to the sample, the other behind the objective lens (TTL - through the lens detector), collect the backscattered and secondary electrons from the sample, building up a picture of its topography.<sup>125</sup>

It is difficult to obtain high-resolution images from insulating sample, such as glass, because of a build up of charge on the sample’s surface. Samples of this type require coating with a thin layer of metal in order to make them conductive, and hence fully compatible with the electron microscope.

#### A.1.5 Atomic Force Microscopy (AFM)

Topographical characterisation of the fabricated structures was carried out using a JPK Nanowizard AFM. Atomic force microscopes use piezoelectrically controlled microscale cantilevers with sharp tips (typically on the order of nanometres) to physically interrogate the surface features of a sample. As the tip is moved across the sample, the cantilever deflects due to interaction with the surface, this deflection being monitored by laser light reflected from the top of the cantilever onto a photodiode array. Two types of operation are available; contact mode, where the tip is dragged across the sample’s surface, and tapping (or intermittent contact) mode, where the cantilever is set to a resonant frequency by the piezoelectric crystal and drawn across the surface. Contact with the surface retards this resonance, allowing a topographical map of the structure to be created (a feedback loop from the photodiodes to the piezo crystal maintains the resonant frequency).<sup>126</sup>

#### A.1.6 TEMPEST Finite Difference Time Domain (FDTD) software

TEMPEST, or Time-domain electromagnetic massively parallel evaluation of scattering from topography, is a simulation package that allows the user to quickly assess the plasmonic properties of a newly designed nanostructure without the need for physical fabrication and testing. Throughout the research process TEMPEST software was used to both inform ring design and enable visualisation of localised electromagnetic fields generated as a consequence of plasmon resonance.

Structures can be optimised in the simulation domain to meet certain optical criteria, minimising the slow and expensive process of iterative fabrication and device characterisation. TEMPEST is FDTD software which breaks up a three dimensional environment, specified by the user, into a series of simulation nodes. Maxwell's equations are solved within each one of these nodes, determining the electric and magnetic fields at these points.<sup>127, 128</sup> With this information, a graphical representation of the localised fields can be constructed, along with relative field strengths at different points or planes within the computational area. For each simulation performed, a three dimensional space was created with appropriate size to encompass a single split-ring structure and its local environment. The materials within the boundaries are specified in terms of their refractive index, which in the case of metals includes both real and imaginary values.<sup>50</sup> The source, direction, wavelength and polarisation of an electromagnetic plane wave must also be specified. In order to prevent reflections from the simulation boundaries interfering with the results, perfectly absorbing layers (referred to in the software as PML - Perfectly Matched Layers), matched to their immediate environment, are positioned at both extremes of the z-plane. Typically, the z-plane of the simulation volume was divided in equal parts representing the substrate and air; the metallic split-ring structure being positioned directly on the surface of the substrate, in the centre of the x and y planes, Figure A.12.

Although the software models the entire simulation volume, only EM values from predetermined slices or points will be included in the output file. In order to obtain both a visual representation of the ring's plasmon, as well as establish its specific resonance wavelength, the sum of the electric field in the x, y and z directions was recorded as a slice through the simulation space at two positions in the z-plane; one through layer of nodes which constitute the boundary between the nanostructure and the air (for visualisation of the induced electromagnetic field amplification), another at the base of the substrate, 30 nm above the PML. Transmission, T, can be measured numerically by comparing the sum of the field intensities at the base of the substrate with an identical measurement taken from a simulation where no ring is present:

$$T=I/I_0 \tag{A.4}$$

Where  $I_0$  is the intensity of the field at the base of the substrate when no metallic structure is present, and I is the intensity of the field at the same point when a metallic structure is present. The extinction cross section,  $\sigma_{ext}$ , can also be determined using:<sup>39, 52</sup>

$$\sigma_{ext} = -(I - I_0 / N I_0) \tag{A.5}$$

Where N is the two-dimensional particle density.

Figure A.12 shows a graphical representation of the simulation stack used to perform the calculations. Table A.1 shows the input parameters used to represent the materials used in the simulation at each excitation wavelength. Au simulations were run from 400 - 2500 nm, whereas Ag simulations were run from 400 - 2000 nm. The Ti adhesion layer, used when fabricating with Au, was simulated for all wavelengths where data existed, 400 - 1900nm. Simulations of Au rings in the wavelength range 1900 - 2500 nm did not include an adhesion layer in the model.

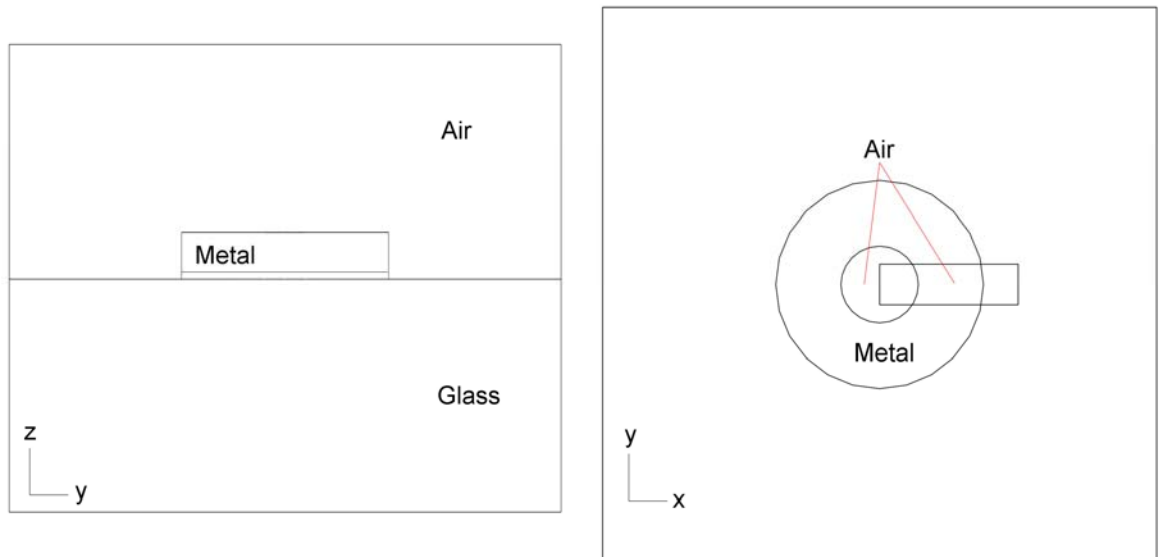


Figure A.12. A graphical representation of the three-dimensional simulation domain used to model the split-ring nanostructures (side view, left; top view, right). The ring structure was defined using 2 cylinders, one metal the other air. A rectangular block with the same z-dimension was used to define the split in the ring geometry. Typically the glass and air blocks had a z-dimension of 100nm each. X and y dimensions were chosen according to the periodicity of the array being modelled. The refractive index of Pyrex glass and air used throughout were 1.47 and 1 respectively.

Wavelength (nm)	Refractive index					
	Au		Ag		Ti	
	n	k	n	k	n	k
400	1.658	1.9560	0.173	1.950	2.090	2.955
500	0.855	1.8953	0.130	2.918	2.373	3.209
600	0.249	2.9906	0.124	3.732	2.637	3.654
700	0.161	3.9523	0.142	4.523	2.851	3.949
800	0.181	5.1178	0.144	5.289	3.146	4.010
900	0.216	6.0050	0.170	6.051	3.296	3.961
1000	0.257	6.8196	0.214	6.757	3.375	3.978
1100	0.300	7.6819	0.244	7.475	3.513	4.034
1200	0.351	8.4734	0.301	8.200	3.607	4.136
1300	0.408	8.3028	0.367	8.582	3.645	4.262
1400	0.469	9.1751	0.418	8.370	3.671	4.382
1500	0.530	9.5070	0.451	9.013	3.681	4.544
1600	0.590	10.1503	0.489	9.636	3.689	4.686
1700	0.651	10.7585	0.529	10.260	3.634	4.853
1800	0.728	12.1245	0.569	10.923	3.578	5.006
1900	0.782	12.0100	0.609	11.545	3.527	5.143
2000	0.850	12.6019	0.650	12.200	-	-

2100	0.962	14.2968	-	-	-	-
2200	0.992	13.8088	-	-	-	-
2300	1.066	14.4230	-	-	-	-
2400	1.142	14.9992	-	-	-	-
2500	1.221	15.6185	-	-	-	-

Table A.1. Refractive index values for Au, Ag and Ti used in the simulations. Au and Ag values were taken from Palik.<sup>50</sup> Ti values were taken from Johnson and Christy.<sup>129</sup>

#### A.1.7 X-ray Photoelectron Spectroscopy (XPS) using a Scienta ESCA300 XPS tool

XPS is a spectroscopic technique that relies on the photoelectric effect to perform analysis of a sample's surface composition. The Scienta ESCA300 XPS located at Daresbury laboratories was used throughout this research to interrogate the surface chemistry of the sensors.

High energy photons, focused onto a 6 x 0.5 mm area of the sample, were absorbed by the sample, their energy transferred to the electrons of the surface elements. Should the subsequent electron energy be greater than that of the electron binding energy, the electron will be emitted from the surface (this emitted electron is referred to as a photoelectron). It is by collecting and analysing these photoelectrons that the elemental composition of the sample can be determined. The binding energy of the surface electrons is the difference between the known energy of the incident X-rays and the kinetic energy of the emitted photoelectrons (measured by the energy analyser and detector)<sup>130</sup>:

$$E_B = hv - E_K - \phi \quad (\text{A.6})$$

where  $E_K$  is the binding energy,  $hv$  is the energy of the X-ray, and  $\phi$  is a constant relating to the spectrometer work function.

The XPS tool consists of five main components; a rotating anode X-ray source with a maximum power of 8kW, a 7 crystal X-ray monochromator which focuses the desired beam energies onto the sample, electrostatic electron lenses which collect the photoelectrons, a hemispherical dispersive energy analyser which controls the range of energies which reach the detector and separates photoelectrons into their individual frequencies, and a multi-channel array detector which counts the number photoelectrons of each frequency which successfully pass through the analyser, Figure A.13.

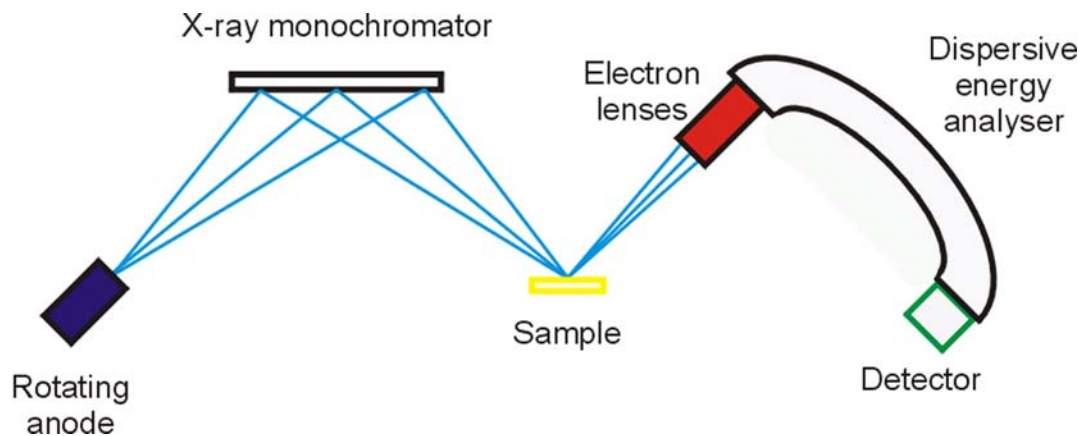


Figure A.13. Schematic showing the basic set-up and primary components of X-ray photoelectron spectrometer (not to scale).<sup>130</sup>

The depth to which the sample is probed can be adjusted by altering the angle of the sample with respect to the incident radiation, which in turn defines the angle at which the photoelectrons are ejected. Known as the Take-Off Angle (TOA), this can be adjusted manually on the Scienta ESCA300.

#### A.1.8 Zeiss LSM 510 META confocal fluorescence microscope

The Zeiss LSM 510 META confocal fluorescence microscope was used as a method of confirming sample modification with a fluorescent probe. Although designed for confocal microscopy, the system was used with the confocal hole set to infinity (i.e. non confocal). Although the system is equipped with a range of laser sources and excitation filters, working primarily with Cy5 meant that the 633 nm HeNe laser and a low-pass 650 nm filter were used as excitation source and fluorescence filter set respectively. Scan times and sensitivities were optimised to correspond to the type and amount of material present on the sample.

#### A.1.9 Horiba Jobin Yvon Raman spectrometer

Figure A.14 shows optical set-up and beam paths for the Horiba Jobin Yvon LabRam INV spectrometer (633 nm and 785 nm operation). This set-up was used in conjunction with an Olympus IX70 microscope.

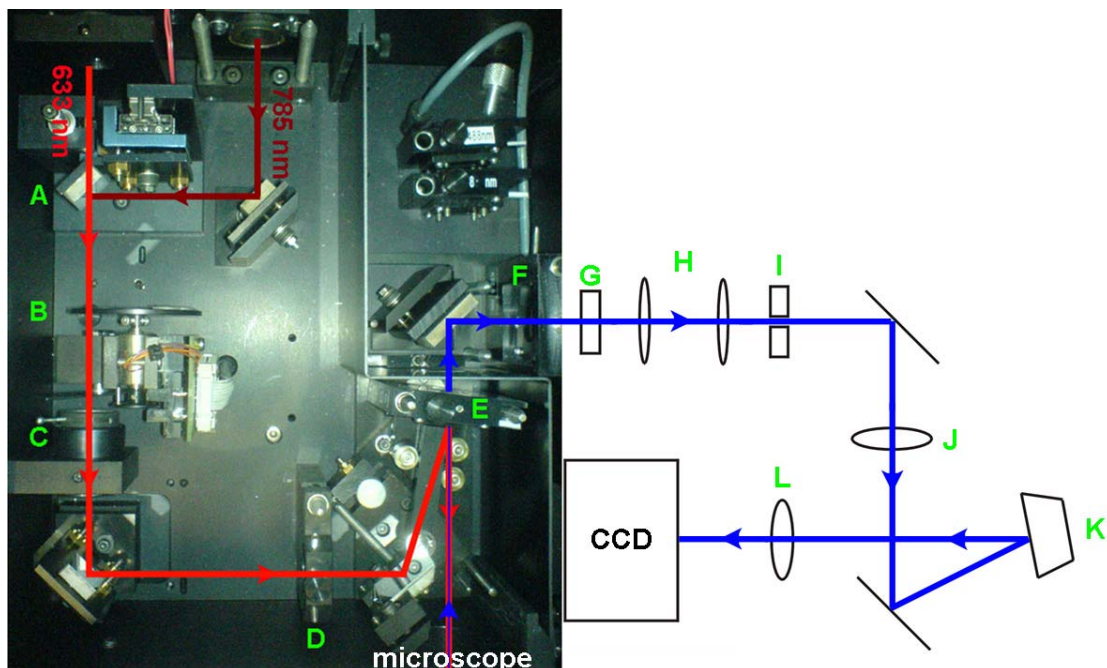


Figure A.14. Optical diagram of LabRam spectrometer: A- moveable mirror allowing 633 or 785 nm laser to be selected; B- neutral density filters; C- focusing lens; D- Pinhole; E- interchangeable notch filter; F- secondary notch filter; G- confocal hole; H- focusing lenses; I- spectrometer entrance slit; J and L- collimating lenses; K- interchangeable diffraction gratings.

An interchangeable mirror arrangement at A allows either the 633 nm HeNe laser or the 785 nm diode laser to be used. A selection of neutral density filters is available at B to adjust the beam's power. The beam is then focused by a lens at C before passing through a pinhole at D. A notch filter at E, angled to align the beam with the microscope, acts to both reflect the laser light toward the sample and transmit the inelastically scattered light (blue line in Figure A.14) gathered by the objective lens toward the spectrometer (this filter can be changed to correspond to the correct excitation wavelength). A second notch filter is positioned at F for further control over the excitation line (only used for the 633 nm laser).

A confocal hole is positioned at G, ensuring that only the light scattered from the focal plane of the laser passes through the spectrometer's entrance slit (I) and is imaged on the CCD. The diameter of the hole, and hence the confocality of the system, can be adjusted from within the software. However altering of the hole's diameter results in a trade-off between system confocality and sensitivity, with smaller holes reducing both the depth of focus and the amount of light entering the spectrometer. For the system to be considered confocal, the diameter of the pinhole must be roughly the size of the focused laser's Airy disk (the diameter termed the Airy unit). The pinhole is considered to be infinitely large if its diameter is greater than 4-5 Airy units. In this case, the system is no longer considered confocal. All Raman measurements carried out with the Horiba Jobin Yvon LabRam INV were done so using a pinhole diameter of 1000  $\mu\text{m}$  in order to maximise the collection of scattered light. As such, the system is not acting in a confocal manner, although since the sensors are fabricated on a substrate, are no more than 30

nm high, and all measurements were obtained in air from molecules immobilised to surface, the confocality of the system is largely irrelevant.

The spectrometer consists, primarily, of two interchangeable diffraction gratings (a 1800 g/mm grating for use with the 633 nm laser, and a 950g/mm grating for use with the 785 nm laser, positioned at K in Figure A.13) and a CCD detector. Also housed within the spectrometer are two collimating lenses, which the beam passes through both before (J) and after (L) the grating.

The power of each unfiltered laser, measured at the objective, was 5mW and 9.5mW for the 633 nm and 785 nm lasers respectively. The laser power can be adjusted using a range of neutral density filters, positioned on a rotating disk in the beam's path and selected using the system's software. These can prove essential when using fluorescent samples that may otherwise saturate the detector (the CCD has an upper limit of approximately 32000 counts per second). The excitation wavelength can also have a bearing on filter choice. Since Raman scattering is considerably less efficient at higher wavelengths (the efficiency of Raman scatter is related to the wavelength of the exciting light by  $1/\lambda^4$ ),<sup>85</sup> more laser power is required to elicit comparable signal strengths. The D1 filter (optical density of 1, corresponding to approximately 10% transmittance) was generally used together with the 633 nm excitation source, the filter acting to reduce the fluorescence from the Cy5 dye used in certain experiments. Although the use of the filter resulted in a laser power drop from 5mW to 0.5mW, this set-up was still capable of recording good Raman spectra from low concentration samples. However, when using the 785 nm laser source, no scattering was evident when using the D1 filter (laser power at objective was measured at 1mW in this case), while good spectra could be obtained from the unfiltered beam (9.5mW).

#### A.1.10 532 nm Raman set-up with Ocean Optics Spectrometer

Figure A.15 shows a schematic of the 532 nm Raman set-up using an Ocean Optics QE65000 spectrometer, a Melles Griot 532 nm, 10mW diode pumped solid state laser and a Zeiss Axiovert 40 CFL microscope.

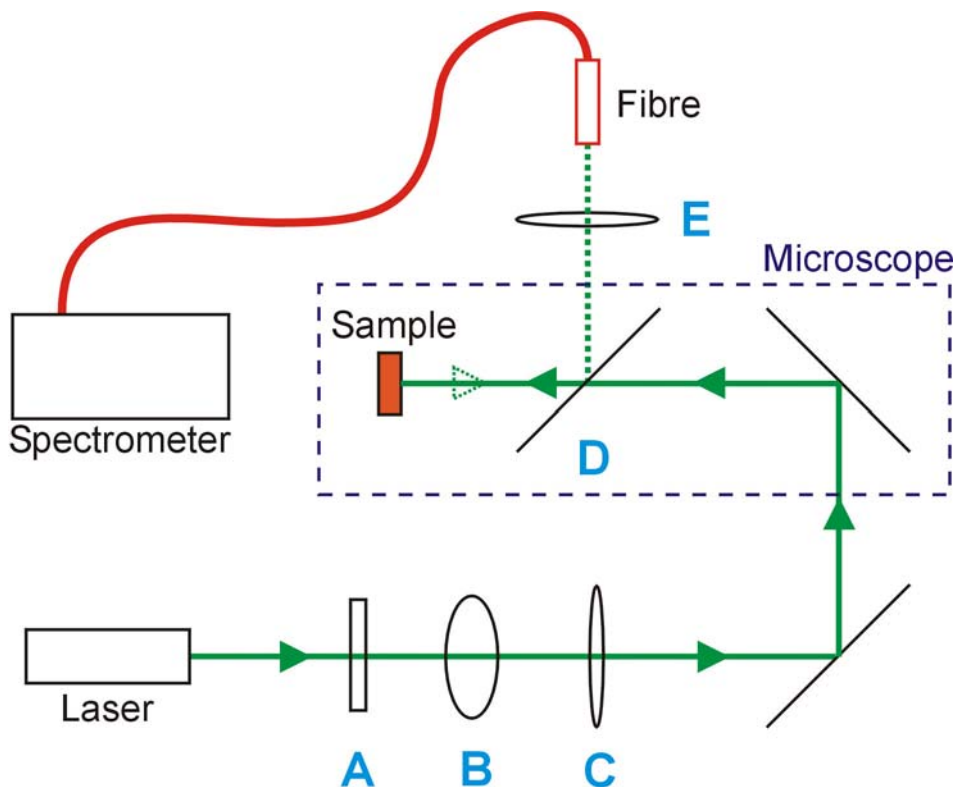


Figure A.15. Set-up for performing SERS at 532 nm. The beam passes through a neutral density filter at A, before being collimated, and subsequently refocused, by lenses B and C. Once inside the microscope, a dichroic, D, transmits the laser line toward the sample and reflects all inelastically scattered light out of the microscope's front/camera port, where it is coupled into a fibre optic cable by lens E. This fibre carries the light to the Ocean Optics portable Raman spectrometer.

#### A.1.11 Chemical structure of 2-mercaptopyridine

Figure A.16 shows the molecular structure of 2-mercaptopyridine.

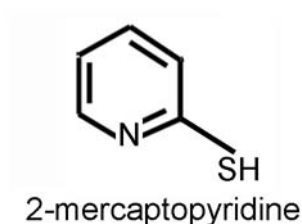


Figure A.16. Structure of 2-mercaptopyridine. The thiol group ensures attachment to the silver sensor. The chemical structure seen in this figure was obtained from Sigma-Aldrich's website.

#### A.1.12 Chemical structure of 3-aminopropyltriethoxysilane

Figure A.17 shows the molecular structure of 3-aminopropyltriethoxysilane.

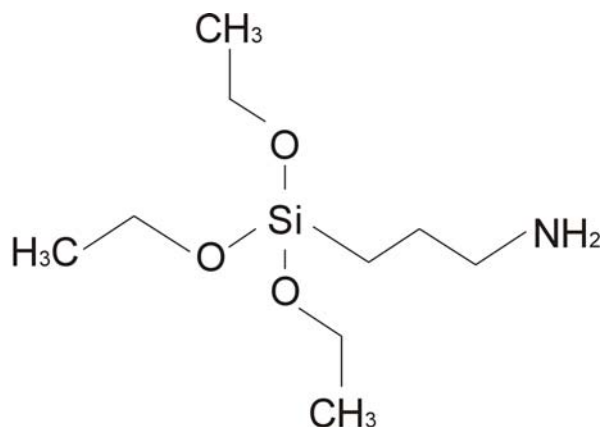


Figure A.17. Structure of 3-aminopropyltriethoxysilane. The chemical structure seen in this figure was obtained from the Sigma-Aldrich website. Details of glass slide modification with 3-aminopropyltriethoxysilane can be found in Section 2.3.1.8.

#### A.1.13 Chemical structures and binding mechanisms of Cysteamine and Cy5 N-Hydroxysuccinimide (NHS)

Figure A.18 depicts the molecular structure of Cy5 N-Hydroxysuccinimide; consisting of a cyanine derived Cy5 dye and an NHS ester compound.

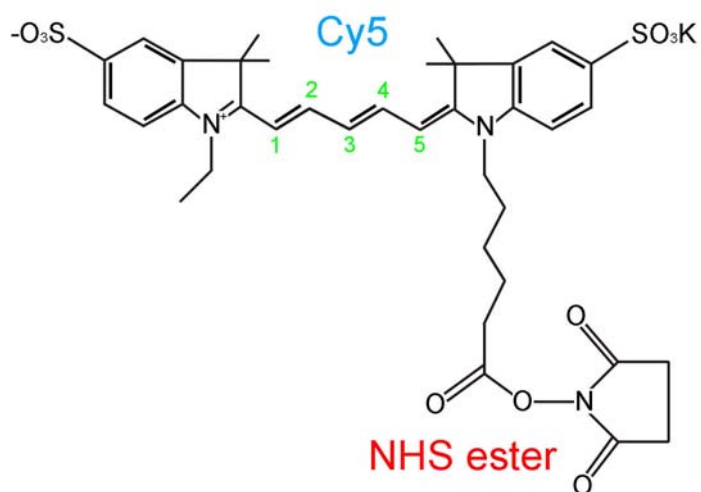


Figure A.18. Cy5 Mono NHS ester. Cy5 is a cyanine derived dye, the number 5 referring to the number of carbon atoms in the molecule's methine chain<sup>131</sup> (the structure seen in this figure was taken from Amersham Biosciences data sheet supplied with the chemical).

Figure A.19 shows the structure of cysteamine (top left), and its reaction with Cy5 NHS.<sup>101</sup>

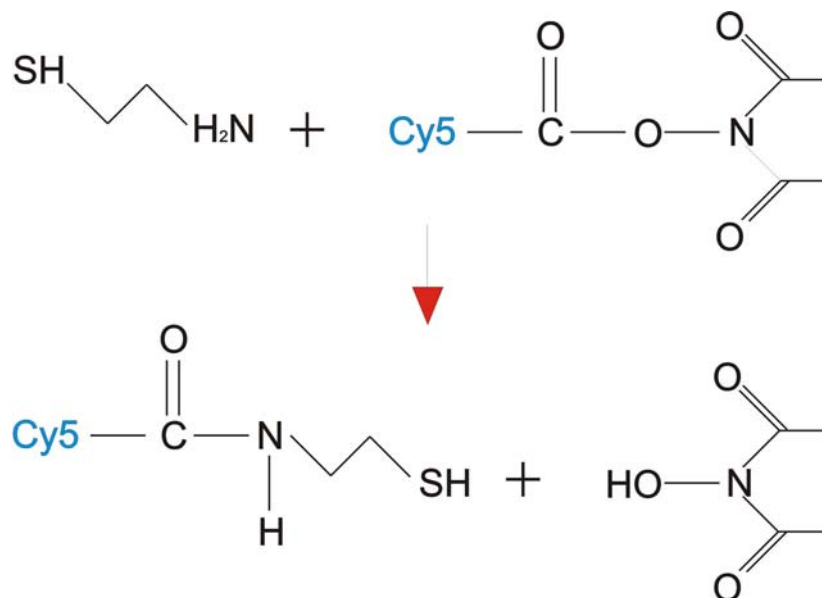


Figure A.19. Cysteamine interaction with Cy5 mono NHS-ester. The amine group of cysteamine (attached to the sensor surface by virtue of its thiol group) reacts with the NHS-ester, forming a covalent amide bond, with the subsequent release of N-hydroxysuccinimide. The sensor surface is modified with a monolayer of Cy5 as a result. The structure of cysteamine was taken from the Sigma-Aldrich website.

#### A.1.14 Modifying the Ag sensor surface with DNA

Deoxyribonucleic acid (DNA) is a polymer structure containing the genetic information necessary for cellular function and is present in all living organisms. These polymers comprise of chains of nucleotides, which in turn are made up of a phosphate, a sugar (2'-deoxyribose), and a heterocyclic amine base<sup>101</sup>, Figure A.20. The phosphate and sugar groups form the backbone of the chain (the phosphate joining the 3<sup>rd</sup> and 5<sup>th</sup> carbon atoms of alternate sugars) while the base is linked to the 1<sup>st</sup> carbon atom of the sugar and allows interaction with another DNA chain via hydrogen bonding, the two chains linking together in a double-helix formation. The sugar's structure dictates that in any polymer chain, one end will have a free hydroxyl group (the 3' end) while the other has a free phosphate group (the 5' end).

Four different bases exist for DNA, these are adenine, guanine, cytosine and thymine (A, G, C and T), Figure A.20. The structure of the bases dictate that only G can bind to C, and only A can bind to T, a process known as complementary base pairing (the binding of two complimentary strands is known as hybridisation).<sup>101</sup>

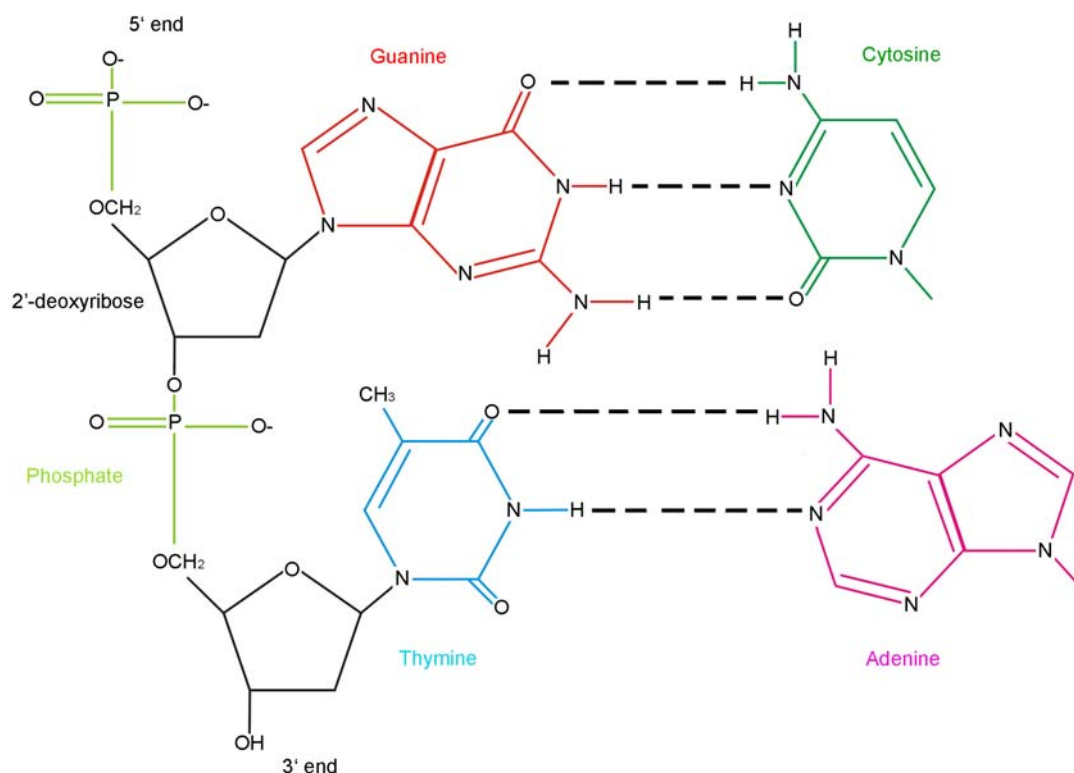


Figure A.20. DNA structure and base pairing diagram. The sugar-phosphate backbone can be seen on the left of the diagram, also shown are the molecular structures of the bases and a representation of their exclusively complementary pairing via hydrogen bonding.<sup>101</sup>

The DNA used throughout this research could more appropriately be described by the term oligonucleotide. This refers to a single DNA polymer chain (i.e. not bound to another in a double-helix) comprising of only a small number of bases, typically around 20. The sequences used in this research had either 16 or 17 bases (see Section 2.2).

#### A.1.15 Chemical structure of Cy5 and Cy7 linked to an oligonucleotide strand

Two Raman active dyes, Cy5 and Cy7, were used as markers in the various DNA experiments described in Chapter 5. Figure A.21 depicts the structure of these dyes.

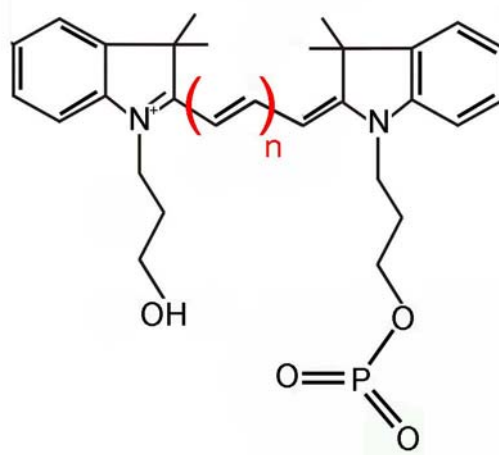


Figure A.21. Structure of Cy5 and Cy7 dye attached to oligonucleotide. The basic structure of Cy5 and Cy7 is the same, differing only by the length of their methine chain;  $n=2$ =Cy5,  $n=3$ =Cy7. Side chains show how the dye can be linked to the oligonucleotide using either the free phosphate group (5') or the free hydroxyl group (3'). The chemical structures in this figure were obtained from Atdbio, University of Southampton, the suppliers of the chemicals.

#### A.1.16 Reduction of the thiol groups on the DNA

Thiol groups on sequences A and B ensured that they attach to the Ag sensor surface, packing together to form a SAM. In solution, thiolated sequences can bond together, forming a disulphide bridge due to oxidation of the sulphhydryl (SH) group. This, in turn, lowers the thiol-Ag binding efficiency. As a result, DNA solutions containing thiol groups must be reduced before they can be attached to the sensor. Figure A.22 shows the reduction of the disulphide groups on the oligonucleotides using dithiothreitol (DTT).<sup>101</sup>

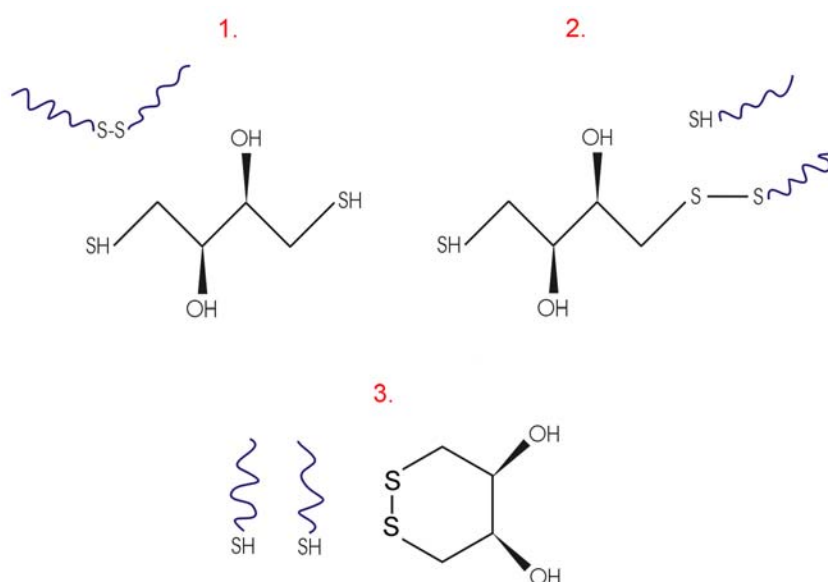


Figure A.22. DTT structure and Thiol-disulphide exchange. 1- DTT and DNA in solution, pairs of DNA are bound together due to disulphide bridges forming between thiol groups. 2- First thiol-disulphide exchange takes place, leaving one oligonucleotide with a reduced thiol group while the other strand forms a disulphide bond with the DTT's recently deprotonated thiol group. 3- The second thiol-disulphide exchange occurs through oxidation of DTT's other thiol group, closing the ring and leaving behind two separated DNA

strands, each with a complete thiol group.<sup>101</sup> The structure of DTT was taken from the Sigma-Aldrich website.

## References

1. K. Kneipp, Y. Wang, H. Kneipp, L.T. Perelman, I. Itzkan, R. Dasari, and M.S. Feld, *Physical Review Letters*, **78**, 1667-1670, (1997).
2. S.M. Nie and S.R. Emery, *Science*, **275**, 1102-1106, (1997).
3. R. Raiteri, M. Grattarola, H.J. Butt, and P. Skladal, *Sensors and Actuators B-Chemical*, **79**, 115-126, (2001).
4. M. Moskovits, *Reviews of Modern Physics*, **57**, 783-826, (1985).
5. M. Moskovits, *Journal of Raman Spectroscopy*, **36**, 485-496, (2005).
6. J. Homola, S.S. Yee, and G. Gauglitz, *Sensors and Actuators B-Chemical*, **54**, 3-15, (1999).
7. A.J. Haes and R.P. Van Duyne, *Analytical and Bioanalytical Chemistry*, **379**, 920-930, (2004).
8. S. Schultz, D.R. Smith, J.J. Mock, and D.A. Schultz, *Proceedings of the National Academy of Sciences of the United States of America*, **97**, 996-1001, (2000).
9. T.A. Taton, G. Lu, and C.A. Mirkin, *Journal of the American Chemical Society*, **123**, 5164-5165, (2001).
10. J. Yguerabide and E.E. Yguerabide, *Analytical Biochemistry*, **262**, 157-176, (1998).
11. Y.C. Cao, R.C. Jin, S. Thaxton, and C.A. Mirkin, *Talanta*, **67**, 449-455, (2005).
12. C.A. Mirkin, R.L. Letsinger, R.C. Mucic, and J.J. Storhoff, *Nature*, **382**, 607-609, (1996).
13. C.S. Tsai, T.B. Yu, and C.T. Chen, *Chemical Communications*, 4273-4275, (2005).
14. M.D. Malinsky, K.L. Kelly, G.C. Schatz, and R.P. Van Duyne, *Journal of the American Chemical Society*, **123**, 1471-1482, (2001).
15. G. Raschke, S. Kowarik, T. Franzl, C. Sonnichsen, T.A. Klar, J. Feldmann, A. Nichtl, and K. Kurzinger, *Nano Letters*, **3**, 935-938, (2003).
16. Fleischm.M, P.J. Hendra, and McQuilla.Aj, *Chemical Physics Letters*, **26**, 163-166, (1974).
17. C.L. Haynes, C.R. Yonzon, X.Y. Zhang, and R.P. Van Duyne, *Journal of Raman Spectroscopy*, **36**, 471-484, (2005).
18. J.N. Anker, W.P. Hall, O. Lyandres, N.C. Shah, J. Zhao, and R.P. Van Duyne, *Nature Materials*, **7**, 442-453, (2008).
19. M. Hu, J.Y. Chen, Z.Y. Li, L. Au, G.V. Hartland, X.D. Li, M. Marquez, and Y.N. Xia, *Chemical Society Reviews*, **35**, 1084-1094, (2006).
20. M.E. Stewart, C.R. Anderton, L.B. Thompson, J. Maria, S.K. Gray, J.A. Rogers, and R.G. Nuzzo, *Chemical Reviews*, **108**, 494-521, (2008).
21. C. Bohren and D. Huffman, *Absorption and Scattering of Light by Small Particles*. 1983: John Wiley & Sons.
22. T.W. Ebbesen, C. Genet, and S.I. Bozhevolnyi, *Physics Today*, **61**, 44-50, (2008).
23. S.A.Maier, *Plasmonics: Fundamentals and Applications*. 2007, New York: Springer.
24. M.L. Brongersma and P.G. Kik, *Surface Plasmon Nanophotonics*. 2007, Dordrecht: Springer.
25. H. Raether, *Surface Plasmons on Smooth and Rough Surfaces and on Gratings*. Springer Tracts in Modern Physics. 1988: Springer.
26. A. Otto, *Zeitschrift Fur Physik*, **216**, 398-&, (1968).
27. K.L. Kelly, E. Coronado, L.L. Zhao, and G.C. Schatz, *Journal of Physical Chemistry B*, **107**, 668-677, (2003).
28. H.X. Xu, J. Aizpurua, M. Kall, and P. Apell, *Physical Review E*, **62**, 4318-4324, (2000).
29. U. Kreibig and M. Vollmer, *Optical properties of metal clusters*. 1995, Berlin Heidelberg: Springer.

30. E. Hutter and J.H. Fendler, *Advanced Materials*, **16**, 1685-1706, (2004).
31. A. Wokaun, J.P. Gordon, and P.F. Liao, *Physical Review Letters*, **48**, 957-960, (1982).
32. T.R. Jensen, M.D. Malinsky, C.L. Haynes, and R.P. Van Duyne, *Journal of Physical Chemistry B*, **104**, 10549-10556, (2000).
33. G.H. Chan, J. Zhao, E.M. Hicks, G.C. Schatz, and R.P. Van Duyne, *Nano Letters*, **7**, 1947-1952, (2007).
34. R. Bukasov and J.S. Shumaker-Parry, *Nano Letters*, **7**, 1113-1118, (2007).
35. J. Kim, G.L. Liu, Y. Lu, and L.P. Lee, *Iee Proceedings-Nanobiotechnology*, **153**, 42-46, (2006).
36. E.M. Larsson, J. Alegret, M. Kall, and D.S. Sutherland, *Nano Letters*, **7**, 1256-1263, (2007).
37. Y. Lu, G.L. Liu, J. Kim, Y.X. Mejia, and L.P. Lee, *Nano Letters*, **5**, 119-124, (2005).
38. J.S. Shumaker-Parry, H. Rochholz, and M. Kreiter, *Advanced Materials*, **17**, 2131-2134, (2005).
39. J. Aizpurua, P. Hanarp, D.S. Sutherland, M. Kall, G.W. Bryant, and F.J.G. de Abajo, *Physical Review Letters*, **90**, (2003).
40. S.Y. Chou, P.R. Krauss, and P.J. Renstrom, *Science*, **272**, 85-87, (1996).
41. B.D. Lucas, J.S. Kim, C. Chin, and L.J. Guo, *Advanced Materials*, **20**, 1129-1134, (2008).
42. C. Enkrich, R. Perez-Willard, D. Gerthsen, J.F. Zhou, T. Koschny, C.M. Soukoulis, M. Wegener, and S. Linden, *Advanced Materials*, **17**, 2547-2549, (2005).
43. B. Lamprecht, G. Schider, R.T. Lechner, H. Ditlbacher, J.R. Krenn, A. Leitner, and F.R. Aussenegg, *Physical Review Letters*, **84**, 4721-4724, (2000).
44. H.G. Craighead and G.A. Niklasson, *Applied Physics Letters*, **44**, 1134-1136, (1984).
45. L. Gunnarsson, E.J. Bjerneld, H. Xu, S. Petronis, B. Kasemo, and M. Kall, *Applied Physics Letters*, **78**, 802-804, (2001).
46. J.J. Mock, M. Barbic, D.R. Smith, D.A. Schultz, and S. Schultz, *Journal of Chemical Physics*, **116**, 6755-6759, (2002).
47. W. Gotschy, K. Vonmetz, A. Leitner, and F.R. Aussenegg, *Applied Physics B-Lasers and Optics*, **63**, 381-384, (1996).
48. P. Hanarp, M. Kall, and D.S. Sutherland, *Journal of Physical Chemistry B*, **107**, 5768-5772, (2003).
49. C. Langhammer, B. Kasemo, and I. Zoric, *Journal of Chemical Physics*, **126**, 194702, (2007).
50. E.D. Palik, *Handbook of Optical Constants of Solids*. 1985, New York: Academic Press.
51. C. Langhammer, M. Schwind, B. Kasemo, and I. Zoric, *Nano Letters*, **8**, 1461-1471, (2008).
52. C. Langhammer, Z. Yuan, I. Zoric, and B. Kasemo, *Nano Letters*, **6**, 833-838, (2006).
53. L.J. Sherry, R.C. Jin, C.A. Mirkin, G.C. Schatz, and R.P. Van Duyne, *Nano Letters*, **6**, 2060-2065, (2006).
54. K.B. Crozier, A. Sundaramurthy, G.S. Kino, and C.F. Quate, *Journal of Applied Physics*, **94**, 4632-4642, (2003).
55. J.P. Kottmann, O.J.F. Martin, D.R. Smith, and S. Schultz, *Optics Express*, **6**, 213-219, (2000).
56. X.L. Li, W.Q. Xu, J.H. Zhang, H.Y. Jia, B. Yang, B. Zhao, B.F. Li, and Y. Ozaki, *Langmuir*, **20**, 1298-1304, (2004).

57. K.H. Su, Q.H. Wei, X. Zhang, J.J. Mock, D.R. Smith, and S. Schultz, *Nano Letters*, **3**, 1087-1090, (2003).
58. W. Rechberger, A. Hohenau, A. Leitner, J.R. Krenn, B. Lamprecht, and F.R. Aussenegg, *Optics Communications*, **220**, 137-141, (2003).
59. C.L. Haynes, A.D. McFarland, L.L. Zhao, R.P. Van Duyne, G.C. Schatz, L. Gunnarsson, J. Prikulis, B. Kasemo, and M. Kall, *Journal of Physical Chemistry B*, **107**, 7337-7342, (2003).
60. D.P. Fromm, A. Sundaramurthy, P.J. Schuck, G. Kino, and W.E. Moerner, *Nano Letters*, **4**, 957-961, (2004).
61. E. Hao and G.C. Schatz, *Journal of Chemical Physics*, **120**, 357-366, (2004).
62. C.E. Talley, J.B. Jackson, C. Oubre, N.K. Grady, C.W. Hollars, S.M. Lane, T.R. Huser, P. Nordlander, and N.J. Halas, *Nano Letters*, **5**, 1569-1574, (2005).
63. H.X. Xu and M. Kall, *Chemphyschem*, **4**, 1001-1005, (2003).
64. L. Gunnarsson, T. Rindzevicius, J. Prikulis, B. Kasemo, M. Kall, S.L. Zou, and G.C. Schatz, *Journal of Physical Chemistry B*, **109**, 1079-1087, (2005).
65. N. Felidj, J. Grand, G. Laurent, J. Aubard, G. Levi, A. Hohenau, N. Galler, F.R. Aussenegg, and J.R. Krenn, *Journal of Chemical Physics*, **128**, (2008).
66. E. Hao, R.C. Bailey, G.C. Schatz, J.T. Hupp, and S.Y. Li, *Nano Letters*, **4**, 327-330, (2004).
67. L.J. Sherry, S.H. Chang, G.C. Schatz, R.P. Van Duyne, B.J. Wiley, and Y.N. Xia, *Nano Letters*, **5**, 2034-2038, (2005).
68. G.W. Bryant, F.J.G. De Abajo, and J. Aizpurua, *Nano Letters*, **8**, 631-636, (2008).
69. S. Link and M.A. El-Sayed, *Journal of Physical Chemistry B*, **103**, 8410-8426, (1999).
70. E.K. Payne, K.L. Shuford, S. Park, G.C. Schatz, and C.A. Mirkin, *Journal of Physical Chemistry B*, **110**, 2150-2154, (2006).
71. W. Gotschy, K. Vonmetz, A. Leitner, and F.R. Aussenegg, *Optics Letters*, **21**, 1099-1101, (1996).
72. C. Rockstuhl, F. Lederer, C. Etrich, T. Zentgraf, J. Kuhl, and H. Giessen, *Optics Express*, **14**, 8827-8836, (2006).
73. C. Rockstuhl, T. Zentgraf, H. Guo, N. Liu, C. Etrich, I. Loa, K. Syassen, J. Kuhl, F. Lederer, and H. Giessen, *Applied Physics B-Lasers and Optics*, **84**, 219-227, (2006).
74. H. Rochholz, N. Bocchio, and M. Kreiter, *New Journal of Physics*, **9**, 53, (2007).
75. S. Linden, C. Enkrich, M. Wegener, J.F. Zhou, T. Koschny, and C.M. Soukoulis, *Science*, **306**, 1351-1353, (2004).
76. C. Enkrich, M. Wegener, S. Linden, S. Burger, L. Zschiedrich, F. Schmidt, J.F. Zhou, T. Koschny, and C.M. Soukoulis, *Physical Review Letters*, **95**, (2005).
77. J.B. Pendry, *Physical Review Letters*, **85**, 3966-3969, (2000).
78. T. Driscoll, G.O. Andreev, D.N. Basov, S. Palit, S.Y. Cho, N.M. Jokerst, and D.R. Smith, *Applied Physics Letters*, **91**, 062511, (2007).
79. H.C. Guo, N. Liu, L.W. Fu, H. Schweizer, S. Kaiser, and H. Giessen, *Physica Status Solidi B-Basic Solid State Physics*, **244**, 1256-1261, (2007).
80. M.W. Klein, C. Enkrich, M. Wegener, and S. Linden, *Science*, **313**, 502-504, (2006).
81. M.W. Klein, C. Enkrich, M. Wegener, C.M. Soukoulis, and S. Linden, *Optics Letters*, **31**, 1259-1261, (2006).
82. J. Zhou, T. Koschny, M. Kafesaki, E.N. Economou, J.B. Pendry, and C.M. Soukoulis, *Physical Review Letters*, **95**, 223902, (2005).
83. N.P. Johnson, A.Z. Khokhar, H.M.H. Chong, R.M. De la Rue, and S. McMeekin, *Electronics Letters*, **42**, 1117-1119, (2006).
84. C.Y. Chen, S.C. Wu, and T.J. Yen, *Applied Physics Letters*, **93**, 034110, (2008).

85. E. Smith and G. Dent, *Modern Raman Spectroscopy*. 2005: John Wiley & Sons.
86. J.R. Lombardi, R.L. Birke, T.H. Lu, and J. Xu, *Journal of Chemical Physics*, **84**, 4174-4180, (1986).
87. F.J. GarciaVidal and J.B. Pendry, *Physical Review Letters*, **77**, 1163-1166, (1996).
88. A. Campion and P. Kambhampati, *Chemical Society Reviews*, **27**, 241-250, (1998).
89. A. Otto, *Journal of Raman Spectroscopy*, **36**, 497-509, (2005).
90. E. Dulkeith, A.C. Morteani, T. Niedereichholz, T.A. Klar, J. Feldmann, S.A. Levi, F. van Veggel, D.N. Reinhoudt, M. Moller, and D.I. Gittins, *Physical Review Letters*, **89**, 203002, (2002).
91. J. Gersten and A. Nitzan, *Journal of Chemical Physics*, **75**, 1139-1152, (1981).
92. P. Anger, P. Bharadwaj, and L. Novotny, *Physical Review Letters*, **96**, 113002, (2006).
93. M.G. Albrecht and J.A. Creighton, *Journal of the American Chemical Society*, **99**, 5215-5217, (1977).
94. D.L. Jeanmaire and R.P. Vanduyne, *Journal of Electroanalytical Chemistry*, **84**, 1-20, (1977).
95. Y. Lu, G.L. Liu, and L.P. Lee, *Nano Letters*, **5**, 5-9, (2005).
96. A. Wei, B. Kim, B. Sadtler, and S.L. Tripp, *Chemphyschem*, **2**, 743-745, (2001).
97. Z.H. Zhu, T. Zhu, and Z.F. Liu, *Nanotechnology*, **15**, 357-364, (2004).
98. J.A. Baldwin, B. Vlckova, M.P. Andrews, and I.S. Butler, *Langmuir*, **13**, 3744-3751, (1997).
99. L. Tong, T. Zhu, and Z. Liu, *Applied Physics Letters*, **92**, 023109, (2008).
100. F. Svedberg, Z.P. Li, H.X. Xu, and M. Kall, *Nano Letters*, **6**, 2639-2641, (2006).
101. J. McMurry, *Organic Chemistry*. 1992: Brooks/Cole Publishing Company.
102. K.B. Li, L.V. Clime, B. Cui, and T. Veres, *Nanotechnology*, **19**, 145305, (2008).
103. H. Ditlbacher, A. Hohenau, D. Wagner, U. Kreibig, M. Rogers, F. Hofer, F.R. Aussenegg, and J.R. Krenn, *Physical Review Letters*, **95**, (2005).
104. K.L. Shuford, M.A. Ratner, and G.C. Schatz, *Journal of Chemical Physics*, **123**, 114713, (2005).
105. J.R. Lakowicz, C.D. Geddes, I. Gryczynski, J. Malicka, Z. Gryczynski, K. Aslan, J. Lukomska, E. Matveeva, J.A. Zhang, R. Badugu, and J. Huang, *Journal of Fluorescence*, **14**, 425-441, (2004).
106. P. Anger, P. Bharadwaj, and L. Novotny, *Physical Review Letters*, **96**, (2006).
107. T. Sawaguchi, F. Mizutani, S. Yoshimoto, and I. Taniguchi, *Electrochimica Acta*, **45**, 2861-2867, (2000).
108. T.A. Taton, C.A. Mirkin, and R.L. Letsinger, *Science*, **289**, 1757-1760, (2000).
109. J.M. Kohler, A. Csaki, J. Reichert, R. Moller, W. Straube, and W. Fritzsche, *Sensors and Actuators B-Chemical*, **76**, 166-172, (2001).
110. R.C. Bailey, J.M. Nam, C.A. Mirkin, and J.T. Hupp, *Journal of the American Chemical Society*, **125**, 13541-13547, (2003).
111. L.M. Demers, C.A. Mirkin, R.C. Mucic, R.A. Reynolds, R.L. Letsinger, R. Elghanian, and G. Viswanadham, *Analytical Chemistry*, **72**, 5535-5541, (2000).
112. S.O. Kelley, J.K. Barton, N.M. Jackson, and M.G. Hill, *Bioconjugate Chemistry*, **8**, 31-37, (1997).
113. D. Cunningham, R.E. Littleford, W.E. Smith, P.J. Lundahl, I. Khan, D.W. McComb, D. Graham, and N. Laforest, *Faraday Discussions*, **132**, 135-145, (2006).
114. H. Sato, M. Kawasaki, K. Kasatani, and M.A. Katsumata, *Journal of Raman Spectroscopy*, **19**, 129-132, (1988).
115. R.J. Stokes, A. Macaskill, P.J. Lundahl, W.E. Smith, K. Faulds, and D. Graham, *Small*, **3**, 1593-1601, (2007).
116. J.P. Yang and R.H. Callender, *Journal of Raman Spectroscopy*, **16**, 319-321, (1985).

117. S. Mahajan, J.J. Baumberg, A.E. Russell, and P.N. Bartlett, *Physical Chemistry Chemical Physics*, **9**, 6016-6020, (2007).
118. S.E.J. Bell and N.M.S. Sirimuthu, *Journal of the American Chemical Society*, **128**, 15580-15581, (2006).
119. K. Kneipp, H. Kneipp, V.B. Kartha, R. Manoharan, G. Deinum, I. Itzkan, R.R. Dasari, and M.S. Feld, *Physical Review E*, **57**, R6281-R6284, (1998).
120. K. Kneipp, W. Pohle, and H. Fabian, *Journal of Molecular Structure*, **244**, 183-192, (1991).
121. R.J. Stokes, A. Macaskill, J.A. Dougan, P.G. Hargreaves, H.M. Stanford, W.E. Smith, K. Faulds, and D. Graham, *Chemical Communications*, 2811-2813, (2007).
122. O.A. Saleh and L.L. Sohn, *Nano Letters*, **3**, 37-38, (2003).
123. M.J. Levene, J. Kurlach, S.W. Turner, M. Foquet, H.G. Craighead, and W.W. Webb, *Science*, **299**, 682-686, (2003).
124. X.G. Liang and S.Y. Chou, *Nano Letters*, **8**, 1472-1476, (2008).
125. O.C. Wells, *Scanning electron microscopy*. 1974, New York; London: McGraw-Hill.
126. N. Gadegaard, *Biotechnic & Histochemistry*, **81**, 87-97, (2006).
127. J.M. Montgomery, T.W. Lee, and S.K. Gray, *Journal of Physics-Condensed Matter*, **20**, 323201, (2008).
128. J. Zhao, A.O. Pinchuk, J.M. McMahon, S.Z. Li, L.K. Alisman, A.L. Atkinson, and G.C. Schatz, *Accounts of Chemical Research*, **41**, 1710-1720, (2008).
129. P.B. Johnson and R.W. Christy, *Physical Review B*, **9**, 5056-5070, (1974).
130. C.S. Fadleys, *Nuclear Instruments & Methods in Physics Research Section a-Accelerators Spectrometers Detectors and Associated Equipment*, **601**, 8-31, (2009).
131. L.A. Ernst, R.K. Gupta, R.B. Mujumdar, and A.S. Waggoner, *Cytometry*, **10**, 3-10, (1989).

